Advances in Experimental Medicine and Biology 1438

Felix Scholkmann
Joseph LaManna
Ursula Wolf *Editors*

Oxygen Transport to Tissue XLIV

Springer

Advances in Experimental Medicine and Biology

Volume 1438

Advances in Experimental Medicine and Biology provides a platform for scientific contributions in the main disciplines of the biomedicine and the life sciences. This series publishes thematic volumes on contemporary research in the areas of microbiology, immunology, neurosciences, biochemistry, biomedical engineering, genetics, physiology, and cancer research. Covering emerging topics and techniques in basic and clinical science, it brings together clinicians and researchers from various fields.

Advances in Experimental Medicine and Biology has been publishing exceptional works in the field for over 40 years, and is indexed in SCOPUS, Medline (PubMed), EMBASE, BIOSIS, Reaxys, EMBiology, the Chemical Abstracts Service (CAS), and Pathway Studio.
2022 CiteScore: 6.2

Felix Scholkmann
Joseph LaManna • Ursula Wolf
Editors

Oxygen Transport to Tissue XLIV

Springer

Editors
Felix Scholkmann
Institute of Complementary and
Integrative Medicine
University of Bern
Bern, Switzerland

Joseph LaManna
Department of Physiology & Biophysics
Case Western Reserve University
Cleveland, OH, USA

Biomedical Optics Research Laboratory
Department of Neonatology
University Hospital Zurich
University of Zurich
Zurich, Switzerland

Ursula Wolf
Institute of Complementary
and Integrative Medicine
University of Bern
Bern, Switzerland

ISSN 0065-2598 ISSN 2214-8019 (electronic)
Advances in Experimental Medicine and Biology
ISBN 978-3-031-42002-3 ISBN 978-3-031-42003-0 (eBook)
https://doi.org/10.1007/978-3-031-42003-0

This Springer imprint is published by the registered company Springer Nature Switzerland AG
The registered company address is: Gewerbestrasse 11, 6330 Cham, Switzerland

Paper in this product is recyclable.

Organization ISOTT 2022

Organizing Committee

Prof. Ursula Wolf (University of Bern, Switzerland)
Dr. Oliver Kress (University of Bern, Switzerland)
Dr. Tarcisi Cantieni (University of Bern, Switzerland)
Dr. Paolo Demaria (Zurich, Switzerland)
PD Dr. Felix Scholkmann (Universities of Bern and Zurich, Switzerland)

Scientific Committee

Prof. Ursula Wolf (University of Bern, Switzerland)
Prof. Michelle Puchowicz (Case Western Reserve University, USA)
Prof. Kaoru Sakatani (University of Tokyo, Japan)
Prof. Oliver Thews (University of Halle, Germany)

Conference Organization

Dr. Paolo Demaria (Zurich, Switzerland)

Group photo of the participants

Awards

The Melvin H. Knisely Award

It was established in 1983 to honor Dr. Knisely's accomplishments in the field of the transport of oxygen and other metabolites and anabolites in the human body. Over the years, he has inspired many young investigators, and this award is to honor his enthusiasm for assisting and encouraging young scientists and engineers in various disciplines. The award is to acknowledge outstanding young investigators. Award recipients:

1983: Antal G. Hudetz (Hungary)
1984: Andras Eke (Hungary)
1985: Nathan A. Bush (USA)
1986: Karlfried Groebe (Germany)
1987: Isumi Shibuya (Japan)
1988: Kyung A. Kang (Korea/USA)
1989: Sanja Batra (Canada)
1990: Stephen J. Cringle (Australia)
1991: Paul Okunieff (USA)
1992: Hans Degens (The Netherlands)
1993: David A. Benaron (USA)
1994: Koen van Rossem (Belgium)
1995: Clare E Elwell (UK)
1996: Sergei A. Vinogradov (USA)
1997: Chris Cooper (UK)
1998: Martin Wolf (Switzerland)
1999: Huiping Wu (USA)
2000: Valentina Quaresima (Italy)
2001: Fahmeed Hyder (Bangladesh)
2002: Geofrey De Visscher (Belgium)
2003: Mohammad Nadeem Khan (USA)
2004: Fredrick Palm (Sweden)
2005: Nicholas Lintell (Australia)
2007: Ilias Tachtsidis (UK)
2008: Kazuto Masamoto (Japan)
2009: Rossana Occhipinti (USA)
2010: Sebatiano Cicco (Italy)
2011: Mei Zhang (USA)

2012: Takahiro Igarashi (Japan)
2013: Malou Friederich-Persson (Sweden)
2014: David Highton (UK)
2015: Alexander Caicedo-Dorado (Belgium)
2016: Sally Pias (USA)
2017: Felix Scholkmann (Switzerland)
2018: Anne Riemann (Germany)
2019: Ting Li (China)
2021: An Ghysels (Belgium)
2022 Alexander Kalyanov (Switzerland)

The Dietrich W. Lübbers Award

It was established in honor of Professor Lübbers's long-standing commitment, interest, and contributions to the problems of oxygen transport to tissue and to the society. Award recipients:
1994: Michael Dubina (Russia)
1995: Philip E. James (UK/USA)
1996: Resit Demit (Germany)
1997: Juan Carlos Chavez (Peru)
1998: Nathan A. Davis (UK)
1999: Paola Pichiule (USA)
2000: Ian Balcer (USA)
2001: Theresa M. Busch (USA)
2002: Link K. Korah (USA)
2003: James J. Lee (USA)
2004: Richard Olson (Sweden)
2005: Charlotte Ives (UK)
2006: Bin Hong (China/USA)
2007: Helga Blockx (Belgium)
2008: Joke Vanderhaegen (Belgium)
2009: Matthew Bell (UK)
2010: Alexander Caicedo Dorado (Belgium)
2011: Malou Friedrich (Sweden)
2012: Maria Papademetriou (UK)
2013: Nannan Sun (China)
2014: Felix Scholkmann (Switzerland)
2015: Shun Takagi (Japan)
2016: Gemma Bale (UK)
2017: Ben Jones (UK)
2018: Hamoon Zohdi (Switzerland)
2019: Kazaki Hotta (Japan)
2021: Masamichi Moriya (Japan)
2022: Frédéric Lange (UK)

The Britton Chance Award

It was established in honor of Professor Chance's long-standing commitment, interest, and contributions to the science and engineering aspects of oxygen transport to tissue and to the society. Award recipients:
2004: Derek Brown (Switzerland)
2005: James Lee (USA)
2006: Hanzhu Jin (China/USA)
2007: Eric Mellon (USA)
2008: Jianting Wang (USA)
2009: Jessica Spires (USA)
2010: Ivo Trajkovic (Switzerland)
2011: Alexander Caicedo Dorado (Belgium)
2012: Felix Scholkmann (Switzerland)
2013: Tharindi Hapuarachchi (UK)
2014: Anne Riemann (Germany)
2015: Wenhao Xie (China)
2016: Linda Ahnen (Switzerland)
2017: Helene Isler (Switzerland)
2018: Jingjing Jiang (Switzerland)
2019: Alexander Kalyanov (Switzerland)
2021: Maheen Siddiqui (UK)
2022: Samaneh Davoudi (Belgium)

The Duane F. Bruley Travel Awards

They were established in 2003. They were created to provide travel funds for student researchers in all aspects of areas of oxygen transport to tissue. It is hoped that receiving the Duane F. Bruley Travel Award will inspire students to excel in their research and will assist in securing future leadership for ISOTT.
2004: Helga Blocks (Belgium), Jennifer Caddick (UK), Charlotte Ives (UK), Nicholas Lintell (Australia), Leonardo Mottola (Italy), Samin Rezania (USA/Iran), Ilias Tachtsidis (UK), Liang Tang (USA/China), Iyichi Sonoro (Japan), Antonio Franco (Italy)
2005: Robert Bradley (UK), Harald Oey (Australia), Kathy Hsieh (Australia), Jan Shah (Australia)
2006: Ben Gooch (UK), Ulf Jensen (Germany), Smruta Koppaka (USA), Daya Singh (UK), Martin Tisdall (UK), Bin Wong (USA), Kui Xu (USA)
2007: Dominique De Smet (Belgium), Thomas Ingram (UK), Nicola Lai (USA), Andrew Pinder (UK), Joke Vanderhaegen (Belgium)
2008: Sebastiano Chicco (Italy)
2009: Lei Gao (UK), Jianting Wang (USA), Obinna Ndubuizu (USA), Joke Vanderhaegen (Belgium)
2010: Zareen Bashir (UK), Tracy Moroz (UK), Mark Muthalib (Australia), Catalina Meßmer (USA), Takashi Eriguchi (Japan), Yoshihiro Murata (Japan), Jack Honeysett (UK), Martin Biallas (Switzerland)

2011: Catherine Hesford (UK), Luke S. Holdsworth (UK), Andreas Metz (Switzerland), Maria D. Papademetriou (UK), Patrik Persson (Sweden), Felix Scholkmann (Switzerland), Kouichi Yoshihara (Japan)
2012: Allann Al-Armaghany (UK), Malou Friederich-Persson (Sweden), Tharindi Hapuarachchi (UK), Benjamin Jones (UK), Rebecca Re (Italy), Yuta Sekiguchi (Japan), Ebba Sivertsson (Sweden), André Steimers (Germany)
2013: Allann Al-Armaghany (UK), Gemma Bale (UK), Alexander Caicedo-Dorado (Belgium), Luke Dunne (UK)
2014: Geraldine De Preter (Belgium), Benjamin Jones (UK), Stefan Kleiser (Switzerland), Nassimsadat Nasseri (Switzerland), Marie-Aline Neveu (Belgium), Shinsuke Nirengi (Japan), Takuya Osawa (Japan)
2015: Gemma Bale (UK), Chenyang Gao (China), Chae Jeong Lim (Korea), Phong Phan (UK), Guennadi Saiko (Canada), Kuangyu Shi (Germany), Nannan Sun (China)
2016: Isabel De Roever (UK), Yuya Enokida (Japan), Jingjing Jiang (Switzerland), Frédéric Lange (UK), Andreas J Metz (Switzerland), Shun Takagi (Japan)
2017: Luca Giannoni (UK), Jingjing Jiang (Switzerland), Alexander Kalyanov (Switzerland), Zuzana Kovacsova (UK), Nassim Nasseri (Switzerland), Maheen Faisal Siddiqui (UK), Shun Takagi (Japan), Yusuke Tsuruno (Japan), Lina Xu (Germany), Hamoon Zohdi (Switzerland)
2018: Andrei Belten (Canada), Aldo Di Costanzo Mata (Switzerland), Yuki Komuro (Japan), Joshua Russell-Buckland (UK), Dries Hendrikx (Belgium), Shun Takagi (Japan)
2019: Gary Angles (USA), Min Feng (USA), Thea Hüsing (Germany), Bhabuk Koirala (USA), Sho Kojima (Japan), Jonathan Nguyen (USA), Labiblais Rahman (Japan), Mandy Rauschner (Germany), Aarti Sethuraman (USA), Eileen Thiessen (USA)
2020: (meeting was omitted due to COVID-19 pandemic)
2021: (online meeting)
2022: Xianyin Hu (Japan), Djazia Yacheur (Switzerland), Victor Ochoa-Gutierrez (UK, Mexico), Tarcisi Cantieni (Switzerland), Tong Li (Switzerland)

Preface

The 2022 ISOTT conference saw a welcome return – following the COVID-19 pandemic – to an in-person event, this year at the famous Conference Center on Monte Verità, Ascona, Switzerland.

One of the unique features of ISOTT is that it is highly interdisciplinary. This was reflected in a rich and varied scientific program comprising all aspects of oxygen transport: from cells to organs and whole organisms; methods to measure oxygen and instrumentation; to clinical evidence. The program included 9 invited speakers, 62 abstracts (35 oral presentations [including invited speakers] and 27 posters) and 65 registered participants (13 students) from 11 countries.

The number of participants was lower than usual due to some remaining uncertainty surrounding the COVID-19 situation. Nevertheless, the wonderful spirit of ISOTT was evident and in full force, with participants taking advantage of ample time for discussion during, but also between, the sessions and at the meals and in the evenings. For many this was the first in-person conference after the pandemic, and people were clearly delighted to meet each other and have private and scientific discussions in a beautiful environment.

As usual, ISOTT 2022 featured an interested, prestigious, and active audience, well-attended sessions, and lively follow-up discussions at a high scientific level. Alongside the atmosphere of enthusiasm and mutual interest, a key highlight was the constructive and stimulating interaction between experts in the field and students. And so it was that we were able to celebrate the huge success of our ISOTT 2022 conference. We would like to thank everyone who participated or assisted in making this event such a memorable occasion.

Bern, Switzerland — Ursula Wolf
President ISOTT, 2022

Acknowledgements

Sponsors

As president of the 2022 Conference of the International Society on Oxygen Transport to Tissue, I, Ursula Wolf, would like to gratefully acknowledge the support of our sponsors:

Contributors

In addition, I would like to thank those who helped make this meeting a success: Oliver Kress, Tarcisi Cantieni, Martin Wolf, and in particular Paolo Demaria.

Reviewers

The manuscripts were reviewed by the following experts:

- Ilias Tachtsidis (University College London, UK)
- Heidrun Wabnitz (Physikalisch-Technische Bundesanstalt, Germany)
- Martin Wolf (University of Zurich, Switzerland)
- Ursula Wolf (University of Bern, Switzerland)
- Felix Scholkmann (Universities of Bern and Zurich, Switzerland)
- Joseph LaManna (Case Western Reserve University, USA)
- Kaoru Sakatani (University of Tokyo, Japan)
- Chris Cooper (University of Essex, UK)
- Harold M. Swartz (Geisel School of Medicine, USA)
- Peter Vaupel (University of Freiburg, Germany)
- Jingjing Jiang (University of Zurich, Switzerland)
- Mada Hashem (University of Calgary, Canada)
- Alexander Kalyanov (University of Zurich, Switzerland)
- Oliver Thews (University of Halle, Germany)
- Edwin Nemoto (University of New Mexico, USA)
- Hamoon Zohdi (University of Bern, Switzerland)
- Eiji Takahashi (Saga University, Japan)
- Sally Pias (New Mexico Institute of Mining and Technology, USA)
- Frederic Lange (University College London, UK)

We also thank Rachel Scholkmann for proofreading all manuscripts.

Contents

Part V Methods and Techniques

Part VI Clinical Application

Part I

Brain

1 Brain Tissue Oxygen and BOLD fMRI Under Different Levels of Neuronal Activity

D. P. Aksenov, K. Rutila, L. Li, M. J. Miller, D. A. Gascoigne, N. A. Serdyukova, E. D. Doubovikov, R. A. Linsenmeier, and A. Drobyshevsky

Abstract

Localized increases in neuronal activity are supported by the hemodynamic response, which delivers oxygen to the brain tissue to support synaptic functions, action potentials and other neuronal processes. However, it remains unknown if changes in baseline neuronal activity, which are expected to reflect neuronal metabolic demand, alter the relationship between the local hemodynamic and oxygen behaviour. In order to better characterize this system, we examine here the relationship between brain tissue oxygen (PO_2) and hemodynamic responses (BOLD functional MRI) under different levels of neuronal activity. By comparing the stimulus-evoked responses during different levels of baseline neuronal activity, the awake state vs isoflurane anesthesia, we were able to measure how a known change in neuronal demand affected tissue PO_2 as well as the hemodynamic response to stimulation. We observed a high correlation between stimulus-evoked PO_2 and BOLD responses in the awake state. Moreover, we found that the evoked PO_2 and BOLD responses were still present despite the elevated tissue oxygen baseline and decreased baseline of neuronal activity under low concentration isoflurane, and that the magnitudes of these responses decreased by similar proportions but the relationship between these signals was distorted. Our findings point to distortion of the BOLD-PO_2 relationship due to anesthesia. The feedback mechanism to adjust the level of brain tissue oxygen, as well

D. P. Aksenov (✉)
Department of Radiology, NorthShore University HealthSystem, Evanston, IL, USA

Department of Anesthesiology, NorthShore University HealthSystem, Evanston, IL, USA

University of Chicago, Pritzker School of Medicine, Chicago, IL, USA

Department of Biomedical Engineering, Northwestern University, Evanston, IL, USA
e-mail: daksenov@northshore.org

K. Rutila
Department of Biomedical Engineering, Northwestern University, Evanston, IL, USA

L. Li · M. J. Miller · D. A. Gascoigne
E. D. Doubovikov
Department of Radiology, NorthShore University HealthSystem, Evanston, IL, USA

N. A. Serdyukova · R. A. Linsenmeier
Department of Biomedical Engineering, Northwestern University, Evanston, IL, USA

Department of Neurobiology, Northwestern University, Evanston, IL, USA

A. Drobyshevsky
University of Chicago, Pritzker School of Medicine, Chicago, IL, USA

Department of Pediatrics, NorthShore University HealthSystem, Evanston, IL, USA

F. Scholkmann et al. (eds.), *Oxygen Transport to Tissue XLIV*, Advances in Experimental Medicine and Biology 1438, https://doi.org/10.1007/978-3-031-42003-0_1

as the correlation between BOLD and PO_2 responses, are impaired even by a small dose of anesthetics.

Keywords

Brain tissue oxygenation · BOLD response · anaesthesia

1.1 Introduction

Brain tissue oxygen (PO_2) level is maintained within a physiological range to avoid brain tissue damage due to hypoxia or accumulation of reactive oxygen species. Cerebrovascular autoregulation provides stable blood flow throughout the brain in response to dynamic fluctuations in arterial pressure [1]. However, during periods of increased, localized neuronal activity, the spatially confined hemodynamic response is essential to deliver sufficient oxygen to support the transient, elevated levels of oxygen demand [2].

The hemodynamic response to stimulation yields increases in both cerebral blood flow (CBF) and PO_2. This coupling has been observed in the brain [3, 4] and led to the interpretation that blood oxygenation level dependent (BOLD) functional magnetic resonance imaging (fMRI) is a strong indicator of PO_2 [5]. However, this relationship has not been directly assessed during neural stimulation [6], nor is it understood how anesthesia, which is used in many experimental situations, affects this relationship. It has been previously shown that isoflurane decreases the spontaneous activity of single units [7], whilst also increasing both intravascular PO_2 [8] and tissue PO_2 [9]. These changes under anesthesia may occur as a result of decreased oxygen demand.

In this study, we examined the relationship between neuronal demand, the hemodynamic response and brain tissue oxygen, by measuring single unit activity, PO_2 and BOLD fMRI in the whisker barrel cortex of the rabbit. By comparing the stimulus-evoked responses in both the awake and lightly anesthetized states, we were able to observe how tissue PO_2 and the hemodynamic response manifest when neuronal activity decreases. In line with previous research [7–9], it was hypothesized that the BOLD and PO_2 evoked responses should be closely related in the awake state, and that this relationship would be preserved under anesthesia only if the PO_2 responses to stimulation still follow hemodynamic function.

1.2 Methods

Animal Preparation Six-month-old Dutch-belted female rabbits were used in accordance with the National Institutes of Health guidelines, and the NorthShore University HealthSystem Institutional Animal Care and Use Committee approved all of the protocols. The animals were implanted with restraining headbolts and electrodes for oxygen/electrophysiology recording and habituated to the MRI environment as previously described [7].

Experimental Design PO_2 and BOLD fMRI responses to whisker stimulation were first recorded simultaneously in the awake state (5 rabbits, 14 experiments). This was followed by simultaneous PO_2 recordings and fMRI during whisker stimulation under the awake state and 0.25 minimum alveolar concentration (MAC) isoflurane, for each subject (5 rabbits, 5 experiments). Each subject followed an identical protocol. Isoflurane (Piramal Healthcare, Mumbai) was delivered at a concentration of 0.5% (~0.25 MAC) in air via a mask (Harvard Apparatus, Holliston, MA) using a calibrated Matrx vaporizer (Midmark, Versailles, OH). Rabbits were habituated to the mask prior to the experiments.

Stimulus Delivery Whisker stimulation was delivered by deflecting two whiskers at an amplitude of 1.5 mm and a frequency of 50 Hz, using a system described previously [10].

fMRI Data Collection and Analysis fMRI experiments were performed using a 9.4 T spec-

trometer (^{1}H, 400 MHz) (BioSpec 94/30USR, Bruker Biospin MRI GmbH), as previously described [11].

PO_2 and Electrophysiological Recording The same electrodes were used for both electrophysiology and PO_2 recordings [12]. For PO_2 recording the gold-plated microwire was polarized to −0.7 V with respect to the reference Ag/AgCl electrode (located between the skull and dura), and the current was measured with a Keithley model 614 electrometer (Keithley Instruments, Cleveland, OH, USA), as described previously [12].

Statistical Analysis The full width at half maximum (FWHM) of the mean response time course was calculated to measure the duration of the BOLD or PO_2 response. The PO_2 data were converted to the BOLD sampling frequency (0.5 Hz) for analysis and the baseline was normalized to zero for stimulation experiments. A paired t-test was used to compare BOLD, PO_2 and single unit response magnitudes and durations (as measured by FWHM) to whisker stimulation, before and during isoflurane delivery. A one-way ANOVA (Statistica, StatSoft, Tulsa, OK) was used to compare the FWHM duration between stimulus-evoked BOLD and PO_2 responses. Pearson correlation analysis was used to calculate the strength and direction of the linear relationship between the BOLD and PO_2 signals during stimulation. A Fisher z-transformation was used to establish the significance of the correlation coefficients. The level for rejection of the null hypotheses was set to $p < 0.05$ in all tests. The data are presented as mean +/− SEM unless otherwise specified.

1.3 Results

Stimulus-Evoked BOLD and PO_2 Responses in the Awake State The BOLD and PO_2 temporal responses were quite similar in terms of duration and post-stimulus undershoot, and were strongly correlated ($r = 0.9$) (Fig. 1.1a, b). From the onset of stimulus presentation, the time to reach FWHM (rise time) was 2.3 ± 0.2 s for the BOLD response, vs. 4.7 ± 1.1 s for the PO_2 response ($p < 0.023$) (Fig. 1.1c). Time to peak was 4.4 ± 0.7 s for the BOLD response, vs. 5.8 ± 0.4 s ($p < 0.006$) (Fig. 1.1d).

BOLD, Single Units and PO_2 Responses During Isoflurane Anesthesia affected BOLD, neuronal activity and, especially, PO_2 (Fig. 1.2). The baseline PO_2 increased during 0.25 MAC isoflurane by 5.5 ± 2.1% ($p < 0.0376$). The single unit baseline ($N = 26$) decreased during isoflurane from 3.0 ± 0.6 to 2.6 ± 0.5 spikes/s ($p < 0.0011$). The BOLD and PO_2 responses both decreased in the average magnitude under isoflurane (Fig. 1.2a, b), and the shape of PO_2 was affected in such a way that the duration of PO_2 responses had high variability. Figure 1.2b shows that during anesthesia BOLD responses exhibited a "peak-plateau" shape, whereas the shape of PO_2 responses diverged from the shape of BOLD responses, such that they had a lower peak magnitude and prolonged duration. Analysis using paired t-test of data averaged across subjects showed significant decreases in the mean BOLD (2.24 ± 0.25% awake vs. 1.52 ± 0.13 during isoflurane, $p < 0.042$), PO_2 (6.76 ± 1.84% for awake vs. 4.65 ± 1.68% under isoflurane, $p < 0.05$) and single unit (Fig. 1.2c, d) (104.54 ± 20.08% for awake vs 44.12 ± 10.27% under isoflurane, $p < 0.025$, normalized to baseline) responses to whisker stimulation during isoflurane, relative to the awake state. The temporal correlation between BOLD and PO_2 responses became non-significant.

1.4 Discussion and Conclusion

The strong correlation and similar temporal behavior indicate a close dependence between the BOLD fMRI and tissue PO_2 responses to sensory stimulation in the awake state. This result was expected, but had not yet been directly demonstrated. BOLD fMRI reflects changes between

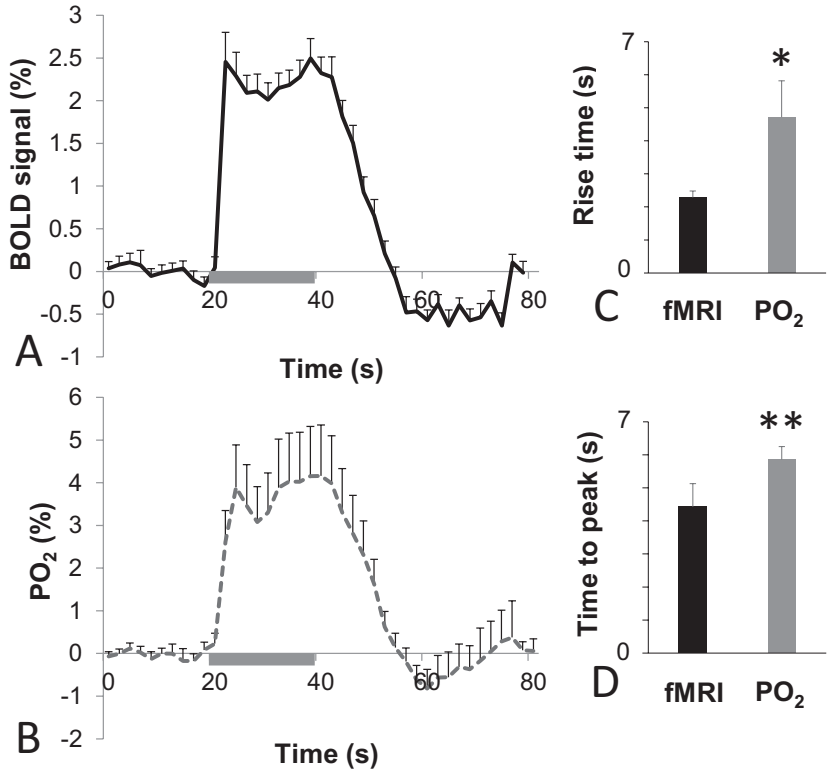

Fig. 1.1 The comparison of PO_2 and BOLD responses in the awake state. (**a**, **b**) PO_2 and BOLD responses were similar in terms of duration and shape and were strongly correlated. (**c**, **d**) The PO_2 response to whisker stimulation (grey bar) had a slower onset. A single asterisk represents a significant difference at $p < 0.05$. Two asterisks represent a significant difference at $p < 0.01$

pools of oxy- and deoxyhemoglobin [13, 14] in the vessels, thus, tissue PO_2 should generally follow the BOLD fMRI time course as both are influenced by changes in cerebral blood volume (CBV) and CBF, due to the neuronal response.

However, in the environment of decreased baseline neuronal activity under isoflurane the PO_2 diverged substantially from the behavior of the BOLD fMRI time course. This decrease in PO_2 response was accompanied by a significant increase in baseline tissue PO_2. Isoflurane at high concentrations can dilate cerebral blood vessels [15], possibly due to the direct effect of GABA on vascular receptors [16], but this effect has not been shown to occur at concentrations below 0.5 MAC [17, 18]. Thus, the increase in baseline tissue PO_2 should be due to decreased oxygen consumption. The proportional change in magnitude and the preservation of the ratio between the BOLD and PO_2 responses under isoflurane supports the observation that the BOLD response can serve as an index of the actual changes in tissue PO_2 [6]. The temporal dynamics of these signals can also depend on the level of neuronal activity, and therefore neuronal consumption as well as oxygen delivery. Under anesthesia, PO_2 does not primarily follow the hemodynamic response, as it does in the awake state, due to the general decrease in neuronal activity and neuronal oxygen consumption.

We can conclude that although BOLD fMRI and tissue PO_2 responses follow each other in the awake state, their relationship is completely altered under general anesthesia. This effect is most likely is due to the decreased oxygen consumption.

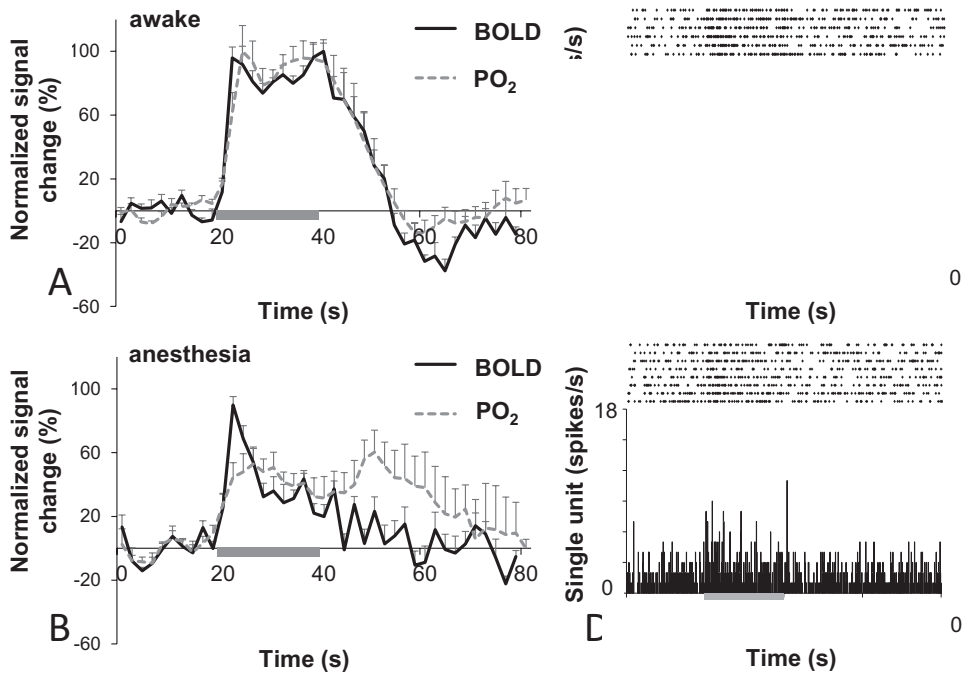

Fig. 1.2 Effect of isoflurane on BOLD, PO_2 and single unit evoked responses. (**a**) In the awake state, the BOLD and PO_2 responses (normalized to the peak) to whisker stimulation (grey bar) exhibited similar temporal behaviour, in terms of shape, duration, and post-stimulus baseline undershoot. (**b**) In the anesthetized state, the averaged BOLD and PO_2 responses decreased and their shapes diverged. Increased neuronal firing was recorded during stimulation in the awake state. (**c**) Single unit activity of a representative example of the recorded cells in the awake state. (**d**) Baseline and stimulus-evoked neuronal firing of single units decreased during isoflurane

Acknowledgments This work was supported by R01GM112715 (National Institute of General Medical Sciences), R01NS107383 (National Institute of Neurological Disorders and Stroke), and R01NS119251 (National Institute of Neurological Disorders and Stroke).

References

1. Willie CK et al (2014) Integrative regulation of human brain blood flow. J Physiol 592(5):841–859
2. Freeman RD, Li B (2016) Neural-metabolic coupling in the central visual pathway. Philos Trans R Soc Lond Ser B Biol Sci 371(1705):20150357
3. Ances BM et al (2001) Temporal dynamics of the partial pressure of brain tissue oxygen during functional forepaw stimulation in rats. Neurosci Lett 306(1–2):106–110
4. Masamoto K et al (2008) Trial-by-trial relationship between neural activity, oxygen consumption, and blood flow responses. NeuroImage 40(2):442–450
5. Bentley WJ et al (2016) Oxygen level and LFP in task-positive and task-negative areas: bridging BOLD fMRI and electrophysiology. Cereb Cortex 26(1):346–357
6. Lowry JP et al (2010) Real-time electrochemical monitoring of brain tissue oxygen: a surrogate for functional magnetic resonance imaging in rodents. NeuroImage 52(2):549–555
7. Aksenov DP et al (2015) Effects of anesthesia on BOLD signal and neuronal activity in the somatosensory cortex. J Cereb Blood Flow Metab 35(11):1819–1826
8. Lyons DG et al (2016) Mapping oxygen concentration in the awake mouse brain. elife 5:e12024
9. Aksenov D et al (2012) Effect of isoflurane on brain tissue oxygen tension and cerebral autoregulation in rabbits. Neurosci Lett 524(2):116–118
10. Li L et al (2012) A MRI-compatible system for whisker stimulation. J Neurosci Methods 205(2):305–311
11. Aksenov DP et al (2019) Role of the inhibitory system in shaping the BOLD fMRI response. NeuroImage 201:116034
12. Aksenov D et al (2022) Brain tissue oxygen dynamics while mimicking the functional deficiency of interneurons. Front Cell Neurosci 16:983298
13. Buxton RB (2013) The physics of functional magnetic resonance imaging (fMRI). Rep Prog Phys 76(9):096601
14. Hyder F, Rothman DL (2017) Advances in imaging brain metabolism. Annu Rev Biomed Eng 19:485–515

15. Matta BF et al (1999) Direct cerebral vasodilatory effects of sevoflurane and isoflurane. Anesthesiology 91:677–680
16. Krause DN et al (1980) GABA receptors in bovine cerebral blood vessels: binding studies with [^{3}H]muscimol. Brain Res 185:51–57
17. Aladj LJ et al (1991) Cerebral blood flow autoregulation is preserved during cardiopulmonary bypass in isoflurane-anesthetized patients. Anesth Analg 72(1):48–52
18. Scheller MS et al (1988) The effects of sevoflurane on cerebral blood flow, cerebral metabolic rate for oxygen, intracranial pressure, and the electroencephalogram are similar to those of isoflurane in the rabbit. Anesthesiology 68(4):548–551

2 Cerebral Microcirculation and Oxygenation Modulation by Transcranial Alternating Current Stimulation in Awake and Anesthetized Mice

Olga A. Bragina, D. A. Atochin, Alex O. Trofimov, Edwin Nemoto, and Denis E. Bragin

Abstract

Transcranial alternating current stimulation (tACS) is a novel non-invasive electrical stimulation technique where a sinusoidal oscillating low-voltage electric current is applied to the brain. TACS is being actively investigated in practice for cognition and behavior modulation and for treating brain disorders. However, the physiological mechanisms of tACS are underinvestigated and poorly understood. Previously, we have shown that transcranial direct current stimulation (tDCS) facilitates cerebral microcirculation and oxygen supply in a mouse brain through nitric oxide-dependent vasodilatation of arterioles. Considering that the effects of tACS and tDCS might be both similar and dissimilar, we tested the effects of tACS on regional cerebral blood flow and oxygen saturation in anesthetized and awake mice using laser speckle contrast imaging and multispectral intrinsic optical signal imaging. The anesthetized mice were imaged under isoflurane anesthesia ~1.0% in 30% O_2 and 70% N_2O. The awake mice were pre-trained on the rotating ball for awake imaging. Baseline imaging with further tACS was followed by post-stimulation imaging for ~3 h. Differences between groups were determined using a two-way ANOVA analysis for multiple comparisons and post hoc testing using the Mann-Whitney U test. TACS increased cerebral blood flow and oxygen saturation. In awake mice, rCBF and oxygen saturation responses were more robust and prolonged as opposed to anesthetized, where the response was weaker and shorter with overshoot. The significant difference between anesthetized and awake mice emphasizes the importance of the experiments on the latter as

O. A. Bragina (✉)
Lovelace Biomedical Research Institute, Albuquerque, NM, USA
e-mail: obragina@lrri.org

D. A. Atochin
Cardiovascular Research Center, Massachusetts General Hospital, Harvard Medical School, Boston, MA, USA

A. O. Trofimov
Department of Neurological Diseases, Privolzhsky Research Medical University, Nizhny Novgorod, Russia

E. Nemoto
Department of Neurology, University of New Mexico School of Medicine, Albuquerque, NM, USA

D. E. Bragin
Lovelace Biomedical Research Institute, Albuquerque, NM, USA

Department of Neurology, University of New Mexico School of Medicine, Albuquerque, NM, USA

F. Scholkmann et al. (eds.), *Oxygen Transport to Tissue XLIV*, Advances in Experimental Medicine and Biology 1438, https://doi.org/10.1007/978-3-031-42003-0_2

anesthesia is not typical for human stimulation and significantly alters the results.

Keywords

Transcranial alternating current stimulation · Cerebral blood flow · Anesthesia

2.1 Introduction

Transcranial alternating current stimulation (tACS) is a novel non-invasive electrical stimulation technique where a sinusoidal oscillating low-voltage electric current is applied to the brain through electrodes on the scalp. It has been shown that tACS causes the cortical neurons to alter their membrane potential towards depolarization or hyperpolarization in an oscillatory fashion [1]. This alternating change in the membrane potential is thought to be sufficient to alter the probability of a neuron generating action potentials; however, it is not strong enough to change the rate of action potentials [1]. As a result, tACS has a modulating (but not imposing) effect on the neurons. TACS is being actively investigated in practice for cognition and behavior modulation in healthy individuals and for treating brain disorders. However, physiological mechanisms underlying tACS effects are largely underinvestigated and still under debate. In previous studies, we have shown that another type of transcranial electrical stimulation, transcranial direct current stimulation (tDCS), directly facilitates cerebral microvascular perfusion and tissue oxygen supply in an intact and traumatized mouse brain through vasodilatation of arterioles [2] and confirmed it in TBI patients [3]. More recently, we demonstrated a significant transient decrease in regional cerebral tissue oxygen saturation during tACS (10 Hz) in TBI patients, probably reflecting neuronal activation in the settings of post-TBI impaired autoregulation [4]. Recent work using Laser Doppler Velocimetry demonstrated that tACS rapidly and transiently increases cerebral blood flow in anesthetized mice; however, possible associated oxygen saturation changes have not been tested [5]. Considering that the effects of tACS and tDCS might be both similar and dissimilar, we tested the effects of tACS (10 Hz, 15 min) on regional cerebral blood flow (rCBF) and associated tissue oxygen saturation in mice using Laser Speckle Contrast Imaging (LSCI) and multispectral intrinsic optical signal imaging (MS-OISI). The study was done in both anesthetized and awake mice because anesthesia, commonly used in animal studies, is not typical for stimulation in humans and might significantly alter the results.

2.2 Methods

2.2.1 Study Design

Protocol #20024 was approved by the Institutional Animal Care and Use Com-mittee of Lovelace Biomedical Research Institute, and the studies were conducted according to the NIH Guide for the Care and Use of Laboratory Animals. Two groups of 3-month-old male C57BL6 wild-type mice (Jackson Laboratories, Bar Harbor, ME) weighing 30–35 g were used in the study: anesthetized (Group I, 8 mice) and awake (Group II, 8 mice). Baseline imaging with further tACS was followed by post-stimulation imaging during ~3 h after tACS.

2.2.2 Pre-imaging Surgical Preparation

One week before the experiment, the anesthetized mice were placed in the prone position, the skull was exposed through a midline scalp incision, and the incised skin was glued around the edges of the frontal and parietal bones using dental cement. To improve spatial resolution, the skull optical clearing treatment was performed in two steps before the experiment. Solution 1 (saturated supernatant solution of 75% (vol/vol) ethanol and urea) was applied to the exposed skull for about 10 min to allow the skull to turn transparent gradually. Then, Solution 1 was removed, and Solution 2 (0.7 M NaOH solution with dodecylbenzenesulfonic acid at a volume-mass

ratio of 24:5, pH 7.2) was added to the same area for further clearing within 5 min (Fig. 2.1b, c) [6]. After that, bilateral, AgCl stimulating electrodes (1 × 3 mm) with female pin pads were glued with Tensive conductive adhesive gel (Parker Laboratories, NJ), allowing simultaneous with tACS imaging, and the cover glass was glued with cyanoacrylate glue to the optical window.

2.2.3 Imaging

The anesthetized mice (Group I) were imaged under isoflurane anesthesia (~1.0%) delivered in 30% O_2 and 70% N_2 and maintained in a mouse stereotaxic setup which allowed spontaneous breathing through a nose cone. The awake mice (Group (II) were pre-trained on the rotating ball for imaging for 5 consecutive days starting on day 3 after optical window preparation (Fig. 2.1a). To prevent movement artifacts, the head was secured in a holder via the head plate. Regional CBF was measured using an RFLSI III Laser Speckle Imaging System (RWD Life Science, Shenzhen, China) at a rate of 120 fps, as we previously described [2]. RCBFs were calculated from the 500 ms consequence of LSCI images [2]. Custom multispectral optical intrinsic signal imaging was used to quantitate regional changes in oxy- and deoxyhemoglobin. MS-OISI data images are acquired at interleaved blue (460 nm) and green (530 nm) illuminations to map of changing oxy-, deoxy- and total hemoglobin concentrations (HbO_2, HbR and HbT) using a custom-made setup developed according to Bouchard et al. [7]. The local CBF and MS-OISI were obtained from the same area in the right somatosensory cortex approx. 2 × 2 cm.

2.2.4 Transcranial ACS

TACS (10 Hz/15 min) was done using an Animal tES system 2100 tES (Soterix Medical, New York, USA). The impedance across the skull pads averaged ~7.5 kΩ.

2.2.5 Statistical Analysis

Statistical analyses were done by Student's t-test using GraphPad Prism 9 (GraphPad Software, Inc., San Diego, CA). Differences between groups were determined using a two-way ANOVA analysis for multiple comparisons and post hoc testing using the Mann-Whitney U test. The significance level was preset to $p < 0.05$.

2.3 Results

TACS transiently and bilaterally increased rCBF and StO_2 in the cortex in both anesthetized and awake animals (Fig. 2.2, $p < 0.05$, from the baseline). Notably, the rCBF peak, time to rCBF peak, and blood flow dynamics varied in anesthetized and awake mice (Fig. 2.2a). In awake mice, rCBF

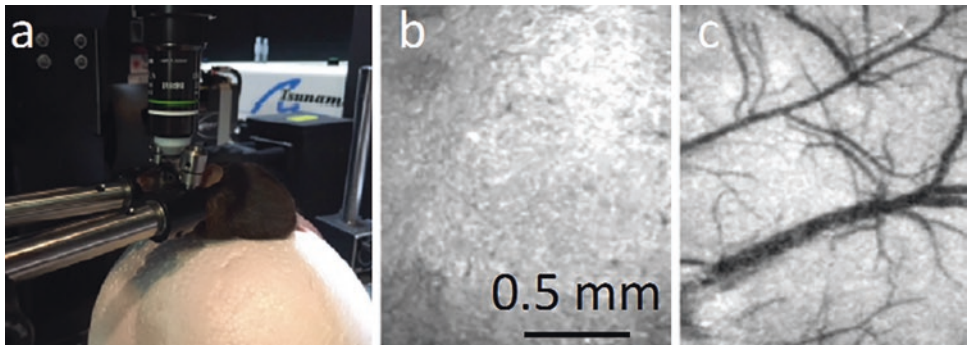

Fig. 2.1 (**a**) Floating ball setup for awake imaging; (**b**) Representative Laser Speckle Contrast Image of a mouse skull parietal bone; and (**c**) same bone after optical clearing optical window preparation

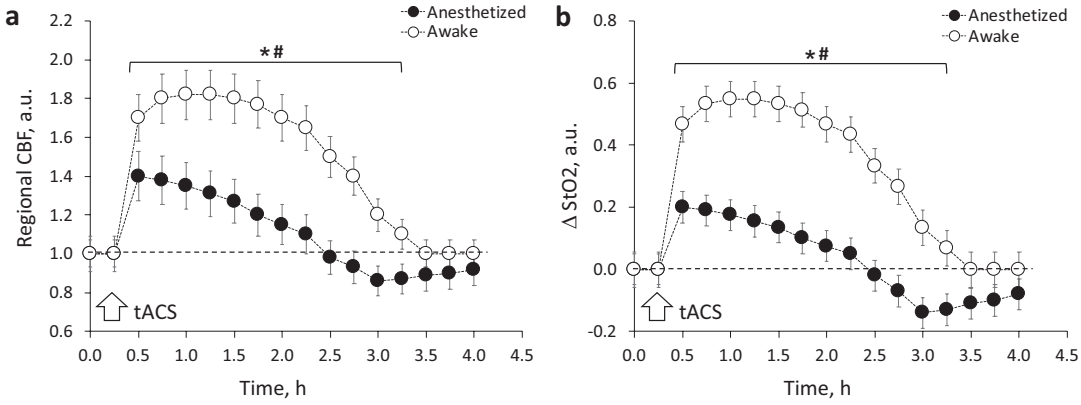

Fig. 2.2 (**a**) Regional cerebral blood flow (rCBF); and (**b**) tissue oxygen saturation (StO_2) response in anesthetized and awake mice to transcranial alternating current stimulation (tACS, 10 Hz/15 min). Mean ± s.e.m, n = 8, * = p < 0.05 from anesthetized, # = p < 0.05 from the baseline, white arrow – tACS, dashed line – baseline

response was more robust (peak 1.82 ± 0.12 a.u.) and prolonged (went back to a baseline by ~3.5 h) as opposed to anesthetized mice ($p < 0.05$). In the mice under anesthesia, the response was weaker (peak 1.4 ± 0.11 a.u.) and shorter (went back to a baseline by ~2.5 h) with overshoot during 1.5 h ($peak_{min}$ 0.86 ± 0.07 a.u.).

Similarly, the StO_2 peak, time to StO_2 peak, and StO_2 dynamics curves also varied in anesthetized and awake mice (Fig. 2.2b). In awake mice, StO_2 response was more robust (peak 0.55 ± 0.06 a.u.) and prolonged (went back to a baseline by ~3.5 h) as opposed to anesthetized mice ($p < 0.05$). In the mice under anesthesia, the response was weaker (peak 0.2 ± 0.04 a.u.), shorter (went back to a baseline by ~2.5 h) with overshoot during 1.5 h ($peak_{min}$ − 0.14 ± 0.07 a.u.).

2.4 Discussion

The aim of our study was to assess the effects of tACS (10 Hz, 15 min) on regional cerebral blood flow and associated tissue oxygen saturation and to evaluate the effect of anesthesia on cerebral hemodynamic and oxygen saturation response to tACS by comparing it in both anesthetized and awake mice. TACS transiently and bilaterally increased rCBF and StO_2 in the cortex in both anesthetized and awake animals, which was more robust and prolonged in awake animals. The mechanisms of the hemodynamic and associated StO_2 response to tACS are unclear but could be explained through one or more mechanisms, including direct neuronal stimulation [8] and neurovascular coupling [9], stimulation of the locus coeruleus [10], endothelial stimulation [11], and astrocytic stimulation [12]. In a recent review in the Brain Stimulation journal, it was concluded that a primary vascular effect of transcranial electrostimulation is highly suggested based on various preclinical and clinical studies and that further studies are warranted to investigate the mechanisms underlying the vascular response [13]. We have shown that another type of electrical stimulation – tDCS directly facilitates cerebral microvascular perfusion and tissue oxygen supply in a mouse brain through nitric oxide (NO)-dependent vasodilatation of arterioles [2, 14], supporting the primary vascular effects of electrical stimulation, which might be similar in the case of tACS. However, this assumption should be tested using eNOS/nNOS inhibitors, NO precursors/scavengers and eNOS/nNOS transgenic mice.

2.5 Conclusion

TACS transiently and bilaterally increases rCBF and StO_2 in the mouse cortex. The significant difference between anesthetized and awake mice emphasizes the importance of the experiments in the latter because anesthesia is not typical for human stimulation and, as we demonstrated here, significantly alters the results.

Acknowledgments Supported by Lovelace Biomedical Startup Funds and NIH R01NS112808.

References

1. Antal A, Herrmann CS (2016) Transcranial alternating current and random noise stimulation: possible mechanisms. Neural Plast 3616807:1–12. https://doi.org/10.1155/2016/3616807
2. Bragina OA, Lara DA, Nemoto EM et al (2018) Increases in microvascular perfusion and tissue oxygenation via vasodilatation after anodal transcranial direct current stimulation in the healthy and traumatized mouse brain. Adv Exp Med Biol 1072:27–31. https://doi.org/10.1007/978-3-319-91287-5_5
3. Trofimov AO, Kalentiev G, Karelsky M et al (2018) Cerebral hemodynamics after transcranial direct current stimulation (tDCS) in patients with consequences of traumatic brain injury. Adv Exp Med Biol 1072:59–62. https://doi.org/10.1007/978-3-319-91287-5_10
4. Trofimov AO, Kopylov AA, Martynov DS et al (2021) The changes in brain oxygenation during transcranial alternating current stimulation as consequences of traumatic brain injury: a near-infrared spectroscopy study. Adv Exp Med Biol 1269:235–239. https://doi.org/10.1007/978-3-030-48238-1_37
5. Turner DA, Degan S, Galeffi F et al (2021) Dose-dependent enhancement of cerebral blood flow by transcranial AC stimulation in mouse. Brain Stimul 14(1):80–87. https://doi.org/10.1016/j.brs.2020.11.012
6. Zhang CFW, Zhao Y et al (2018) A large, switchable optical clearing skull window for cerebrovascular imaging. Theranostics 8(10):2696–2708. https://doi.org/10.7150/thno.23686
7. Bouchard MB, Chen BR, Burgess SA et al (2009) Ultra-fast multispectral optical imaging of cortical oxygenation, blood flow, and intracellular calcium dynamics. Opt Express 17(18):15670–15678. https://doi.org/10.1364/OE.17.015670
8. Voroslakos M, Takeuchi Y, Brinyiczki K et al (2018) Direct effects of transcranial electric stimulation on brain circuits in rats and humans. Nat Commun 9(1):483. https://doi.org/10.1038/s41467-018-02928-3
9. Pulgar VM (2015) Direct electric stimulation to increase cerebrovascular function. Front Syst Neurosci 9:54. https://doi.org/10.3389/fnsys.2015.00054
10. Sherwood MS, Madaris AT, Mullenger CR et al (2018) Repetitive transcranial electrical stimulation induces quantified changes in resting cerebral perfusion measured from arterial spin labeling. Neural Plast 2018:5769861. https://doi.org/10.1155/2018/5769861
11. Longden TA, Dabertrand F, Koide M et al (2017) Capillary K(+)-sensing initiates retrograde hyperpolarization to increase local cerebral blood flow. Nat Neurosci 20(5):717–726. https://doi.org/10.1038/nn.4533
12. Masamoto K, Unekawa M, Watanabe T et al (2015) Unveiling astrocytic control of cerebral blood flow with optogenetics. Sci Rep 5:11455. https://doi.org/10.1038/srep11455
13. Bahr-Hosseini M, Bikson M (2021) Neurovascular-modulation: a review of primary vascular responses to transcranial electrical stimulation as a mechanism of action. Brain Stimul 14(4):837–847. https://doi.org/10.1016/j.brs.2021.04.015
14. Bragina OA, Semyachkina-Glushkovskaya OV, Trofimov AO et al (2018) On the mechanisms of modulation of cerebral blood flow during transcranial electrical stimulation. Medical. Almanac 5(56):68–71. https://doi.org/10.21145/2499-9954-2018-5-68-71. (In Rusian)

3 The Effect of Hypercapnia on Cortical Metabolic Rate and Mitochondrial Redox Status

Mada Hashem, Ying Wu, and Jeff F. Dunn

Abstract

Hypercapnia is commonly used as a vasodilatory stimulus in both basic and clinical research. There have been conflicting reports about whether cerebral metabolic rate of oxygen ($CMRO_2$) is maintained at normal levels during increases of cerebral blood flow (CBF) and oxygen delivery caused by hypercapnia.

This study aims to provide insight into how hypercapnia may impact $CMRO_2$ and brain mitochondrial function. We introduce data from mouse cortex collected with a novel multimodality system which combines MRI and near-infrared spectroscopy (NIRS). We quantify CBF, tissue oxygen saturation (S_tO_2), oxidation state of the mitochondrial enzyme cytochrome c oxidase (CCO), and $CMRO_2$.

During hypercapnia, $CMRO_2$ did not change while CBF, S_tO_2, and the oxidation state of CCO increased significantly. This paper supports the conclusion that hypercapnia does not change $CMRO_2$. It also introduces the application of a multimodal NIRS-MRI system which enables non-invasive quantification of $CMRO_2$, and other physiological variables, in the cerebral cortex of mouse models.

Keywords

Hypercapnia · Cortical metabolic rate · Mitochondrial redox status

3.1 Introduction

Hypercapnia, or increased CO_2 in blood, is used as a vascular challenge to assess cerebrovascular reactivity, study neurovascular coupling, or calibrate functional MRI signals [1]. It is also used to test the protective effects of CO_2 in pathological conditions such as ischemic injury [2]. Such applications are feasible because hypercapnia is known to increase CBF, and it is assumed that changes in CO_2 partial pressure have no effect on neuronal activity.

An important marker of neuronal activity is the cerebral metabolic rate of oxygen ($CMRO_2$). Investigating this marker under hypercapnia did not yield consistent results [3, 4]. This may be due to factors such as data misinterpretation, high between-subject variation, species differences or anesthesia. Hypercapnia might affect oxygen consumption through control at the mitochondrial level as well. Therefore, the effect of CO_2

M. Hashem (✉) · Y. Wu · J. F. Dunn
Department of Radiology, University of Calgary, Calgary, AB, Canada

Hotchkiss Brain Institute, University of Calgary, Calgary, AB, Canada

Experimental Imaging Centre, Cumming School of Medicine, University of Calgary, Calgary, AB, Canada
e-mail: mada.hashem@ucalgary.ca

F. Scholkmann et al. (eds.), *Oxygen Transport to Tissue XLIV*, Advances in Experimental Medicine and Biology 1438, https://doi.org/10.1007/978-3-031-42003-0_3

inhalation on neuronal activity is not very clear, despite the wide application of hypercapnia in cerebrovascular research.

In this study we applied a multimodal technique, which combines near-infrared spectroscopy (NIRS) and MRI, on mouse models to determine if the CO_2 stimulus used to manipulate CBF, impacts $CMRO_2$ and the oxidation state of the mitochondrial enzyme, cytochrome c oxidase (CCO), which is responsible for the oxygen consumption in the cell. These parameters are measured in healthy controls; therefore, our findings may not be translatable to pathological conditions.

Having a means to measure CBF, $CMRO_2$, CCO oxidation state and other physiological parameter simultaneously will provide a comprehensive picture of the mechanisms involved in neurovascular coupling and the regulation of cerebral oxidative metabolism.

3.2 Methods

C57BL/6 J male mice (n = 5, 24–26 g, 17 weeks old) were maintained in the University of Calgary Animal Care facility. Animal protocols were approved by the Animal Care Committee of the University of Calgary and conformed to the guidelines of the Canadian Council of Animal Care.

The experimental setup of the multimodal NIRS-MRI system was described in detail in our previous publications [5, 6]. The system consists of a 9.4 T horizontal bore MRI (Bruker Biospin GmbH) with a 35 mm quadrature volume coil, and a continuous-wave broadband NIRS system. Arterial Spin Labelling (ASL) MRI was applied to measure perfusion. A single axial slice was acquired around the bregma, using a CASL-HASTE sequence [5]. Four perfusion images, followed by a T1 map obtained with a RARE-VTR sequence, were collected to generate a perfusion map for each condition [5]. A ROI was created in the region of sensitivity for NIRS in the cortex and used to calculate average CBF.

The mice were anesthetized with 2% isoflurane added to a gas mixture of 70% N_2 and 30% O_2. Two optic fibers were secured 4 mm apart on top of the shaved head of the mouse, near bregma. The optic fibers used here allow us to look at NIRS data in the cortex only. Localized data could be investigated in future, by using other NIRS fiber geometries, such as implanted optic fiber. NIR spectra between 705 and 960 nm were collected from the mouse cortex. The experiment started with a baseline measurement where the mice were supplied by a 70% N_2, 30% O_2, 0% CO_2 mixture for 15 min. Then, ASL-MRI acquisition was initiated for perfusion measurement, and required 14 min. Afterwards, the gas mixture was changed to 65% N_2, 30% O_2, 5% CO_2. After stabilization for 10 min, ASL-MRI measurement was repeated. The gas mixture was restored to baseline conditions for additional 5 min, and then an anoxia pulse (100% N_2, 0% O_2) was given for 50 s. During data acquisition, heart rate, breathing rate and S_aO_2 were monitored by the MouseOx MRI-compatible pulse oximeter (Starr Life Sciences, USA) placed on the mouse thigh. Rectal temperature was monitored and maintained at 36.5 ± 0.1 °C.

The absolute concentrations of deoxyhemoglobin (dHb), oxidized CCO (oxCCO) and reduced CCO (reCCO), were quantified from the attenuation spectra using the NIR-AQUA algorithm [6]. The concentration of hemoglobin during normocapnia was determined using the anoxia pulse method [7], in which it is assumed that during the anoxia pulse the total hemoglobin (tHb) is approximated by the total dHb concentration ([tHb] = [dHb]). To avoid unnecessary stress for the animals, only one anoxia pulse was applied. To estimate tHb during hypercapnia, the Grubb's equation was used to correlate between the change in tHb and CBF [8]. Tissue oxygen saturation (S_tO_2)was determined using dHb and tHb concentrations. The oxygen extraction fraction (OEF) was calculated as the arterial saturation minus the venous saturation divided by the arterial oxygen saturation (S_aO_2) [9]. S_aO_2 was measured with the MouseOx MRI-compatible

pulse oximeter from the thigh of the animal. Venous oxygen saturation (S_vO_2) was estimated from S_aO_2 and S_tO_2 values, where the arterial/venous Hb ratio used is 0.25/0.75 [5, 10]. $CMRO_2$ was quantified using the modified Fick principle [10]:

$$CMRO_2 = k \times CBF \times \frac{4}{3}\left(S_aO_2 - S_tO_2\right) \times \frac{[tHb]}{CBV \times \rho}$$

$k = 1.39$ (ml(O_2)/g(Hb)) is the maximum capacity of Hb. S_aO_2, S_tO_2 and tHb values were averaged over the period of perfusion acquisition. $CBV \times \rho$ is the cerebral blood volume to tissue volume ratio, where the CBV in the cortical GM is 0.045 ml/g [11], and the cerebral tissue density $\rho = 1.05\ g/ml$ [12]. A paired t-test was performed in IBM SPSS Statistics v24, to determine significant changes ($p < 0.05$) in oxidative metabolism correlates when measured before and during 5% CO_2 intervention. All data were expressed as mean ± SD.

3.3 Results

Multimodal NIRS-MRI was used to quantify CBF, tHb, S_tO_2, OEF, and $CMRO_2$, and the oxidation state of CCO from the cortex of mice under anesthesia before and during the inhalation of 5% CO_2. Figure 3.1a shows a representative perfusion map from one mouse before and during the hypercapnia challenge. Average CBF (Fig. 3.1b), quantified from the ROI in the cortex, showed a significant increase during hypercapnia ($p = 0.03$). Figure 3.2 shows the absolute values of S_tO_2, OEF and $CMRO_2$ under normocapnia and hypercapnia. There was a significant increase in S_tO_2 ($p = 0.02$) during hypercapnia, whereas OEF decreased ($p = 0.01$) and $CMRO_2$ remained constant ($p = 0.3$). Figure 3.3 shows the absolute values of oxCCO, reCCO and totCCO. There was a significant increase in oxCCO ($p = 0.01$) and a significant decrease in reCCO ($p = 0.04$) while the total amount of the enzyme remained constant ($p = 0.6$) during hypercapnia.

3.4 Discussion

We combined NIRS and MRI to investigate the effect of hypercapnia on $CMRO_2$, CCO and CBF in the cortex of healthy control mice. Increasing the level of inhaled CO_2 caused a significant increase in CBF with no change in $CMRO_2$. The tissue oxygen content was also higher during hypercapnia, as indicated by an increase in S_tO_2. The increase in CBF is consistent with the reported relationship between CO_2 levels in

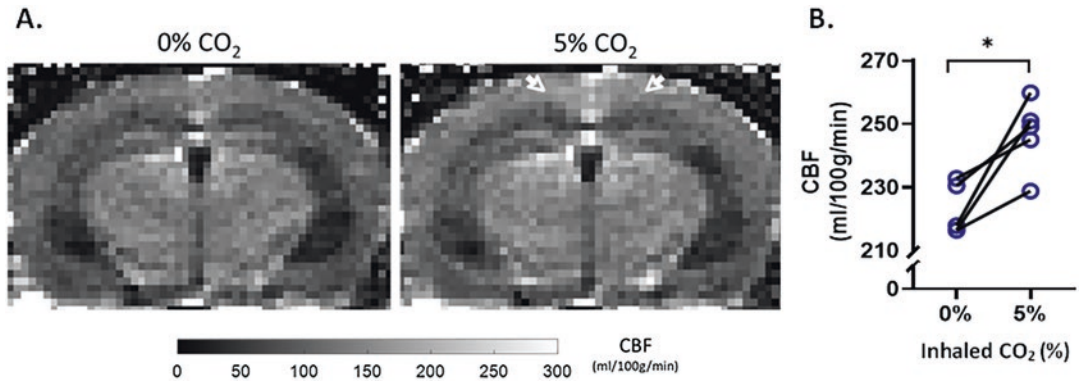

Fig. 3.1 (**a**) Representative perfusion maps at normocapnia (0% CO_2) and hypercapnia (5% CO_2). Hyperintensity (white arrows) indicates an increase in cortical CBF during hypercapnia. (**b**) Average cortical CBF quantified in each mouse before and during hypercapnia. Paired t-test was performed to compare normocapnia and hypercapnia ($n = 5$, $^*p < 0.05$)

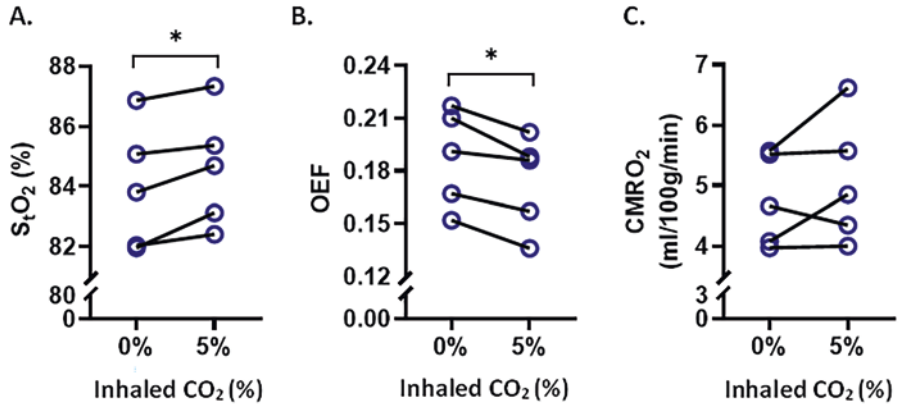

Fig. 3.2 Quantification of (**a**) S_tO_2, (**b**) OEF, and (**c**) $CMRO_2$ before (0% CO_2) and during hypercapnia (5% CO_2). Each symbol represents a different mouse. Paired t-test was performed to compare normocapnia and hypercapnia ($n = 5$, $^*p < 0.05$)

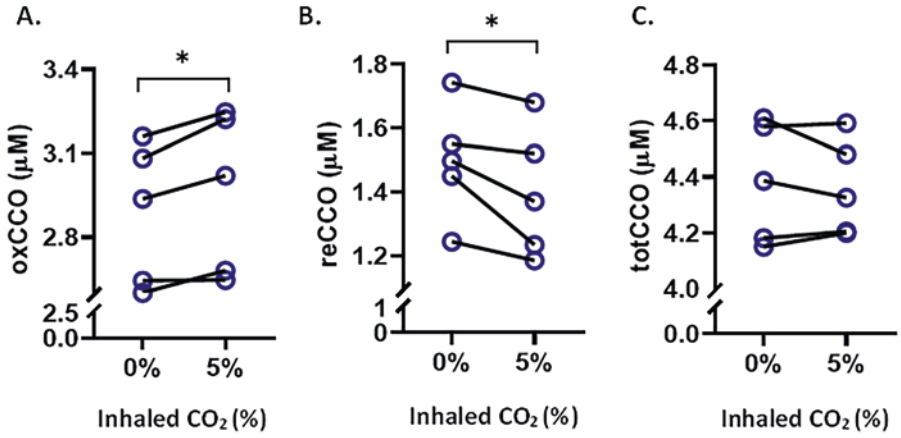

Fig. 3.3 Quantification of (**a**) oxCCO, (**b**) reCCO, and (**c**) totCCO before (0% CO_2) and during hypercapnia (5% CO_2). Each symbol represents a different mouse. Paired t-test was performed to compare normocapnia and hypercapnia ($n = 5$, $^*p < 0.05$)

blood and CBF both in animals [13] and humans [14]. While the effect of hypercapnia on CBF is well established, there have been conflicting reports about whether hypercapnia can increase $CMRO_2$ [3, 4]. Constant $CMRO_2$ demonstrates that increases in CBF during mild hypercapnia are caused primary due to the effect of CO_2 on blood vessels and not due to cerebral tissue metabolism. The reduced OEF values observed here can explain the mismatch between the change in CBF and $CMRO_2$. The oxidation state of CCO, defined here as the difference between the concentration of oxCCO and reCCO, increased during hypercapnia. Such an increase has been shown to be highly associated with high brain tissue oxygenation in anesthetized piglets [15], lambs [16], and humans [17]. However, combining hypercapnia with anoxic or hypoxic challenges proved that the oxidation changes of CCO were not the result of the increase in oxygen delivery [15, 16]. There are factors, other than oxygen availability in the tissue, that could change the regulation of CCO during hypercapnia. High levels of CO_2 decrease pH. As a result, $[H^+]$ concentration increases in the tissue and slows down the process of electron

transport through the electron transport chain (ETC). Hypercapnia may also alter carbohydrate metabolism in the brain which in turn affects the ETC substrates supply and the electron flux [15, 18]. These alterations are likely to affect the oxidation state of CCO and consequently decrease the consumption of oxygen [19]. Moreover, nitric oxide (NO) production increases during hypercapnia [20]. NO is a competitive inhibitor of CCO, and may reduce CCO's affinity to oxygen [21]. Thus, all the factors mentioned above, could impact CCO and contribute to the maintenance of stable $CMRO_2$ despite the increase in CBF and oxygen availability (S_tO_2).

3.5 Conclusions

The applied NIRS-MRI system enabled non-invasive absolute quantification of $CMRO_2$, CBF, CCO, S_tO_2 and OEF in the mouse cerebral cortex *in vivo*. CBF increased while $CMRO_2$ remained constant, supporting the assumption that mild hypercapnia does not change metabolic rate, and therefore can be used in cerebrovascular studies and fMRI calibration. We suggest that part of the explanation that CCO oxidation state increases without an increase in $CMRO_2$ is that that the regulation of CCO has changed due to hypercapnia, resulting in a tight coupling between the metabolic requirements of the brain and oxidative metabolism.

Acknowledgments We acknowledge funding by National Institutes of Health [R21 EB021397]; the Canada Foundation for Innovation [Project 4933]; the Natural Sciences and Engineering Research Council, Canada [RGPIN-2015-06517]; the Canadian Institutes of Health Research [Project 436461]; Alberta Graduate Excellence Scholarship (AGES).

References

1. Zappe A et al (2008) The influence of moderate hypercapnia on neural activity in the anesthetized nonhuman primate. Cereb Cortex 18(11):2666–2673
2. Lin L-T et al (2019) Protective effects of hypercapnic acidosis on ischemia–reperfusion-induced retinal injury. PLoS One 14(1):e0211185
3. Jones M et al (2005) The effect of hypercapnia on the neural and hemodynamic responses to somatosensory stimulation. NeuroImage 27(3):609–623
4. Chen JJ, Pike GB (2010) Global cerebral oxidative metabolism during hypercapnia and hypocapnia in humans: implications for BOLD fMRI. J Cereb Blood Flow Metab 30(6):1094–1099
5. Hashem M et al (2020) Using a multimodal near-infrared spectroscopy and MRI to quantify gray matter metabolic rate for oxygen: a hypothermia validation study. NeuroImage 206:116315
6. Hashem M, Wu Y, Dunn JF (2021) Quantification of cytochrome c oxidase and tissue oxygenation using CW-NIRS in a mouse cerebral cortex. Biomed Opt Express 12(12):7632–7656
7. Zhang Q et al (2010) A near-infrared calibration method suitable for quantification of broadband data in humans. J Neurosci Methods 188(2):181–186
8. Grubb RL Jr et al (1974) The effects of changes in $PaCO_2$ cerebral blood volume, blood flow, and vascular mean transit time. Stroke 5(5):630–639
9. Qin Q, Grgac K, Van Zijl PC (2011) Determination of whole-brain oxygen extraction fractions by fast measurement of blood T2 in the jugular vein. Magn Reson Med 65(2):471–479
10. Tichauer KM et al (2006) Measurement of cerebral oxidative metabolism with near-infrared spectroscopy: a validation study. J Cereb Blood Flow Metab 26(5):722–730
11. Hamberg LM et al (1996) Measurement of cerebral blood volume with subtraction three-dimensional functional CT. AJNR Am J Neuroradiol 17(10):1861–1869
12. Sabatini U et al (1991) Quantitative assessment of cerebral blood volume by single-photon emission computed tomography. Stroke 22(3):324–330
13. Lu J et al (2009) Characterization of cerebrovascular responses to hyperoxia and hypercapnia using MRI in rat. NeuroImage 45(4):1126–1134
14. Kety SS, Schmidt CF (1948) The effects of altered arterial tensions of carbon dioxide and oxygen on cerebral blood flow and cerebral oxygen consumption of normal young men. J Clin Invest 27(4):484–492
15. Springett R et al (2000) Oxygen dependency of cerebral oxidative phosphorylation in newborn piglets. J Cereb Blood Flow Metab 20(2):280–289
16. Shadid M et al (1999) Near infrared spectroscopy-measured changes in cerebral blood volume and cytochrome aa3 in newborn lambs exposed to hypoxia and hypercapnia, and ischemia: a comparison with changes in brain perfusion and O_2 metabolism. Early Hum Dev 55(2):169–182
17. Kolyva C et al (2013) Dependence on NIRS source-detector spacing of cytochrome c oxidase response to hypoxia and hypercapnia in the adult brain. Adv Exp Med Biol 789:353–359
18. Kasbekar DK (1966) Effect of carbon dioxide-bicarbonate mixtures on rat liver mitochondrial oxidative phosphorylation. Biochim Biophys Acta 128(1):205–208

19. Fukuda R et al (2007) HIF-1 regulates cytochrome oxidase subunits to optimize efficiency of respiration in hypoxic cells. Cell 129(1):111–122
20. Fathi AR et al (2011) Carbon dioxide influence on nitric oxide production in endothelial cells and astrocytes: cellular mechanisms. Brain Res 1386:50–57
21. Taylor CT, Moncada S (2010) Nitric oxide, cytochrome C oxidase, and the cellular response to hypoxia. Arterioscler Thromb Vasc Biol 30(4):643–647

4 Relationship Between Left-Right Dominancy of Prefrontal Cortex Activity and Heart Rate During Rest and Task Periods: An fNIRS Study

Xianyin Hu, Yuki Ban, Yukio Yamada, Shin'ichi Warisawa, and Kaoru Sakatani

Abstract

Background
Functional near-infrared spectroscopy (fNIRS) studies demonstrated that regulation of stress response of the autonomic nervous system is mediated by the left-right asymmetry of prefrontal cortex (PFC) activity. However, it is not yet clear whether PFC regulation of stress response is functioning only when the subject was under stress or even at rest without stress. In addition, the temporal responsivity of PFC regulation of stress response is not known.

Aim
This study aims to investigate the relationship between the left-right asymmetry of PFC activity and heart rate during both resting state and stressful state while performing a working memory task.

Approach
Twenty-nine subjects were recruited to rest and conduct 2-back task, during which fNIRS and ECG were measured simultaneously.

Results
We found weak correlation ($r = 0.28$, $p = 0.137$) between laterality index (LI) and heart rate in the task session, but no correlation in rest sessions at a group level. Moreover, weak but significant correlation was found only in the task session for all analysis intervals ranged from 2 s to 1 min.

Conclusion
It is suggested that regulation of stress responses was mediated by the left-right asymmetry of PFC activity only when the subject was under stress stimuli and embody stress response did not affect PFC in reverse. This regulation can be observed at an analysis interval of no less than 2 s.

Keywords

fNIRS · PFC left-right asymmetry · Working memory task

4.1 Introduction

Stress responses of the autonomic nervous system (ANS) and neuroendocrine system are important biological responses in coping with environmental changes. The prefrontal cortex (PFC) plays an important role in the cerebral regulation of stress responses. Previous studies have reported that stress responses are controlled by the left-right neural activity balance of the PFC. On a theoretical level, the approach-avoidance model pointed out three core personality systems – approach, avoidance and a

X. Hu (✉) · Y. Ban · Y. Yamada · S. Warisawa
K. Sakatani
Graduate School of Frontier Sciences,
University of Tokyo, Tokyo, Japan
e-mail: shenyin@s.h.k.u-tokyo.ac.jp

F. Scholkmann et al. (eds.), *Oxygen Transport to Tissue XLIV*, Advances in Experimental Medicine and Biology 1438, https://doi.org/10.1007/978-3-031-42003-0_4

regulatory governing the two motivational system, are essential to human behavior. A thorough literature review [1] suggests that this regulatory system is linked with greater relative right frontal asymmetry than avoidance motivation. Numerous research utilizing advanced brain-imaging and sensing technology provides additional evidence. For example, electroencephalographic studies have demonstrated that greater right frontal activation was associated with increases in heat rate (HR) or blood pressure during unpleasant emotional stimuli [2]. Neuroimaging studies have demonstrated that the right frontal cortex, particularly the PFC, was predominantly activated during negative emotional states [3]. Functional near-infrared spectroscopy (fNIRS) studies demonstrated that right PFC activity during a mental arithmetic task played a greater role in cerebral regulation of HR [4]. It should be noted that fNIRS techniques measure cerebrovascular changes in the oxygenation state of hemoglobin rather than the neural activity, and that the applied fNIRS technique was sensitive to the superficial tissue layer. Therefore, it is important to apply a signal processing method that separates the functional component from a mixture of neural activity, motion artifacts and psychophysiological changes in the raw fNIRS signal.

However, there is an absence of discussion on whether PFC regulation of stress response is functioning only when the subject is under stress or even at rest as a background idling function. In addition, physical stress responses such as respiration may influence stress-induced PFC activity, but the causal relationship between the central and peripheral activities during stress tasks is not yet clear. Moreover, the temporal responsivity of the PFC regulation of the stress response remains unknown.

To clarify these issues, we investigated the relationship between the left-right asymmetry of PFC activity and HR during both resting state and stress task performance. In addition, we compared the correlation under a cognitive task where stress was induced by cognitive workload, with that under a rest session where subjects' respiratory rates were controlled at a high frequency to mimic stress-induced physical responses (e.g., hyperventilation) without cognitive workload to evaluate the causal relationship. Finally, we evaluated the temporal responsivity of PFC regulation of stress response using real-time analysis of NIRS signals.

4.2 Methods

We studied 29 graduate students (28 males and one female, average age: 24.9 ± 2.4 years) at the University of Tokyo. We measured bilateral PFC activity by a two-channel NIRS system (Hb-133, ASTEM Inc., Japan); the sensors were set on the left and right forehead. We also measured the ECG signal simultaneously by an ECG sensor (Plux Wireless Biosignals, Portugal) [5]. Both the oxygen hemoglobin signal as well as the ECG signal were measured for about 30 min, but only the data during sessions of interest were processed further.

4.2.1 The Stress Task: N-Back Task

We employed the N-back task as the stress task. Specifically, N was set to 2 and an auditory presentation with a pace of 1 item every second was utilized. In the auditory 2-back task (Fig. 4.1a), a sequence of numeric items will be presented in a noise canceling headphone, and subjects are instructed to remember the sequence of items and give a response (e.g., press the space key) when the present item matches the one they heard two items ago.

Although arithmetic tasks such as consecutive subtraction are often used in the literature to induce stress, there exists some concerns that arithmetic tasks are not optimal as the performance is not monitored in any form and is too simple for graduate students. N-back task is also used as a cognitively challenging stressor [6, 7]. Stress will be evoked due to task difficulty and performance pressure. A setting with $N = 2$ and a pace of 1 item per second was reported by most of the subjects to be considerably difficult.

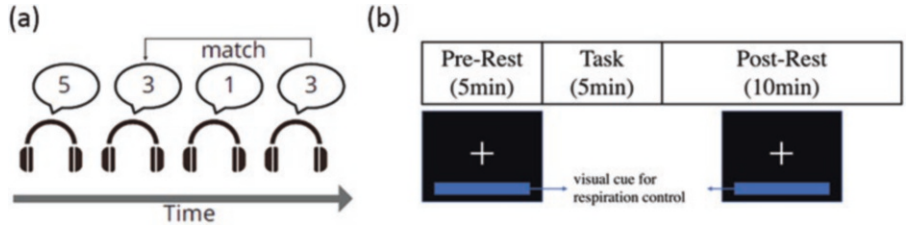

Fig. 4.1 (**a**) The auditory 2-back task. (**b**) The experimental procedure

4.2.2 Experimental Procedure

The experimental procedure is shown in Fig. 4.1b. Subjects were instructed to rest for 5 min (pre-rest), then they conducted the 2-back task for 5 min (task), and, finally, they rested for another 10 min (post-rest). During the pre-rest session and post-rest session, we have subjects' visual attention fixed at the cross mark presented in the center of the monitor. Respiratory rate was controlled during the rest sessions by telling the subjects to breathe at the same pace as the visual cue presented at the bottom of the monitor, which will expand and contract in length at a fixed pace. Respiration was controlled in this way at 12 breaths per minute and 20 breaths per minute in pre-rest and post-rest, respectively. The pre-rest session was considered a baseline rest state without cognitive load as well as embody stress response. The task session was considered a stressful state where stress was induced by the cognitive workload. The post-rest was considered a state with embody stress response which was not induced by cognitive workload but by a deliberately high reparatory rate.

4.2.3 Data Analysis

After removing outliers in the raw data, we employed the algorithm of hemodynamic modality separation to remove the systemic hemodynamic changes mainly caused by body movements [8]. Then we calculated the laterality index (LI) [9] to assess the asymmetry of PFC as follows:

$$LI = \frac{\sum_{t \in \text{analysis interval}} \left(\begin{array}{l} \left(\Delta oxyR_t - \Delta oxyR_{\min} \right) \\ -\left(\Delta oxyL_t - \Delta oxyL_{\min} \right) \end{array} \right)}{\sum_{t \in \text{analysis interval}} \left(\begin{array}{l} \left(\Delta oxyR_t - \Delta oxyR_{\min} \right) \\ +\left(\Delta oxyL_t - \Delta oxyL_{\min} \right) \end{array} \right)}$$

where $\Delta oxyR$ and $\Delta oxyL$ denote oxy-Hb concentration changes of the right and the left PFC, respectively, t is time in the analysis interval, and subscript *min* denotes the minimum value in the analysis interval. The LI defined by the above equation provides values in the range of $[-1, +1]$. A positive LI indicates that the right PFC is more active than the left PFC, on average, while a negative LI indicates that the left PFC is more active than the right PFC, on average.

Then, we performed Pearson's correlation analysis between the LI and HR during task periods and rest periods with different respiratory control. Moreover, we did the analysis in both offline manner and online manner to discover the temporal responsivity of this relationship. Online analysis was also referred to as real-time analysis. In the offline analysis, the whole rest/task period was treated as the analysis interval and one pair of LI and HR were calculated for each subject. In the online/real-time analysis, a time window ranging in length from 2 s to 1 min was treated as the analysis interval and multiple pairs of LI and HR were calculated for each subject.

There was no overlap between the segmented intervals in the online analysis.

4.3 Results

In the offline analysis, the Pearson's correlation between LI and HR was $r = 0.09$ ($p = 0.654$) in the pre-rest period, $r = 0.28$ ($p = 0.137$) in the task period and $r = 0.03$ ($p = 0.87$) in post-rest period as shown in Fig. 4.2a. All the data was tested for normality using Shapiro–Wilk test. Only during the task session did we observe a weak correlation between LI and HR. We also observed a weak positive correlation between the ΔHR and LI at task as shown in Fig. 4.2b.

In the online analysis of the task period, weak ($0.1 < r < 0.3$) but significant ($p < 0.01$) correlations were found between LI and HR for all the time intervals of 2, 5, 10, 20, 30, 40, 50 and 60 seconds. In the pre-rest period, significant correlations were found for time intervals of 2, 5 and 10 s, but all the strengths were under the level of a weak correlation of 0.2. Similarly, significant correlations were found in the post-rest period for time intervals of 5 and 10 s, but both strengths were too small to be considered to have a correlation. For details, please refer to Table 4.1.

4.4 Discussions

The present study demonstrated that the left-right asymmetry of PFC activity mediates stress response of ANS only when under stress stimuli. It was reported in a previous study that the LI at resting condition was correlated with state anxiety, but not with trait anxiety [10]. These results suggest that the PFC modulates stress responses of the ANS and levels of anxiety only in the pres-

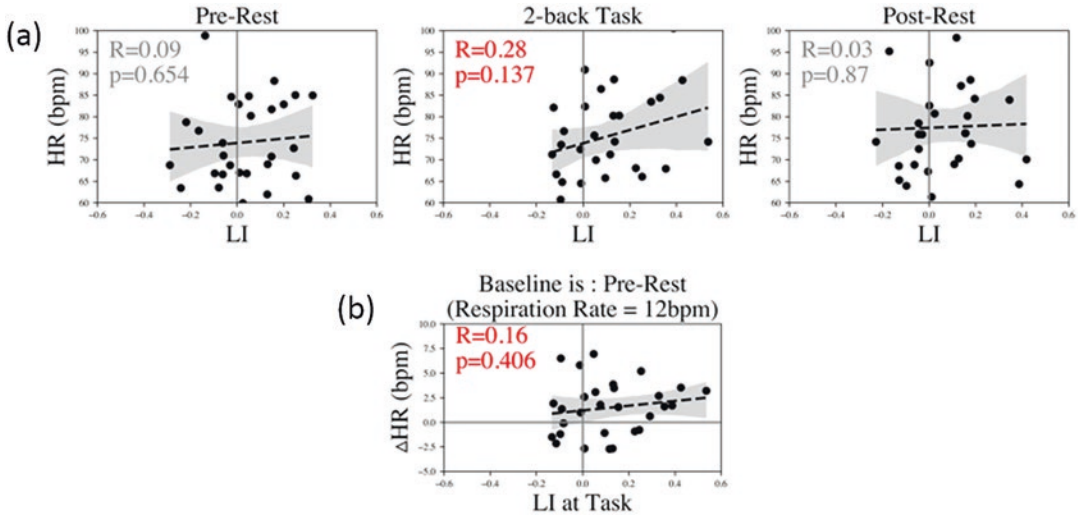

Fig. 4.2 (**a**) Correlation between LI and HR in offline analysis during different sessions. (**b**) Correlation between the ΔHR and LI at Task. $\Delta HR = HR_{Task} - HR_{pre-Rest}$

Table 4.1 Pearson's correlations between LI and HR analyzed at different intervals during rest and task sessions

Analysis interval Session	2 s	5 s	10 s	20 s	30 s	40 s	50 s	60 s
Pre-rest	0.08**	0.06*	0.07*	0.08 n.s.	0.07 n.s.	0.09 n.s.	0.08 n.s.	0.07 n.s.
Task	0.24**	0.22**	0.22**	0.22**	0.24**	0.26**	0.27**	0.28**
Post-rest	0.02 n.s.	0.04*	0.05*	0.05 n.s.	0.05 n.s.	0.06 n.s.	0.06 n.s.	0.05 n.s.

**$p < 0.01$, *$p < 0.05$, n.s.: $p > 0.05$

ence of environmental influences. That is, when the PFC integrates input signals from the five senses and determines that there is a stressor, it turns into a right-dominant PFC activity, which activates the sympathetic nervous system and increases the anxiety level.

On the other hand, as no statistical correlation was observed in the post-rest session, a stress response without stress stimuli does not appear to affect PFC in reverse. This is consistent with a precedent study which demonstrated that the difference in right and left absolute tissue oxygen saturation (ΔStO_2) at a group level did not depend on respiration rate [11]. Other previous studies showed the respiration state does have an influence, revealing that lateralization at the PFC during resting state correlated significantly with respiration rate [12, 13]. There are two main considerations regarding the difference in these results. The first is that the fNIRS data in this study were processed using an advanced algorithm [8] that separates the functional component and the systematic component. We only used the functional component to calculate LI, therefore we ensured that the systematic component mainly influenced by respiration was removed. On the other hand, respiration during the resting phase of this study was artificially controlled rather than being voluntarily regulated by the participants as in the previous studies. Therefore, it is suggested that such a pure embodied response rather than physiological condition may not have been mediated by regulation of the PFC.

Moreover, the weak positive correlation between ΔHR and LI in the task (Fig. 4.2b) is consistent with studies demonstrating that subjects with more right-dominant PFC activity have more heart rate increases than subjects with less right-dominant PFC activity [14].

Finally, the temporal responsivity of the PFC to stress tasks can be no less than 2 s, which is the shortest interval to observe at least one heartbeat. The present findings provided practical knowledge for real-time applications of NIRS such as neurofeedback, i.e., that the regulation of PFC asymmetry of stress response can be observed at an analysis interval as short as 2 s.

4.5 Conclusion

The present study demonstrated that left-right asymmetry of PFC activity regulates the stress response of ANS only when subjects are under stress stimuli, and that the stress response did not affect PFC asymmetry activity in reverse. In addition, the temporal responsivity of PFC is indicated to be as short as 2 s, which is the shortest interval to observe at least one heartbeat.

Acknowledgments We sincerely appreciate ASTEM Inc. for renting out the NIRS sensor, Hb-133.

References

1. Gable PA, Neal LB, Threadgill AH (2018) Regulatory behavior and frontal activity: considering the role of revised-BIS in relative right frontal asymmetry. Psychophysiology 55:e12910
2. Waldstein SR, Kop WJ, Schmidt LA et al (2000) Frontal electrocortical and cardiovascular reactivity during happiness and anger. Biol Psychol 55(1):3–23
3. Fischer H, Anderson JL, Furmark T et al (2002) Right-sided human prefrontal brain activation during acquisition of conditioned fear. Emotion 2(3):233–241
4. Sakatani K (2012) Optical diagnosis of mental stress. Oxygen Trans Tissue XXXIII:89–95
5. PLUX wireless biosignals S.A. Biosignalplux, Wearable body sensing
6. van Well S, Kolk AM, Klugkist IG (2008) Effects of sex, gender role identification, and gender relevance of two types of stressors on cardiovascular and subjective responses: sex and gender match and mismatch effects. Behav Modif 32(4):427–449
7. Hu MX, Lamers F, de Geus EJ et al (2016) Differential autonomic nervous system reactivity in depression and anxiety during stress depending on type of stressor. Psychosom Med 78(5):562–572
8. Yamada T, Umeyama S, Matsuda K (2012) Separation of fNIRS signals into functional and systemic components based on differences in hemodynamic modalities. PLoS One 7(11):e50271
9. Tanida M, Sakatani K, Takano R et al (2004) Relation between asymmetry of prefrontal cortex activities and the autonomic nervous system during a mental arithmetic task: near infrared spectroscopy study. Neurosci Lett 369(1):69–74
10. Ishikawa W, Sato M, Fukuda Y et al (2014) Correlation between asymmetry of spontaneous oscillation of hemodynamic changes in the prefrontal cortex and anxiety levels: a near-infrared spectroscopy study. J Biomed Opt 19(2):027005
11. Scholkmann F, Zohdi H, Wolf U (2020) Right-left asymmetry of prefrontal cerebral oxygenation: does it depend

on systemic physiological activity, absolute tissue oxygenation or hemoglobin concentration? In: Oxygen transport to tissue XLI. Springer, Cham, pp 105–112
12. Zohdi H, Scholkmann F, Wolf U (2020) Frontal cerebral oxygenation asymmetry: intersubject variability and dependence on systemic physiology, season, and time of day. Neurophotonics 7(2):025006
13. Scholkmann F, Zohdi H, Wolf M, Wolf U (2022) Frontal cerebral oxygenation in humans at rest: a Mirror symmetry in the correlation with cardio-respiratory activity. In: Oxygen transport to tissue XLIII. Springer International Publishing, Cham, pp 45–51
14. Brugnera A, Zarbo C, Adorni R, Compare A, Sakatani K (2017) Cortical and autonomic stress responses in adults with high versus low levels of trait anxiety: a pilot study. Oxygen Transp Tissue XXXIX:127–132

5 Relationship Between Cognitive Function, Oral Conditions and Systemic Metabolic Function in the Elderly

Kenji Karako, Yu Chen, Katsunori Oyama, Lizhen Hu, and Kaoru Sakatani

Abstract

Systemic metabolic disorders, including lifestyle-related diseases, are known risk factors for dementia. Furthermore, oral diseases such as periodontal disease and tooth decay are also associated with systemic metabolic disorders such as lifestyle-related diseases, and have also been reported to be indicators of risk factors for developing dementia. In this study, we investigated the relationship between cognitive function, oral conditions and systemic metabolic function in the elderly. We investigated the number of healthy teeth, the number of prosthetic teeth fitted, the number of missing prosthetic teeth, etc., in 41 elderly patients (69.7 ± 5.6 years old). Cognitive function was evaluated by the Mini Mental State Examination (MMSE). We also estimated MMSE scores for each subject using deep learning-based assessment of MMSE scores. This deep learning method enables the estimation of the MMSE score based on basic blood test data from medical examinations and reflects the systemic metabolic state including lifestyle-related diseases. The estimated MMSE score correlated negatively with age ($r = -0.381$), correlated positively with the number of healthy teeth ($r = 0.37$), and correlated negatively with the number of missing prosthetic teeth ($r = -0.39$). This relationship was not found in the measured MMSE scores. A negative correlation ($r = -0.36$) was found between age and the current number of teeth and a positive correlation ($r = 0.37$) was found between age and the number of missing prosthetic teeth. A positive correlation was found between the number of teeth requiring prosthesis and lifestyle-related diseases. The deep learning-based estimation method of cognitive function clearly demonstrated the close relationship between oral health condition, systemic metabolic function and the risk of cognitive impairment. It was determined that the smaller the number of existing teeth and the larger the number of missing prosthetic teeth, the higher is the risk of cognitive impairment. Systemic metabolic function is presumed to affect oral health and cognitive function. Interestingly, no such relationship was found in the measured MMSE scores. There are two possible reasons for this. The first is that MMSE is a subjective test and is less accurate in assessing cognitive function. The second is that because the MMSE

K. Karako (✉) · Y. Chen · L. Hu · K. Sakatani
Department of Human and Engineered Environmental Studies, Graduate School of Frontier Sciences, The University of Tokyo, Kashiwa, Japan
e-mail: k.karako@edu.k.u-tokyo.ac.jp; k.sakatani@edu.k.u-tokyo.ac.jp

K. Oyama
Department of Computer Science, College of Engineering, Nihon University, Koriyama, Japan

F. Scholkmann et al. (eds.), *Oxygen Transport to Tissue XLIV*, Advances in Experimental Medicine and Biology 1438, https://doi.org/10.1007/978-3-031-42003-0_5

estimated based on blood data using deep learning is calculated based on the metabolic function, it has a stronger correlation with the oral health condition affected by the metabolic function. In conclusion, oral health condition may predict cognitive impairment in the elderly.

Keywords

Oral health · Cognitive function · Systemic metabolic function

5.1 Introduction

In recent years, the relationship between dementia and oral findings has been reported. In patients with Alzheimer's disease, loss of more than half of the teeth and use of complete dentures have been reported to be indicative factors for significant risk of developing Alzheimer's disease [1]. A long-term follow-up study in the United States found that having fewer teeth indicated an increased risk of developing Alzheimer's dementia [2]. Furthermore, the relationship between multiple tooth loss, decreased masticatory strength, and cognitive function in 557 elderly people was reported to be high [3], suggesting a relationship between cognitive function and masticatory strength.

Recent studies demonstrated a close relationship between the onset of cognitive dysfunction and systemic metabolic disorders. Lifestyle-related diseases can result in vascular cognitive impairment (VCI) due to atherosclerosis [4]. VCI plays an important role not only in vascular dementia but also in the development of dementia in the elderly with Alzheimer's disease. Similarly, malnutrition [5], anemia [6], diabetes mellitus [7] and renal dysfunction [8] can cause cognitive impairment and increase the risk of dementia. Based on the relation between cognitive impairment and systemic metabolic disorders, we previously developed a deep learning algorithm (i.e., feedforward deep neural network; DNN) that can estimate the risk of cognitive impairment from basic blood test data obtained during a health check. This shows systemic metabolic disorders including lifestyle diseases [9]. The estimation accuracy of the DNN model ($r = 0.66$, $p < 0.001$) was validated using subjects who were not included in its training.

In this study, to clarify the relationship between cognitive function, oral conditions and systemic metabolic function in the elderly, we analyzed the data of oral findings, the Mini Mental State Examination (MMSE) scores and the MMSE scores estimated by DNN from blood data.

5.2 Methods

5.2.1 Subjects

We studied 41 elderly patients (28 males, 13 females, 69.7 ± 5.6 years old). A dentist investigated oral conditions, including the number of healthy teeth, the number of prosthetic teeth required and the number of missing prosthetic teeth, in all of the subjects. Cognitive function was evaluated using the most commonly used test, which is the MMSE [8]. The average MMSE score was 26.7 ± 2.1.

5.2.2 Deep learning-Based Estimation of Cognitive Function

We employed a deep learning-based screening test that predicts cognitive impairment expressed by MMSE score based on basic blood test data and subject age [9]. Briefly, to implement the DNN we used the H2O open-source machine learning library, which enables the configuration of multilayer feedforward neural networks [9]. The input data to the DNN consists of 24 variables including the subject's age plus 23 blood test items (Table 5.1), all applied to the input layer. The DNN has two hidden layers with 400 neurons in each.

Table 5.1 Blood test items input to the deep learning-based estimation of cognitive function

Complete blood count	General biochemical examination	
WBC count	Total protein	BUN
RBC count	Albumin	Creatinine
Hemoglobin	A/G ratio	Uric acid
Hematocrit	AST	Glucose
MCV	ALT	Na
MCH	r-GTP	K
MCHC	Total cholesterol	CI
Platelet count	Triglyceride	

MCV mean corpuscular volume, *MCH* mean corpuscular hemoglobin, *MCHC* mean corpuscular hemoglobin concentration, *BUN* blood urea nitrogen, *A/G ratio* Albumin/Globulin ratio, *AST* aspartate aminotransferase, *ALT* alanine aminotransferase, *r-GTP* γ-Glutamyl Transpeptidase, *Na* sodium, *Cl* chloride, *K* potassium

Table 5.2 Correlation between MMSE scores (estimated and measured), lifestyle habits and oral condition

	Age	*p*	Estimated MMSE	*p*	Measured MMSE	*p*
Age	–		−0.381	*	−0.274	
Lifestyle diseases	0.020		0.100		−0.123	
Smoking	0.212		−0.243		−0.152	
Frequency of toothbrushing per day	−0.136		0.070		0.239	
Number of healthy teeth	−0.261		0.235		0.031	
Number of untreated teeth	0.120		0.117		−0.172	
Number of treated teeth	−0.176		0.172		0.110	
Current number of teeth	−0.361	*	0.368	*	0.115	
Number of prostheses required	−0.103		−0.002		−0.302	
Number of missing prosthetic teeth	0.371	*	−0.387	*	−0.023	

*$p < 0.05$, **$p < 0.01$

5.3 Results

We analyzed correlations between lifestyle habits, oral conditions, age, measured MMSE and estimated MMSE collected from 41 elderly patients. The results are shown in Table 5.2. The estimated MMSE score correlated negatively with age ($r = -0.381$), correlated positively with the number of healthy teeth ($r = 0.37$) and correlated negatively with the number of missing prosthetic teeth ($r = -0.39$). Interestingly, this relationship was not found in the measured MMSE scores. A negative correlation ($r = -0.36$) was found between age and the current number of teeth and a positive correlation ($r = 0.37$) was found between age and the number of missing prosthetic teeth. A positive correlation was found between the number of teeth requiring prosthesis and lifestyle-related diseases.

Table 5.3 shows the correlation between oral condition and lifestyle habits. We found negative correlation between the number of healthy teeth and smoking ($r = -0.314$). Furthermore, there was a negative correlation between current number of prostheses and smoking ($r = -0.451$). In contrast, there was a positive correlation between number of prostheses required and lifestyle diseases ($r = 0.326$).

5.4 Discussion and Conclusion

The estimated MMSE score showed a positive correlation with the number of current teeth and a negative correlation with the number of missing prosthetic teeth. The higher the number of current teeth was, the higher the estimated MMSE score; and the higher the number of missing dentures was, the lower the estimated MMSE score. Interestingly, such a relationship was only found for MMSE scores estimated from blood data and not for measured MMSE scores. Although the

Table 5.3 Correlation between lifestyle habits and oral conditions

	Lifestyle-diseases (R)	p	Smoking (R)	*p*	Frequency of brushing teeth per day (R)	*p*
Number of healthy teeth	−0.136		**−0.314**	*	0.019	
Number of untreated teeth	−0.030		0.086		−0.045	
Number of treated teeth	0.150		−0.211		0.111	
Current number of teeth	0.007		**−0.451**	**	0.082	
Number of prostheses required	**0.326**	*	0.137		−0.204	
Number of missing prosthetic teeth	−0.048		0.302		−0.009	

*$p < 0.05$, **$p < 0.01$

underlying mechanism for this is still unclear, the following possibilities should be considered: First, the MMSE is a subjective questionnaire test, whereas the estimated MMSE from blood test data is derived from objective data. Therefore, estimated MMSE scores may more accurately reflect cognitive function. Another possibility is that both estimated MMSE scores and oral condition reflect systemic metabolic status. Given that the estimated MMSE predicts future cognitive function, oral condition may also reflect future cognitive function.

Our results support previous studies showing that the number of teeth lost is negatively correlated with cognitive function [3]. However, the pathophysiological mechanism of the relationship between oral conditions and cognitive function is still unclear. We propose the following two possible mechanisms: First, the relationship between occlusal function and cognitive function. It has been reported that occlusal disharmony decreases working memory performance associated with a reduced activity of the prefrontal cortex [10]; tooth loss can cause occlusal disharmony. Second, the relationship between cognitive function and systemic metabolic activity. Tooth loss may induce systemic metabolic disorders such as malnutrition [5] and anemia [6], which can lead to cognitive decline. In this study, the degree of cognitive impairment estimated from blood test data reflecting systemic metabolic disorders showed a negative correlation with the number of lost teeth, supporting this possibility [11].

There was a negative correlation between age and the number of current teeth, and a positive correlation between the number of missing prosthetic teeth. These results indicate that older people have fewer teeth and more missing prosthetic teeth. A negative correlation was found between smoking and the number of current teeth and the number of healthy teeth. Smoking is a cause of periodontal disease [12], suggesting that the reduction of the number of current teeth and healthy teeth was caused by smoking-induced periodontal disease.

In conclusion, this study demonstrated a close relationship between cognitive function, oral health and systemic metabolic function in the elderly. Analysis of basic blood test data using deep learning may be useful in evaluating the relationship between systemic metabolic disorders and cognitive impairment.

References

1. Kondo K, Niino M, Shido K (1994) A case-control study of Alzheimer's disease in Japan – significance of life-styles. Dement Geriatr Cogn Disord 5:314–326
2. Stein PS, Desrosiers M, Donegan SJ, Yepes JF, Kryscio RJ (2007) Tooth loss, dementia and neuropathology in the Nun study. J Am Dent Assoc 138:1314–1322
3. Lexomboon D, Trulsson M, Wårdh I, Parker MG (2012) Chewing ability and tooth loss: association with cognitive impairment in an elderly population study. J Am Geriatr Soc 60:1951–1956
4. Van Der Flier WM, Skoog I, Schneider JA et al (2018) Vascular cognitive impairment. Nat Rev Dis Primers 4:1–16
5. Sugimoto T, Arai H, Sakurai T (2022) An update on cognitive frailty: Its definition, impact, associated factors and underlying mechanisms, and interventions. Geriatr Gerontol Int 22:99–109
6. Hong CH, Falvey C, Harris TB et al (2013) Anemia and risk of dementia in older adults: findings from the Health ABC study. Neurology 81:528–533
7. Li T, Cao HX, Ke D (2021) Type 2 Diabetes Mellitus Easily Develops into Alzheimer's Disease via Hyperglycemia and Insulin Resistance. Curr Med Sci 41:1165–1171
8. Folstein MF, Folstein SE, McHugh PR (1975) "Mini-mental state" A practical method for grading the cognitive state of patients for clinicians. J Psychiatr Res 12:189–198
9. Candel A, Parmar V, LeDell E, Arora A (2016) Deep learning with H2O. H2O. ai Inc., pp 1–21
10. Sakatani K, Tsujii T, Hirayama T et al (2013) Effects of occlusal disharmony on working memory performance and prefrontal cortex activity induced by working memory tasks measured by NIRS. Adv Exp Med Biol 765:239–244
11. Sakatani K, Oyama K, Hu L (2020) Deep learning-based screening test for cognitive impairment using basic blood test data for health examination. Front Neurol 11:588140
12. Duarte PM, Nogueira CFP, Silva SM, Pannuti CM, Schey KC, Miranda TS (2021) Impact of smoking cessation on periodontal tissues. Int Dent J 72:31–36

6 Pro-survival Phenotype of HIF-1α: Neuroprotection Through Inflammatory Mechanisms

Michelle A. Puchowicz, Kehkashan Parveen, Aarti Sethuraman, Tauheed Ishrat, Kui Xu, and Joseph LaManna

Abstract

Hypoxia-inducible factor 1 (HIF-1) is a major player in the oxygen sensor system as well as a transcription factor. HIF-1 is also associated in the pathogenesis of many brain diseases including Alzheimer's disease (AD), epilepsy and stroke. HIF-1 regulates the expression of many genes such as those involved in glycolysis, erythropoiesis, angiogenesis and proliferation in hypoxic condition. Despite several studies, the mechanism through which HIF-1 confers neuroprotection remains unclear, one of them is modulating metabolic profiles and inflammatory pathways. Characterization of the neuroprotective role of HIF-1 may be through its stabilization and the regulation of target genes that aid in the early adaptation to the oxidative stressors. It is interesting to note that mounting data from recent years point to an additional crucial regulatory role for hypoxia-inducible factors (HIFs) in inflammation. HIFs in immune cells regulate the production of glycolytic energy as well as innate immunity, pro-inflammatory gene expression, and mediates activation of pro-survival pathways. The present review highlights the contribution of HIF-1 to neuroprotection where inflammation is the crucial factor in the pathogenesis contributing to neural death. The potential mechanisms that contribute to neuroprotection as a result of the downstream targets of HIF-1α are discussed. Such mechanisms include those mediated through IL-10, an anti-inflammatory molecule involved in activating pro-survival signaling mechanisms via AKT/ERK and JAK/STAT pathways.

Keywords

HIF-1α · Neuroinflammation · Neuroprotection

M. A. Puchowicz (✉)
Department of Pediatrics, University of Tennessee Health Science Center, Memphis, TN, USA

Department of Physiology & Biophysics, Case Western Reserve University, Cleveland, OH, USA
e-mail: mpuchowi@uthsc.edu

K. Parveen · A. Sethuraman
Department of Pediatrics, University of Tennessee Health Science Center, Memphis, TN, USA

T. Ishrat
Department of Anatomy and Neurobiology, University of Tennessee Health Science Center, Memphis, TN, USA

K. Xu · J. LaManna
Department of Physiology & Biophysics, Case Western Reserve University, Cleveland, OH, USA

F. Scholkmann et al. (eds.), *Oxygen Transport to Tissue XLIV*, Advances in Experimental Medicine and Biology 1438, https://doi.org/10.1007/978-3-031-42003-0_6

6.1 HIF-1 in Hypoxia and Inflammation

Under various pathologies and metabolic conditions, hypoxia and inflammation appear to have a complex interaction [1, 2]. The formation of hypoxic signaling intermediates are known to accompany inflammatory conditions, which in turn initiate inflammatory responses by activating cytokines and inflammatory cells [3]. In the recent years HIF-1 has been described to be a significant modulator of hypoxia signaling in inflammation. HIF-1 is a heterodimeric protein complex that plays a significant role in responding to low concentrations of oxygen or hypoxia and is constitutively expressed as a subunit-β and an oxygen-dependent subunit-α. During normoxic conditions, HIF-1α is synthesized and degraded by the ubiquitin-proteasome system [2]. Oxygen-independent mechanisms can also regulate HIF-1 transcription and translation under normoxia during altered metabolic states. Thus, HIF-1 is a crucial transcriptional factor that regulates thousands of genes for maintaining cellular homeostasis. This process is crucial for the survival and function of immune cells by regulating gene transcription. It has been observed that the blood levels of inflammatory cytokines such IL-1, IL-6, and tumor necrosis factor alpha (TNF-α) are elevated in hypoxia conditions [4]. Intriguingly, HIF-1 stability has shown to regulate the production of inflammatory cytokines like TNF-α and as a result inflammation and hypoxia signaling augment one another through a positive feedback loop [5–7].

Mechanism and Role of HIF-1α in Pathophysiology HIF-1α may be the major contributor behind beneficial and deleterious effects throughout the emergence of the most important dysfunctionality connected to neurodegeneration. Depending on the degree of hypoxia, HIF-1α has been shown to play a dual role as a "protective transcription factor" or a "killing factor" (when linked to p53) [8]. Once HIF-1α is stabilized, the HIF-1 complex is subsequently moved into the nucleus where it acts as a transcriptional activator for over thousands of genes [9]. The activation of HIF-1α during moderate hypoxia can enhance tolerance to a more severe hypoxic lesion later on and thus enable the adaptive changes needed for a quicker and better recovery of the afflicted tissue. HIF-1 functions as an endogenous biological defense mechanism that confers protection against global cerebral ischemia or potential fatal damages under ischemic conditions [10]. Additionally, it has been shown that HIF-1 is up-regulated in a variety of disorders, including several neurological diseases, as a brain neuroprotective response element against stresses including reactive oxygen species (ROS) and inflammation [11].

HIF-1α and Inflammation in Neurological Disorders Inflammation is known to exacerbate disease related pathologies by releasing pro-inflammatory cytokines IL-1β, IL-6 and triggering ERK1/2/AKT, JNK/MAPK and JAK/STAT signaling pathways and thus resulting in severe neural dysfunctionality. Neurological disorders such as Alzheimer's disease (AD), epilepsy, amyotrophic lateral sclerosis (ALS), Parkinson's disease (PD) and stroke are characterized by progressive loss of neural functions. During pathogenesis of neurological disorders, the inflammatory cytokines, including as macrophage-derived TNF-α and IL-1β, upregulate HIF-1 through mechanisms that inhibit prolyl hydroxylase (PHD) enzymes and increase HIF-1 stability and transcriptional activity [12–14]. Additionally, HIF-1 may inhibit the production of pro-inflammatory cytokine receptors, which reduces the dangers of severe neuroinflammation during ischemic insult [15]. HIF-1α-mediated down regulation of pro-inflammatory cytokines such as IL-6 and TNF-α has been recently described to act through IL-10-mediated attenuation of NLRP3 inflammasome or via IL-10/JAK1/STAT3-mediated transcriptional attenuation [16, 17]. IL-10-mediated immune regulation occurs through the downregulation of pro-inflammatory cytokines. IL-10-mediated inflammatory pathways have been studied for its implications in the design of targeted approaches aiming at controlling deleterious inflammation in

the brain [18]. Additionally, IL-10 receptor activation has been shown to specifically activate the JAK1-STAT3-mediated downregulation of pro-inflammatory cytokines [19, 20]. Further, IL-10/JAK1/STAT3 pathway has been described as the negative regulator of inflammation that controls both the degree and duration of inflammation [21, 22].

6.2 Inhibition of NLRP3 Inflammasome by HIF-1α

Activation of the NLRP3 inflammasome plays a crucial role in the outcome of various brain diseases and injury such as Alzheimer's and traumatic brain injury [23]. The authors describe that the contribution of NLRP3 inflammasome is associated with cellular damage and increased inflammatory responses following traumatic brain injury. Furthermore, blocking or inhibiting the activation of the NLRP3 inflammasome may have substantial potential to salvage tissue damage during traumatic brain injury. The binding of HIF-1α to IL-10 promoter has been reported to be involved in HIF-1α-mediated IL-10 expression and its role in modulation of cell metabolism and inflammatory responses. Reports have shown that HIF-1α stabilization elicits a neuroprotective response through modification of inflammatory pathways via modulation of cytokine regulation. Figure 6.1 shows a proposed scheme of the mechanisms of how HIF-1α mediates downstream inflammatory pathways. Once HIF-1α is stabilized, it acts to activate the JAK-STAT3 pathways and/or inhibit the NLRP3 inflammasome, and thus resulting in neuroprotection. Diet-induced stabilization of HIF-1α and upregulation of IL-10 in rodent brain under normoxic ketotic conditions has been shown to play a role in the upregulation of the IL-10 and downregulation IL-6 and TNF-α [17, 24, 25, 26], whereby HIF-1α transcriptionally regulates IL-10 levels by direct binding to hypoxia responsive elements (HREs) on the IL-10 promoter [24, 27]. Recent studies bring together ketosis-mediated stabilization of HIF-1α as a potential neuroprotective phenotype in mice and rats in an oxygen-independent manner via IL-10-mediated activation of JAK1-STAT3, AKT/ERK pathways [17, 28].

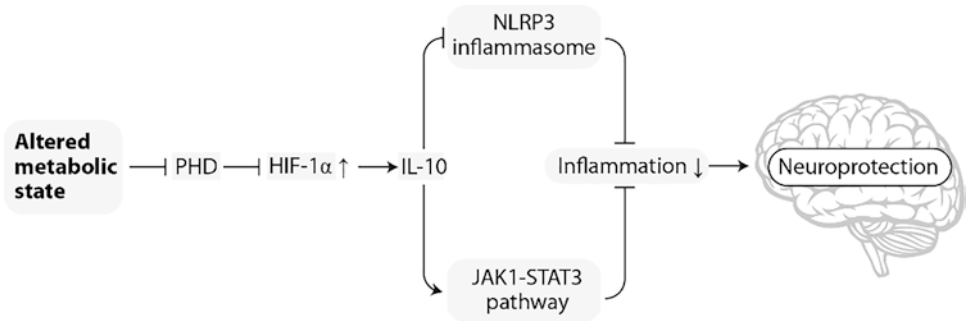

Fig. 6.1 Neuroprotective Phenotype & HIF-1α. Working model of IL-10-mediated JAK1-STAT3 pathway activation following HIF-1α stabilization through a metabolic induced inhibition of prolyl hydroxylase (PHD). Accumulation of HIF-1α as a result of an altered metabolic state activates IL-10, whereby resulting in an upregulation of pro-survival pathways involving JAK1-STAT3, ERK/AKT and inhibition of NLRP3 inflammasome

References

1. Semenza GL (2004) Hydroxylation of HIF-1: oxygen sensing at the molecular level. Physiology 19:176–182
2. Semenza GL (2011) Oxygen sensing, homeostasis, and disease. N Engl J Med 365(6):537–547
3. Eltzschig HK, Carmeliet P (2011) Hypoxia and inflammation. N Engl J Med 364(7):656–665
4. Crifo B, Taylor CT (2016) Crosstalk between toll-like receptors and hypoxia-dependent pathways in health and disease. J Investig Med 64(2):369–375
5. Shin DH, Li SH, Yang SW, Lee BL, Lee MK, M.K., Park J.W. (2009) Inhibitor of nuclear factor-kappaB alpha derepresses hypoxia-inducible factor-1 during moderate hypoxia by sequestering factor inhibiting hypoxia-inducible factor from hypoxia-inducible factor 1alpha. FEBS J 276(13):3470–3480
6. Fong GH, Takeda K (2008) Role and regulation of prolyl hydroxylase domain proteins. Cell Death Differ 15:635–641
7. Masson N, Ratcliffe PJ (2003) HIF prolyl and asparaginyl hydroxylases in the biological response to intracellular O_2 levels. J Cell Sci 116:3041–3049
8. Piret JP, Mottet D, Raes M, Michiels C (2002) Is HIF-1 a pro- or an anti-apoptotic protein? Biochem Pharmacol 64(5–6):889–892
9. Sharp FR, Bernaudin M (2004) HIF1 and oxygen sensing in the brain. Nat Rev Neurosci 5(6):437–448
10. Chen S, Sang N (2016) Hypoxia-inducible Factor-1: a critical player in the survival strategy of cells. J Cell Biochem 117(2):267–278
11. Bhatia D, Ardekani MS, Shi Q, Movafagh S (2017) Chapter 21: Hypoxia and its emerging therapeutics in neurodegenerative, inflammatory and renal diseases. In: Hypoxia and human diseases. INTECH. https://doi.org/10.5772/66089
12. Dehne N, Brune B (2009) HIF-1 in the inflammatory microenvironment. Exp Cell Res 315:1791–1797
13. Hellwig-Burgel T, Rutkowski K, Metzen E, Fandrey J, Jelkmann W (1999) Interleukin-1beta and tumor necrosis factor-alpha stimulate DNA binding of hypoxia-inducible factor-1. Blood 94:1561–1567
14. Zhou J, Fandrey J, Schumann J, Tiegs G, Brune B (2003) NO and TNF-alpha released from activated macrophages stabilize HIF-1alpha in resting tubular LLC-PK1 cells. Am J Physiol Cell Physiol 284:C439–C446
15. Xing J, Lu J (2016) HIF-1 alpha activation attenuates IL-6 and TNF-alpha pathways in hippocampus of rats following transient global ischemia. Cell Physiol Biochem Int J Exp Cell Physiol Biochem Pharmacol 39:511–520
16. Gurung P, Li B, Subbarao Malireddi RK et al (2015) Chronic TLR stimulation controls NLRP3 Inflammasome activation through IL-10 mediated regulation of NLRP3 expression and Caspase-8 activation. Sci Rep 5:14488
17. Sethuraman A, Rao P, Pranay A, Xu K, LaManna JC, Puchowicz MA (2021) Chronic ketosis modulates HIF1α-mediated inflammatory response in rat brain. Adv Exp Med Biol 1269:3–7
18. Lobo-Silva D, Carriche GM, Castro AG et al (2016) Balancing the immune response in the brain: IL-10 and its regulation. J Neuroinflammation 13(1):297
19. Hwang CJ, Yun HM, Jung YY et al (2015) Reducing effect of IL-32alpha in the development of stroke through blocking of NF-kappaB, but enhancement of STAT3 pathways. Mol Neurobiol 51(2):648–660
20. Verma R, Balakrishnan L, Sharma K et al (2016) A network map of Interleukin-10 signaling pathway. J Cell Commun Signal 10(1):61–67
21. Riley JK, Takeda K, Akira S et al (1999) Interleukin-10 receptor signaling through the JAK-STAT pathway. Requirement for two distinct receptor-derived signals for anti-inflammatory action. J Biol Chem 274(23):16513–16521
22. Hutchins AP, Diez D, Miranda-Saavedra D (2013) The IL-10/STAT3-mediated anti-inflammatory response: recent developments and future challenges. Brief Funct Genomics 12(6):489–498
23. Ismael S, Ahmed HA, Adris T, Parveen K, Thakor P, Ishrat T (2021) The NLRP3 inflammasome: a potential therapeutic target for traumatic brain injury. Neural Regen Res 16(1):49–57. PMID: 32788447
24. Puchowicz MA, Zechel JL, Valerio J et al (2008) Neuroprotection in diet-induced ketotic rat brain after focal ischemia. J Cereb Blood Flow Metab 28(12):1907–1916
25. Xu K, Ye L, Sharma K et al (2017) Diet-induced ketosis protects against focal cerebral ischemia in mouse. Adv Exp Med Biol 977:205–213
26. Zhang Y, Xu K, Kerwin T et al (2018) Impact of aging on metabolic changes in the Ketotic rat brain: glucose, oxidative and 4-HNE metabolism. Adv Exp Med Biol 1072:21–25
27. Cai Z, Luo W, Zhan H et al (2013) Hypoxia-inducible factor 1 is required for remote ischemic preconditioning of the heart. Proc Natl Acad Sci 110:17462–17467
28. Garcia JM, Stillings SA, Leclerc JL et al (2017) Role of Interleukin-10 in acute brain injuries. Front Neurol 8:244

7 Infradian Rhythms in Cerebrovascular Oxygenation and Blood Volume in Humans at Rest: A 5-Year Study

Felix Scholkmann, Hamoon Zohdi, Martin Wolf, and Ursula Wolf

Abstract

Background: All parameters of human physiology show chronobiological variability. While circadian (cycle length ~ 24 h) rhythms of the neuronal, hemodynamic and metabolic aspects of human brain activity are increasingly being explored, infradian (cycle length > 24 h) rhythms are largely unexplored. Aim: We investigated if cerebrovascular oxygen saturation (StO_2) and blood volume ([tHb]) values measured over many years in many subjects during resting show infradian rhythmicity.

Subjects and Methods: Absolute StO_2 and [tHb] values (median over a 5 min resting-phase while sitting) were measured in 220 healthy subjects (age: 24.7 ± 3.6 years, 87 males, 133 females) 2–4 times on different days over the right and left frontal lobe (FL) and occipital lobe (OL) by employing frequency-domain NIRS as part of different systemic physiology augmented functional near-infrared spectroscopy, SPA-fNIRS, studies. The data set consisted of 708 single measurements performed over a timespan of 5 years (2017–2021). General additive models (GAM) and cosinor modelling were used to analyze the data.

Results: The GAM analysis revealed (i) a non-linear trend in the StO_2 and [tHb] values over the 5-year span, (ii) a circannual (cycle length ~ 12 months) rhythm in StO_2 at the FL (amplitude (A): 3.4%, acrophase (φ): June) and OL (A: 1.5%, φ: May) as well as in [tHb] at the OL (A: 1.2 μM, bathyphase (θ): June), and (iii) a circasemiannual (cycle length ~ 6 months) rhythm in [tHb] at the FL (A: 2.7 μM, φ: March and September, respectively). Furthermore, the circannual oscillations of StO_2 (at the FL) and [tHb] (at the OL) were statistically significantly correlated with the day length, outdoor temperature, humidity and air pressure.

Discussion and Conclusion: We conclude that absolute values of StO_2 and [tHb] show chronobiological variability on the group-level with a long-term nonlinear trend as well as circannual/circasemiannual rhythmicity. These rhythms need to be taken into account

F. Scholkmann (✉) · H. Zohdi
Institute of Complementary and Integrative Medicine, University of Bern, Bern, Switzerland

Biomedical Optics Research Laboratory, Department of Neonatology, University Hospital Zurich, University of Zurich, Zurich, Switzerland
e-mail: Felix.Scholkmann@unibe.ch

M. Wolf
Biomedical Optics Research Laboratory, Department of Neonatology, University Hospital Zurich, University of Zurich, Zurich, Switzerland

U. Wolf
Institute of Complementary and Integrative Medicine, University of Bern, Bern, Switzerland

F. Scholkmann et al. (eds.), *Oxygen Transport to Tissue XLIV*, Advances in Experimental Medicine and Biology 1438, https://doi.org/10.1007/978-3-031-42003-0_7

when defining reference values for StO_2 and [tHb] and may correlate with the variability of cerebrovascular disease incidents over the year.

Keywords

Chronobiology · Cerebral oxygenation · Infradian rhythms

7.1 Introduction

In a previous study by our group, we found that resting-state values of cerebrovascular oxygen saturation (StO_2) (averaged over the left and right frontal lobe) in humans ($n = 126$) were correlated with the heart rate (HR) but not the respiration rate (RR) [1]. This insight is, for example, relevant for the definition of StO_2 reference values, where HR needs, therefore, to be included. In another study by us (with $n = 134$), we observed (i) a correlation of resting-state StO_2 over the frontal lobe with partial pressure of end-tidal CO_2 ($P_{ET}CO_2$), as well as (ii) a circannual (cycle length ~ 12 months) variability of StO_2 and the concentration of hemoglobin ([tHb]; a marker of blood volume) [2]. Therefore, the interpretation of StO_2 needs to consider the state of systemic physiology as well as chronobiological variability. In the present study, we aimed to further investigate the chronobiological variability of StO_2 and [tHb] by using a novel data set, including measurements performed over a timespan of 5 years on more than 200 adults.

7.2 Subjects and Methods

Participants and Measurements Data from previously published and ongoing systemic physiologic augmented functional near-infrared spectroscopy (SPA-fNIRS) studies conducted by us [1–7] were combined to a data set of absolute StO_2 and [tHb] values. The data was obtained by measuring 220 healthy subjects (age: 24.7 ± 3.6 years, 87 males, 133 females) 2–4 times on different days and times of day between subjects (i.e. same time of day for each subject but different times of day between subjects) over the right and left frontal lobe (FL) and occipital lobe (OL) by employing a frequency-domain NIRS device (FD-NIRS; Imagent, ISS Inc., Champaign, Illinois, USA). The data set consisted of 708 single measurements performed over a timespan of 5 years (2017–2021) in Bern, Switzerland.

Signal Processing and Data Analysis After low-pass filtering with a robust second-order moving average filter (window length: 2 min), median values of StO_2 and [tHb] (mean of the right and left FL and mean of right and left OL) were calculated based on 5 min long time-series from the resting-phase of the respective SPA-fNIRS studies. Outliers in the data due to measurement artifacts (three standard deviations away from the group mean) were removed before further analysis. Local weather data were obtained by CustomWeather, Inc. (Mill Valley, CA, USA) and day-to-day values for the length of day during a year by Time and Date AS (Stavanger, Norway).

To investigate the infradian variability (cycle length > 24 h) of the data, general additive models (GAM) were employed to investigate if the data exhibited a circannual rhythm and a trend over the 5 years. To this end, the following GAMs were employed: (i) $g(StO_2\text{-FL}) = \beta_0 + f_1(T_{days}) + f_2(T_{months}) + f_3(\text{Age}) + \text{Sex} + \text{Subject} + \varepsilon$, (ii) $g(StO_2\text{-OL}) = \beta_0 + f_1(T_{days}) + f_2(T_{months}) + f_3(\text{Age}) + \text{Sex} + \text{Subject} + \varepsilon$, (iii) $g([\text{tHb}]\text{-FL}) = \beta_0 + f_1(T_{days}) + f_2(T_{months}) + f_3(\text{Age}) + \text{Sex} + \text{Subject} + \varepsilon$, and (iv) $g([\text{tHb}]\text{-OL}) = \beta_0 + f_1(T_{days}) + f_2(T_{months}) + f_3(\text{Age}) + \text{Sex} + \text{Subject} + \varepsilon$, with β_0 the intercept, f_1 a regression spline function with 182 knots (i.e. every second day), f_2 a cyclic cubic regression spline with a yearly period,, f_3 a thin plate regression spline, g a smooth monotonic link function, ε the residual, 'Sex' a categorical variable with the sex of the subject, and 'Subject' a categorical variable with the individual subject identification

number. Both categorical variables were modelled as random effects in order to correct both parameters while modeling the data. The models were fitted by penalized likelihood maximization and taking into account the autocorrelation of the data. From the fitted spline functions, the circannual function was further analyzed by a cosinor analysis [8, 9] to determine the amplitude (A), acrophase (φ, phase at maximum deflection) and bathyphase (θ, phase at minimum deflection). Furthermore, the circannual components of StO_2 and tHb were analyzed for possible correlations with the monthly values of the local weather (temperature, humidity, air pressure) and day length.

Signal processing was performed by Matlab (R2017a, MathWorks, Inc., Massachusetts, USA) and statistical analysis in JASP (version 0. 10.0.0) and R (version 4.1.2) [10] using the *ggplot2* [11] and *mgcv* [12] packages.

7.3 Results

Cerebrovascular Oxygenation and Blood Volume: Infradian Changes The GAM analysis revealed (i) a statistically significant ($p < 0.01$) non-linear trend in StO_2 and [tHb] (FL and OL) over the 5-year span, (ii) a statistically significant ($p < 0.01$) circannual rhythm in StO_2 at the FL (A: 3.4%, φ: June) and OL (A: 1.5%, φ: May) as well as in [tHb] at the OL (A: 1.2 µM, θ: June), and (iii) a circasemiannual (cycle length ~ 6 months) rhythm in [tHb] at the FL (A: 2.7 µM, φ: March and September, respectively) (Figs. 7.1 and 7.2). All GAM models modelled the variability of the data to a significant degree: StO_2-FL (GAM adjusted R^2: 0.519), StO_2-OL (R^2: 0.285), [tHb]-FL (R^2: 0.311) and [tHb]-OL (R^2: 0.254). Interestingly, at the OL, the circannual rhythms of StO_2 and [tHb] were in anti-phase.

Correlations with Environmental Parameters The correlation analysis showed the following statistically significant ($p < 0.05$) links between the cyclic changes in the environmental parameters (Fig. 7.3; Table 7.1) and the StO_2 and [tHb] data: (i) the day length was positively correlated with the circannual rhythm of StO_2-FL, StO_2-OL and negatively correlated with [tHb]-OL, (ii) outdoor temperature showed a positive correlation with the circannual rhythm of StO_2-FL and a negative with [tHb]-OL, (iii) humidity was positively correlated with the circannual rhythm of StO_2-FL and negatively with [tHb]-OL, and (iv) air pressure showed a negative correlation with the circannual rhythm of StO_2-FL and StO_2-OL, and a positive one with [tHb]-OL.

7.4 Discussion, Conclusion and Outlook

In our study, we showed that absolute values of StO_2 and [tHb] exhibit infradian chronobiological variability on the group-level with a long-term nonlinear trend as well as circannual/circasemiannual rhythmicity. Furthermore, the circannual rhythms of StO_2/[tHb] were correlated with the circannual variability of environmental parameters.

Circannual rhythms in human physiology are known for different physiological parameters, e.g. blood pressure [13, 14], body temperature [15], body weight [16], plasma fibrinogen [17], salivary cortisol [18], β electroencephalography activity [19], brain µ-opioid receptor availability [20], brain serotonin transporter binding [21] and the spatial similarity of resting-state networks measured with functional magnetic resonance imaging (fMRI) [22]. It is therefore not surprising that StO_2 and [tHb] measured on the head exhibit an infradian variability with a circannual rhythm in particular too. Our study is, however, the first that documents this phenomenon with FD-NIRS data and a 5-year timespan.

As far as the cause of the infradian changes in StO_2 and [tHb] is concerned, it is very likely that environmental factors play a decisive role. This is supported by our correlation analysis with the environmental data. Looking at the phase differences of the annual oscillations in StO_2, [tHb] and the environmental data, one can note that the

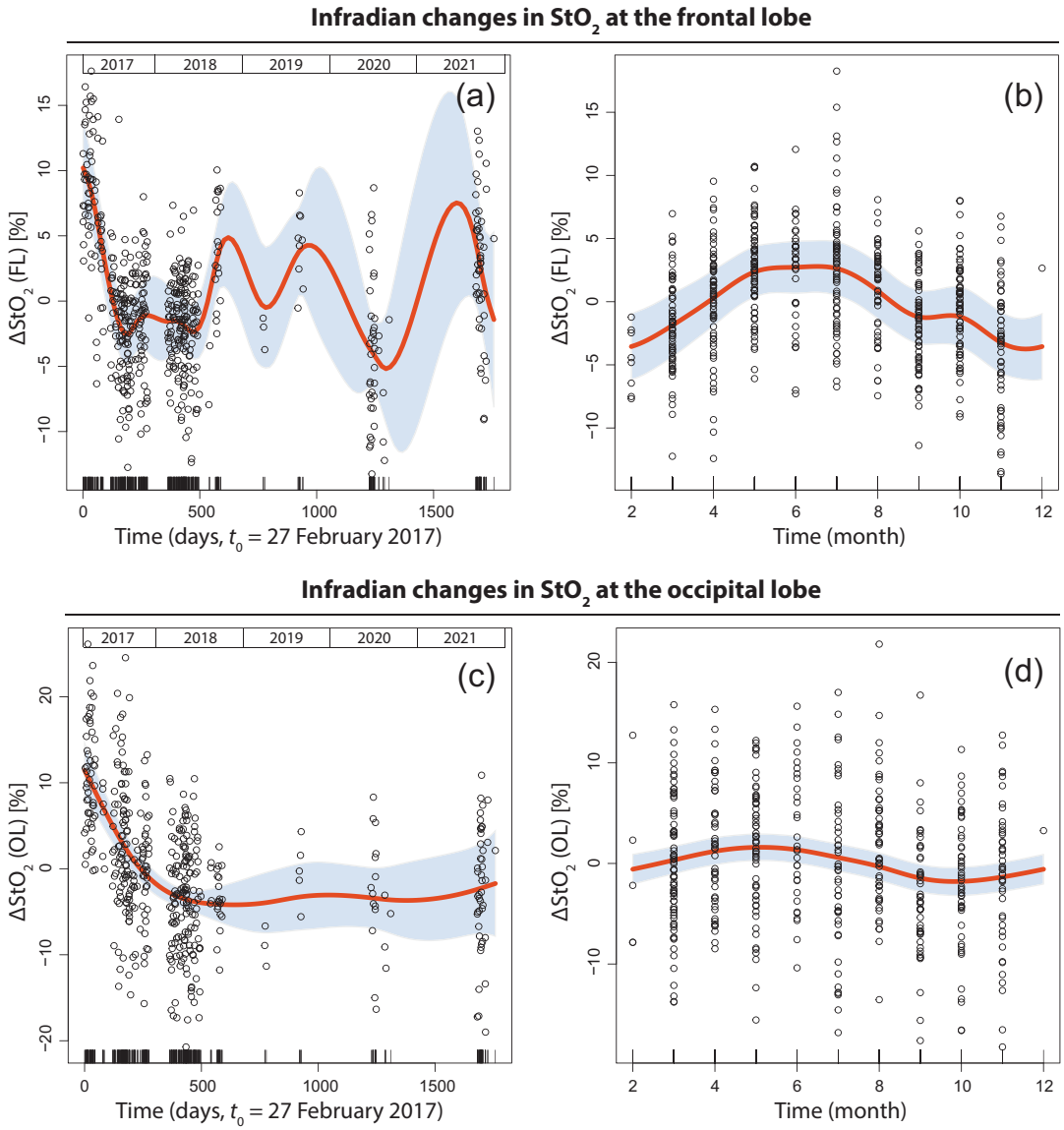

Fig. 7.1 Results of two GAM models decomposing the StO_2 data into a non-linear trend and a circannual component: (**a**, **b**) $g(StO_2\text{-FL}) = \beta_0 + f_1(T_{days}) + f_2(T_{months}) + f_3(\text{Age}) + \text{Sex} + \text{Subject} + \varepsilon$, and (**c**, **d**) $g(StO_2\text{-OL}) = \beta_0 + f_1(T_{days}) + f_2(T_{months}) + f_3(\text{Age}) + \text{Sex} + \text{Subject} + \varepsilon$

annual temperature oscillation is shifted back by about 1 month with respect to the circannual oscillations in StO_2 and [tHb]. This indicates that temperature is rather not responsible for the phenomenon. Humidity, air pressure and the day length exhibit a better phase relationship, indicating that these factors might play an important role in generating the circannual oscillation of StO_2 and [tHb].

In a planned further analysis, we will investigate whether the phenomenon also appears independently in the data from both sexes. This question is relevant because differences in the annual oscillations of hormone concentrations

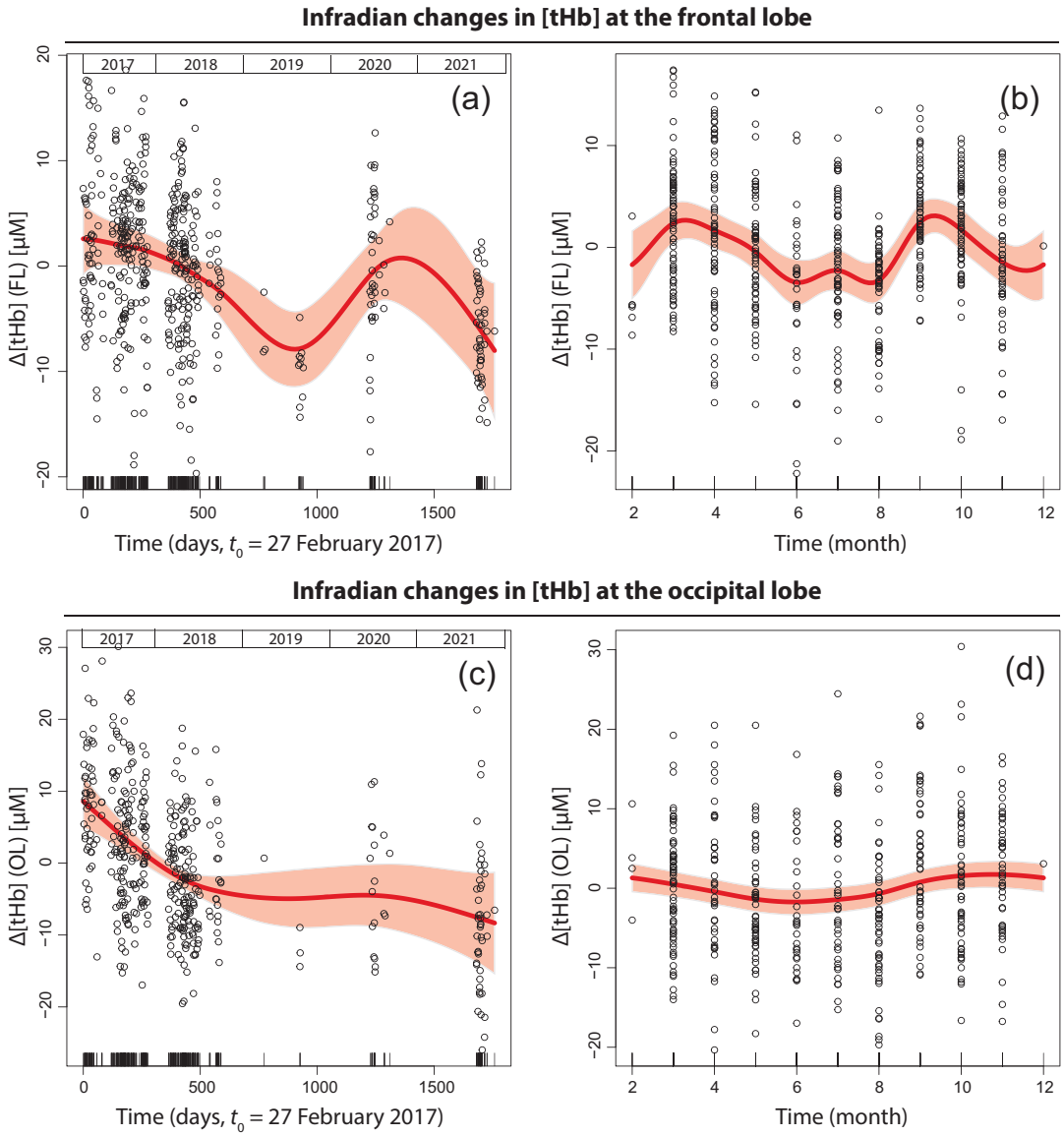

Fig. 7.2 Results of two GAM models decomposing the [tHb] data into a non-linear trend and a circannual component: (**a**, **b**) g([tHb]-FL) = $\beta_0 + f_1(T_{\text{days}}) + f_2(T_{\text{months}}) + f_3(\text{Age}) + \text{Sex} + \text{Subject} + \varepsilon$, and (**c**, **d**) g([tHb]-OL) = $\beta_0 + f_1(T_{\text{days}}) + f_2(T_{\text{months}}) + f_3(\text{Age}) + \text{Sex} + \text{Subject} + \varepsilon$

were found in men and women [23]. Our findings have the following implications: The infradian variability (and the circannual rhythmicity in particular) of StO_2 and [tHb] measured on the head needs to be taken into account when performing studies with FD-NIRS and interpreting StO_2 and [tHb] with regard to their absolute values or with respect to reference values. Furthermore, the definition of reference values for StO_2 and [tHb] need to consider the infradian variability. In addition, the infradian variability of StO_2 and [tHb] is an interesting phenomenon in itself that needs more research. Measuring and analyzing this infradian variability might be relevant for medi-

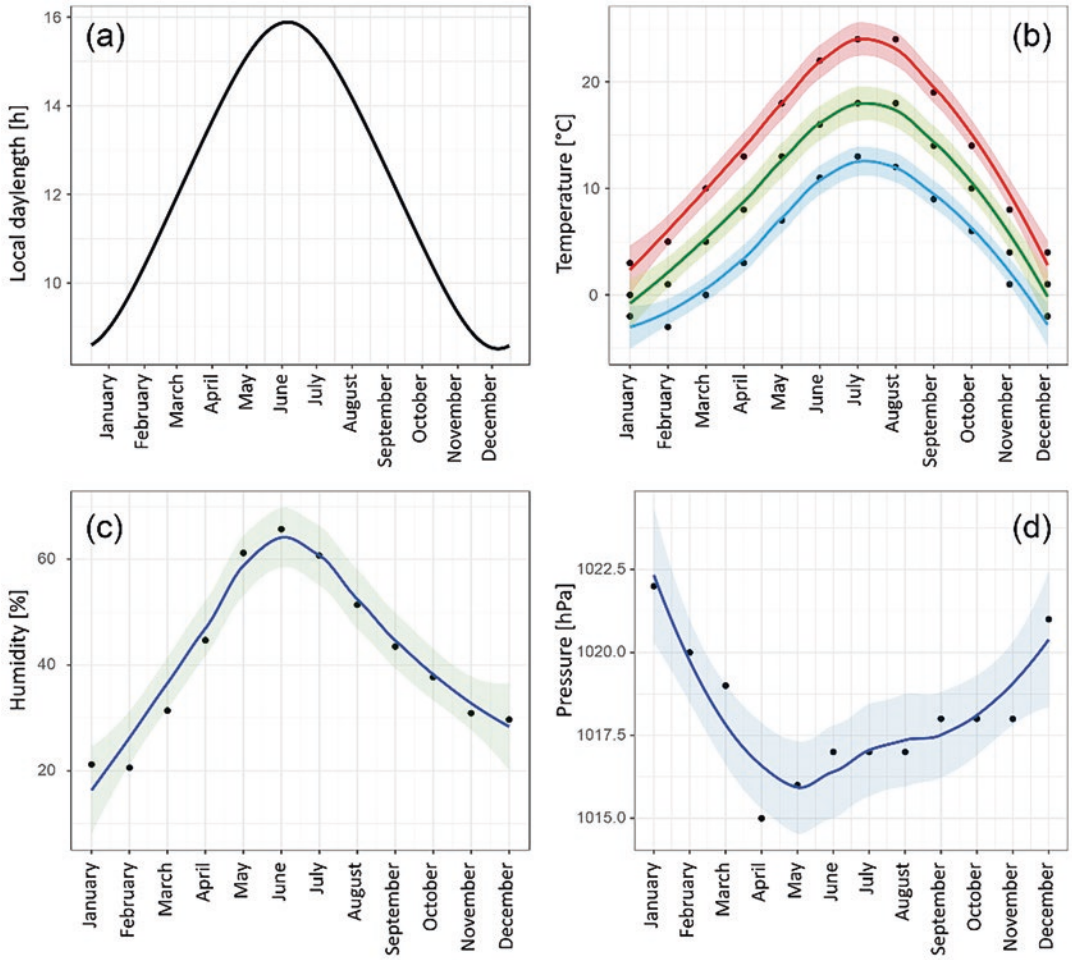

Fig. 7.3 Changes in local day length, outdoor temperature (minimum, maximum, mean), humidity and air pressure throughout the year. Data are for Bern, Switzerland. The climate parameters are monthly averages (1985–2015) (monthly values shown as black dots and regression curves (locally weighted scatterplot smoothing, LOWESS) shown as lines (with 95% CI)

cal applications and research questions. It is known that susceptibility to disease and the incidence of disease generally follow a circannual rhythm. For example, the host susceptibility to certain infectious diseases [24], the occurrence of acute myocardial infarctions [25, 26] or the relapse rate in multiple sclerosis [25]. The circannual variability of cerebrovascular StO_2 and [tHb] documented in this study could possibly be linked to these epidemiological observations.

Table 7.1 Correlations between environmental and physiological parameters with respect to the circannual oscillation

		r (95% CI)	*p*
StO_2 (FL)	Day length	0.970 (0.887, 0.993)	< 0.01**
	Temperature	0.879 (0.591, 0.968)	< 0.01**
	Humidity	0.975 (0.903, 0.994)	< 0.01**
	Air pressure	−0.897 (−0.973-, 0.645)	< 0.01**
StO_2 (OL)	Day length	0.635 (0.052, 0.894)	0.036*
	Temperature	0.242 (−0.419, 0.735)	0.473
	Humidity	0.589 (−0.017, 0.879)	0.057
	Air pressure	−0.644 (−0.897, 0.072)	0.033*
[tHb] (FL)	Day length	−0.323 (−0.773, 0.343)	0.332
	Temperature	−0.287 (−0.757, 0.378)	0.392
	Humidity	−0.318 (−0.777, 0.334)	0.318
	Air pressure	0.046 (−0.570, 0.628)	0.894
[tHb] (OL)	Day length	−0.938 (−0.984, −0.775)	< 0.001***
	Temperature	−0.724 (−0.923, −0.220)	0.012*
	Humidity	−0.866 (−0.965, −0.553)	< 0.001***
	Air pressure	0.784 (0.347, 0.941)	0.004**

*$p < 0.05$, **$p < 0.01$, ***$p < 0.001$. *r*: Spearman correlation coefficient

Acknowledgments The authors thank Rachel Scholkmann for proofreading the manuscript. We gratefully acknowledge funding from the Software AG Foundation. MW declares that he is president of the board and co-founder of OxyPrem AG.

References

1. Scholkmann F et al (2022) Frontal cerebral oxygenation in humans at rest: a mirror symmetry in the correlation with cardiorespiratory activity. Adv Exp Med Biol 1395:45–51
2. Zohdi H, Scholkmann F, Wolf U (2020) Frontal cerebral oxygenation asymmetry: intersubject variability and dependence on systemic physiology, season, and time of day. Neurophotonics 7(2):025006
3. Zohdi H et al (2021) Color-dependent changes in humans during a verbal fluency task under colored light exposure assessed by SPA-fNIRS. Sci Rep 11(1):9654
4. Zohdi H, Scholkmann F, Wolf U (2021) Individual differences in hemodynamic responses measured on the head due to a long-term stimulation involving colored light exposure and a cognitive task: A SPA-fNIRS study. Brain Sci 11(1):54
5. Scholkmann F, Zohdi H, Wolf U (2022) The role of systemic physiology in individual hemodynamic responses measured on the head due to long-term stimulation involving colored light exposure and a cognitive task: an SPA-fNIRS study. Brain Sci 12(5):597
6. Zohdi H, Scholkmann F, Wolf U (2021) Long-term blue light exposure changes frontal and occipital cerebral hemodynamics: not all subjects react the same. Adv Exp Med Biol 1269:217–222
7. Scholkmann F, Zohdi H, Wolf U (2020) Right-left asymmetry of prefrontal cerebral oxygenation: does it depend on systemic physiological activity, absolute tissue oxygenation or hemoglobin concentration? Adv Exp Med Biol 1232:105–112
8. Cornelissen G (2014) Cosinor-based rhythmometry. Theor Biol Med Model 11:16
9. Molcan L (2019) Time distributed data analysis by Cosinor. Online application. BioRxiv
10. Team RC (2014) R: a language and environment for statistical computing. R Foundation for Statistical Computing, Vienna
11. Wickham H (2016) eggplot2: elegant graphics for data analysis. Springer-Verlag, New York
12. Wood SN (2017) Generalized additive models. Chapman and Hall/CRC, Boca Raton
13. Brennan PJ et al (1982) Seasonal variation in arterial blood pressure. Br Med J (Clin Res Ed) 285(6346):919–923
14. Narita K, Hoshide S, Kario K (2021) Seasonal variation in blood pressure: current evidence and recommendations for hypertension management. Hypertens Res 44(11):1363–1372
15. Harding C et al (2019) The daily, weekly, and seasonal cycles of body temperature analyzed at large scale. Chronobiol Int 36(12):1646–1657
16. Billewicz WZ (1967) A note on body weight measurements and seasonal variation. Hum Biol 39(3):241–250
17. Stout RW, Crawford V (1991) Seasonal variations in fibrinogen concentrations among elderly people. Lancet 338(8758):9–13

18. Persson R et al (2009) Seasonal variation in human salivary cortisol concentration. Chronobiol Int 25(6):923–937
19. Barbato G et al (2018) Seasonal variation of spontaneous blink rate and beta EEG activity. Psychiatry Res 270:126–133
20. Sun L et al (2021) Seasonal variation in the brain μ-opioid receptor availability. J Neurosci 41(6):1265–1273
21. Praschak-Rieder N et al (2008) Seasonal variation in human brain serotonin transporter binding. Arch Gen Psychiatry 65(9):1072
22. Choe AS et al (2015) Reproducibility and temporal structure in weekly resting-state fMRI over a period of 3.5 Years. PLoS One 10(10):e0140134
23. Tendler A et al (2021) Hormone seasonality in medical records suggests circannual endocrine circuits. Proc Natl Acad Sci 118(7):e2003926118
24. Dowell SF (2001) Seasonal variation in host susceptibility and cycles of certain infectious diseases. Emerg Infect Dis 7(3):369–374
25. Kriszbacher I et al (2008) Seasonal variations in the occurrence of acute myocardial infarction in Hungary between 2000 and 2004. Int J Cardiol 129(2):251–254
26. González Hernández E et al (2004) Seasonal variations in admissions for acute myocardial infarction. The primvac study. Revista Española de Cardiología (English Edition) 57(1):12–19

8 Mechanisms of Photostimulation of Brain's Waste Disposal System: The Role of Singlet Oxygen

Oxana Semyachkina-Glushkovskaya, Denis Bragin, Ivan Fedosov, Inna Blokhina, Alexander Khorovodov, Andrey Terskov, Alexander Shirokov, Alexander Dubrovsky, Valeria Vinnik, Arina Evsukova, Daria Elovenko, Viktoria Adushkina, Maria Tzoy, Alexander Dmitrenko, Valeria Krupnova, Maria Manzhaeva, Ilana Agranovich, Elena Saranceva, Tatyana Iskra, Ekaterina Lykova, Sergey Sokolovski, Edik Rafailov, and Jürgen Kurths

Abstract

There is strong evidence that augmentation of the brain's waste disposal system via stimulation of the meningeal lymphatics might be a promising therapeutic target for preventing neurological diseases. In our previous studies, we demonstrated activation of the brain's waste disposal system using transcranial photostimulation (PS) with a laser 1267 nm, which stimulates the direct generation of singlet oxygen in the brain tissues. Here we

O. Semyachkina-Glushkovskaya
Physics Department, Humboldt University, Berlin, Germany

Department of Biology, Saratov State University, Saratov, Russia

D. Bragin (✉)
Lovelace Biomedical Research Institute, Albuquerque, NM, USA

Department of Neurology, University of New Mexico School of Medicine, Albuquerque, NM, USA
e-mail: dbragin@lrri.org

I. Fedosov · I. Blokhina · A. Khorovodov · A. Terskov
A. Dubrovsky · V. Vinnik · A. Evsukova · D. Elovenko
V. Adushkina · M. Tzoy · A. Dmitrenko · V. Krupnova
M. Manzhaeva · I. Agranovich · E. Saranceva
T. Iskra · E. Lykova
Department of Biology, Saratov State University, Saratov, Russia

A. Shirokov
Department of Biology, Saratov State University, Saratov, Russia

Institute of Biochemistry and Physiology of Plants and Microorganisms, Russian Academy of Sciences, Saratov, Russia

S. Sokolovski · E. Rafailov
Optoelectronics and Biomedical Photonics Group, AIPT, Aston University, Birmingham, UK

J. Kurths
Physics Department, Humboldt University, Berlin, Germany

Department of Biology, Saratov State University, Saratov, Russia

Potsdam Institute for Climate Impact Research, Potsdam, Germany

F. Scholkmann et al. (eds.), *Oxygen Transport to Tissue XLIV*, Advances in Experimental Medicine and Biology 1438, https://doi.org/10.1007/978-3-031-42003-0_8

investigate the mechanisms underlying this phenomenon. Our results clearly demonstrate that PS-mediated stimulation of the brain's waste disposal system is accompanied by activation of lymphatic contractility associated with subsequent intracellular production of the reactive oxygen species and the nitric oxide underlying lymphatic relaxation. Thus, PS stimulates the brain's waste disposal system by influencing the mechanisms of regulation of lymphatic pumping.

Keywords

Photostimulation · Brain's waste disposal system · Meningeal lymphatics · Singlet oxygen

8.1 Introduction

The peripheral lymphatics have been implicated in the mechanisms of regulation of transport of waste and immune cells that have been found to be compromised in different neurodegenerative, vascular, traumatic, and inflammatory diseases affecting the central nervous system. Recent findings of the meningeal lymphatic vessels (MLVs) began a new era in the study of the mechanisms of brain diseases [1]. A better understanding of MLVs plays a pivotal role in the treatment of many neurological conditions, including Alzheimer's and Parkinson's diseases, multiple sclerosis, traumatic brain injury, brain tumors, epilepsy, and stroke [2]. There is strong evidence that augmentation of the brain's waste disposal system via stimulation of MLVs might be a promising therapeutic approach for preventing neurological diseases [3]. Transcranial photostimulation (PS) is a non-pharmacological and non-invasive therapy that has shown efficacy for numerous brain diseases [3]. It has been shown that PS can regulate the relaxation and permeability of the lymphatic vessels (LVs), activate the movement of immune cells in the lymph, and effectively manage lymphedema [4–6]. Recently, we demonstrated that near-infrared PS (1267 nm) activates the clearance of different compounds from the brain via modulation of the MLVs tone [4–6]. We also reported that transcranial PS increases the lymphatic delivery of liposomes to the brain after injection into the deep cervical lymph nodes (dcLNs) [6]. Here, we studied the mechanisms underlying PS-mediated effects on the brain's waste disposal system focusing on the investigation of the 1267 nm-stimulation of (1) the reactive oxygen species (ROS) production in response to PS-induced $^1O_2$ generation in the blood-brain barrier (BBB) cells; (2) production of nitric oxide (NO) in the lymphatic endothelial cells (LECs); (3) the contractility of mesenteric LVs; (4) the lymphatic clearance of fluorescein isothiocyanate–dextran 70 kDa (FITCD) from the mouse brain to dcLNs.

8.2 Methods

All procedures were performed in accordance with the "Guide for the Care and Use of Laboratory Animals". The experimental protocols were approved by the Local Bioethics Commission of the Saratov State University (Protocol No. 7). Male C57BL/6 mice (25–28 g) were used in all experiments.

A fiber Bragg grating wavelength locked high-power laser diode (LD-1267-FBG-350, Innolume, Dortmund, Germany) emitting at 1267 nm was used as a source of irradiation. The unanesthetized awake mice with pre-shaved heads were fixed using the adapted protocol for two-photon laser scanning microscopy of the cortical vessels in awake-behaved rodents [5] and irradiated in the area of the basal MLVs [1] using a single laser dose of 9 J/cm^2 (on the skull) and 3 J/cm^2 on the brain surface. We irradiated the skull with a collimated 1267 nm laser beam of 5 mm in diameter. Laser output was attenuated to 1.8 mW. With a laser spot area of 0.2 cm^2, the irradiance at the skull surface was 9 mW/cm^2. A single dose of 9 J/cm^2 was obtained during 17 min procedure that was repeated 3 times with an interval of 5 min (the total time was 61 min). Skull transmittance measured *ex vivo* with an integrated sphere was in average 0.4. Taking into consideration the widening of the collimated

beam due to the light scattering in the skull, we assumed the illuminated area at the brain surface to be 20% larger, i.e., 0.24 cm^2, thus the irradiance at the brain surface was 0.4/1.2 = 0.33 of that at the skull surface, i.e., 3 mW/cm^2. For 17 min procedure, the dose at the brain surface was 3 J/cm^2. A sufficient laser dose of at least 0.9 J/cm^2 could be obtained down to 2 mm depth within the brain tissue [7].

The MLVs express all of the molecular hallmarks of lymphatic proteins typical for peripheral LVs [1]. There are no real-time technologies for monitoring MLVs functions because they are extremely thin and small vessels. Therefore, as a lymphatic function model, we used the mesenteric lymphangion to monitor the PS effects on the lymphatic contractility (*in vivo* experiments) and the NO production in LECs (*in vitro* experiments).

To measure the contractility of the mesenteric LVs, the video sequences of the LVs were captured using transmitted light Axio Imager A1 microscope with 10 × 0.2 Epiplan Lens (Zeiss, Germany) and monochrome CMOS camera acA1920-40um (Basler AG, Germany). Image sequences were captured with a resolution of 1920 × 1200 pixels, 8 bit, 40 fps and stored in AVI video format.

To study the NO production in LECs, the freshly isolated primary LECs were obtained from the mesentery of intact mice using an earlier published protocol [8]. The level of nitrite/nitrate (NOx) produced by LECs was determined using the CLD88 NO analyzer (Ecophysics), as previously described [8].

To analyze lymphatic removal of FITCD 70 kDa from the brain to dcLNs, this tracer was injected into the right lateral ventricle (AP, 1.0 mm; ML, −1.4 mm; DV, 3.5 mm) and 3 h after its injection, the brains and dcLNs were taken for *ex vivo* visualization of the distribution of FITCD in the brains and its accumulation in dcLNs using confocal microscopy system (Nikon, Japan). For the quantitative analysis of intensity signal from FITCD in the brain and in dcLNs, the ImageJ was used with the plugin "Analyze Particles" in the "Analyze" tab, which calculates the total area of fluorescence intensity tissue elements – the indicator "Total Area".

The assessment of the level of intracellular ROS was performed fluorometrically with dihydroethidium (DHE) using an *in vitro* model of the BBB [9].

8.3 Results

8.3.1 PS Increases Lymphatic Cleansing of the Brain Tissues

To answer the question of whether PS directly affects the lymphatic clearance of substances from the brain, we analyzed the PS effects on the lymphatic clearance of FITCD from the brain to dcLNs. Figures 8.1a, b demonstrate that the intraventricular injection of FITCD was accompanied by the brain distribution of the tracer. The spread of FITCD was higher on the ventral than on the dorsal aspects of the brain 3 h after its injection. These data reflect the FITCD distribution from the ventricle to the basal MLVs, playing an important role in brain drainage and clearance [5, 10]. The dcLNs are the first anatomical station of exit of the cerebral spinal fluid with dissolved waste substances from the brain [1, 5, 10]. Indeed, we observed an accumulation of FITCD in dcLNs, suggesting a lymphatic pathway of clearance of FITCD from the brain (Fig. 8.1c).

In the next step, we discover that PS significantly increases the brain distribution of FITCD and lymphatic removal of the tracer from the brain to dcLNs (Fig. 8.1d–f). The quantitative analysis shows that the fluorescent signal from FITCD was significantly higher in the brain and in dcLNs in mice treated by PS vs. untreated animals (0.55 ± 0.03 a.u. vs. 0.24 ± 0.03 a.u., $p < 0.01$, in the ventral aspect of the brain; 0.37 ± 0.06 a.u. vs. 0.12 ± 0.01 a.u., $p < 0.01$, in the dorsal aspect of the brain, 0.47 ± 0.02 a.u. vs. 0.16 ± 0.05 a.u., $p < 0.05$ in dcLNs, the Mann–Whitney–Wilcoxon test, $n = 7$ in each group).

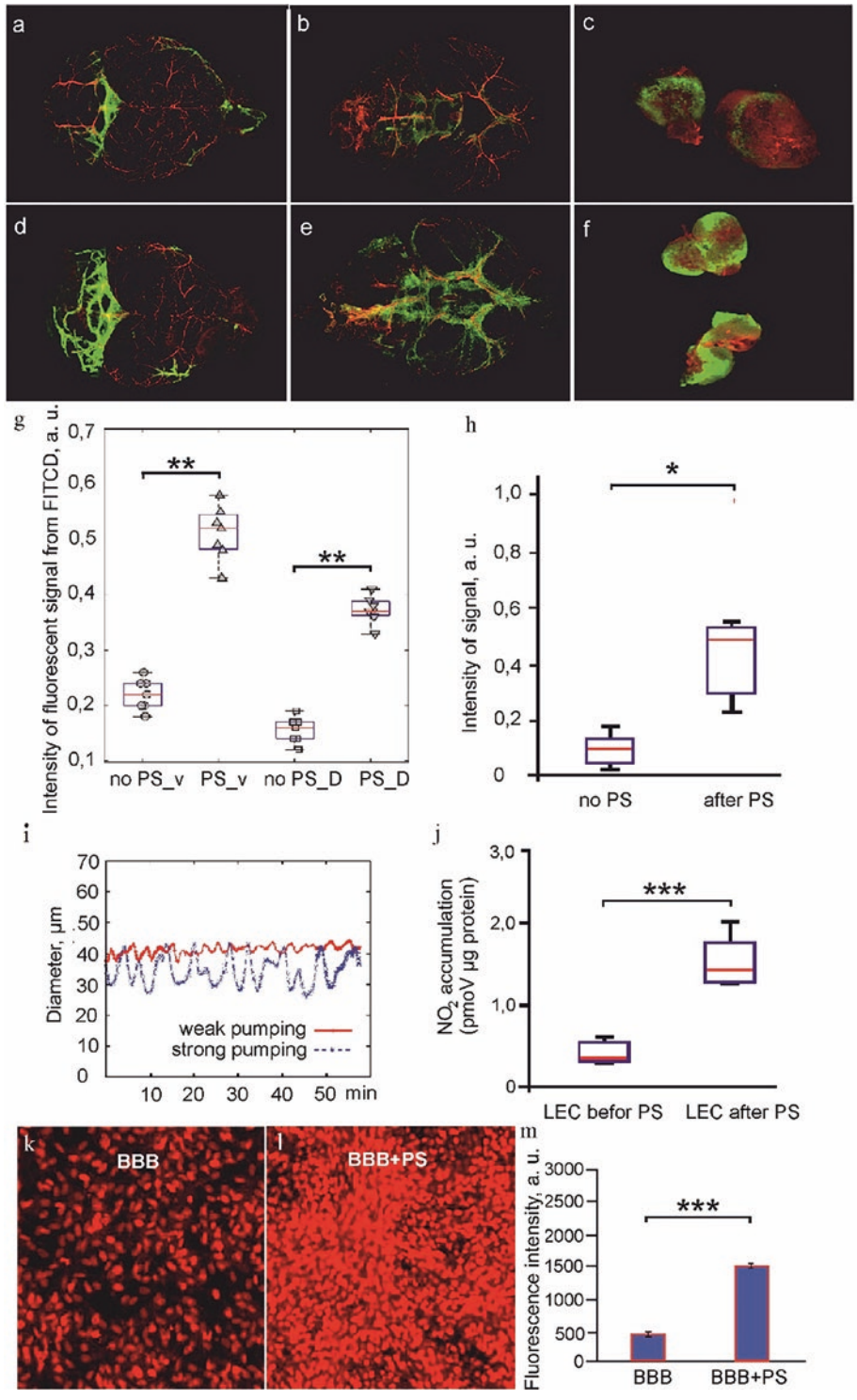

Fig. 8.1 Mechanisms of the PS effects on the LVs: (**a**) representative confocal images of FITCD distribution in dorsal (**a**, **d**) and ventral (**b**, **e**) parts of the brain and the FITCD removal to dcLN (**c**, **f**) without (**a**–**c**) and after PS (**d**–**f**); (**g**, **h**) the quantitative analysis of the fluorescent signal from FITCD in ventral (V) and dorsal (D) parts of the brain (**g**) and in the dcLN (**h**), $n = 7$, $^{*}p < 0.05$, $^{**}p < 0.01$, the Mann–Whitney–Wilcoxon test; i – the PS effects on the lymphatic contractility; (**j**) the production of NO in LEC without and after PS, $n = 7$, $p < 0.001$, Wilcoxon, Mann-Whitney U tests; (**k**, **l**) the confocal images of DHE-FI in the BBB cells without and after PS; (**m**) the quantitative analysis of fluorescent signal DHE-FI in the BBB cells without and after PS, $n = 7$, $p < 0.001$, Wilcoxon, Mann-Whitney U tests

8.3.2 Mechanisms of the PS Effects on the Lymphatic Vessels

The mechanism by which PS affects lymphatics has not been sufficiently explored. Here, in our *in vivo* data, we demonstrate that PS 3 J/cm^2 (PS dose was similar to those on the brain surface) increases lymphangion contraction (Fig. 8.1i). The NO plays an important role in the regulation of the relaxation of LVs after their contraction [11, 12]. The contraction cycle of LVs is combined mechanical and conducted electrophysiological events. The relaxation phase is a component of locally generated NO in LEC in response to transiently elevated shear forces. The NO is a vasodilator that acts via stimulation of soluble guanylate cyclase to form cyclic-GMP, which activates protein kinase G, causing the opening of calcium-activated potassium channels and reuptake of Ca^{2+}. The decrease in the concentration of Ca^{2+} prevents myosin light-chain kinase from phosphorylating the myosin molecule, leading to the relaxation of LVs after their contraction. Based on these facts, we studied the NO production in *in vitro* experiments on the mesenteric LEC without and after PS. Our results reveal a significant increase in the 24 h accumulation of NO_2^- in the cell culture medium after PS 3 J/cm^2 compared with the accumulation of NO_2^- produced by LECs without PS (Fig. 8.1j).

In our previous study using different cell lines, we showed that PS induces the production of ROS [13]. Therefore, we analyzed the intracellular ROS production in response to PS-induced $^1O_2$ generation in the neuronal cell models, including the BBB cells using DHE fluorescent single-cell imaging. The data presented in Fig. 8.1k, l display the confocal imaging of oxidized DHE fluorescence intensity (DHE-FI) in cell culture models before and after PS. Figure 8.1m illustrates the quantitative analysis of DHE-FI changes before and after PS in cell lines. The results unambiguously demonstrate that the DHE FI value was 3.0-fold higher in the BBB cells + PS vs. the BBB cells without PS (1502.1 ± 54.2 a.u. vs. 493.5 ± 42.5 a.u., $p < 0.001$, Wilcoxon, Mann-Whitney U tests).

8.4 Conclusions

Our results clearly demonstrate that PS stimulates the brain's waste disposal system by influencing the mechanisms of regulation of lymphatic pumping via regulation of the contraction cycle of LVs and phase of relaxation of LVs by activation of the intracellular ROS and NO production.FundingO.S-G., A.Sh., A.T., A.D., I.F., A.K., I.B., A.E., D.E., V.A., V.T., I.A., V.A., J.K. were supported by RF Governmental Grant № 075-15-2022-1094, Grant from RSF № 21-75-10088, D.B. was supported by NIH 1R01NS112808.

References

1. Louveau A, Smirnov I, Keyes TJ et al (2015) Structural and functional features of central nervous system lymphatic vessels. Nature 523:337–341
2. Hershenhouse KS, Shauly O, Gould DJ et al (2019) Meningeal lymphatics: a review and future directions from a clinical perspective. Neurosci Insights 14:1179069519889027
3. Salehpour F, Khademi M, Bragin D (2022) Photobiomodulation therapy and the Glymphatic system: promising applications for augmenting the brain lymphatic drainage system. Int J Mol Sci 23:2975
4. Semyachkina-Glushkovskaya O, Abdurashitov A, Dubrovsky A et al (2020) Photobiomodulation of lymphatic drainage and clearance: perspective strategy for augmentation of meningeal lymphatic functions. Biomed Opt Express 11(2):725–734
5. Semyachkina-Glushkovskaya O, Penzel T, Blokhina I et al (2021) Night Photostimulation of clearance of beta-amyloid from mouse brain: new strategies in preventing Alzheimer's disease. Cell 10(12):3289
6. Semyachkina-Glushkovskaya O, Fedosov I, Shirokov A et al (2021) Photomodulation of lymphatic delivery of liposomes to the brain bypassing the blood-brain barrier: new perspectives for glioma therapy. Nanophoton 10(12):3215–3227
7. Henderson TA, Morries L (2015) Near-infrared photonic energy penetration: can infrared phototherapy effectively reach the human brain? Neuropsychiatr Dis Treat 21(11):2191–2208
8. Ribera J, Pauta M, Melgar-Lesmes P et al (2013) Increased nitric oxide production in lymphatic endothelial cells causes impairment of lymphatic drainage in cirrhotic rats. Gut 62:138–145
9. Liu Y, Xue Q, Tang Q et al (2013) A simple method for isolating and culturing the rat brain microvascular endothelial cells. Microvasc Res 90:199–205

10. Ahn J, Cho H, Kim J et al (2019) Meningeal lymphatic vessels at the skull base drain cerebrospinal fluid. Nature 572:62–66
11. Bohlen H, Gasheva O, Zawieja D (2011) Nitric oxide formation by lymphatic bulb and valves is a major regulatory component of lymphatic pumping. Am J Physiol Heart Circ Physiol 301:H1897–H1906
12. Kunert C, Baish JW, Liao S, Padera TP, Munn LL (2015) Mechanobiological oscillators control lymph flow. Proc Natl Acad Sci U S A 112:10938–10943
13. Khokhlova A, Zolotovskii I, Sokolovski S et al (2019) The light-oxygen effect in biological cells enhanced by highly localized surface plasmon-polaritons. Sci Rep 9(1):18435

9

Changes of Arterial and Venous Cerebral Blood Flow Correlation in Moderate-to-Severe Traumatic Brain Injury: A CT Perfusion Study

Alex O. Trofimov, Darya I. Agarkova, Kseniia A. Trofimova, Kyrill V. Lidji-Goryaev, Edwin Nemoto, Olga A. Bragina, and Denis E. Bragin

Abstract

We compared differences in perfusion computed tomography (PCT)-derived arterial and venous cerebral blood flow (CBF) in moderate-to-severe traumatic brain injury (TBI) as an indication of changes in cerebral venous outflow patterns referenced to arterial inflow. Moderate-to-severe TBI patients (women 53; men 74) underwent PCT and were stratified into 3 groups: I (moderate TBI), II (diffuse severe TBI without surgery), and III (diffuse severe TBI after the surgery). Arterial and venous CBF was measured by PCT in both the middle cerebral arteries (CBFmca) and the upper sagittal sinus (CBFuss). In group I, CBFmca on the left and right sides were significantly correlated with each other ($p < 0.0001$) and with CBFuss ($p = 0.048$). In group II, CBFmca on the left and right sides were also correlated ($p < 0.0000001$) but not with CBFuss. Intracranial pressure reactivity (PRx) and CBFuss were correlated ($p = 0.00014$). In group III, CBFmca on the side of the removed hematoma was not significantly different from the opposite CBFmca ($p = 0.680$) and was not correlated with CBFuss. Conclusions: The increasing severity of TBI is accompanied by an impairment of the correlation between the arterial and venous CBF in the supratentorial vessels suggesting shifting in arterial and venous CBF in severe TBI associated with increased ICP reflected by PRx.

Keywords

Cerebral blood flow · Traumatic brain injury · Arteriovenous correlation · Arterial compliance · Traumatic brain injury · Perfusion CT

A. O. Trofimov (✉) · D. I. Agarkova
K. A. Trofimova · K. V. Lidji-Goryaev
Department of Neurological Diseases, Privolzhsky Research Medical University,
Nizhny Novgorod, Russia

E. Nemoto
Department of Neurology, University of New Mexico School of Medicine, Albuquerque, NM, USA

O. A. Bragina
Lovelace Biomedical Research Institute,
Albuquerque, NM, USA

D. E. Bragin
Lovelace Biomedical Research Institute,
Albuquerque, NM, USA

Department of Neurology, University of New Mexico School of Medicine, Albuquerque, NM, USA

F. Scholkmann et al. (eds.), *Oxygen Transport to Tissue XLIV*, Advances in Experimental Medicine and Biology 1438, https://doi.org/10.1007/978-3-031-42003-0_9

9.1 Introduction

The concept of cerebral microcirculation evaluation based on the axis-voxel analysis of brain tissue X-ray density changes during the passage of contrast agent through the cerebrovascular bed by perfusion computed tomography (PCT) was proposed by Axel L. in 1980 [1]. The use of PCT in the routine treatment of cerebral strokes has achieved revolutionary results. However, the potential of PCT is still underutilized but has been used in acute stroke in predicting outcomes [2, 3]. One such possibility is to assess the volumetric characteristics not only of the microcirculatory bed but also the blood flow in large vessels: arteries, veins, and brain sinuses [4]. This is important for cerebral blood flow (CBF) studies because other techniques (ultrasonic doppler, duplex, triplex systems, etc.) operate only with speed and resistive characteristics [5]. As shown earlier, the linear velocity of blood flow using ultrasound Doppler and volumetric velocity in the cerebral arteries using PCT were significantly correlated in healthy individuals but not in patients with vasospasm, critical intracranial hypertension conditions and severe traumatic brain injury (TBI) [6]. Moreover, ultrasound Doppler studies showed a correlation between the velocities in the main arteries and veins in healthy individuals, but these correlations were impaired in severe TBI [7]. Thus, to date, the relationship between arterial and venous blood flow in moderate-to-severe TBI is poorly understood. We assessed the differences in PCT-derived arterial and venous CBF in patients with moderate-to-severe TBI and after surgical removal of intracranial hematomas and hypothesized that an increase in the severity of TBI correlates with arterial and venous CBF uncoupling.

9.2 Methods

9.2.1 Study Design and Population

This non-randomized retrospective single-center study was conducted as an analysis of a prospectively maintained database cohort (2013–2022). The study protocol was approved by the Regional Clinical Hospital named Local Ethical Committee. Inclusion criteria were: moderate and severe TBI within 6 h after injury, Glasgow Coma Scale (GCS) < 12, multiphase PCT follow-up for at least 12 h, and available mortality data. Exclusion criteria were: age < 16 years and > 75 years, serum blood creatinine level > 120 mg/l, and GCS 3. 127 moderate-to-severe TBI patients (w 53; m 74) were stratified into 3 groups: group I (moderate TBI, 18 to 59 years old (yo), $n = 49$); group II (severe diffuse TBI without the intracranial hematoma, 19–56 yo, $n = 47$); and group III (severe TBI after the intracranial surgery, 19–58 yo, $n = 31$).

9.2.2 Perfusion Computed Tomography

All patients were subjected to PCT 1–2 days after TBI using a 64-slice Philips Ingenuity CT (Philips Medical Systems, Cleveland, USA). The PCT examination included an initial non-contrast CT of the brain. Extended scanning was further performed in 16 "areas of interest", 160-mm coverage in the z-axis within 60 s with a contrast agent administered ("Perfusion JOG" mode). The scanning parameters were 80 kVp, 150 mA, effective dose = 3.3 mSv, slice thickness = 5 mm, collimation = 64 × 0.625 mm. A total of 50 mL of contrast agent Ultravist 370 (Schering, Germany) was administered with a syringe injector Stellant (Medrad, PA, USA) into a right cubital vein through a standard catheter (20G) at a rate of 5 ml/s. Received data were transferred to the workstation Philips Extended Brilliance Workspace (Philips Health Care, Best, the Netherlands). The artery and vein marks were automatically recorded, followed by a cluster-analysis algorithm by the manual control of indices in the time-concentration plot. Perfusion maps were derived by the Bayesian probabilistic method from the tissue time-attenuation curve, which is linearly related to iodine concentration on an aper-voxel basis with the time. Quantitative PCT parameters of CBF as well as other

parameters (cerebral blood volume, mean transit time, time-to-peak), were calculated on a voxel-wise basis and were used to generate color-coded maps. Region of interest was established in the projection of both middle cerebral arteries (MCA) and in the posterior third projection of the upper sagittal sinus (USS) near *confluens sinuum*. Thus, we measured CBF directly inside both the middle cerebral arteries and the upper sagittal sinus.

9.2.3 Intracranial Pressure and Pressure-Reactivity Index Monitoring

ICP was monitored using the parenchymal probe (Codman MicroSensors ICP, Codman & Shurtleff, Raynham, MA, USA). In non-surgery diffuse TBI cases, ICP probes were inserted into the frontal lobe non-dominant globe. In the surgery case, the ICP probes were placed in white matter on the side of the maximal lesion. A neuromonitoring complex «Centaurus» was used during the study (Ver. 2.0, Nizhny Novgorod State Medical Academy, RF). The physiological variables and ICP were recorded continuously every 3 s during the PCT using a bedside monitor (IntelliView MP5, Philips Medizin Systeme, Germany). The pressure reactivity index (PRx) was calculated from the measured parameters as described early [7, 8].

9.2.4 Statistical Analysis

The data are presented as median [interquartile range] for continuous variables. Fisher's exact test was used for categorical variables. Statistical analysis of continuous variables was done by Wilcoxon signed-rank test (T-criterion Wilcoxon) as appropriate. The nonparametric Spearman rank correlation coefficients (R) were used to correlate the variables. The significance level was set at $p < 0.05$. Statistical analysis was done by Statistica 12 (TIBCO Software Inc., Palo Alto, USA).

9.3 Results

The obtained data are summarized in Table 9.1 and Fig. 9.1. In group I (moderate TBI), there were no significant differences between CBF in the middle cerebral arteries on the left and right side ($Z = 1.56$, $p = 0.119$). The left and right CBFmca were significantly correlated with each other ($R = 0.783$, $p < 0.0001$) and with CBFuss ($R = 0.346$, $p = 0.0385$, $R = 0.332$, $p = 0.048$, respectively) (Fig. 9.2). ICP in this group was not monitored.

In group II (severe diffuse TBI without the intracranial hematoma), the left and right CBFmca were also similar ($Z = 1.027$, $p = 0.304$) and were significantly correlated ($R = 0.76$, $p < 0.0000001$). However, there was no correlation between CBFma and CBFuss ($p > 0.05$) (Fig. 9.2). The mean ICP in the second group was 22 mmHg [10,5–33,4] and PRx was 0,33 [0,23–0,44]. A significant correlation was observed between PRx and CBFuss ($R = 0.628$, $p = 0.00014$). A correlation between PRx and both CBFmca (left and right) was almost significant ($p = 0.052$ and $p = 0.057$, respectively).

In group III (severe TBI after the intracranial surgery) CBFmca on the side of the removed hematoma was not significantly different from CBFmca on the opposite side ($Z = 0.411$; $P = 0.680$). Moreover, there was no correlation between both CBFmca and CBFuss (on the side of removed hematoma, $R = -0.129$, $p = 0.47$; on the opposite side, $R = -0.043$, $p = 0.81$; $R = 0.113$, $p = 0.529$ – between MCA) (Fig. 9.2). The mean ICP in this group was 25 mmHg [9,5–33,5], and PRx was 0,38 [0,10–0,56]. We found a significant correlation between PRx and CBFuss ($R = 0.485$, $p = 0.002$). However, there was no significant correlation between PRx and both CBFmca ($p > 0.05$). In group III, we found a statistically significant correlation between the level of wakefulness by GCS and CBFuss ($R = 0.349$, $p = 0.046$), which was not observed in groups I and II.

Although there were no significant differences in ICP between groups II and III ($p = 0{,}078$), PRx values in these groups were significant

Table 9.1 Comparison of the obtained values of the studied parameters

	I CBFmca left (ml/100 g/s)	II CBFmca right (ml/100 g/s)	III CBFuss (ml/100 g/s)	IV GCS	V ICP (mmHg)	VI PRx
Group 1 *N* = 49	15.33 [9.81–21.01]	14.17 [8.98–18.80]	10.21 [8.54–12.92]	12.5 [12–13]	–	–
Group 2 *N* = 47	11.45 [9.01–18.01]	14.82 [9.45–26.10]	11.23 [7.61–13.88]	10 [9–11]	22 [10.5–33.4]	0,33 [0.23–0.44]
Group 3 (ipsilateral and contralateral side former hematoma) *N* = 31	12.68 [7.49–16.40]	10.58 [6.73–18.35]	10.64 [8.23–14.63]	9 [7–11]	25 [9.5–33.5]	0,38 [0,10-0,56]
P (1–2)	ns	ns	ns	0,00001 *	–	–
P (1–3)	ns	ns	ns	0,00001 *	–	–
P (2–3)	ns	ns	ns	ns	ns	ns

CBFmca cerebral blood flow in middle cerebral artery, *CBFuss* cerebral blood flow in up-per sagittal sinus, *GCS* Glasgow Coma Score, *MAP* mean arterial pressure, *ICP* intracranial pressure, *PRx* pressure reactivity index, data are presented as median values [inter-quartile range], *ns* not significant ($p > 0.05$), *$p < 0.05$

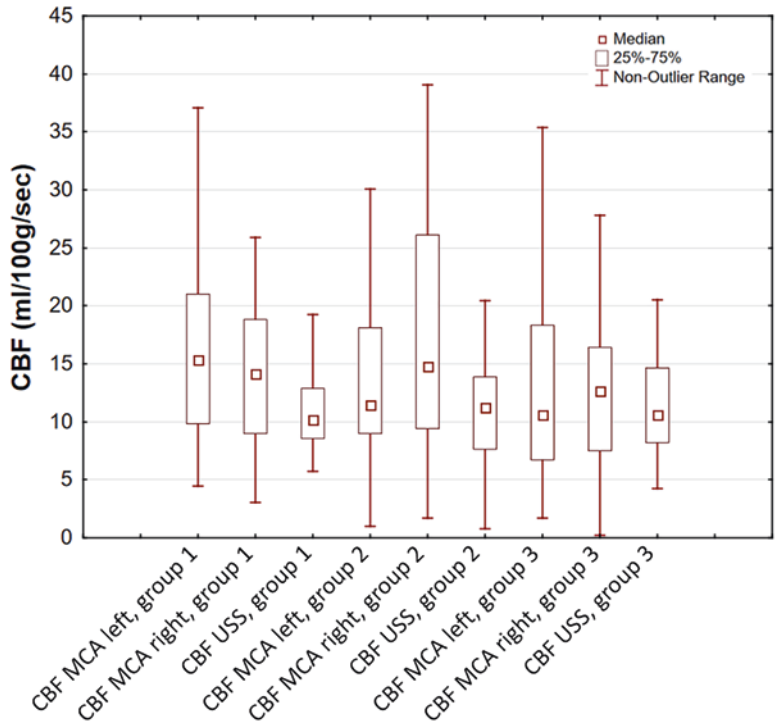

Fig. 9.1 Boxplots demonstrating cerebral blood flow (mm/100 g/s) in all groups of the study. Data are presented as median values [inter-quartile range]. Group 1: moderate TBI. Group 2: diffuse severe TBI without surgery. Group 3: diffuse severe TBI after the surgery

(p = 0,048). Two-tailed Fisher test shows that arterial-venous CBF uncoupling was frequently observed in PRx > 0.3 and ICP > 21 mmHg patients ($p < 0.0001$).

9.4 Discussion

Dynamic PCT allows the estimation of the volume of blood flowing through a given ROI per second (i.e., volume velocity or CBF in ml/100 g/s), not just the blood flow velocity (cm/s) as in ultrasound Doppler [9]. In contrast to conventional TCD and even transcranial robotic duplex devices, dynamic multiphase PCT allows direct visualization of all large cerebral vessel segments and the measurement of CBF in specific intracranial segments with high accuracy [9]. PCT-derived CBF data do not depend on the angle of insonation errors, which leads to more accurate measurements of CBF, approaching the accuracy of 3D rotational settings [10].

In severe TBI, volume blood flow does not correlate with its linear velocity, and the development of this disruption reflects a serious disturbance of CBF autoregulation [6]. Cardim et al. showed significant correlations between TCD-derived CBF velocity of USS and both hemispheric blood flow in healthy volunteers; however, these characteristics do not persist consistently in TBI patients [7]. Moreover, the arteriovenous correlation between volume velocity in large arterial (both MCAs) and venous (USS) vessels in moderate-to-severe TBI is still uninvestigated. We measured instantaneous values of volume flow in both MCA and USS using PCT instead of time-averaged TCD-derived values obtained with conventional 'blind' TCD devices, and, to our knowledge, this study is the first where dynamic multiphasic PCT has been used to quantify CBF in large cerebral vessels in patients to document shifts in arterial and venous CBF correlations after severe TBI correlated with the outcome [11].

Using this technique, we correlated CBF in USS and both MCA in various groups of moderate-to-severe TBI patients and found that the increasing severity of TBI is accompanied by a growing uncoupling between the arterial and venous CBF in the supratentorial vessels. One of

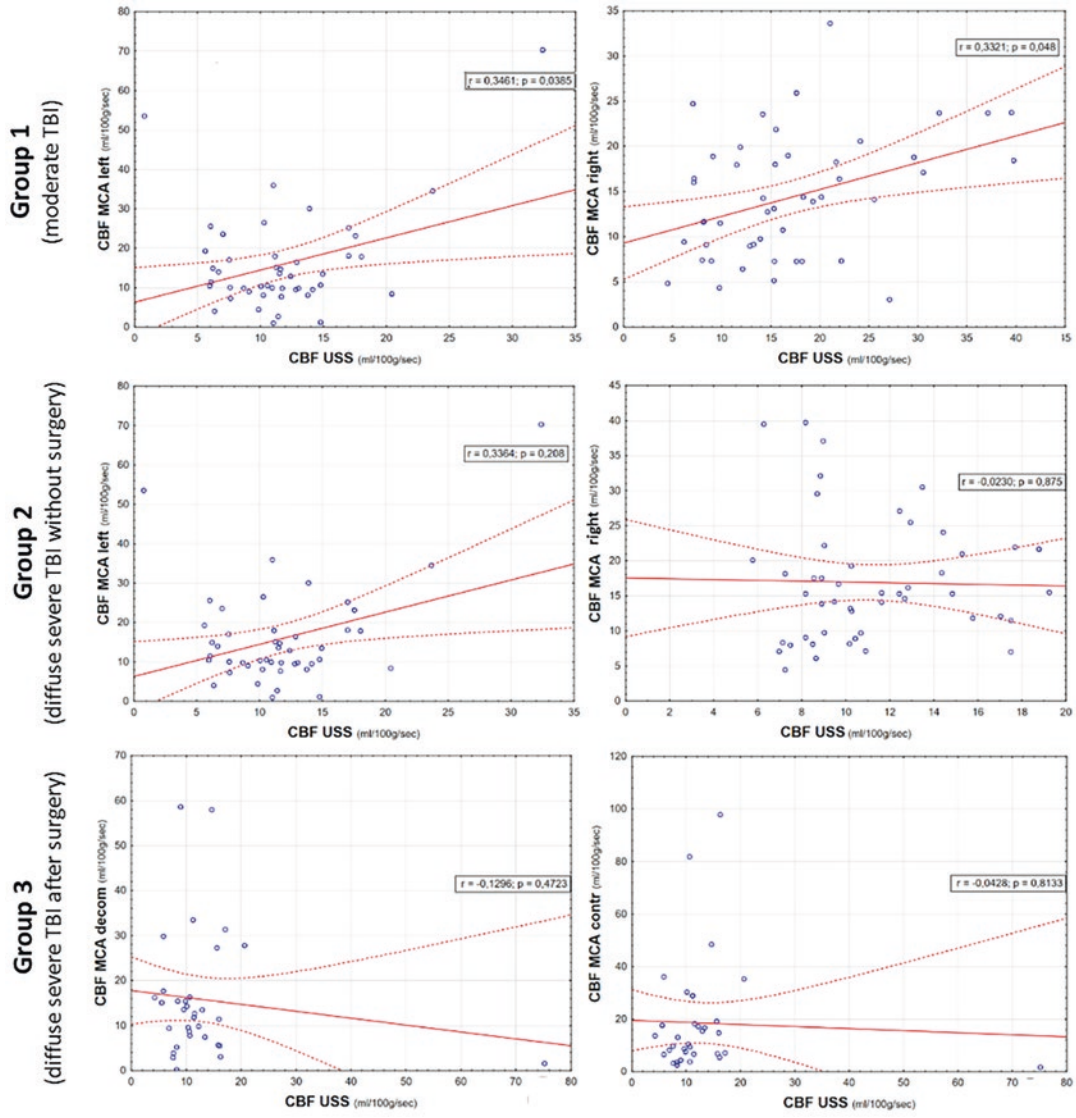

Fig. 9.2 CBF MCA plotted against CBF USS on the left side and right side in all three groups. Dashed red lines represent 95% confidence intervals for the regression (solid red line). For group 3, data are shown for the case of surgical removal of intracranial hematomas on the side of the removed hematoma and on the contralateral side. Dashed red lines represent 95% confidence intervals for the regression (solid red line)

the probable reasons for the discordance in the arterio-venous correlation of CBF may be due to changes in cerebral vascular compliance in TBI. An arterial compliance reduction in TBI has been previously shown, especially after the removal of intracranial hematomas. Edema of the arterial wall and endothelial dysfunction, leading to an increase in the stiffness of the arterial wall, were indicated as a cause of this reduction [12]. The walls of the veins and cerebral sinuses can be compressed by brain edema [13]. Thus, cerebral veins and sinuses are more susceptible than the arteries to tissue edema and ICP rise. Large vessel wall stiffness changes with an increase in the severity of TBI may not be proportional, leading to arterial and venous CBF correlation impairments consistent with previous work [14].

Another possible reason for the alteration in arterial and venous CBF correlation might be increased cerebrovascular resistance. Although a large body of data has been collected on the growth in arterial and arteriolar resistance in various types of TBI [15], venous resistance changes after head injury remain poorly understood. However, it is known that a modification in the vessel lumen from circular to any other configuration causes an increase in cerebrovascular resistance [16].

In the extremis, a capillary compression due to cerebral edema in the region where the hematoma was removed can even stop microcirculation blood flow [17]. It could lead to a decrease in the number of functioning capillaries (i.e., capillary rarefaction) and even more cerebrovascular resistance increase.

All these processes lead to an uneven growth of the arterial and venous components of cerebrovascular resistance, which is reflected in the correlation impairments between arterial and venous CBF.

Although our study examines a relatively large cohort, some limitations remain. First, the bone artifacts seriously limit the assessment of subtentorial CBF by PCT, and we are unable to study CBF in the main arteries and veins in those brain regions. Second, the study design was cross-sectional, so the lack of CBF-age correlation in moderate-to-severe TBI requires further validation. Third, although venous ROI was near to *confluens sinuum* we cannot completely eliminate a mathematical error associated with ROI space measurement. And last, although the arterial and venous CBF are measured in the same values (ml/100 g/s), we cannot conclude with certainty that the arterial flow was carried out in the same compartmental volume from which the venous outflow occurred. To clarify this, more detailed multiphase PCT studies are needed, including an assessment of the CBF in the straight sinus, as well as in the internal carotid and basilar arteries.

9.5 Conclusion

The increasing severity of TBI is accompanied by uncoupling of arterial and venous CBF in the supratentorial vessels. These findings suggest a shift in venous outflow with increased ICP after severe TBI, which may be related to shifts in venous vascular compartments due to brain edema, reduced cerebral vascular compliance and increased cerebrovascular resistance. Further studies are needed to identify the mechanisms of the development of this mismatch.

Acknowledgments AT was supported by a Grant-in-Aid for Exploratory Research from the Privolzhsky Research Medical University. DB was supported by NIH R01 NS112808.

References

1. Axel L (1980) Cerebral blood flow determination by rapid-sequence computed tomography: theoretical analysis. Radiology 137(3):679–686. https://doi.org/10.1148/radiology.137.3.7003648
2. Zahn CD, Smith HL, Hurdelbrink JR, Kluesner NH (2023) Evaluation of computed tomography perfusion and angiogram use in stroke evaluation for thrombectomy at a community emergency department setting. Emerg Radiol:1–9. https://doi.org/10.1007/s10140-023-02116-x. Advance online publication
3. Zhang R, Yan S, Zhong W, Chen L, Luo Z, Xu C, Li Q, Xu J, Zhang W, Liu C, Lou M (2023) Impaired intracranial venous outflow profiles are associated with poor outcome in stroke after reperfusion therapy: a hypoperfusion-matched intracranial venous scale. Eur J Radiol 161:110745. https://doi.org/10.1016/j.ejrad.2023.110745. Epub ahead of print. PMID: 36804310
4. Tao J, Cai Y, Dai Y, Xie Y, Liu H, Zang X (2022) Value of 4D CT angiography combined with whole brain CT perfusion imaging feature analysis under deep learning in imaging examination of acute ischemic stroke. Comput Intell Neurosci 2022:2286413. https://doi.org/10.1155/2022/2286413
5. Chandrapatham K, Cardim D, Corradi F et al (2021) Arterial and venous cerebral blood flow velocities in healthy volunteers. Acta Neurochir Suppl 131:131–134. https://doi.org/10.1007/978-3-030-59436-7_27
6. Trofimov A, Kopylov A, Dobrzeniecki M et al (2020) Comparative analysis of simultaneous transcranial Doppler and perfusion computed tomography for

cerebral perfusion evaluation in patients with traumatic brain injury. Adv Exp Med Biol 1232:55–62. https://doi.org/10.1007/978-3-030-34461-0_8
7. Cardim D, Czosnyka M, Chandrapatham K et al (2020) Arterial and venous cerebral blood flow velocities and their correlation in healthy volunteers and traumatic brain injury patients. J Neurosurg Anesthesiol. https://doi.org/10.1097/ANA.0000000000000704
8. Czosnyka M, Hutchinson PJ, Balestreri M, Pickard JD (2006) Monitoring and interpretation of intracranial pressure after head injury. Acta Neurochir Suppl 96:114–118. https://doi.org/10.1007/3-211-30714-1_26
9. Westermaier T, Pham M, Stetter C, Willner N, Solymosi L, Ernestus RI, Vince GH, Kunze E (2014) Value of transcranial Doppler, perfusion-CT and neurological evaluation to forecast secondary ischemia after aneurysmal SAH. Neurocrit Care 20(3):406–412. https://doi.org/10.1007/s12028-013-9896-0
10. van der Zijden T, Mondelaers A, Voormolen M, Parizel PM (2022) Flat detector CT with cerebral pooled blood volume perfusion in the angiography suite: from diagnostics to treatment monitoring. Diagnostics (Basel, Switzerland) 12(8):1962. https://doi.org/10.3390/diagnostics12081962
11. Mills JN, Mehta V, Russin J, Mack WJ (2013) Advanced imaging modalities in the detection of cerebral vasospasm. Neurol Res Int 2013:415960. https://doi.org/10.1155/2013/415960
12. Dobrzeniecki M, Trofimov A, Bragin DE (2018) Cerebral arterial compliance in traumatic brain injury. Acta Neurochir Suppl 126:21–24. https://doi.org/10.1007/978-3-319-65798-1_5
13. Takahashi A, Ushiki T, Abe K, Houkin K, Abe H (1994) Cytoarchitecture of periendothelial cells in human cerebral venous vessels as compared with the scalp vein. A scanning electron microscopic study. Arch Histol Cytol 57:331–339
14. Chen S, Chen Y, Xu L, Matei N, Tang J, Feng H, Zhang J (2015) Venous system in acute brain injury: mechanisms of pathophysiological change and function. Exp Neurol 272:4–10. https://doi.org/10.1016/j.expneurol.2015.03.007
15. Sharples PM, Matthews DSF, Eyre JA (1995) Cerebral blood flow and metabolism in children with severe head injuries. Part 2: cerebrovascular resistance and its determinants. J Neurol Neurosurg Psychiatry 58:153–159. https://doi.org/10.1136/jnnp.58.2.153
16. Eckert M (2021) Pipe flow: a gateway to turbulence. Arch Hist Exact Sci 75:249–282. https://doi.org/10.1007/s00407-020-00263-y
17. Dewey R (1974) Experimental cerebral hemodynamics. Vasomotor tone, critical closing pressure, and vascular bed resistance. J Neurosurg 41(5):597–606

Cerebral Net Water Uptake in Posttraumatic Cerebral Ischemia

10

Alex O. Trofimov, Kseniia A. Trofimova, Kyril Lidji-Goryaev, Dmitry Martynov, Edwin Nemoto, Olga A. Bragina, and Denis E. Bragin

Abstract

We assessed net water uptake changes (NWU) in regions of posttraumatic ischemia in relation to cerebral microcirculation mean transit time (MTT) at moderate-to-severe traumatic brain injury (TBI). Materials and Methods: 128 moderate-to-severe traumatic brain injury patients (44 women, 84 men, age: 37 ± 12 years) were stratified into 3 groups: Marshall 2–3: 48 patients, Marshall 4: 44 patients, Marshall 5: 36 patients. The groups were matched by sex and age. Patients received multiphase perfusion computed tomography (PCT) 1–5 days after admission. Net water uptake was calculated from non-contrast computed tomography. Data are shown as a median [interquartile range]. $P < 0.05$ was considered statistically significant. Results: Cerebral blood flow in posttraumatic ischemia foci in Marshall 4 group was significantly higher than that in the Marshall 5 group ($p = 0.027$). Net water uptake in posttraumatic ischemia zones was significantly higher than in zones without posttraumatic ischemia (8.1% versus 4.2%, $p < 0.001$). Mean transit time in posttraumatic ischemia zones was inversely and significantly correlated with higher net water uptake ($R^2 = 0{,}089$, $p < 0.01$). Conclusions: Delay of blood flow through the cerebral microvascular bed was significantly correlated with the increased net water uptake in posttraumatic ischemia foci. Marshall's classification did not predict the progression of posttraumatic ischemia.

Keywords

Cerebral blood flow · Net water uptake · Traumatic brain injury

A. O. Trofimov (✉) · K. A. Trofimova
K. Lidji-Goryaev
Department of Neurological Diseases, Privolzhsky Research Medical University, Nizhny Novgorod, Russia

D. Martynov
Technical State University Named After RE Alexeev, Nizhny Novgorod, Russia

E. Nemoto
Department of Neurology, University of New Mexico School of Medicine, Albuquerque, NM, USA

O. A. Bragina
Lovelace Biomedical Research Institute, Albuquerque, NM, USA

D. E. Bragin
Department of Neurology, University of New Mexico School of Medicine, Albuquerque, NM, USA

Lovelace Biomedical Research Institute, Albuquerque, NM, USA

F. Scholkmann et al. (eds.), *Oxygen Transport to Tissue XLIV*, Advances in Experimental Medicine and Biology 1438, https://doi.org/10.1007/978-3-031-42003-0_10

10.1 Introduction

One of the most frequent consequences of the acute stage of moderate and severe traumatic brain injury (TBI) is a secondary insult, leading to cerebral ischemia, increased intracranial pressure, cytotoxic edema, and risk of brain herniation [1]. The incidence of malignant ischemic stroke in the acute period of traumatic brain injury is only about 3%, but with a sharp increase in mortality and poor outcome [2]. Recently, an elegant tool was suggested to study the evolution of brain edema based on the assessment of net water uptake (NWU) by comparing computed-tomographic (CT) brain density (Hounsfield Unit-HU) in the ischemic and contralateral hemispheres [3]. Several meta-analyses have shown that net water uptake is a biomarker of malignant post-stroke cerebral edema and Diffusion-Weighted Imaging/Fluid-Attenuated Inversion Recovery (DWI/FLAIR) mismatch [4, 5]. Although net water uptake measurements by perfusion computed tomography (PCT) allow a more accurate measurement of brain edema in foci of cerebral ischemia, such studies are rare, even in cerebrovascular diseases and strokes, and have never been used for the study of posttraumatic ischemia [6]. The aim of our work was to study brain net water uptake in foci of posttraumatic ischemia foci in moderate-to-severe TBI and its effects on the cerebral microcirculation.

10.2 Methods

10.2.1 Study Design and Population

In a protocol reviewed and approved by the Institutional Ethical Committee and conforming to the standards of the Declaration of Helsinki, a retrospective, observational, and non-randomized single-center study was conducted as an analysis of a prospectively maintained database cohort (2015–2022). We analyzed 128 patients (44 women, 84 men, age: 37 ± 12 years) with PTI after moderate-to-severe traumatic brain injury. Inclusion criteria were: moderate-to-severe TBI < 6 h after head injury Glasgow Coma Score (GCS) < 12, >4; perfusion CT performed <5 days after injury; unilateral posttraumatic ischemia foci by perfusion computed tomography (PCT). The exclusion criteria were: age less than 18 and more than 60 years; Glasgow Coma Score at admission to the clinic of more than 12 points; gunshot and explosive skull brain injuries; the severity on the injury severity scale (ISS) more than 16 points. Posttraumatic ischemia was determined using perfusion CT, and brain edema was determined using net water uptake on baseline CT images. The patients were stratified into 3 groups according to the Marshall classification (Table 10.1): Marshall 2–3: 48 patients, Marshall 4: 44 patients, Marshall 5: 36 patients. The groups were matched by sex and age.

10.2.2 Image Acquisitions

All patients received multiphase PCT on days 1–5 after the TBI (mean 3.3 ± 0.5 days) on a 160-slice scanner (Canon Aquilion Prime SP, Canon Medical Imaging, Japan). The perfusion examination report included an initial contrast-free CT of the brain. Extended scanning was further performed in 16 "areas of interest", 160 mm in thickness, within 60 s with a contrast agent. The scanning parameters were 160 kVp, 160 mA, 70 mAs, 512 × 512 The contrast agent Ultravist 370 (Schering AG, Germany) was administered with a syringe injector (Stellant, Medrad, USA) into a

Table 10.1 Marshall classification

Marshall class	Characteristic
I	No intracranial pathology seen with computed tomography
II	Cisterns present with midline shift of 0–5 mm and/or lesions/densities present; no high- or mixed-density lesions >25 cm^3;
III	Cisterns compressed or absent with midline shift of 0–5 mm; no high- or mixed-density lesions >25 cm^3
IV	Midline shift >5 mm; no high or mixed density lesions >25 cm^3
V	Any lesion surgically evacuated
VI	High- or mixed-density lesion >25 cm^3; not surgically evacuated

peripheral vein through a standard catheter (20 G) at a rate of 5 mL/s in a dose of 50 mL per one examination. After scanning, the data were transferred to a PACS (KIR, Russia) and perfusion CT data were processed using the workstation by Vitrea (Vitrea FX, Vital Images, USA), where standard perfusion maps were built, including: cerebral blood volume (CBV), cerebral blood flow (CBF), mean transit time (MTT). Artery and vein marks were automatically recorded, followed by the manual control of indices in the time-concentration diagram. The region of interest (ROI) was established based on subcortical areas of the middle cerebral artery. Errors introduced by delay and dispersion of the contrast bolus before arrival in the cerebral circulation were corrected by block-circulant deconvolution algorithm [7]. Quantitative perfusion indices, including cerebral blood flow, were calculated voxelwise and used to generate color-coded maps. The voxels with cerebral blood flow > 100 mL/100 g/min and/or cerebral blood volume > 8 mL/100 g were assumed to contain large vessels and removed from the perfusion map calculation (Fig. 10.1). The thresholds of cerebral ischemia (core and penumbra) were: a decrease in cerebral blood volume < 2.0 mL/100 g, or a cerebral blood flow decrease <145% compared with the contralateral hemisphere [8, 9]. Net water uptake was calculated using following equation [7]:

$$\mathrm{NWU} = \left(1 - D_{\mathrm{ischemic}} / D_{\mathrm{normal}}\right) \times 100\%, \tag{10.1}$$

with D_{ischemic} the ischemic "core" density and D_{normal} the density of normal brain tissue in the symmetrical zone of the contralateral hemisphere (Hounsfield Unit – HU).

10.2.3 Statistical Analysis

Data are shown as a median [interquartile range]. Statistical analysis was performed using T-criterion Wilcoxon. Pearson's correlation coefficients were used to assess agreement between computed variables. The regression line and confidence limits for each are for illustrative purposes only. $P < 0.05$ was considered statistically significant.

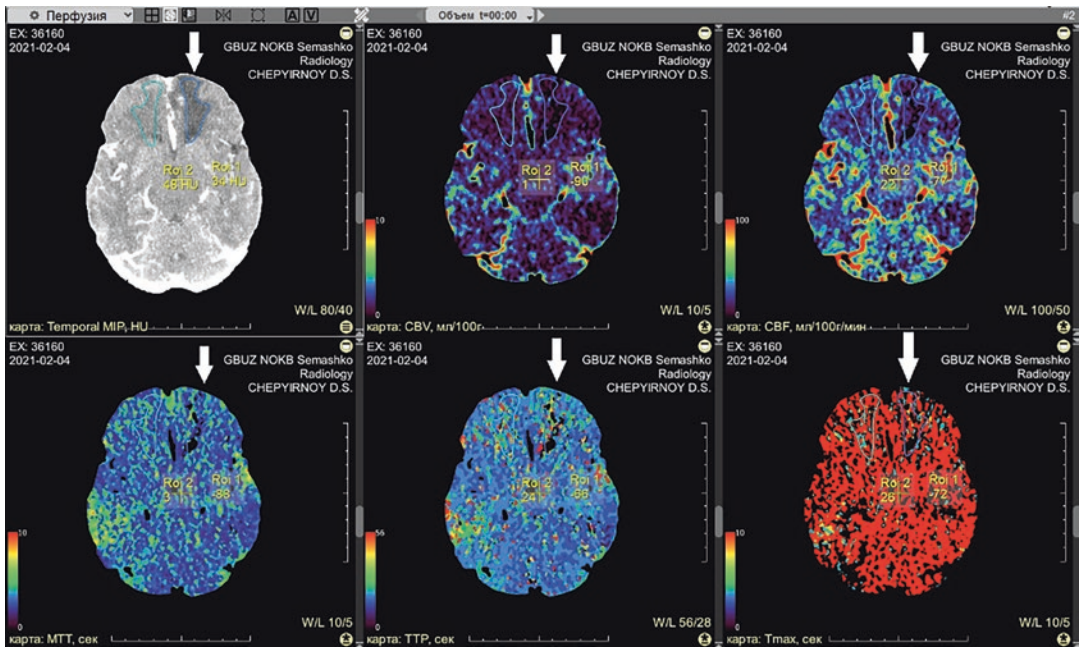

Fig. 10.1 Perfusion maps of the posttraumatic ischemia at moderate traumatic brain injury. A white arrow indicates a zone of posttraumatic ischemia in cerebral blood volume, cerebral blood flow, mean transit time, and time to peak

10.3 Results

The mean values and standard deviations of the data are summarized in Table 10.2. There were no significant differences between the net water uptake in posttraumatic ischemia foci in Marshall 2–3 groups, and only cerebral blood flow in posttraumatic ischemia foci in Marshall 4 group was significantly higher than cerebral blood flow in posttraumatic ischemia foci in Marshall 5 ($Z = 2.197$, $p = 0.027$). The net water uptake in posttraumatic ischemia zones was higher than in zones without posttraumatic ischemia (8.1% versus 4.2%; $p < 0.001$). In posttraumatic ischemia zones, cerebral blood volume was not significantly correlated with net water uptake ($p > 0.05$). The increase in MTT in posttraumatic ischemia zones was significantly and inversely correlated with net water uptake ($R^2 = 0{,}089$, $p < 0.01$) (Fig. 10.2).

Table 10.2 Analyzed data

	NWU (%)	CBFi (ml/100 g/sec)	CBVi (ml/100 g)	MTTi (sec)	CBFn (ml/100 g/sec)	CBVn (ml/100 g)	MTTn (sec)
Marshall II-III	44.12 [36.11;51.58]	20.9 [11.9;22.6]	1.4 [0.8;1.6]	4 [3.4;4.5]	21.4 [18.7;36.7]	1.8 [1.3;2.5]	4.7 [3.6;5.0]
Marshall IV	42.92 [40,63;56.66]	15.9 [7.3;19.1]	1.01 [0.5;1.4]	4.8 [4.1;7.7]	21.1 [16.6;27.9]	1.8 [1.3;2.2]	4.6 [3.8;5.4]
Marshall V	46.41 [36.66;55.88]	3.2 [1.5;12.1]	0.5 [0.2;0.8]	5.1 [3.0;8.5]	10.9 [4.8;24.8]	1.1 [0.5;1.9]	4.5 [3.6;16.1]
P (1–2)	0.213	0.236	0.612	0.24	0.43	0.612	0.352
P (2–3)	0.794	0.980	0.310	0.498	0.499	0.150	0.612
P (1–3)	0.858	0.028*	0.063	0.064	0.735	0.176	0.062

NWU net water uptake, *CBVi* cerebral blood volume in PTI focus, *CBFi*: cerebral blood flow in PTI focus, *MTTi* mean transit time in PTI focus, *CBVn* cerebral blood volume in the symmetrical zone, *CBFn* cerebral blood flow in the symmetrical zone, *MTTn* mean transit time in the symmetrical zone
*Significant difference ($p < 0.05$)

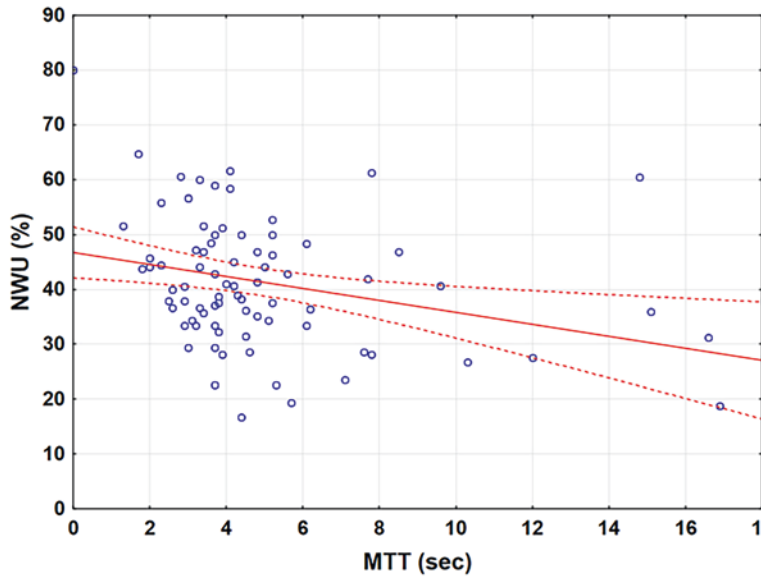

Fig. 10.2 The linear regression result: mean transit time vs. net water uptake in the posttraumatic ischemia zone. Dashed red lines represent 95% confidence intervals for the regression (solid red line)

10.4 Discussion

The aim of our study was to assess regional changes in net water uptake in relation to the changes in the cerebral microcirculation in moderate-to-severe TBI. There were no significant differences between the net water uptake values in posttraumatic ischemia foci between the Marshall groups. Earlier, we considered that Marshall classification indicated the development of posttraumatic ischemia, which was not confirmed in this study probably because it does not consider cerebral vasospasm, changes in the cerebral microcirculation parameters (cerebrovascular resistance, cerebral arterial compliance, cerebrovascular time constant and critical closing pressure), and the volume and localization of posttraumatic ischemia foci, all of which play a significant role in the development of posttraumatic ischemia [10].

We showed that cerebral microcirculation impairments significantly correlated with an increase in brain net water uptake in foci of posttraumatic ischemia, which, we suggest, is due to the following reasons. First, posttraumatic ischemia is associated with an increase in blood-brain barrier permeability that increases net water uptake [11]. Second, venous outflow in the posttraumatic ischemia focus decreases, leading to an overload of the venous microcirculatory bed and an increase venous pressure and net water uptake. Third, as described earlier, the gradient between intravascular and extravascular (parenchymal) oncotic pressure in the ischemic focus makes a significant contribution to the increase in net water uptake in the lesion [12]. Our study has several limitations. The main limitations are the single-center and retrospective design as well the lack of a control group. This can lead to a potential selection bias regarding posttraumatic ischemia recognition. Another limitation is the difficult postprocessing in the foci of perfusion CT artifacts. The last limitation is the unknown cerebral collateral circulation status, which might have a significant impact on secondary ischemia progression.

10.5 Conclusion

The delay in blood flow through the cerebral microvascular bed was significantly and inversely correlated with brain net water uptake in the posttraumatic ischemia foci. The Marshall's classification did not predict posttraumatic ischemia.

Acknowledgments AT and KT were supported by a Grant-in-Aid for Exploratory Research from the Privolzhsky Research Medical University; DB was supported by NIH R01 NS112808.

References

1. Smith BG, Whiffin CJ, Esene IN et al (2022) Neurotrauma clinicians' perspectives on the contextual challenges associated with traumatic brain injury follow up in low-income and middle-income countries: a reflexive thematic analysis. PLoS One 17(9):e0274922. https://doi.org/10.1371/journal.pone.0274922
2. Wu YG, Chao Y, Gao G et al (2021) Risk factors for cerebral infarction after moderate or severe traumatic brain injury. Ther Clin Risk Manag 17:433–440. https://doi.org/10.2147/TCRM.S309662
3. Broocks G, Flottmann F, Scheibel A et al (2018) Quantitative lesion water uptake in acute stroke computed tomography is a predictor of malignant infarction. Stroke 49(8):1906–1912. https://doi.org/10.1161/STROKEAHA.118.020507
4. Nawabi J, Elsayed S, Morotti A et al (2021) Perihematomal Edema and clinical outcome in intracerebral Hemorrhage related to different Oral anticoagulants. J Clin Med 10(11):2234. https://doi.org/10.3390/jcm10112234
5. Broocks G, Leischner H, Hanning U et al (2020) Lesion age imaging in acute stroke: water uptake in CT versus DWI-FLAIR mismatch. Ann Neurol 88(6):1144–1152. https://doi.org/10.1002/ana.25903
6. Haupt W, Meyer L, Wagner M et al (2022) Assessment of irreversible tissue injury in extensive ischemic stroke-potential of quantitative cerebral perfusion. Transl Stroke Res. https://doi.org/10.1007/s12975-022-01058-9
7. Lin L, Bivard A, Kleinig T, Spratt NJ et al (2018) Correction for delay and dispersion results in more accurate cerebral blood flow ischemic core measurement in acute stroke. Stroke 49:924–930. https://doi.org/10.1161/STROKEAHA.117.019562
8. Meyer L, Schönfeld M, Bechstein M et al (2021) Ischemic lesion water homeostasis after thrombectomy for large vessel occlusion stroke within the anterior circulation: the impact of age. J Cereb Blood

Flow Metab 41(1):45–52. https://doi.org/10.1177/0271678X20915792
9. Lin L, Bivard A, Krishnamurthy V et al (2016) Whole-brain CT perfusion to quantify acute ischemic penumbra and core. Radiology 279:876–887. https://doi.org/10.1148/radiol.2015150319
10. Trofimov A, Dubrovin A, Martynov D et al (2021) Microcirculatory biomarkers of secondary cerebral ischemia in traumatic brain injury. Acta Neurochir Suppl 131:3–5. https://doi.org/10.1007/978-3-030-59436-7_1
11. Jungner M, Siemund R, Venturoli D et al (2016) Blood-brain barrier permeability following traumatic brain injury. Minerva Anestesiol 82(5):525–533
12. van Horn N, Broocks G, Kabiri R et al (2022) Cerebral Hypoperfusion intensity ratio is linked to progressive early Edema formation. J Clin Med 11(9):2373. https://doi.org/10.3390/jcm11092373

11 Brainstem Damage Underlies Changes in Hypoxic Ventilatory Response Following Cardiac Arrest and Resuscitation in Rats

Kui Xu, Alireza Abdollahifar, Xiaoyen Sun, and Joseph LaManna

Abstract

People resuscitated after sudden cardiac arrest remain at high risk for mortality, with treatment for survivors varying from monitoring to life support. With respect to assessing survivability post cardiac arrest and resuscitation (CAR), we previously demonstrated the potential of the hypoxic ventilatory response (HVR) as a reliable indicator for discerning between survivors and non-survivors in the early stages of recovery following CAR in rats. Since HVR describes the increase in ventilation in response to hypoxia, we hypothesize that damage to cardiorespiratory regulatory centers in the brainstem underlie the loss of HVR observed post resuscitation in nonsurvivors. Wistar rats underwent cardiac arrest (12-min) and resuscitation. At 1 day post-resuscitation, rats were perfused transcardially and the brains were harvested and processed for immunohistostaining of caspase-3, a marker of apoptosis. Positive caspase-3 staining was observed in brainstem regions such as the rostral ventral lateral medulla (RVLM); Co-localization of caspase-3 and NeuN was observed in the RVLM as well, suggesting that apoptosis most likely occurs in neurons. Our results showed positive markers for neuronal apoptosis present in pathways of the brainstem involved in respiratory and cerebrovascular regulation, suggesting brain stem damage underlies changes in HVR following CAR.

Keywords

Cardiac arrest and resuscitation · Brainstem damage · Hypoxia

11.1 Introduction

Cardiac arrest (CA) results in global ischemia, to which the brain is especially sensitive. After resuscitation restores blood flow, the brain is subject to a second insult referred to as reperfusion injury. Regarding survival, we hypothesize that brainstem pathophysiology following cardiac arrest and resuscitation (CAR) is the critical determinant due to its essential role in regulating cardiovascular and respiratory functions. We have developed a rodent CAR model, in which after 12 min of ischemic exposure during cardiac arrest, the 4-day post resuscitation survival rate was 50%. Immediately after resuscitation, cardiovascular and respiratory variables return to normal, but vasogenic edema can result from reperfusion injury leading to a secondary chal-

K. Xu (✉) · A. Abdollahifar · X. Sun · J. LaManna
Department of Physiology and Biophysics, School of Medicine, Case Western Reserve University, Cleveland, OH, USA
e-mail: kxx@case.edu

F. Scholkmann et al. (eds.), *Oxygen Transport to Tissue XLIV*, Advances in Experimental Medicine and Biology 1438, https://doi.org/10.1007/978-3-031-42003-0_11

lenge to brainstem function [1]. Ischemia/reperfusion injury generates an excess of free radicals that initiate chain reactions and damage cellular macromolecules, including proteins, DNA and lipids, ultimately leading to cell death [2–4]. Within 2–4 days following CAR, signs of neuronal apoptosis, including upregulation of Bax and activated caspase-3 were detected via Western Blotting in brainstem tissue. Terminal deoxynucleotidyl transferase (TdT) dUTP Nick-End Labeling (TUNEL)-expression appear in neurons of the rostral ventrolateral medulla (RVLM), and other brainstem nuclei involved in cardiovascular and respiratory regulation, 4 days post resuscitation [5]. We further tested the hypoxic ventilatory response (HVR) of rats following CAR and found that decreased HVR was associated with post-resuscitation mortality [6, 7]. In this study, we assessed brainstem damage with immunohistochemical detection of apoptosis in the early stages of recovery post CAR.

11.2 Methods

11.2.1 Rat Model of Cardiac Arrest and Resuscitation

Male Wistar rats (3 months old) were acclimatized to the animal facility for 1 week before the experiment. As described previously [1], anesthesia was induced with 2.5% isoflurane in air and maintained with 1% isoflurane via nasal cone. We inserted a polyethylene cannula (Intramedic PE-50, 0.058 and 0.965 mm inner- (id) and outer- diameter (od), respectively; Becton Dickson) in the ventral tail artery to monitor arterial blood pressure and to collect arterial blood gas samples; and a Silastic cannula (Dimensions: 0.64 mm id, 1.19 mm od (Dow Corning) in the right atrium via the right external jugular vein to administer drugs directly to the heart. The rats recovered for an hour after surgery in plastic cages. Their body temperature was maintained at 37 °C by an infrared heat lamp (250 W, positioned 45 cm above the body), which was regulated by feedback from a rectal thermoprobe.

Transient global brain ischemia was induced by cardiac arrest and resuscitation as described previously [1, 6]. Cardiac arrest was caused by the rapid sequential intra-atrial injection of D-tubocurare (0.3 mg) followed by ice-cold KCl solution (0.5 M; 0.12 ml/100 g of body weight), marking the beginning of ischemia. Then rats were intubated orotracheally with a 14-gauge polyethylene tube and attached to a rodent ventilator. Resuscitation was initiated 7 min after cardiac arrest, and consisted of: (1) ventilation (inhaled gas, 100% O_2; tidal volume, 10 ml/kg; respiratory rate, 80 breaths/min), (2) chest compressions (~160 times/min) and 3) intra-atrial administration of normal saline (~0.5 ml/min) to washout the KCl. Once a spontaneous heartbeat returned, then epinephrine (4–10 μg) was administered intra-atrially to restore mean blood pressure above 80% of pre-arrest value. At this point, the rat was resuscitated and the duration of ischemia was approximately 12 min.

After resuscitation, the ventilation was adjusted (inhaled gas, ~30% oxygen in nitrogen, respiratory rate, ~70 times/min, tidal volume, 10 ml/kg body weight), on the basis of the arterial blood gases, to normal ranges until the rats regained their spontaneous respiration. Artificial ventilation was maintained until the rats resumed spontaneous breathing, usually within 3 h post cardiac arrest and resuscitation. Non-arrested controls underwent all surgical procedures except cardiac arrest.

The surgical procedures and experimental protocols performed in this study were approved by the Institutional Animal Care and Use Committee at Case Western Reserve University were executed in strict adherence to the guidelines published by NIH.

11.2.2 Caspase-3 Immunohistochemistry

To examine the brainstem for neural damage, one non-arrested control rat and one 1-day recovery rat were deeply anesthetized with isoflurane. Rats were perfused transcardially with 200 ml 0.1 M PBS (pH 7.4) and then with 4% paraformalde-

hyde. Brains were removed and stored in the fixative for 24 h and then transferred to 30% sucrose. Using a cryomicrotome we cut frozen coronal sections (20 μm in thickness) from a block of medullary tissue at levels from Bregma −6.36 mm to Bregma −7.2 mm [8].

Every other section was placed sequentially in tissue trays and double-stained. We used the neuronal marker, NeuN, to identify neurons. These sections were exposed to anti-NeuN (1:200, Chemicon International, Temecula, CA, USA) overnight at 4 °C. To identify cleaved caspase-3, which is an accepted marker of apoptosis, sections were exposed to anti-caspase-3 antibody (1:100; Cell Signaling Technology, Danvers, MA, USA) overnight at 4 °C. The next day we incubated each set of sections with their appropriate biotinylated IgG secondary antibody (1:200, Vector Laboratories, INC, Burlingame, CA, USA) for 1 h and then with avidin-biotin horseradish peroxidase solution (ABC kit, Vector Laboratories, INC, Burlingame, CA, USA) for 30 min. Sections were mounted to slides and staining was visualized by using fluorescence microscopy.

11.3 Results

Double-staining of caspase-3 and neuronal marker NeuN was performed in brainstem samples of non-arrested controls and 1 day post-resuscitation rats. Positive staining was observed at 1 day post-resuscitation in brainstem regions such as RVLM, raphe pallidus nucleus and inferior olive medial nucleus. Co-localization of caspase-3 and NeuN was observed in multiple brainstem regions, suggesting that apoptosis most likely occurs in neurons (Fig. 11.1).

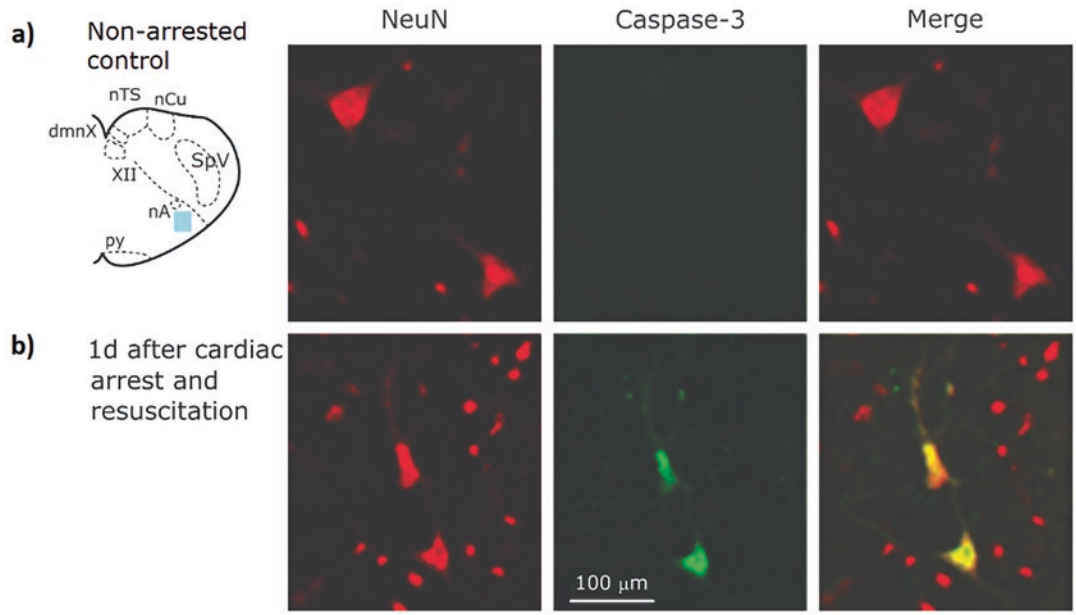

Fig. 11.1 Histology indicating the transient 12-min ischemia initiated apoptosis in the ventrolateral medulla at 400×. (**a**) In the naïve rat, ventrolateral medulla was not positive for caspase-3 staining. (**b**) In contrast, 1d after cardiac arrest and resuscitation, the ventrolateral medulla was positive for caspase-3 staining. The merged image showed that apoptosis occurred in neurons. The atlas reference in the top left illustrates respiratory control regions of the brainstem, with the blue box highlighting the region of staining. Abbreviations: *dmnX* dorsal motor nucleus of the Vagus, *nA* nucleus Ambiguus, *nCu* nucleus Cuneatus, *nTS* nucleus tractus solitaries, *py* pyramidal tract, *SpV* Spinal trigeminal nucleus, XII: Hypoglossal nucleus and nerve root. Labeling – *NeuN* neuronal nuclear antigen, caspase-3: apoptosis detection

11.4 Discussion

In this study, we detected neuronal apoptosis, particularly in the RVLM of the brainstem, 1 day post resuscitation. The localization of damage to this region is consistent with previous studies reporting brainstem nuclei degradation post CAR [5]. The neurons of the RVLM region are involved in regulation of cerebrovascular dilation, respiration, glycemia and blood pressure. Ultrastructural studies of brainstem mitochondria demonstrated significant pathology after 15 min of global ischemia but relatively quick recovery 5 min after reperfusion [9]. However, our previous study has shown mitochondrial respiratory function was still impaired in the brainstem 2 days post resuscitation [7]. Hypoperfusion in the brainstem also persisted 1-day post resuscitation [1]. In our rat CAR model, most of the non-surviving rats die from cardio-respiratory collapse, suggesting that brainstem function, in particular the generation and maintenance of spontaneous respiration, becomes compromised during the first few days after resuscitation. The positive markers for neuronal apoptosis present in pathways of the brainstem involved in respiratory and cerebrovascular regulation suggest brainstem damage underlies the loss of HVR observed in nonsurviving rats in the early phase recovery following CAR.

References

1. Xu K, Puchowicz MA, Lust WD, LaManna JC (2006) Adenosine treatment delays postischemic hippocampal CA1 loss after cardiac arrest and resuscitation in rats. Brain Res 1071:208–217
2. Nita DA, Nita V, Spulber S, Moldovan M, Popa DP, Zagrean AM, Zagrean L (2001) Oxidative damage following cerebral ischemia depends on reperfusion – a biochemical study in rat. J Cell Mol Med 5:163–170
3. Piantadosi CA, Zhang J (1996) Mitochondrial generation of reactive oxygen species after brain ischemia in the rat. Stroke 27:327–331
4. Warner DS, Sheng H, Batinic-Haberle I (2004) Oxidants, antioxidants and the ischemic brain. J Exp Biol 207:3221–3231
5. LaManna JC, Pichule P, Xu K, Chavez JC (2009) Brain stem sensitivity to hypoxia and ischemia. In: Haddad GG, Yu SP (eds) Brain hypoxia and ischemia. Humana Press, a part of Springer Science + Bussiness Media, LLC, pp 213–223
6. Xu K, LaManna JC (2009) The loss of hypoxic ventilatory responses following resuscitation after cardiac arrest in rats is associated with failure of long-term survival. Brain Res 1258:59–64
7. Xu K, Puchowicz MA, Sun X, LaManna JC (2010) Decreased brainstem function following cardiac arrest and resuscitation in aged rat. Brain Res 1328:181–189
8. Michael J, Palkovits M, Brownstein (1988) Maps and guide to microdissection of rat brain. Elsevier, New York
9. LaManna JC, Kaiserman-Abramof IR, Xu K, Daugherty S, Chavez JC, Pichiule P (2001) Acute and delayed effects of transient global cerebral ischemia on rat brain capillary endothelial cells in vivo. In: Ischemic Keio University symposia for life science and medicine. Blood Flow in the Brain

12

Differences Between Good, Moderate and Poor Performers of a Verbal Fluency Task under Blue Light Exposure: An SPA-fNIRS Study

Hamoon Zohdi, Vanessa Amez-Droz, Felix Scholkmann, and Ursula Wolf

Abstract

Individuals have different performance levels for cognitive tasks. Are these performance levels reflected in physiological parameters? The aim of this study was to address this question by systemic physiology augmented functional near-infrared spectroscopy (SPA-fNIRS). We aimed to investigate whether different verbal fluency task (VFT) performances under blue light exposure were associated with different changes in cerebrovascular oxygenation and systemic physiological activity. The VFT performance of 32 healthy subjects (17 female, 15 male, age: 25.5 ± 4.3 years) was investigated under blue light exposure (120 lux). The VFT, which contained letter and category fluency tasks, lasted 9 min. There were rest periods without light exposure before and after the VFT for 8 min and 15 min, respectively. Based on their number of correct responses, subjects were classified into three groups, i.e., good, moderate, and poor performers. During the entire experiment, we simultaneously measured changes in cerebral and systemic physiological parameters using the SPA-fNIRS approach. We found that the better the subject's performance was, the smaller the task-evoked changes in cerebrovascular hemodynamics and oxygenation in the prefrontal cortex. Performance-dependent changes were also evident for skin conductance, arterial oxygen saturation and mean arterial pressure. This is the first VFT study that applies the comprehensive SPA-fNIRS approach to determine the relationship between task performance and changes in cerebral oxygenation and systemic physiology. Our study shows that these parameters are indeed related and the performance is reflected in the task-evoked cerebrovascular and systemic physiological changes.

Keywords

Verbal fluency task · Blue light exposure · SPA-fNIRS · Systemic physiology · Cerebral hemodynamics · Task performance

H. Zohdi (✉) · F. Scholkmann
Institute of Complementary and Integrative Medicine, University of Bern, Bern, Switzerland

Biomedical Optics Research Laboratory, Department of Neonatology, University Hospital Zurich, University of Zurich, Zurich, Switzerland
e-mail: hamoon.zohdi@unibe.ch

V. Amez-Droz · U. Wolf
Institute of Complementary and Integrative Medicine, University of Bern, Bern, Switzerland

F. Scholkmann et al. (eds.), *Oxygen Transport to Tissue XLIV*, Advances in Experimental Medicine and Biology 1438, https://doi.org/10.1007/978-3-031-42003-0_12

12.1 Introduction

How well someone performs a cognitive task depends on various reasons, such as cognitive factors (e.g., knowledge and cognitive abilities) and non-cognitive factors (e.g., personality and environmental influences) [1, 2]. Although different performance levels and the factors affecting them have been well investigated in behavioral studies, whether these differences in performance are reflected in physiological parameters is not yet clear.

The physical learning environment, as a non-cognitive factor, plays an important role in the task performance of students. For example, colored light and colors can be used as a part of these environments to boost the students' moods and performance [3]. Employing systemic physiology augmented functional near-infrared spectroscopy (SPA-fNIRS) [4] in our previous research, we studied a mixed effect of a cognitive verbal fluency task (VFT) and blue light exposure at the behavioral and physiological levels [5–8]. The aim here is to determine whether differences in cognitive performance are reflected in changes in cerebral oxygenation and systemic physiology.

12.2 Subjects and Methods

Thirty-two healthy subjects (17 female, 15 male, age: 25.5 ± 4.3 years) were recruited in this study. SPA-fNIRS measurements were carried out by a setup containing a multi-channel frequency-domain near-infrared spectroscopy system (FD-NIRS; Imagent, ISS Inc., Champaign, IL, USA) and three devices to measure systemic physiological parameters. The FD-NIRS enabled the measurements to be less sensitive to the superficial layers and physiological noise coming from the extracerebral tissue compartment. The following parameters were measured concurrently: absolute concentration of oxyhemoglobin ($[O_2Hb]$), deoxyhemoglobin ([HHb]), total hemoglobin ([tHb]), and cerebrovascular oxygen saturation (StO_2) bilaterally over the prefrontal cortex (PFC) and visual cortex (VC) as well as end-tidal CO_2 ($P_{ET}CO_2$), mean arterial blood pressure (MAP), skin conductance (SC) and arterial oxygen saturation (SpO_2). Subjects sat in a reclining chair and were asked to perform a VFT while being exposed to blue light (spectral peak: 450 nm, illuminance: 120 lux). The total duration of the VFT was 9 min. Before (baseline, 8 min) and after (recovery, 15 min) the VFT, subjects were in a rest phase in darkness. A detailed description of the SPA-fNIRS measurement setup and the experimental protocol can be found in our previous publications [5, 6].

Based on their number of correct responses (CR), subjects were classified into three groups as good, moderate and poor VFT performers. The total number of CR articulated by the participants was 55 ± 15 (mean ± SD; range: 23–100). The first third of the subjects belonged to the poor performers' group (33rd percentile = 48.8; CR < 49). The second third of the subjects were categorized as the moderate performers' group (66th percentile = 57.7; 49 < CR < 58), and the rest were in the good performers' group (CR > 58).

Movement artifacts were removed, and a low pass filter (RLOESS) with a window length of 3 min was applied to remove high-frequency noise from the fNIRS signals. Signals from the left and right PFC and VC were averaged to obtain signals for the whole PFC and VC, respectively. All systemic physiological signals, except the SC, were also smoothed by the RLOESS with a window length of 3 min. The SC signals were processed with the Ledalab toolbox using the continuous decomposition analysis. All signals were then normalized to the second last minute of the baseline phase. Signals for each group of subjects (poor, moderate and good) were block-averaged.

12.3 Results

Cerebrovascular Hemodynamics and Oxygenation The group-averaged long-term changes of $[O_2Hb]$, [HHb], [tHb] and StO_2 at the PFC and VC for poor, moderate and good VFT performers are displayed in Fig. 12.1. The typical

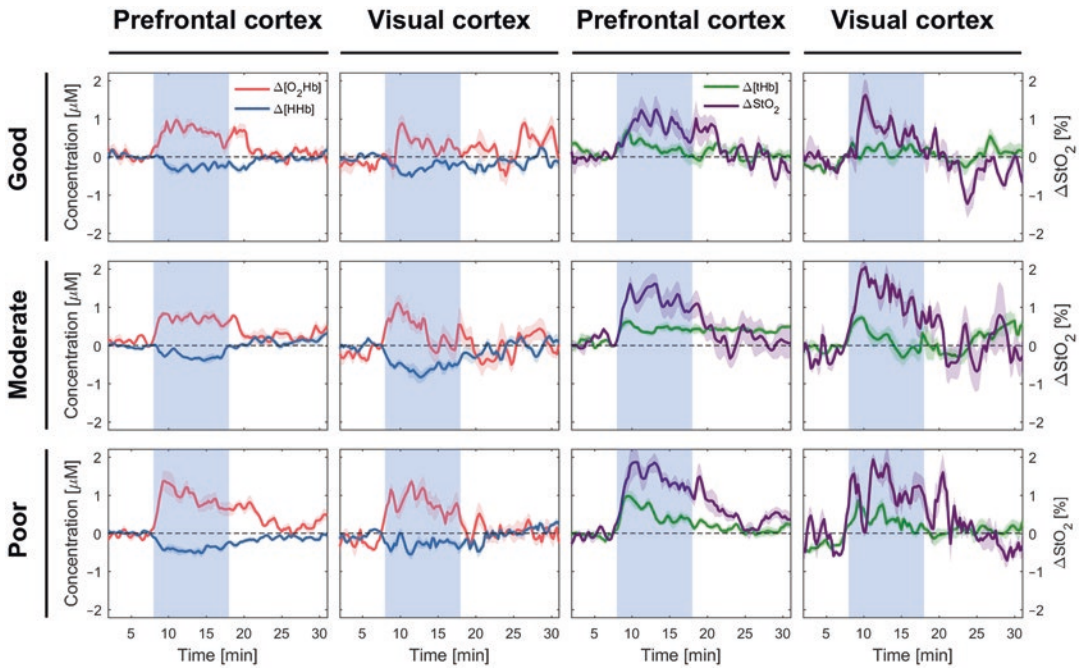

Fig. 12.1 Group-averaged changes in hemodynamic and oxygenation responses of the PFC and VC for good, moderate and poor performers' groups. The shaded areas represent the VFT periods during which the subjects were also exposed to the blue light. Median ± standard error of median (SEM) are shown

pattern of a cerebrovascular change due to an increase in brain activity (i.e., increase in [O_2Hb] and decrease in [HHb]) was observed during the VFT in the PFC and VC for all VFT performance groups. The changes in fNIRS signals were different between groups: Changes in cerebrovascular hemodynamics and oxygenation in the PFC were generally the highest in the poor performers' group, followed by the moderate and good performers' groups, respectively. Among all groups, changes in tissue oxygen saturation at the PFC were the lowest in the good performers' group (good vs. moderate: Cohen's d = 1.4; good vs. poor: d = 2.0; moderate vs. poor, d = 0.7). No significant differences were observed for changes in the fNIRS signals from the VC among all groups.

Systemic Physiological Parameters Figure 12.2 shows the group-averaged changes of systemic physiological parameters for poor, moderate and good VFT performers. Performance-dependent changes were observed for MAP (good vs. moderate: d = 1.5; good vs. poor: d = 3.6; moderate vs. poor: d = 2.4), SC (good vs. moderate: d = 4.4; good vs. poor: d = 4.7; moderate vs. poor: d = 0.8) and SpO_2 (good vs. moderate: d = 2.3; good vs. poor: d = 2.3). Changes in MAP and SC were as follows: poor > moderate > good; and in SpO_2, changes in good performers' group were smaller compared to moderate and poor groups. All these differences mentioned above were significantly different at $p < 0.05$.

12.4 Discussion and Conclusions

Human performance is a product of many interacting factors. Some of them play a role before the actual task, such as the level of training and expertise achieved and the family's socioeconomic status. Some other factors have an impact during tasks, including workload, fatigue, stress, situation awareness and decision-making [2, 9]. In this study, we classified subjects into three

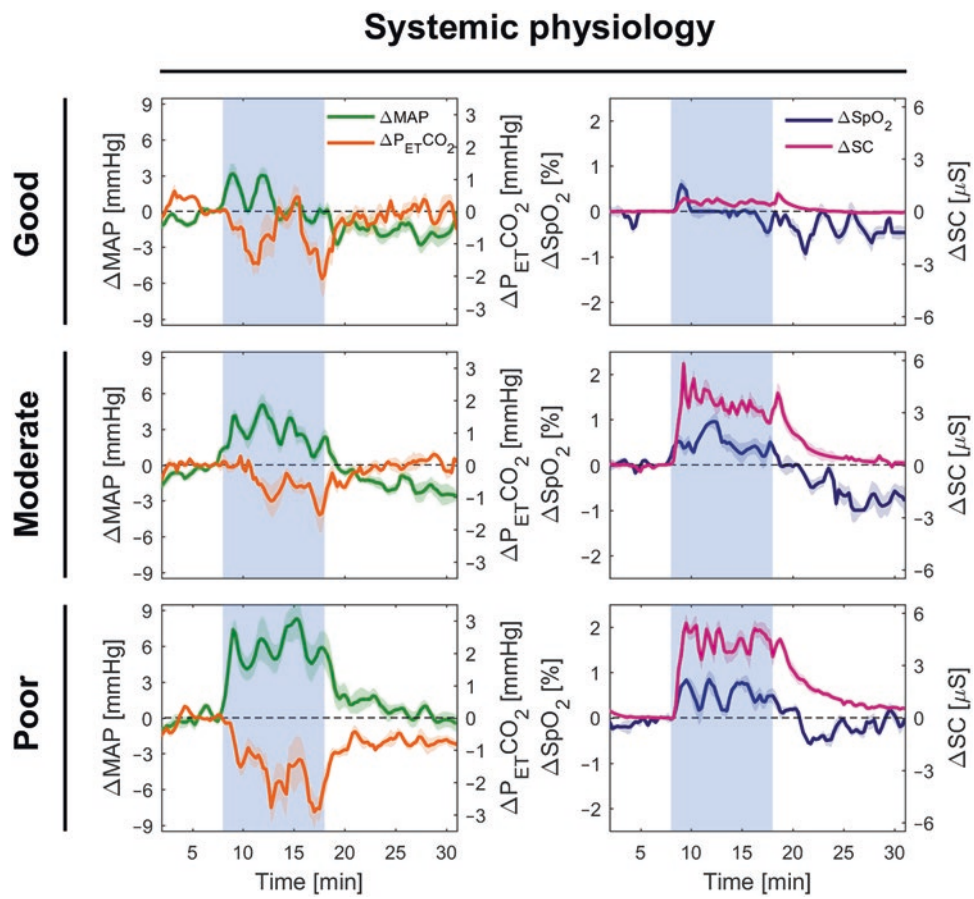

Fig. 12.2 Group-averaged changes in systemic physiological parameters for good, moderate and poor performers' groups. The shaded areas represent the VFT periods during which the subjects were also exposed to blue light. Median ± SEM are shown

groups based on their VFT performance. We found that changes in cerebrovascular oxygenation in the PFC were inversely related to the performance, i.e., less changes in fNIRS signals with better performance. There are generally two ways to explain these findings:

(i) The fNIRS changes could primarily reflect changes in brain activity, and the brain activity is different for the three groups. There is considerable evidence that, in general, experts show lower brain activity compared to novices, particularly in the PFC [10, 11]. One could argue that the relatively high changes in fNIRS signals in the poor performers' group are due to the increased task engagement of performers in this group, indicating that more effortful processing is needed to manage the workload for the poor performers. On the other hand, we found that the better the subject's performance was, the fewer changes in cerebral oxygenation. Lower oxygenation may accurately reflect lower mental effort. The good performers managed to better perform the VFT tasks without much effort. Sufficient knowledge and skills as well as the preferred environmental conditions (e.g., blue light exposure) might be the reasons for their success. In parallel research performed with this study, the same behavioral and physiological results were not observed for red light exposure (data not shown).

(ii) The fNIRS changes could be reflected to a significant degree changes in systemic physiology. The finding that the poor performers (with respect to the good performers) showed a large change in fNIRS signals (Fig. 12.1) as well as in systemic physiology (Fig. 12.2) could be interpreted that the stress induced by the poor performers caused a stress reaction, leading to an increase in cardiac output, increasing the MAP and finally an increase in cerebrovascular hemodynamics and oxygenation. That fNIRS signals are affected by systemic physiology has been addressed by our research group in various papers [12–15].

A variety of physiological responses can be elicited in the presence of stressors such as performing a VFT task, e.g., an increase in SC and MAP. This phenomenon was observed more in poor performers during the VFT. Poor stress management and a lack of skills can be the main causes of poor performance under stress [16]. The reason for further increased stress and consequently increased MAP and SC in the poor performers' group could be that they put themselves under higher pressure since they were not pleased with their achievements. Thus, they were more stressed and struggled even more. People are very different in their tendency to experience stress based on their self-confidence, referred to as self-efficacy [17]. Good performance is associated with lower stress and smaller SC and MAP changes, can be due to the high self-efficacy of these performers. People with higher self-efficacy, show less stress in the face of high task demands [18].

In conclusion, this first VFT research employing the SPA-fNIRS method underlines the importance to monitor systemic physiology along with fNIRS measurements. In this study, the relationship between task performance and changes in cerebrovascular oxygenation and systemic physiology was investigated, and it has been shown that these parameters are indeed related and the performance is reflected in cerebrovascular and systemic parameters. The well-aligned brain and systemic physiology data suggest that the better the performance, the less effort was needed by the subjects. Our findings have implications for future functional brain studies involving cognitive tasks.

References

1. Mather N, Gregg N (2001) Assessment with the woodcock-Johnson III. In: Handbook of psychoeducational assessment; ability, achievement, and behavior in children. Academic, pp 133–165
2. Lövdén M, Fratiglioni L, Glymour MM et al (2020) Education and cognitive functioning across the life span. Psychol Sci Public Interest 21:6–41
3. Al-Ayash A, Kane RT, Smith D, Green-Armytage P (2016) The influence of color on student emotion, heart rate, and performance in learning environments. Color Res Appl 41:196–205
4. Scholkmann F, Tachtsidis I, Wolf M, Wolf U (2022) Systemic physiology augmented functional near-infrared spectroscopy: a powerful approach to study the embodied human brain. Neurophotonics 9:030801
5. Zohdi H, Scholkmann F, Wolf U (2021) Individual differences in hemodynamic responses measured on the head due to a long-term stimulation involving colored light exposure and a cognitive task: a SPA-fNIRS study. Brain Sci 11:54
6. Zohdi H, Egli R, Guthruf D et al (2021) Color-dependent changes in humans during a verbal fluency task under colored light exposure assessed by SPA-fNIRS. Sci Rep 11:9654
7. Scholkmann F, Zohdi H, Wolf U (2022) The role of systemic physiology in individual hemodynamic responses measured on the head due to long-term stimulation involving colored light exposure and a cognitive task: an SPA-fNIRS study. Brain Sci 12:597
8. Zohdi H, Natale L, Scholkmann F, Wolf U (2022) Intersubject variability in cerebrovascular hemodynamics and systemic physiology during a verbal fluency task under colored light exposure : clustering of subjects by unsupervised machine learning. Brain Sci 12:1449
9. Aricò P, Borghini G, Di Flumeri G et al (2017) Human factors and neurophysiological metrics in air traffic control: a critical review. IEEE Rev Biomed Eng 10:250–263
10. Bunce SC, Izzetoglu K, Ayaz H et al (2011) Implementation of fNIRS for monitoring levels of expertise and mental workload. In: International conference foundations of augmented cognition, pp 13–22
11. Bracken BK, Festa EK, Sun HM et al (2019) Validation of the fNIRS Pioneer™, a portable, durable, rugged functional near-infrared spectroscopy (fNIRS) device. In: Proceedings of the HEALTHINF 2019—12th international conference on health informatics, proceedings; part of 12th international joint

conference on biomedical engineering systems and technologies, BIOSTEC 2019, pp 521–531
12. Tachtsidis I, Scholkmann F (2016) False positives and false negatives in functional near-infrared spectroscopy: issues, challenges, and the way forward. Neurophotonics 3:031405
13. Scholkmann F, Gerber U, Wolf M, Wolf U (2013) End-tidal CO_2: an important parameter for a correct interpretation in functional brain studies using speech tasks. NeuroImage 66:71–79
14. Caldwell M, Scholkmann F, Wolf U et al (2016) Modelling confounding effects from extracerebral contamination and systemic factors on functional near-infrared spectroscopy. NeuroImage 143:91–105
15. Nasseri N, Caicedo A, Scholkmann F et al (2018) Impact of changes in systemic physiology on fNIRS/NIRS signals: analysis based on oblique subspace projections decomposition. Adv Exp Med Biol 1072:119–125
16. Sarlija M, Popovic S, Jagodic M et al (2021) Prediction of task performance from physiological features of stress resilience. IEEE J Biomed Health Inform 25:2150–2161
17. Tams S, Thatcher JB, Grover V (2018) Concentration, competence, confidence, and capture: an experimental study of age, interruption-based technostress, and task performance. J Assoc Inf Syst 19:857–908
18. Nauta MM, Liu C, Li C (2010) A cross-national examination of self-efficacy as a moderator of autonomy/job strain relationships. Appl Psychol 59:159–179

Part II

Tissue Oxygenation

13 Sex-Specific and Dose-Dependent Effects of Drag-Reducing Polymers on Microcirculation and Tissue Oxygenation in Rats After Traumatic Brain Injury

Denis E. Bragin, Olga A. Bragina, Marina V. Kameneva, Alex O. Trofimov, and Edwin M. Nemoto

Abstract

Traumatic brain injury (TBI) ultimately leads to a reduction in the cerebral metabolic rate for oxygen due to ischemia. Previously, we showed that 2 ppm i.v. of drag-reducing polymers (DRP) improve hemodynamic and oxygen delivery to tissue in a rat model of mild-to-moderate TBI. Here we evaluated sex-specific and dose-dependent effects of DRP on microvascular CBF (mvCBF) and tissue oxygenation in rats after moderate TBI. *In vivo* two-photon laser scanning microscopy over the rat parietal cortex was used to monitor the effects of DRP on microvascular perfusion, tissue oxygenation, and blood-brain barrier (BBB) permeability. Lateral fluid-percussion TBI (1.5 ATA, 100 ms) was induced after baseline imaging and followed by 4 h of monitoring. DRP was injected at 1, 2, or 4 ppm within 30 min after TBI. Differences between groups were determined using a two-way ANOVA analysis for multiple comparisons and post hoc testing using the Mann-Whitney U test. Moderate TBI progressively decreased mvCBF, leading to tissue hypoxia and BBB degradation in the pericontusion zone ($p < 0.05$). The i.v. injection of DRP increased near-wall flow velocity and flow rate in arterioles, leading to an increase in the number of erythrocytes entering capillaries, enhancing capillary perfusion and tissue oxygenation while protecting BBB in a dose-dependent manner without significant difference between males and females ($p < 0.01$). TBI resulted in an increase in intracranial pressure (20.1 ± 3.2 mmHg, $p < 0.05$), microcirculatory redistribution to non-nutritive microvascular shunt flow, and stagnation of capillary flow, all of which were dose-dependently mitigated by DRP. DRP at 4 ppm

D. E. Bragin (✉)
Lovelace Biomedical Research Institute, Albuquerque, NM, USA

Department of Neurology, University of New Mexico School of Medicine, Albuquerque, NM, USA
e-mail: dbragin@lovelacebiomedical.org

O. A. Bragina
Lovelace Biomedical Research Institute, Albuquerque, NM, USA

M. V. Kameneva
McGowan Institute for Regenerative Medicine, University of Pittsburgh, Pittsburgh, PA, USA

A. O. Trofimov
Department of Neurological Diseases, Privolzhsky Research Medical University, Nizhny Novgorod, Russia

E. M. Nemoto
Department of Neurology, University of New Mexico School of Medicine, Albuquerque, NM, USA

F. Scholkmann et al. (eds.), *Oxygen Transport to Tissue XLIV*, Advances in Experimental Medicine and Biology 1438, https://doi.org/10.1007/978-3-031-42003-0_13

was most effective, with a non-significant trend to better outcomes in female rats.

Keywords

Cerebral blood flow · Drag-reducing polymers · Microvascular flow · NADH autofluorescence · Intracranial pressure · Traumatic brain injury · Microcirculation · Tissue oxygenation

13.1 Introduction

Traumatic brain injury (TBI) is a significant health problem, responsible for a third of all injury-related deaths and 70% of disabilities [1]. Decades of TBI research focused almost exclusively on neuroprotective strategies have failed to develop any therapeutics for clinical treatment. One less explored potential target is cerebral microcirculation (mvCBF). Recent studies suggest that the peri-contusional and diffuse injury areas represent salvageable tissue where diffusional hypoxia and nutrient deprivation occur at the microcirculation level, much like the penumbra in stroke [2]. We recently proposed a modulation of hemodynamics by blood-soluble drag-reducing polymers (DRP) as a novel treatment modality for TBI that specifically targets cerebral microcirculation based on physical but not pharmacological principles. Nanomolar concentrations of intravascular blood soluble drag-reducing polymers (DRP) were shown to increase tissue perfusion and oxygenation and decrease peripheral vascular resistance by rheological modulation of hemodynamics. The greatest impact of the DRP-enhanced flow is at the level of the microcirculation and capillaries, where the shear rate is highest [3]. We hypothesized that drag-reducing polymers (DRPs) would improve mvCBF and reduce tissue hypoxia in TBI and have proven it experimentally [4]. In this work, we evaluated the dose-dependent efficacy of DRP (1, 2, and 4 ppm) in the treatment of post-TBI ischemia using a rat lateral fluid percussion injury model of moderate TBI. We have shown that at 4 ppm, the drag-reducing effect is near the plateau (unpublished data). Since an increasing body of evidence suggests that cerebral blood flow differs between males and females in the intact and injured brain, we dissected possible sex-dependent effects.

13.2 Methods

13.2.1 Study Design

The procedures used in the study have already been described [3] and were conducted according to the approval granted by the Institutional Animal Care and Use Committee of the Lovelace Biomedical Research Institute under Protocol #20034. In-vivo two-photon laser scanning microscopy over the rat parietal cortex was used to monitor the dose-dependent effects of DRP on microvascular perfusion, tissue oxygenation (NADH) and blood-brain barrier permeability in male and female rats subjected to moderate TBI. Lateral fluid-percussion TBI was induced after baseline imaging and followed by 4 h of monitoring. DRP was injected at 1, 2, or 4 ppm within 30 min after TBI induction. Brain and rectal temperatures, mean arterial (MAP) and intracranial pressures (ICP), blood gases and electrolytes were monitored.

For DRP preparation, polyethylene oxide (PEO, MW ~4000 kDa) was dissolved in saline to 0.1% (1000 ppm), dialyzed against saline using a 50 kD cutoff membrane, diluted in saline to 50 ppm, slow rocked for ~2 h and sterilized using a 0.22 μm filter [4].

13.2.2 Surgical Preparation

Acclimatized male Sprague-Dawley rats (250–300 g) were mechanically ventilated on isoflurane (2%) in a mix of nitrous oxide (69%) and oxygen (29%) anesthesia. The femoral artery and venous, and intracranial catheters were inserted. For TBI and imaging, a craniotomy (5 mm) over the left parietal cortex was filled with agarose in saline (2%) and sealed by a cover glass. The fluid percussion TBI was induced by a pulse from the

Pneumatic Impactor connected to the brain through a transducer filled with artificial cerebrospinal fluid (1.5 ATA, 100 ms).

13.2.3 Two-Photon Laser Scanning Microscopy

Fluorescent serum (tetramethylrhodamine isothiocyanate (TAMRA) dextran, 500 kDa in physiological saline, 5% wt/vol) was visualized using an Olympus BX 51WI upright microscope and water-immersion LUMPlan FL/IR 20X/0.50 W objective. Excitation was provided by a PrairieView Ultima multiphoton microscopy laser scan unit powered by a Millennia Prime 10 W diode laser source pumping a Tsunami Ti: Sapphire laser (Spectra-Physics, Mountain View, CA, USA) tuned to 750 nm center wavelength. Band-pass-filtered epifluorescence (560–660 nm for TAMRA and 425–475 nm for NADH) was collected by photomultiplier tubes of the Prairie View Ultima system. Images (512 × 512 pixels, 0.15 um/pixel in the x- and y-axes) or line scans were acquired using Prairie View software. Red blood cell flow velocity was measured in microvessels ranging from 3–50 μm diameter up to 500 μm below the surface of the parietal cortex, as previously described [4]. Tissue hypoxia was assessed by measurement of NADH autofluorescence and BBB permeability by TAMRA transcapillary extravasation. In offline analyses using NIH ImageJ software, three-dimensional anatomy of the vasculature in areas of interest was reconstructed from two-dimensional (planar) scans of the fluorescence intensity obtained at successive focal depths in the cortex (XYZ stack).

13.2.4 Statistical Analysis

Statistical analyses were done by Student's t-test or Kolgomorov-Smirnov test where appropriate using GraphPad Prism 9 (GraphPad Software, Inc., San Diego, CA). Differences between groups were determined using a two-way ANOVA analysis for multiple comparisons and post hoc testing with the significance level was preset to $p < 0.05$.

13.3 Results

At a baseline, we observed intact microcirculation with a capillary flow velocity of 0.81 ± 0.04 and 0.82 ± 0.05 mm/s and the number of perfused capillaries per 0.075 mm^3 of 211 ± 17 and 215 ± 18 in male and female rats, respectively (Fig. 13.1a, b). ICP was also within the normal range without differences between male and female rats, 8.1 ± 0.7 and 8.5 ± 0.6 mm Hg, respectively (Fig. 13.1c).

Moderate TBI progressively decreased microvascular circulation (capillary flow velocity and the number of perfused capillaries), leading to tissue hypoxia in the pericontusion zone (Fig. 13.1a–c, $p < 0.05$). The i.v. injection of DRP increased near-wall flow velocity and flow rate in arterioles, leading to an increase in the number of erythrocytes entering capillaries, enhancing capillary perfusion and restoring perfusion in collapsed capillaries in a dose-dependent manner without significant differences between males and females (Fig. 13.1a–c, $p < 0.05$). At the end of the monitoring period, capillary flow velocity was 0.57 ± 0.06, 0.63 ± 0.05, 0.66 ± 0.06, and 0.72 ± 0.06 mm/sec in male rats and 0.59 ± 0.04, 0.63 ± 0.05, 0.67 ± 0.06 and 0.73 ± 0.06 mm/s in female rats with saline, DRP 1 ppm, 2 ppm and 4 ppm treatment, respectively (Fig. 13.1a, $p < 0.05$ between DRP and saline treatments). At the same time, the number of perfused capillaries per 0.075 mm^3 was 150 ± 18, 165 ± 14, 173 ± 15 and 190 ± 19 in male rats and 155 ± 14, 164 ± 15, 175 ± 15 and 190 ± 18 in female rats with saline, DRP 1 ppm, 2 ppm and 4 ppm treatment, respectively (Fig. 13.1b, $p < 0.05$ between DRP and saline treatments). Microcirculation improvement after DRP treatment led to tissue oxygen supply enhancement. By the end of the monitoring period, NADH, inversely reflecting mitochondrial respiration and tissue oxygenation, was 1.29 ± 0.11, 1.21 ± 0.12, 1.18 ± 0.12 and 1.15 ± 0.13 a.u. in male rats and 1.26 ± 0.14, 1.18 ± 0.11, 1.14 ± 0.10 and 1.12 ± 0.11 a.u. in

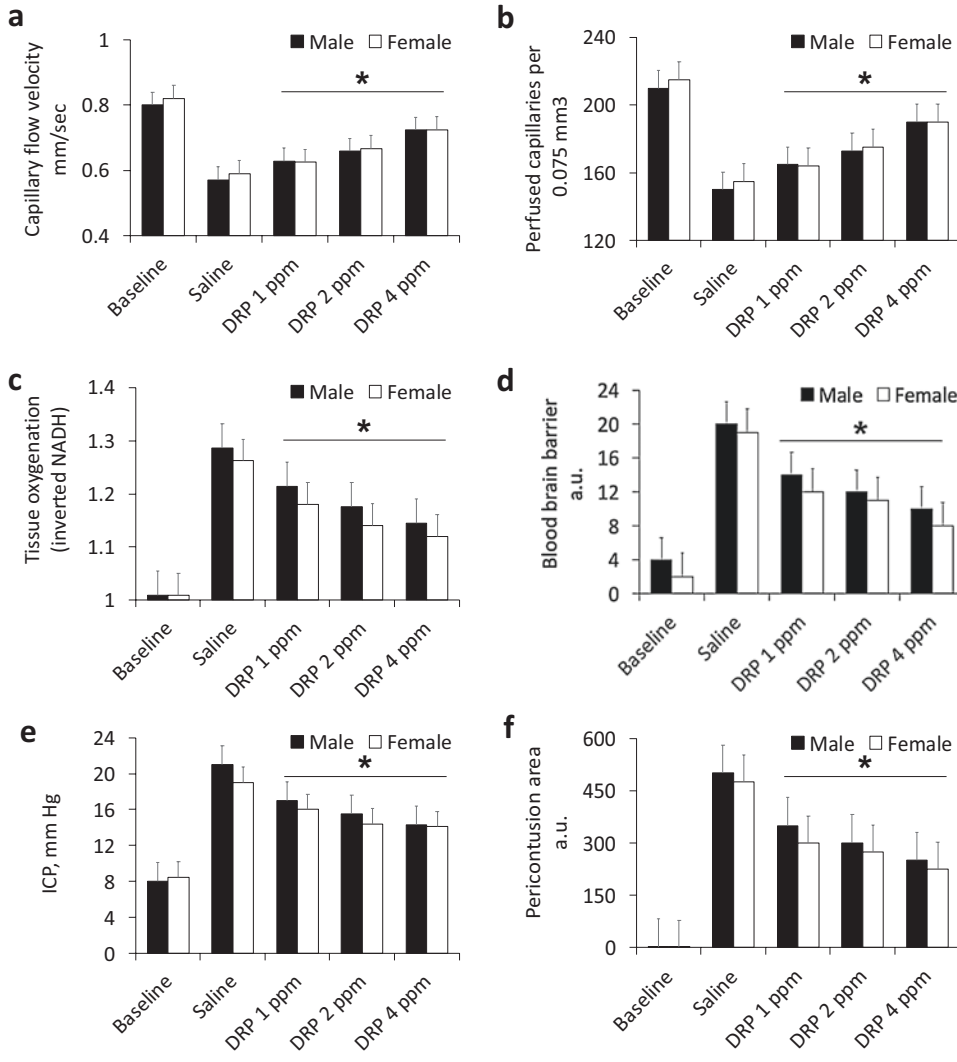

Fig. 13.1 Sex-specific and dose-dependent effects of DRP on (**a**) Capillary flow velocity; (**b**) Number of perfused capillaries; (**c**) Tissue oxygenation status (NADH); (**d**) Blood-brain barrier; (**e**) Intracranial pressure; and (**f**) Pericontusion area. Mean ± SEM, $N = 10$ rats per group, *$p < 0.05$

female rats with saline, DRP 1 ppm, 2 ppm and 4 ppm treatment, respectively (Fig. 13.1c, $p < 0.05$ between DRP and saline treatments).

TBI led to BBB breakdown, reflected by TAMRA extravasation, which was reduced by DRP in a dose-dependent manner (Fig. 13.1d, $p < 0.05$). At the end of the monitoring period, the extravascular fluorescence was 20.1 ± 1.1, 14.0 ± 1.2, 12.2 ± 1.3 and 10.1 ± 1.3 a.u. in male rats and 19.0 ± 1. 4, 12.3 ± 1.3, 11.2 ± 1.1 and 8.4 ± 1.0 a.u. in female rats with saline, DRP 1 ppm, 2 ppm and 4 ppm treatment, respectively (Fig. 13.1d, $p < 0.05$ between DRP and saline treatments). Increased BBB permeability presumably led to vasogenic edema, reflected by an increase in ICP, mitigated by DRP in a dose-dependent manner (Fig. 13.1e, $p < 0.05$). The ICP was 21.1 ± 1.4, 17.2 ± 1.3, 15.5 ± 1.4 and 14.3 ± 1.2 mm Hg in male rats and 19.1 ± 1. 4, 16.2 ± 1.2, 14.4 ± 1.3 and 14.1 ± 1.1 mm Hg in female rats with saline, DRP 1 ppm, 2 ppm and 4 ppm treatment, respectively (Fig. 13.1e,

$p < 0.05$ between DRP and saline treatments). Reduced by DRP vasogenic and, probably, cytogenic edema, reflected by a decrease in BBB breakdown and ICP build-up, led to a reduction in a pericontusion area, which by the end of the study was 504 ± 36.2, 352 ± 21.5, 313 ± 33.4 and 254 ± 18.9 a.u. in male rats and 475 ± 34. 4, 302 ± 31.3, 274 ± 28.4 and 226 ± 21.1 a.u in female rats with saline, DRP 1 ppm, 2 ppm and 4 ppm treatment, respectively (Fig. 13.1f, $p < 0.05$ between DRP and saline treatments).

13.4 Discussion

We demonstrated a dose-dependent efficacy of DRP (1, 2 and 4 ppm) in the treatment of post-TBI pericontusion ischemia in a rat lateral fluid percussion injury model of TBI. The i.v. injection of DRP increased near-wall flow velocity and flow rate in arterioles, leading to an increase in the number of erythrocytes entering capillaries, enhancing capillary perfusion and tissue oxygen supply in a dose-dependent manner. Treatment with DRPs effectively mitigated an increase in ICP, and protected BBB from degradation.

We did not find a statistically significant sex-specific difference in response to TBI or DRP, which does not necessarily contradict several studies observing significantly better outcomes in female animals as this is an acute study without long term survival [5–8]. However, there was a clear trend in better-preserved tissue oxygen supply, BBB permeability, intracranial pressure and pericontusion area in females (Fig. 13.1c–f), which corresponds to works, also reporting notable but insignificant sex-dependent difference suggesting better outcomes in female animals [7]. Considering the current body of research on sex differences in TBI, the overall picture is not a straightforward one that points to better outcomes in one sex versus the other, and the findings are complicated and often contradictory [8]. A closer examination of the sex-dependent responses to TBI and TBI treatment will provide new insights that will move the field forward in a meaningful way.

Acknowledgments Supported by NIH R01NS112808.

References

1. Faul M, Xu L, Wald MM et al (2010) Traumatic brain injury in the United States: Emergency Department Visits, Hospitalizations and Deaths Atlanta, GA2010. Available from: http://braininjury.blogs.com/brain-injury/2010/03/cdc-releases-latest-statistics-on-traumatic-brain-injury.html
2. Veenith TV, Carter EL, Geeraerts T et al (2016) Pathophysiologic mechanisms of cerebral ischemia and diffusion hypoxia in traumatic brain injury. JAMA Neurol 73(5):542–550
3. Papaioannou TG, Stefanadis C (2005) Vascular wall shear stress: basic principles and methods. Hell J Cardiol 46:9–15
4. Bragin DE, Kameneva MV, Bragina OA et al (2017) Rheological effects of drag-reducing polymers improve cerebral blood flow and oxygenation after traumatic brain injury in rats. J Cereb Blood Flow Metab 37(3):762–775. https://doi.org/10.1177/0271678X16684153
5. O'Connor CA, Cernak I, Vink R (2006) The temporal profile of edema formation differs between male and female rats following diffuse traumatic brain injury. Acta Neurochir Suppl 96:121–124. https://doi.org/10.1007/3-211-30714-1_27
6. Rubin TG, Lipton ML (2019) Sex differences in animal models of traumatic brain injury. J Exp Neurosci 13(13):1179069519844020. https://doi.org/10.1177/1179069519844020
7. Scott MC, Prabhakara KS, Walters AJ et al (2022) Determining sex-based differences in inflammatory response in an experimental traumatic brain injury model. Front Immunol 9(13):753570. https://doi.org/10.3389/fimmu.2022.753570
8. Gupte R, Brooks W, Vukas R et al (2018) Sex differences in traumatic brain injury: what we know and what we should know. J Neurotrauma 36(22):3063–3091. https://doi.org/10.1089/neu.2018.6171

14 Accuracy of Tissue Oxygen Saturation Measurements of a Textile-Based NIRS Sensor

Tarcisi Cantieni, Oliver da Silva-Kress, and Ursula Wolf

Abstract

Pressure injuries (PI) are dangerous tissue lesions that heal very slowly and pose a high risk of serious infections. They are caused by pressure applied to the tissue, which stops blood circulation and therefore induces hypoxia, i.e., low tissue oxygen saturation (StO_2). PI cause severe suffering and are expensive to treat. Hence it is essential to prevent them with a device that detects a dangerous situation, e.g., by measuring StO_2 using near-infrared spectroscopy (NIRS). For such a device to be wearable without causing PI, it must not introduce pressure points itself. This can be achieved by integrating optical fibers into a textile to transport light to and from the tissue.

The aim of this paper is to investigate the accuracy of StO_2 measurements using a NIRS device based only on textile-integrated optical fibers.

Bundles of fibers were stitched into a textile in such a way that loops of <1 mm diameters were formed at the stitching locations. Detection points (DPs) on the fabric consisted of 8 fibers with 3 loops each. Emission points (EPs) were made from 4 fibers with 3 loops each. All fiber ends of a DP were connected to an avalanche photodiode. One end of each fiber belonging to an EP was connected to an LED (740 nm, 810 nm, or 880 nm; 290, 560, or 610 mW).

To verify the accuracy of this textile-based sensor, we placed it on a subject's forearm and compared the derived StO_2 during arterial occlusion to the values of a gold-standard NIRS device (ISS Imagent), which was placed on the forearm too.

We found that our textile-based sensor repeatedly measured StO_2 values over a range of 40% with a deviation of <10% from the reference device.

By showing the ability to measure StO_2 using textile-integrated optical fibers accurately, we have reached a significant milestone on our way to building a wearable device to monitor tissue health and prevent PI.

Keywords

Tissue oxygenation · Textile-based NIRS sensor · Near-infrared spectroscopy

14.1 Introduction

Hypoxia can lead to tissue necrotization and thus plays a vital role in pressure injury (PI) development [1]. Hypoxia results from localized pressure

T. Cantieni (✉) · O. da Silva-Kress · U. Wolf
Institute of Complementary and Integrative Medicine, University of Bern, Bern, Switzerland
e-mail: tarcisi.cantieni@unibe.ch

F. Scholkmann et al. (eds.), *Oxygen Transport to Tissue XLIV*, Advances in Experimental Medicine and Biology 1438, https://doi.org/10.1007/978-3-031-42003-0_14

on the tissue, which impedes blood circulation. Because PI are a severe problem for the individual and the health care system [2], it is essential to improve PI prevention. This can be accomplished by measuring tissue oxygen saturation (StO_2) [3] using near-infrared spectroscopy (NIRS) in body areas that are exposed to prolonged pressure. For a device to be applicable in such sites, it must not induce pressure points itself. The solution to achieve this is to use a textile-based NIRS sensor.

In this work, the signal-to-noise ratio and the accuracy of measurements made by such a sensor are investigated.

14.2 Materials and Methods

The textile-based sensor used is shown in Fig. 14.1a. It consists of 4 emission points (EP) in the center and 8 detection points (DP) in the outer ring. Optical coupling by the EP/DP to the tissue is accomplished by looping optical fibers in a tight radius to overcome the total internal reflection to leave/enter light from/to the fibers. Each EP/DP comprises 8 fibers with 3 loops each. For DPs, all 16 fiber ends are connected to an avalanche photodiode (APD), while for the EPs, 4 fiber ends are connected to an LED. Consequently, each EP is connected to 3 LEDs of different wavelengths. The red circles in Fig. 14.1a indicate the 4 DPs and 3 EPs used.

The hardware to which the textile-based sensor was connected to consists of time-multiplexed APDs and LEDs (740 nm, 810 nm, or 880 nm; 290, 560, or 610 mW; due to coupling losses only ~10% of the intensity enters the fibers and this intensity fulfills the safety regulations for incoherent light).

Measurements on a muscle phantom were performed to assess the sensor's capabilities and signal-to-noise ratio (SNR). The muscle phantom's absorption coefficient was 0.1 cm^{-1} for all wavelengths, and the reduced scattering coefficient was 6.8 cm^{-1} for 740 nm and 6.0 cm^{-1} for 810 and 880 nm.

To test the textile-based sensor's accuracy, an arterial occlusion test protocol was established, in which the textile-based sensor was compared to an industry-standard frequency-domain NIRS device (Imagent, ISS Inc.). In this protocol, the pressure cuff was placed on the upper arm, while the textile-based sensor and the reference sensor were placed as closely as possible on the forearm. The protocol consisted of 1 min baseline measurement followed by 2.5 min arterial occlu-

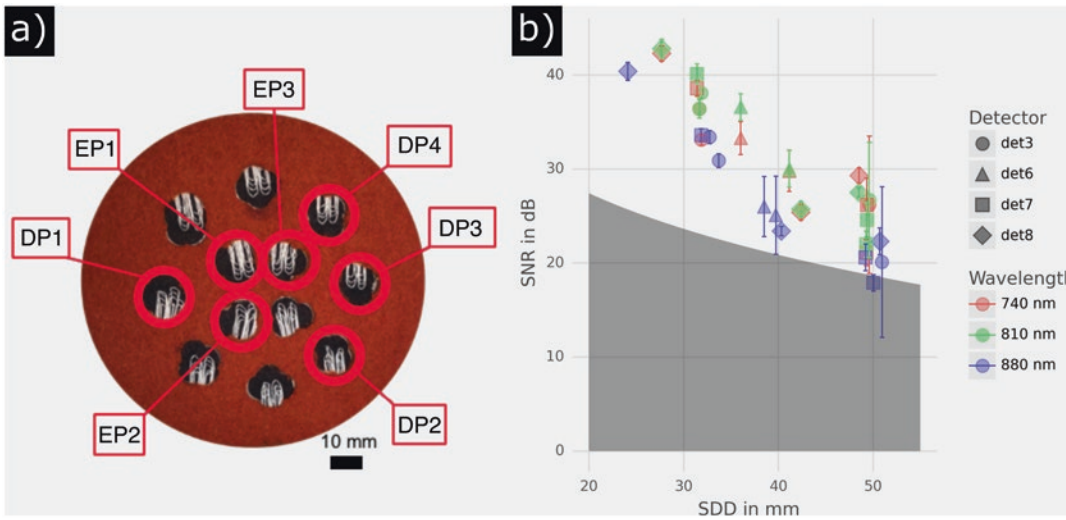

Fig. 14.1 (**a**) Textile-based NIRS sensor. Connected EPs and DPs used in this work are circled red and labeled. (**b**) Measured signal-to-noise ratio of textile-based NIRS sensor for three wavelengths

sion at 250 mmHg. After StO_2 values had returned to baseline levels after ~2.5–3 min, the arterial occlusion was repeated.

A total of 7 measurements were performed on 4 different subjects. Our setup enabled to measure ΔStO_2 using 18 configurations simultaneously (when using 2 wavelengths per configuration).

To quantify the comparison of the textile-based sensor with the reference: First, the ΔStO_2 was calculated for every configuration and measurement using the modified Beer-Lambert law at two wavelengths, assuming an initial O_2Hb of 0.03 mM and tHb of 0.04 mM (values in agreement with [4]). The resulting time curve was then fitted to the corresponding curve of the reference device. The parameter used for this fitting procedure was the differential pathlength factor (DPF). The fitting method yielded the optimal DPF per wavelength for each configuration. The average DPF per wavelength and source-detector distance (SDD; bins: <30 mm, 30–35 mm, 35–45 mm, >45 mm) of all those fits was calculated (realistic DPF values range between 2 and 10 according to the literature [5]; consequentially, fit values that came to lie outside this range were omitted). For those average DPF values, ΔStO_2 was recalculated, and all curves were compared to the reference device according to [6].

For a device to ultimately prevent PI, as described in the introduction, it needs to be able to measure absolute StO_2 values. Using principles of the spatially resolved spectroscopy [7] and the self-calibrating algorithm [8], the data were used to calculate such absolute StO_2 values and compared to the reference device.

14.3 Results and Discussion

The textile-based sensor, in combination with the electronic components, shows very good SNR for distances up to 40 mm and for the 740 nm and 810 nm wavelengths even beyond, as can be seen in Fig. 14.1b. The shaded area in this plot represents the minimal required SNR as described in [9]. The systematic difference between the wavelengths can be explained by the different amounts of power of the LEDs in combination with the spectral sensitivity of the APD.

Our measurements show the ability of the textile-based sensor to measure ΔStO_2 with a high degree of accuracy.

The fitting methodology produced SDD-independent DPFs (mean ± SD) of 3.6 ± 0.6, 3.6 ± 0.5 and 3.8 ± 0.5 for 740 nm, 810 nm, and 880 nm, respectively, in good agreement with literature values for the human forearm [5].

Looking at the data set produced with those DPFs of the comparisons in Fig. 14.2a, one can see that up to 40 mm, an average precision of well below 10% is achieved for the textile-based sensor. 10% is a limit that the ISO norm for cerebral tissue oximetry [6] demands, a norm that does not directly apply but can serve to orient. Furthermore, it is not surprising that the applied approach results in a bias close to zero, but the approach does expose the outliers. The observed SDD dependency corresponds well with the measured SNRs above.

Figure 14.2b top shows the comparison of the calculated ΔStO_2 values of the textile-based sensor with the reference device. Figure 14.2b bottom shows the Altman-Bland plot of the same comparison. This plot also shows the accuracy and bias parameters used to quantify these comparisons.

The absolute StO_2 values showed a good correlation with the reference device. However, as the calculation of the absolute values included 4 signals of an SDD of more than 40 mm, the resulting StO_2 values were strongly afflicted by noise. The strong filtering consequently required resulted in an offset in StO_2 levels.

14.4 Conclusion

In conclusion, we found the textile-based NIRS sensor to accurately measure changes in tissue oxygenation for SDDs of up to 40 mm. Furthermore, we found the sensor to be able to measure absolute tissue oxygenation and are confident that minor modifications in the sensor design, in combination with improvements to fiber bundling and connections, will enable us to measure absolute tissue oxygenation with high accuracy.

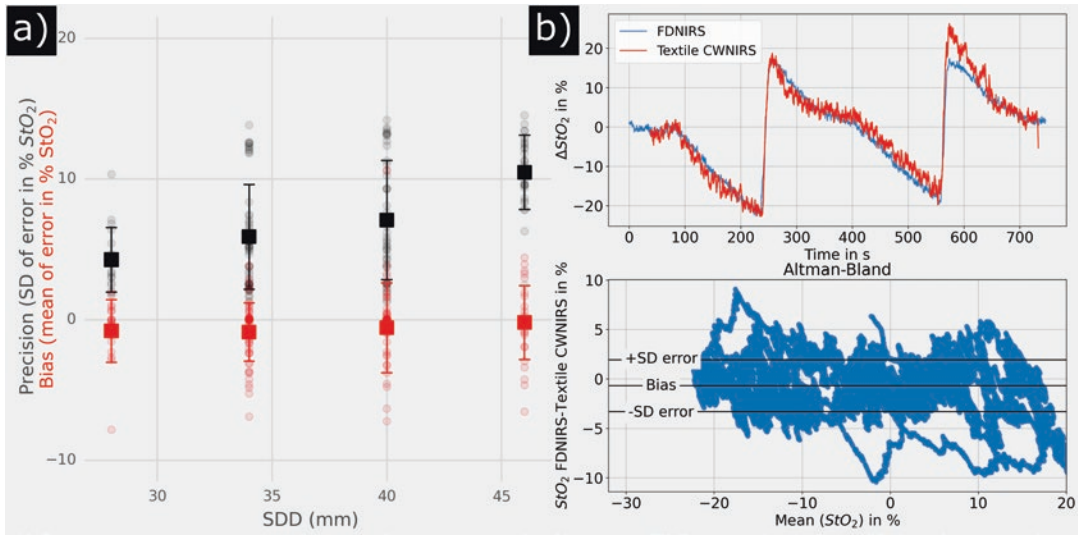

Fig. 14.2 (**a**) Precision and bias calculated from a comparison of textile-based NIRS sensor with industry-standard frequency-domain NIRS device (faded individual points stand for individual measurement configurations while solid squares and brackets stand for the mean and standard deviation of configurations in the respective bins). (**b**) Top: ΔStO_2 comparison of textile-based NIRS sensor to the reference device. Measured over an SDD of 42 mm. Bottom: Altman-Bland plot of the same comparison. The standard deviation of error is shown together with bias

A comfortable and long-time wearable NIRS sensor to measure absolute tissue oxygenation will be a milestone in pressure injury prevention and research.

Acknowledgments We gratefully acknowledge funding of the project by the SNSF and Innosuisse Bridge Discovery (project no. 180983).

References

1. Berg G, Nyberg S, Harrison et al (2010) Near-infrared spectroscopy measurement of sacral tissue oxygen saturation in healthy volunteers immobilized on rigid spine boards. Prehosp Emerg Care 14:419–424
2. Mortenson WB, Miller WC (2008) A review of scales for assessing the risk of developing a pressure ulcer in individuals with SCI. Spinal Cord 46:168–175
3. Damert H-G, Meyer F, Altmann S (2015) Therapieoptionen bei Dekubitalulzera. Zentralblatt für Chirurgie Zeitschrift für Allgemeine Viszeral- Thorax- und Gefäßchirurgie 140:193–200
4. Lutjemeier BJ, Ferreira LF, Poole DC et al (2008) Muscle microvascular hemoglobin concentration and oxygenation within the contraction–relaxation cycle. Respir Physiol Neurobiol 160:131–138
5. van der Zee P, Cope M, Arridge SR et al (1992) Experimentally measured optical pathlengths for the adult head, calf, and forearm and the head of the newborn infant as a function of inter optode spacing. Adv Exp Med Biol 316:143–153
6. ISO 80601-2-85:2021 (2021) Medical electrical equipment—part 2-85: particular requirements for the basic safety and essential performance of cerebral tissue oximeter equipment. https://www.iso.org/standard/72442.html
7. Suzuki S, Takasaki S, Ozaki T et al (1999) Tissue oxygenation monitor using NIR spatially resolved spectroscopy. Opt Tomogr Spectrosc Tissue III 3597:582–592
8. Hueber DM, Fantini S, Cerussi AE et al (1999) New optical probe designs for absolute (self-calibrating) NIR tissue hemoglobin measurements. In: Proceedings of SPIE 3597, optical tomography and spectroscopy of tissue III, vol 3597, pp 618–631
9. Pagano R, Libertino S, Sanfilippo D et al (2016) Improvement of sensitivity in continuous wave near infrared spectroscopy systems by using silicon photomultipliers. Biomed Opt Express 7(4):1183–1192

15 Understanding the Role of Caveolae in Oxygen Buffering: The Effect of Membrane Curvature

Samaneh Davoudi, Qi Wang, Hemal H. Patel, Sally C. Pias, and An Ghysels

Abstract

The "oxygen paradox" can be explained as two opposing biological processes with oxygen (O_2) as a reactant. On the one hand, oxygen is essential to aerobic metabolism, powering oxidative phosphorylation in mitochondria. On the other hand, an excess supply of oxygen will generate reactive species which are harmful for the cell. In healthy tissues, the first process must be maximized relative to the second one. We have hypothesized that curved and cholesterol-enriched membrane invaginations called caveolae help maintain the proper oxygen level by taking up oxygen and attenuating its release to the mitochondria. The mechanism by which caveolae may help to buffer the oxygen level in cells is still unclear. Here, we aim to assess how structural aspects of caveolae, the curvature of the membrane, influence the local oxygen abundance and the membrane partitioning. We have modelled a flat bilayer and a liposome composed of dipalmitoylphosphatidylcholine (DPPC), using molecular dynamics simulation. Associated changes in the membrane-level oxygen partition coefficient and free energy profiles will be presented.

Keywords

Caveolae · Oxygen buffering · Molecular dynamics simulation · Oxygen supply

15.1 Introduction

Oxygen is a vital for life, yet it can be toxic at the same time, known as the "oxygen paradox" [1, 2]. This molecule is necessary to the metabolic machinery of a living cell by fueling oxidative phosphorylation in the process of cellular energy generation [1, 2]. However, in a high concentration, it can generate reactive species which leads to the cellular damage [3]. It is suggested that during evolution, the response to this paradox was creating cholesterol inside the membrane to control the concentration of oxygen which are inside the cell and minimize its toxicity [4]. Caveolin, a scaffold protein, plays an important role in controlling the oxygen concentration by regulating caveolae, cholesterol enriched microdomains in the plasma membrane [5, 6]. Caveolae

S. Davoudi (✉) · A. Ghysels
IBiTech – Biommeda Research Group, Ghent University, Ghent, Belgium
e-mail: samaneh.davoudi@ugent.be

Q. Wang · S. C. Pias
Department of Chemistry, New Mexico Institute of Mining and Technology (New Mexico Tech), Socorro, NM, USA

H. H. Patel
Department of Anesthesiology, University of California, San Diego, CA, USA

F. Scholkmann et al. (eds.), *Oxygen Transport to Tissue XLIV*, Advances in Experimental Medicine and Biology 1438, https://doi.org/10.1007/978-3-031-42003-0_15

have been proposed to function as "oxygen capacitors", or storage sites, to optimize cellular metabolic function and promote stress adaptation [7]. With aging, the expression of the caveolin protein decreases in some organs, and it may be associated with increased oxygen toxicity and related disease [8]. Manipulating caveolin protein levels within cells has therapeutic potential for treating oxygen related disorders such as cardiovascular diseases, cancer, and aging.

However, the role of caveolin in the plasma membrane and the mechanism by which it regulates oxygen levels in cells are not yet clear. Simulations, especially molecular dynamics (MD), have made it more feasible to examine oxygen transport at the molecular scale, such as the permeation through the phospholipid bilayers [9–12]. In this paper, we use MD simulations to investigate how a key structural aspect of caveolae, i.e., membrane curvature, may affect oxygen partitioning into the membrane. Two DPPC bilayers with different curvature are simulated at the atomic scale: a flat bilayer with zero curvature and a curved bilayer forming a spherical particle (liposome) with very high curvature. The results feature partition coefficient and free energy profiles for oxygen, spanning the membrane.

15.2 Methods

Two systems with DPPC lipids were simulated using the Gromacs-2021.4 [13]: a flat bilayer consisting of 128 lipids (Fig. 15.1 right) and a 50 Å-radius liposome consisting of 518 lipids (Fig. 15.1 middle). A detailed description of the systems can be found in Table 15.1. Both systems were simulated using all-atom MD. For the system with a liposome, we first generated the model as a coarse-grained structure with CHARMM-GUI [14]. Then, the Martini backmapping tool was used to convert the coarse-grained model to an all-atom one [15]. The two systems were simulated at 323 K, coupled to velocity rescale thermostats with a coupling constant of 1.0 ps [16]. The Parrinello–Rahman barostat was employed to couple the pressure in the system with the flat bilayer, while the system with the liposome was coupled with the Berendsen barostat. Periodic

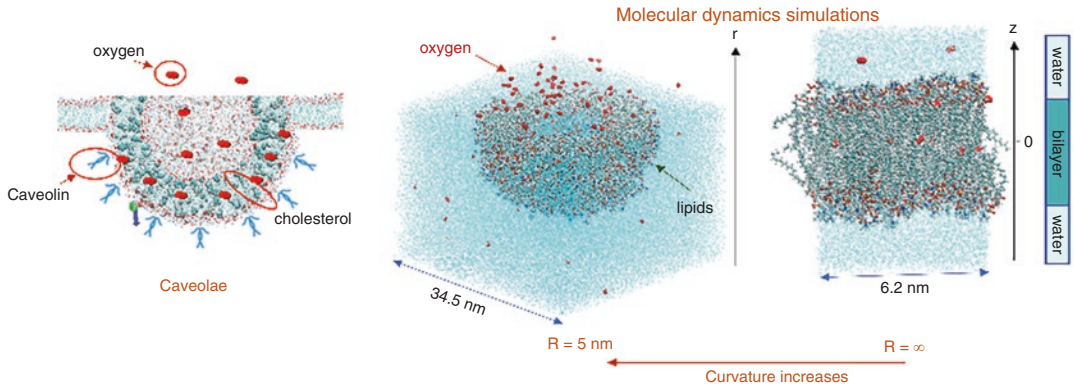

Fig. 15.1 Left: the schematic picture of caveolae. Middle: the system with a liposome, only the lower part is shown. Right: the system with the flat bilayer

Table 15.1 The detailed description of the two systems: flat bilayer and liposome

Systems	# Lipid	# Water	# O_2	Thickness (nm)	Area per lipid (nm^2)		<K>
					Inside layer	Outside layer	
Flat bilayer	128	6341	18	4.02	0.61		4.06
Liposome	518	78,804	164	3.06	0.65	1.02	3.95

boundary conditions were applied in all three dimensions and the box vectors were subjected to semi-isotropic pressure coupling (flat bilayer) or isotropic pressure coupling (liposome), using a reference pressure of 1 bar, a coupling parameter of 5 ps, and an isothermal compressibility of 3×10^{-4} bar^{-1} and 4.5×10^{-4} bar^{-1}. The coordinates were saved every 2 ps. The particle mesh Ewald approach was employed to calculate the Coulombic interactions. At the cutoff of 1.2 nm, the Coulombic and the van der Waals potentials were shifted to zero using force-switch modifiers. CHARMM36 forcefield was implemented to model the lipid and oxygen molecules [17]. Water was modeled by applying the TIP3P model [18]. Using the Verlet neighbor search algorithm, the neighbor list length was updated at 1.2 nm. The equation of motion was integrated with a time step of 2 fs, using the leapfrog integrator. At every time step, the center of mass motion of the system was removed. After adding oxygen molecules at a concentration of 86 μM, an energy minimization was performed, followed by a 50 ns equilibration and 200 ns production run with constant pressure and constant temperature (NPT ensemble).

15.3 Results

15.3.1 Effect of Curvature on Membrane Thickness and Area per Lipid

The thickness of the membranes was determined by measuring the distance between the two highest peaks in the histogram of the phosphates *z*-coordinates. The results (Table 15.1) indicate that the thickness of the flat bilayer at a temperature of 323 K and at a pressure of 1 bar is 4.02 nm, which is consistent with the experimental value of 3.9 nm [19]. Increasing the membrane's curvature reduces the membrane thickness, to 3.06 nm. The opposite trend occurs with the area per lipid. To calculate the area per lipid for the flat bilayer, the area of the box in the *xy* direction was divided by the number of the lipids in one leaflet. For the liposome, two areas per lipid (inside and outside) were computed, dividing the area of each layer by the number of the lipids in that layer. The highest peaks in the phosphate atoms' histogram were chosen as radii to calculate the areas of the leaflets. As shown in Table 15.1, the area per lipid in the outer lipid layer of the liposome, 1.02 nm^2, was almost twice the flat bilayer's area per lipid, 0.61 nm^2. The area per lipid for the liposome's inner layer, 0.65 nm^2, was close to that of the flat bilayer and to the experimental value at 323 K and 1 bar, namely 0.63 nm^2 [19].

15.3.2 Effect of Curvature on Oxygen Free Energy Profile

The oxygen free energy profile in both the flat bilayer and the liposome were plotted in Fig. 15.2 as a function of the membrane depth, also called permeation coordinate. For the flat bilayer, this is the normal to the membrane, i.e., the *z*-coordinate (Fig. 15.1 right). For the curved membrane, this is the radial distance *r* from the liposome center (Fig. 15.1 center). The relatively small size of the liposome results in poor statistics in the water phase inside the liposome (as seen in Fig. 15.2, right). As can be observed in Fig. 15.2, for the liposome, oxygen prefers to stay in the lipid part of the membrane, with two free energy wells, rather than in the middle part of two leaflets compared to the flat bilayer, with one free energy well. This preference may be a consequence of the decrease in the membrane thickness. Additionally, the barrier that oxygen needs to overcome to reach the water phase from the membrane's outer leaflet was reduced from 3 k_BT to 2 k_BT, where k_B represents Boltzmann constant.

15.3.3 Effect of Curvature on Oxygen Partition Coefficient

To calculate the oxygen partition coefficient (K) through the membrane, the free energy was set to zero in the water phase. K was calculated along the permeation direction for both systems using $\Delta F = k_BT \ln K$. As depicted in Fig. 15.3 left, oxy-

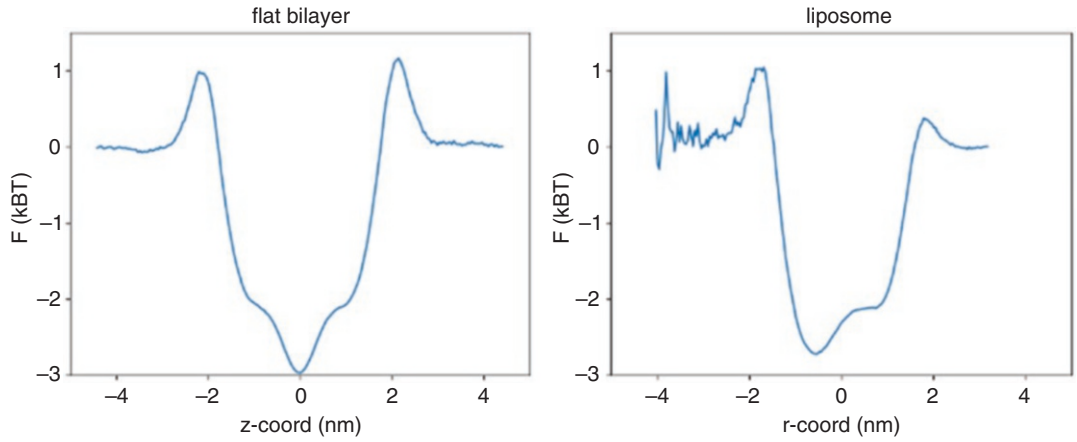

Fig. 15.2 The oxygen free energy profile as a function of the permeation coordinate of the flat bilayer (z, left) or the liposome (r, right)

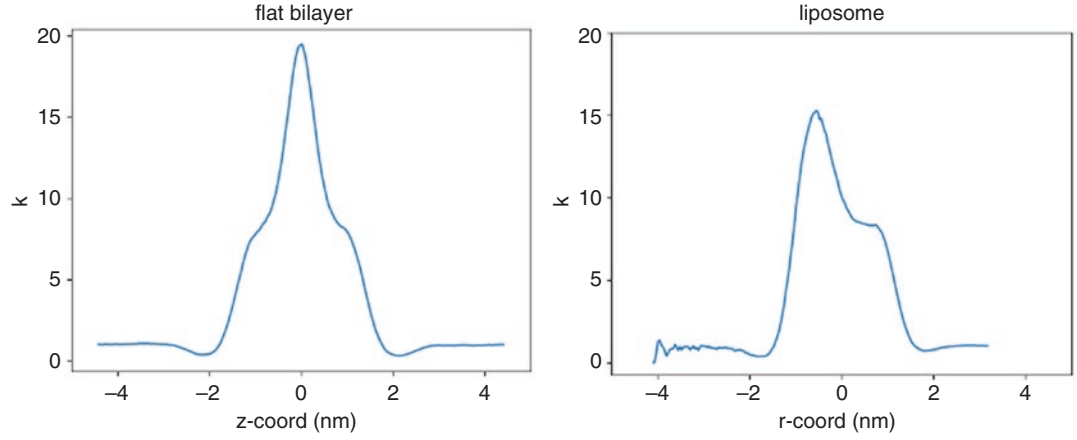

Fig. 15.3 The oxygen partition coefficient profile as a function of the permeation coordinate of the flat bilayer (z, left) or the liposome (r, right)

gen is more soluble in the mid-membrane than the water phase, which is expected. This behavior is slightly altered with an increase in the curvature, with the highest solubility observed in both lipid phases. As the area per lipid is smaller for the inner leaflet, oxygen tends to get trapped more in this layer, resulting in the highest K and deepest free energy well, as shown in the plots. As reported in Table 15.1, the average K ($\langle K \rangle$) for the flat bilayer, 4.06, is only slightly larger than for the liposome, 3.95, indicating that the relative oxygen concentration is smaller in the liposome compared to the flat bilayer. It is assumed that the asymmetricity of the free energy and partition coefficient profiles is likely due to the smaller thickness and different area per lipid in each layer in the liposome.

15.4 Conclusion

The free energy and partition coefficient profiles demonstrate that the oxygen preference to stay in the membrane decreases as the membrane's curvature increases, resulting in the smaller partition coefficient. This leads to lower oxygen concentration in the membrane. In the liposome, oxygen needs to overcome a smaller energy barrier to

permeate from the outer leaflet to the water phase, which facilitates the permeation process. This can be also related to the smaller thickness and the larger area per lipid of the outer layer of the curved membrane. These results differ from our initial hypothesis regarding the role of curvature in storing oxygen in caveolae. However, it is worth noting that our simulation did not include cholesterol or the caveolin protein, which may have a significant impact on the results. In summary, curvature may have a negligible effect in the oxygen partition coefficient, and it is unlikely that membrane curvature is the only mechanism by which caveolae store oxygen. In future work, also the timeliness of oxygen transport, i.e., oxygen permeability, should be investigated. Based on previous work on water permeability through curved membranes [20, 21], we plan to consider all structural aspects of caveolae and to examine the combined effect of curvature and cholesterol on oxygen permeability through the membrane.

References

1. Woese CR, Kandler O, Wheelis ML (1990) Towards a natural system of organisms: proposal for the domains archaea, bacteria, and eucarya. Proc Natl Acad Sci U S A 87(12):4576–4579
2. Carter R (2003) Oxygen: the molecule that made the world. J R Soc Med 96(1):46–47
3. Shields HJ, Traa A, Van Raamsdonk JM (2021) Beneficial and detrimental effects of reactive oxygen species on lifespan: a comprehensive review of comparative and experimental studies. Front Cell Dev Biol 9:628157
4. Brown AJ, Galea AM (2010) Cholesterol as an evolutionary response to living with oxygen. Evolution 64(7):2179–2183
5. Porta JC, Han B, Gulsevin A et al (2022) Molecular architecture of the human caveolin-1 complex. Sci Adv 8(19):eabn7232
6. Patel HH, Tsutsumi YM, Head BP et al (2007) Mechanisms of cardiac protection from ischemia/reperfusion injury: a role for caveolae and caveolin-1. FASEB J 21(7):1565–1574
7. Schilling JM, Head BP, Patel HH (2018) Caveolins as regulators of stress adaptation. Mol Pharmacol 93(4):277–285
8. Head BP, Peart JN, Panneerselvam M et al (2010) Loss of caveolin-1 accelerates neurodegeneration and aging. PLoS One 5:e15697
9. Riccardi E, Krämer A, van Erp TS et al (2020) Permeation rates of oxygen through a lipid bilayer using replica exchange transition interface sampling. J Phys Chem B 125(1):193–201
10. Ghysels A, Venable RM, Pastor RW et al (2017) Position-dependent diffusion tensors in anisotropic media from simulation: oxygen transport in and through membranes. J Chem Theory Comput 13(6):2962–2976
11. Nemoto EM, Harrison EM, Pias SC et al (2021) Oxygen transport to tissue XLII. Springer, Cham
12. Wang Q, Dotson RJ, Angles G et al (2021) Simulation study of breast cancer lipid changes affecting membrane oxygen permeability: effects of chain length and cholesterol. Adv Exp Med Biol 1269:15–21
13. Abraham MJ, Murtola T, Schulz R et al (2015) GROMACS: high performance molecular simulations through multi-level parallelism from laptops to supercomputers. SoftwareX 1:19–25
14. Qi Y, Ingólfsson HI, Cheng X et al (2015) CHARMM-GUI martini maker for coarse-grained simulations with the martini force field. J Chem Theory Comput 11(9):4486–4494
15. Wassenaar TA, Pluhackova K, Böckmann RA (2014) Going backward: a flexible geometric approach to reverse transformation from coarse grained to atomistic models. J Chem Theory Comput 10(2):676–690
16. Bussi G, Donadio D, Parrinello M (2007) Canonical sampling through velocity rescaling. J Chem Phys 126(1):014101
17. Huang J, MacKerell AD Jr (2013) CHARMM36 all-atom additive protein force field: validation based on comparison to NMR data. J Comput Chem 34(25):2135–2145
18. Jorgensen WL, Chandrasekhar J, Madura JD et al (1983) Comparison of simple potential functions for simulating liquid water. J Chem Phys 79(2):926–935
19. Kučerka N, Nieh MP, Katsaras J (2011) Fluid phase lipid areas and bilayer thicknesses of commonly used phosphatidylcholines as a function of temperature. Biochim Biophys Acta Biomembr 1808(11):2761–2771
20. Davoudi S, Ghysels A (2021) Sampling efficiency of the counting method for permeability calculations estimated with the inhomogeneous solubility–diffusion model. J Chem Phys 154(5):054106
21. Davoudi S, Ghysels A (2023) Defining permeability of curved membranes in molecular dynamics simulations. Biophys J 122:1–10. https://doi.org/10.1016/j.bpj.2022.11.028

16

The Significance of Lipids for the Absorption and Release of Oxygen in Biological Organisms

Alessandro Maria Morelli and Felix Scholkmann

Abstract

A critically important step for the uptake and transport of oxygen (O_2) in living organisms is the crossing of the phase boundary between gas (or water) and lipid/proteins in the cell. Classically, this transport across the phase boundary is explained as a transport by proteins or protein-based structures. In our contribution here, we want to show the significance of passive transport of O_2 also (and in some cases probably predominantly) through lipids in many if not all aerobic organisms. In plants, the significance of lipids for gas exchange (absorption of CO_2 and release of O_2) is well recognized. The leaves of plants have a cuticle layer as the last film on both sides formed by polyesters and lipids. In animals, the skin has sebum as its last layer consisting of a mixture of neutral fatty esters, cholesterol and waxes which are also at the border between the cells of the body and the air. The last cellular layers of skin are not vascularized therefore their metabolism totally depends on this extravasal O_2 absorption, which cannot be replenished by the bloodstream. The human body absorbs about 0.5% of O_2 through the skin. In the brain, myelin, surrounding nerve cell axons and being formed by oligodendrocytes, is most probably also responsible for enabling O_2 transport from the extracellular space to the cells (neurons). Myelin, being not vascularized and consisting of water, lipids and proteins, seems to absorb O_2 in order to transport it to the nerve cell axon as well as to perform extramitochondrial oxidative phosphorylation inside the myelin structure around the axons (i.e., myelin synthesizes ATP) – similarly to the metabolic process occurring in concentric multilamellar structures of cyanobacteria. Another example is the gas transport in the lung where lipids play a crucial role in the surfactant ensuring incorporation of O_2 in the alveoli where there are lamellar body and tubular myelin which form multilayered surface films at the air-membrane border of the alveolus. According to our view, the role played by lipids in the physical absorption of gases appears to be crucial to the existence of many, if not all, of the living aerobic species.

Keywords

Lipids · Oxygen transport · Metabolism

A. M. Morelli
Biochemistry Lab, Pharmacy Department, University of Genova, Genova, Italy

F. Scholkmann (✉)
Institute of Complementary and Integrative Medicine, University of Bern, Bern, Switzerland

Biomedical Optics Research Laboratory, Department of Neonatology, University Hospital Zurich, University of Zurich, Zurich, Switzerland
e-mail: Felix.Scholkmann@usz.ch

F. Scholkmann et al. (eds.), *Oxygen Transport to Tissue XLIV*, Advances in Experimental Medicine and Biology 1438, https://doi.org/10.1007/978-3-031-42003-0_16

16.1 Introduction

The absorption and transport of oxygen (O_2) is a fundamental step for all aerobic living organisms. The first step of this process is the crossing of the phase boundary between gas (or water) and the exposed surfaces of the organism, i.e., the liquid or semi-solid phase. Since membrane proteins are (partially) immersed (i) in the cytosolic aqueous phase that borders the membranes and (ii) in the lipid phase of the membranes themselves (and can never be exposed "naked" to the cell-air or cell-water boundary), proteins are not directly responsible for bridging these phase boundaries. The protein (e.g., hemoglobin) acts only as an O_2 transmitter if it is dissolved in a liquid medium – the passage of O_2 can generally only occur by purely physical passive diffusion. A special case is seen with proteins that also act as membrane channels for O_2, like aquaporin-1 and rhesus proteins in red blood cells [1].

In this article, we summarize the significance of passive diffusion of carbon dioxide (CO_2) and O_2 through neutral lipids in living organisms. We discuss modes of O_2 transport in some marine organisms, which is possible without O_2-carrying proteins like hemoglobin in some cases. Finally, we hypothesize that the O_2 absorption capacity by neutral lipids as a primordial transmission form that preceded the appearance of O_2-binding chromoproteins.

16.2 Oxygen Solubility in Lipids

The solubility of O_2 in water depends on many factors (like temperature, salts, dissolved proteins, acidity), but is generally very low, around 9.17 µg/ml at 20 °C (6.41 µL/mL) [2]. The idea that multicellular organisms can use lipids for a greater availability of O_2 is demonstrated by the Atlantic striped bass which is acclimatized to living at temperatures of 5 °C (compared to the usual 25 °C for bass) and shows a 13-fold increase in the lipid content of the muscles and almost a doubling of the O_2 diffusion constant [3, 4].

Olive oil is a mixture of various lipids where mono-unsaturated oleic acid is present in a large majority (63–83%). The solubility of O_2 in olive oil is 4–5 times greater than O_2 in water [5], while neutral lipids such as waxes exhibit even greater absorption [6]. For example, paraffin oil Bunsen solubility coefficient (α, i.e., the ratio between the volume of gas in the unit of volume that is absorbed by the unit of the volume of liquid that it laps) for pure O_2 is 0.137 (at 35 °C) [7], which is higher than that of H_2O (α = 0.028 at 25 °C), human blood (α = 0.022 at 37 °C and hemoglobin concentration of 13.3 g/dL) and olive oil (α = 0.102 at 37.8 °C). Paraffin oil is a stronger oxygen absorbing agent than blood.

16.3 Gas Exchange in Plants

Gas exchange takes place in the leaves of plants which is crucial to enable life on earth. CO_2 is absorbed and O_2 is released as a result of photosynthesis involving chlorophyll. Absorption of CO_2 is even more difficult than the process of absorbing O_2 in animals because the concentration of CO_2 in the air is much lower than that of oxygen (i.e., 0.4% versus 21%). The boundary with air in plants consists of the cuticle which is mainly composed of waxes on both the upper and lower side [8]. The cuticle likely has the function of physically absorbing the gas thanks to the high content of waxes. The cuticle is permeable to CO_2 [9], and most probably also to O_2. After the absorption phase of an essentially physical nature, the carbonic anhydrase (CA) enzyme facilitates a chemical reaction of the gaseous CO_2 to form bicarbonate which is soluble in water and therefore indispensable in circulation. The leaf is by far the richest part of the plant in CA and it has been ascertained that the leaf can contain even a thousand times more CA than the rest of the plant [10]. CA is found in the thylakoid disks of chloroplasts and is effective for the concentration of CO_2 [11] which reacts with the photosynthesis enzymes.

16.4 Gas Exchange in Animals

For the vast majority of animal multicellular organisms, the absorption and distribution of O_2 is linked to the blood circulatory system which contains densely packed hemoglobin inside the red blood cells. (An exception are specific types of icefish that are devoid of chromoproteins such as myoglobin but O_2 is still transported by the circulatory system).

The organ that provides for the absorption of O_2 are the lungs (in terrestrial animals) or the gills (in fish), while the skin can also absorb O_2. In the lungs, the boundary between circulating blood and air is located in the pulmonary alveoli, and the passage from air to blood is ensured by the surfactant which is stratified inside the membrane of the alveoli which is in direct contact with the inhaled-exhaled air. The surfactant has a membranous basic structure [12] (Fig. 16.1a). It contains only 8% protein and the remainder is lipid. The most abundant lipid (41%) is glycerophosphatidylcholine or lecithin [13]. The basic structure that characterizes the surfactant film is a membrane that starts from a concentric multilamellar shape (lamellar body) which then transforms into tubular myelin, similar to that of the myelin of the nervous system [14] (Fig. 16.1b, c). It is worth noting that the typical chromoproteins that ensure the transport and storage of O_2 in animals are completely absent in the surfactant, confirming that (i) the cell-air interface interaction with O_2 is exclusively of a physical nature, and (ii) it cannot really resort to proteins or other molecular transporters.

16.5 Oxygen Absorption in Icefish

Many fish living at extremely low temperatures in the Antarctic seas have a very similar circulatory system to other fish (with a heart, blood vessels and gills) but do not have hemoglobin-like chromoproteins. These fish have been called white-

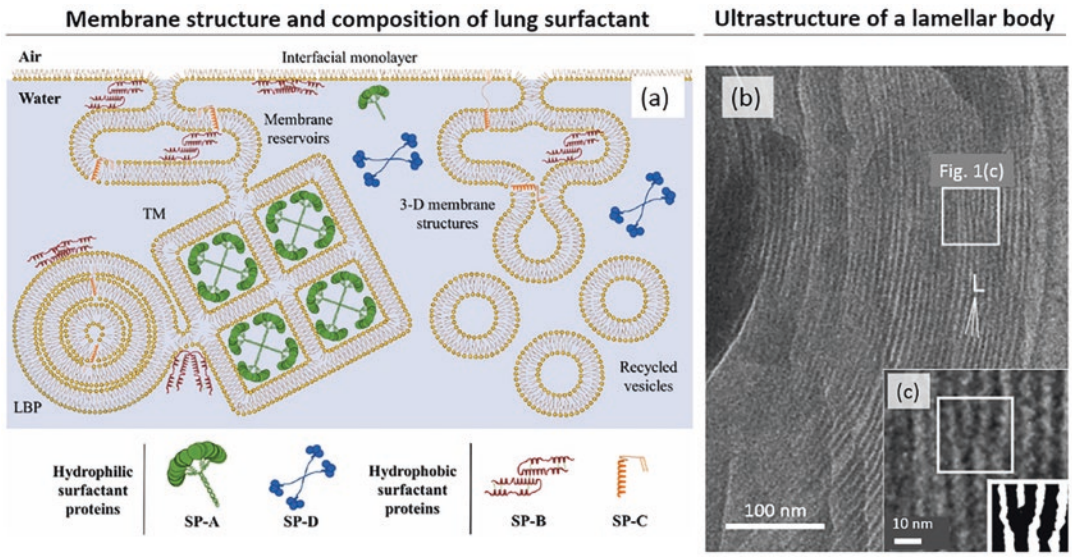

Fig. 16.1 (**a**) The structure of the lung surfactant. The membranous lipid-protein assemblies of the surfactant form different structures, including the highly packed multilamellar membranous lamellar body (LBP). (Reprinted from Castillo-Sánchez et al. [12], with permission from the publisher). (**b**, **c**) Cryo-electron microscopic image of a lamellar body of the surfactant of a rat lung. The lamellar structure is clearly visible with a relatively electron-translucent gap that separates the limiting membrane from the concentric lamellae. (**c**) Magnification of the lamellar structure. The average periodicity of the multilamellar structure is 7.4 ± 1.4 nm, i.e. a bit more compact than the similar structure of myelin with an interlamellar distance of 12 nm. (Reprinted and modified from Vanhecke et al. [14], with permission from the publisher)

blooded fish or icefish and almost totally lack the genes for alpha and beta-globin [15]. Studies have been carried out on these fish to understand how the supply of O_2 to the whole body could take place. It has been found that they have a vascular mass that is about double that of other fish, and very developed gills. They also consume about twice as much energy to ensure blood circulation [4]. The mitochondria contained in the heart of these fish have been studied in detail and found to occupy a very high volume in percentage: 36.53 ± 2.07% in *Chaenocephalus aceratus*, a typical icefish [16]. This raises the following question: how do these fish manage to transport the O_2 in their vessels in the body? One explanation is that at the very low temperatures at which icefish live, the solubility of oxygen increases – almost double compared to 25 °C [17]. Another explanation is provided by lipids. Desaulniers et al. [3] found a 13-fold increase in lipids in the form of droplets in the muscles of striped bass (*Morone saxatilis*) acclimatized to 5 °C against the 25 °C at which they usually live. The authors also measured the diffusion of O_2 which was found to be nearly doubled in the muscles of fish acclimatized to 5 °C. These data support the notion that lipids contribute to the diffusion of O_2 and presumably allow the transport of O_2 by icefish. This is confirmed by Palmerini et al. [18] who also found a noticeable increase in blood lipids of the icefish *Chionodraco hamatus*. Interestingly, a high triglyceride content was noted in the blood of icefish too [19]. All of this speaks for the hypothesis that the transport of O_2 in transparent blood of icefish is due to the high content of lipids. It should also be borne in mind that icefish, like other organisms that live at extremely low temperatures, are largely endowed with antifreeze proteins in their blood vessels [20]. Since these proteins have the ability to strongly bind O_2 [21, 22] it is plausible that they possibly facilitate the solubility of O_2 in the blood.

16.6 Oxygen Absorption in the Brain

It is known that the human brain consume 10 times more O_2 than the rest of the body. In fact, 100 g of human brain consumes 3.5 ml O_2 per minute, while the oxygen consumed in 1 min by 100 g of body tissue is on average 0.35 ml [23]. There is not yet a convincing explanation for this enormous increase in O_2 consumed by the brain. In our view, the role of myelin, which makes up about 40% of the cerebral mass, could solve this conundrum.

The myelin sheath has been indicated by us as an efficient site of O_2 consumption, so much so that an O_2-sponge effect can be attributed to it [24–27]. The stacked phospholipid membranes in myelin most likely act as an oxygen reservoir [27]. Concerning the presence of myoglobin and neuroglobin in the brain, both molecules are present in brain tissue and have the ability to absorb oxygen [28, 29], but their concentration is generally too low in brain tissue to explain the amount of oxygen absorption taking place, especially under physiological conditions. During hypoxia, the expression of myoglobin is upregulated in the brain [29] and neuroglobin migrates towards the source of O_2 to help neuronal oxygenation [30]. The fact that myelin is not vascularized and therefore 40% of the mass of the brain is not vascularized supports our notion that passive diffusion of O_2 plays an important part in oxygen storage and delivery in the brain. In our view, lipids and waxes (and myelin) are of great relevance for this.

Analyzed up to now in various aspects of living organisms (i.e. concentric lamellar thylakoids of cyanobacteria, pulmonary surfactant, icefish blood, cuticle on leaf surfaces – all with a high lipid content), the concentric multilamellar sheath of myelin could possibly absorb O_2 by passive diffusion where, in myelin, the ultimate force that sucks oxygen in is the oxidative phosphorylation operating in it [24, 31, 32]. This plausible ability to absorb O_2 by myelin might also explain the "oxygen paradox" of neurovascular coupling, which until now has not had a reasonable explanation [33, 34]. When an increase in neuronal activity produces an immediate increase in cerebral blood flow it is known that this exceeds the cerebral metabolic rate of oxygen, and therefore a surplus of O_2 is absorbed by the brain. The O_2 sponge effect exerted by myelin can principally explain this phenomenon, which up to now has not found plausible explanations.

On the other hand, it is known that white matter has good recovery capabilities to anoxia, while gray matter does not have it [35–37]. The O_2 absorption of myelin and its extramitochondrial energy production might also explain this finding.

16.7 Oxygen Absorption by the Skin

The human body absorbs ~0.5% O_2 through the skin (ratio of transcutaneous O_2 uptake to pulmonary oxygen uptake) [38]. In animals, the skin has sebum as its last layer consisting of a mixture of neutral fatty esters and waxes which are also at the border between the cells of the body and the air [39]. Figure 16.2 depicts the depth-dependent O_2 partial pressure of the skin and the transcutaneous O_2 flux with normal and reduced skin partial pressure of O_2 values [38, 40]. Stücker et al. showed that "under normal conditions, atmospheric oxygen can supply the upper skin layers to a depth of 0.25–0.40 mm" [38], which according to the authors is 3–10 times deeper than based on analytical calculations [40, 41]. Stücker et al. concluded that the "whole epidermis and the upper corium can therefore be supplied with oxygen from the atmosphere" which "may have significant consequences with regard to the treatment of lesions such as venous and ischaemic ulcers" [38]. Since the last cellular layers of skin are not vascularized, their metabolism totally depends on the extravasal O_2 absorption. Even in icefish, which have a reduced supply of O_2 from the blood circulation devoid of hemoglobin, it has been hypothesized that the skin contributes more to the absorption of O_2 than in other species; in fact, the icefish do not have the scales that isolate the skin of the fish from the water [42].

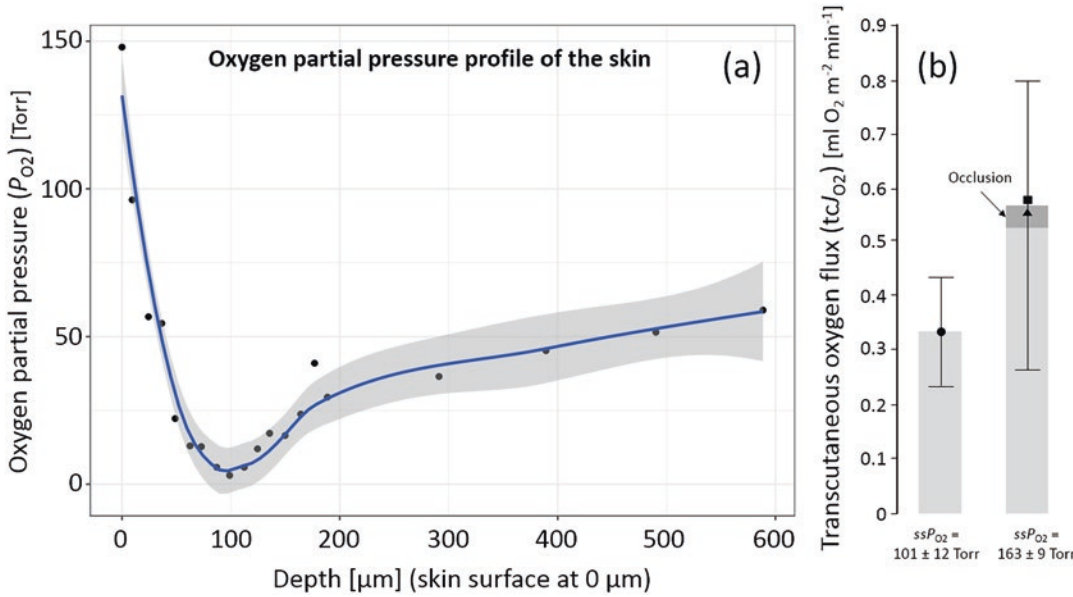

Fig. 16.2 (**a**) Oxygen partial pressure (P_{O2}) profile of the skin obtained by a needle electrode into the skin. Measurement conducted by Baumgärtl et al. [40], reanalyzed by Stücker et al. [38] and newly visualized by us (LOESS trend line and confidence interval). The measurement was conducted with a water film covering the skin surface (causing a reduced skin surface P_{O2}). (**b**) Transcutaneous oxygen flux (tcJ_{O2}; 33 °C, humidified skin) under two skin surface P_{O2} (ssP_{O2}) conditions (normal ssP_{O2} [with and without a 5 min suprasystolic occlusion] and reduced ssP_{O2}). The occlusion resulted in a small increase in tcJ_{O2}. (Data from Stücker et al. [38])

16.8 Summary, Conclusions and Outlook

We presented many different cases of biological structures that bind O_2 not in the classical way via hemoglobin-like chromoproteins. It emerged that in many situations lipids (and probably neutral lipids and waxes) are the substances that can bind O_2 in purely physical ways [43, 44]. These lipids are extremely important as they carry out the first phase of O_2 absorption and their absence would compromise the entire chain of events downstream that determines the actual consumption of it in a non-equilibrium situation. Emblematic is the O_2 absorption phase at the air-pulmonary alveolus interface where the surfactant forms a series of membranous layers based on neutral lipids and phospholipids which is crucial for proper O_2 absorption and also the release of CO_2. This function appears to be crucial in cases of bronchopulmonary diseases (like pathologies caused by infection with the SARS-CoV-2 virus) where reduction in the amount of surfactant has been ascertained [45] and pharmacological treatments aimed at correcting this anomaly have been implemented [46–48].

The widespread presence of icefish in Antarctica where sea temperatures are extremely low and some fish are completely devoid of hemoglobin and myoglobin underscores the importance of lipids. These fish they have all the systems – gills, heart, blood vessels – which in most fish ensure the absorption of O_2 and its distribution to all organs. This leads to the hypothesis that the richness of lipids both in the blood and in the muscles can support the transport and storage function of oxygen guaranteed basically by the hemoglobin in the blood and by the myoglobin in the muscles.

In our view, it is not surprising that concentric multilamellar structures very rich in lipids such as the thylakoids of cyanobacteria and myelin sheaths would perform the function of absorption of CO_2 and O_2 – a process intimately linked to the realization of photosynthesis and to oxidative phosphorylation with coupled aerobic synthesis of ATP [26].

The role of lipids in physical absorption of gases appears to be a crucial contribution to ensure the existence of many if not all of the living aerobic species.

References

1. Zhao P et al (2020) Role of channels in the oxygen permeability of red blood cells. BioarXIv
2. Roppongi T et al (2021) Solubility and mass transfer coefficient of oxygen through gas- and water-lipid interfaces. J Food Sci 86(3):867–873
3. Desaulniers N, Moerland TS, Sidell BD (1996) High lipid content enhances the rate of oxygen diffusion through fish skeletal muscle. Am J Physiol Regul Integr Comp Physiol 271(1):R42–R47
4. Sidell BD, O'Brien KM (2006) When bad things happen to good fish: the loss of hemoglobin and myoglobin expression in Antarctic icefishes. J Exp Biol 209(Pt 10):1791–1802
5. Battino R, Evans FD, Danforth WF (1968) The solubilities of seven gases in olive oil with reference to theories of transport through the cell membrane. J Am Oil Chem Soc 45(12):830–833
6. Battino R (ed) (1981) Solubility data series. Oxygen and ozone, vol Vol. 7. Pergamon Press, Oxford/New York/Toronto/Sydney/Paris/Frankfurt
7. Ruppel D (1971) Oxygen solubility measurements in liquid paraffin. Can J Chem 49(22):3762–3764
8. Bourgault R et al (2020) Constructing functional cuticles: analysis of relationships between cuticle lipid composition, ultrastructure and water barrier function in developing adult maize leaves. Ann Bot 125(1):79–91
9. Monda K et al (2021) Cuticle permeability is an important parameter for the trade-off strategy between drought tolerance and CO2 uptake in land plants. Plant Signal Behav 16(6):1908692
10. DiMario RJ et al (2017) Plant carbonic anhydrases: structures, locations, evolution, and physiological roles. Mol Plant 10(1):30–46
11. Fridlyand LE, Kaler VL (1987) Possible CO2 concentrating mechanism in chloroplasts of C3 plants. Role of carbonic anhydrase. Gen Physiol Biophys 6(6):617–636
12. Castillo-Sanchez JC, Cruz A, Perez-Gil J (2021) Structural hallmarks of lung surfactant: lipid-protein interactions, membrane structure and future challenges. Arch Biochem Biophys 703:108850
13. Parra E, Perez-Gil J (2015) Composition, structure and mechanical properties define performance of pulmonary surfactant membranes and films. Chem Phys Lipids 185:153–175

14. Vanhecke D et al (2010) Lamellar body ultrastructure revisited: high-pressure freezing and cryo-electron microscopy of vitreous sections. Histochem Cell Biol 134(4):319–326
15. Cheng CH, Detrich HW 3rd (2007) Molecular ecophysiology of Antarctic notothenioid fishes. Philos Trans R Soc Lond B Biol Sci 362(1488):2215–2232
16. O'Brien KM, Sidell BD (2000) The interplay among cardiac ultrastructure, metabolism and the expression of oxygen-binding proteins in Antarctic fishes. J Exp Biol 203(Pt 8):1287–1297
17. Rennie J (2019) Icefish study adds another color to the story of blood. Quanta Magazine
18. Palmerini CA et al (2009) Blood lipids in Antarctic and in temperate-water fish species. J Membr Biol 230(3):125–131
19. Lund ED, Sidell BD (1992) Neutral lipid compositions of Antarctic fish tissues may reflect use of fatty acyl substrates by catabolic systems. Mar Biol 112(3):377–382
20. Gharib G et al (2022) Antifreeze proteins: a tale of evolution from origin to energy applications. Front Bioeng Biotechnol 9:770588.
21. Eto TK, Rubinsky B (1993) Antifreeze glycoproteins increase solution viscosity. Biochem Biophys Res Commun 197(2):927–931
22. Lee J-H, Lee S-G, Kim H-J (2011) Recent advances in structural studies of antifreeze proteins. Ocean Polar Res 33(2):159–169
23. Rink C, Khanna S (2011) Significance of brain tissue oxygenation and the arachidonic acid cascade in stroke. Antioxid Redox Signal 14(10):1889–1903
24. Ravera S et al (2009) Evidence for aerobic ATP synthesis in isolated myelin vesicles. Int J Biochem Cell Biol 41(7):1581–1591
25. Morelli A et al (2011) Exportability of the mitochondrial oxidative phosphorylation machinery into myelin sheath. Theor Biol Forum 104(2):67–74
26. Morelli AM et al (2021) Myelin sheath and cyanobacterial thylakoids as concentric multilamellar structures with similar bioenergetic properties. Open Biol 11(12):210177
27. Vervust W, Ghysels A (2022) Oxygen storage in stacked phospholipid membranes under an oxygen gradient as a model for myelin sheaths. Adv Exp Med Biol 1395:301–307
28. Elsherbiny ME et al (2021) Expression of myoglobin in normal and cancer brain tissues: correlation with hypoxia markers. Front Oncol 11:590771
29. Fraser J et al (2006) Hypoxia-inducible myoglobin expression in nonmuscle tissues. Proc Natl Acad Sci U S A 103(8):2977–2981
30. Li CY et al (2023) Neuroglobin facilitates neuronal oxygenation through tropic migration under hypoxia or anemia in rat: how does the brain breathe? Neurosci Bull
31. Ravera S et al (2016) Evaluation of the acquisition of the aerobic metabolic capacity by myelin, during its development. Mol Neurobiol 53(10):7048–7056
32. Ravera S, Morelli AM, Panfoli I (2020) Myelination increases chemical energy support to the axon without modifying the basic physicochemical mechanism of nerve conduction. Neurochem Int 141:104883
33. Leithner C, Royl G (2014) The oxygen paradox of neurovascular coupling. J Cereb Blood Flow Metab 34(1):19–29
34. Drew PJ (2022) Neurovascular coupling: motive unknown. Trends Neurosci 45(11):809–819
35. Fern R et al (1998) Axon conduction and survival in CNS white matter during energy deprivation: a developmental study. J Neurophysiol 79(1):95–105
36. Falcao AL et al (2004) The resistance to ischemia of white and gray matter after stroke. Ann Neurol 56(5):695–701
37. Adriano E et al (2011) A novel hypothesis about mechanisms affecting conduction velocity of central myelinated fibers. Neurochem Res 36(10):1732–1739
38. Stücker M et al (2002) The cutaneous uptake of atmospheric oxygen contributes significantly to the oxygen supply of human dermis and epidermis. J Physiol 538(Pt 3):985–994
39. Picardo M et al (2009) Sebaceous gland lipids. Dermatoendocrinol 1(2):68–71
40. Baumgärtl H et al (1987) Initial results of intracutaneous measurements of PO2 profiles. In: Clinical Oxygen Pressure Measurement, edited: Ehrly, A.M. & Huch, J.H., pp 121–128
41. Fitzgerald LR (1957) Cutaneous respiration in man. Physiol Rev 37(3):325–336
42. Traczyk R, Meyer-Rochow VB, Hughes RM (2021) Age determination in the icefish Pseudochaenichthys georgianus (Channichthyidae) based on multiple methods using otoliths. Aquat Biol 30:1–18
43. Longmuir IS (1981) Channels of oxygen transport from blood to mitochondria. In: Oxygen Transport to Tissue, pp 19–22
44. Longmuir IS et al (1981) Intracellular microheterogeneity of oxygen concentrations. In: Oxygen Transport to Tissue, p 43
45. Schousboe P et al (2022) Reduced levels of pulmonary surfactant in COVID-19 ARDS. Sci Rep 12(1):4040
46. Wang S et al (2021) The role of pulmonary surfactants in the treatment of acute respiratory distress syndrome in COVID-19. Front Pharmacol 12:698905
47. Veldhuizen RAW et al (2021) The COVID-19 pandemic: a target for surfactant therapy? Expert Rev Respir Med 15(5):597–608
48. Piva S et al (2021) Surfactant therapy for COVID-19 related ARDS: a retrospective case-control pilot study. Respir Res 22(1):20

How Skin Color Depends on Tissue Oxygenation

17

Gennadi Saiko

Abstract

Background: Skin color is essential to skin and wound assessment as it brings valuable information about skin physiology and pathology. An approach, which can help deconvolute and isolate various mechanisms affecting skin color, could be helpful to drive the remote photoplethysmography (rPPG) utility beyond its current applications. Aim: The present work aims to create a simple analytical framework that links skin color with blood oxygenation and perfusion. Material and methods: The model consists of two parts. First, the model's core connects changes in tissue chromophore concentrations with changes in tissue reflectance. In the second step, the tissue reflectance is convoluted with the response curves of a sensor (tristimulus response in the case of the human eye) and the light source's spectrum. Results: The model allows linking changes in blood oxygenation and perfusion with changes in skin color. Conclusion: The model can be helpful for the interpretation of the amplitudes of various components of the rPPG signal.

Keywords

Skin color · Tissue oxygenation · Remote photoplethysmograph

17.1 Introduction

Remote photoplethysmography (rPPG) is an emerging optical modality explored for multiple healthcare applications [1]. Due to its simplicity and affordability, rPPG may become a valuable tool in investigating skin physiology and diagnostics. However, existing research is focused mainly on practical applications of the rPPG based on waveform analysis as the rPPG signal, affected by multiple autoregulation processes in the skin, both local and systemic, is relatively complex.

With very little research on the PPG signal's origins and competing accounts on its nature [2, 3], we have little visibility on how underlying autoregulation processes manifest themselves in PPG. The lack of such insights is a critical gap in the literature. As a result, at the current state, rPPG's utility is mainly limited to simple applications like heart rate extraction and heart rate variability determination. The current status begs the ubiquitous question: what kind of information can be derived from rPPG beyond the waveforms?

G. Saiko (✉)
Swift Medical Inc., Toronto, Canada

Department of Physics, Toronto Metropolitan University, Toronto, Canada
e-mail: gsaiko@torontomu.ca

F. Scholkmann et al. (eds.), *Oxygen Transport to Tissue XLIV*, Advances in Experimental Medicine and Biology 1438, https://doi.org/10.1007/978-3-031-42003-0_17

A potential approach to address this question is to explore skin color. Skin color is essential to skin and wound assessment as it brings valuable information about skin physiology and pathology. Its utility can be attributed to the small penetration depth of the visible light in the skin (less than 2 mm), which makes the visible range of the spectrum particularly suitable for microcirculation investigations. Thus, an approach, which can help deconvolute and isolate various mechanisms, could be helpful to drive the rPPG utility beyond its current applications.

The critical step in that direction is using objective (non-device specific) color representation. This task differs but is closely related to finding optimal color space for skin classification [4]. RGB, by far, is the most common color space; however, it suffers several drawbacks. The International Commission on Illumination (CIE) adopted the CIE XYZ color space to overcome the disadvantages of trichromatic additive color spaces like RGB. However, CIE XYZ space demonstrates perceptual nonuniformity [5]. In adopting the CIELUV color space, the CIE attempted to address this concern [6].

It should be noted that while the color representation for additive color schemas (emissive case) can be considered absolute, it is not the case for subtractive color schemas (reflection and transmission), where the response needs to be convoluted with the spectral power distribution of the illuminant. Thus, perceived color in a subtractive color scheme is light source dependent.

The current work aims to create a simple analytical framework that links skin color with blood oxygenation and perfusion. Ultimately this framework can help extract additional information from rPPG signals.

17.2 Methods

In a typical imaging scenario, an rPPG signal bears tissue reflectance information aggregated into three color bands captured by an imaging sensor. Based on this observation, the model consists of two parts. First, the model's core is based on a simple analytical approach, which links changes in tissue chromophore concentrations with changes in tissue reflectance. In the second step, the tissue reflectance is convoluted with the response curves (tristimulus response in the case of the human eye) and the light source spectrum.

17.2.1 Quasi Two-Layer Model

The skin is a multi-layer structure. Typically, it is subdivided into three primary layers: epidermis, dermis, and subcutaneous tissue. However, considering the spectrum's visible range, the light penetration depth does not exceed 2 mm, and subcutaneous tissue does not contribute much to the reflectance. Therefore, in this case, we can consider the skin as a two-layer structure: the bloodless epidermis and underlying, blood-containing tissue with optical properties of the dermis.

In healthy non-glabrous skin, the dermis and epidermis are approximately 2 mm and 100–120 μm thick, respectively. As visible light does not penetrate more than 2 mm into it, we can approximate the dermis as a semi-infinite layer. Thus, if we ignore the surface layer (epidermis), we can consider tissue semi-space with the dermis' optical parameters.

However, the epidermis' optical properties are very different from dermis ones, especially for dark skin tones. In the general case, the skin contains melanin located in the bottom basal layer of the epidermis. Its concentration there varies from 1% to 43% [7]. In addition to that, the stratum corneum demonstrates much stronger scattering than the dermis [7]. Thus, one-layer models are generally inadequate for characterizing the optical properties of the skin.

A quasi-two-layer model has been proposed [8] to accommodate a layered structure while retaining the simplicity of single-layer models. In this model, the epidermis layer is considered a thin film just under the surface of the bulk tissue layer. Two parameters characterize a "thin film" of the epidermis: absorption ρ and scattering χ, which depends on absorption $\mu_{a,e}$ and reduced scattering $\mu'_{s,e}$ of the epidermal layer (denoted by letter e):

$$\rho = \int_L \mu_{a,e} dz \tag{17.1}$$

$$\chi = \frac{1}{2}\int_L \mu'_{s,e} dz \tag{17.2}$$

Here we have integration over the epidermis layer with the thickness L. In the presence of such "thin film," the reflectance of the semi-space with mismatched boundaries can be written as [8].

$$R = r_{01} + \left(1 - r_{01}\right)\left(1 - r_{10}\right) \frac{\chi + \left(\left(1-\rho-\chi\right)^2 - \chi^2\right) R_d}{1 - \chi\left(R_d + r_{10}\right) - \left(\left(1-\rho-\chi\right)^2 - \chi^2\right) R_d r_{10}} \tag{17.3}$$

Here r_{01} is the specular reflectance for the light coming from the air to the tissue, r_{10} is the specular reflectance of the light coming from the tissue into the air, and R_d is the diffuse reflectance of the bulk tissue.

The quasi-two-layer model has been tested in numerical simulations. It was found that it significantly (by a factor of 10) outperforms the single-layer model in accuracy and is in close agreement with the two-layer model [9]. Furthermore, it emulates tissue reflectance within 1% of the values derived from the two-layer model.

17.2.2 Tristimulus Color Space

The human eye and typical imaging systems interpret colors using three color channels. Thus, in step 2, we need to aggregate the tissue reflectance spectra into three-channel responses. The CIE XYZ color space encompasses all color sensations visible to a person with average eyesight using the CIE's color matching functions ($\bar{x}(\lambda)$, $\bar{y}(\lambda)$, $\bar{z}(\lambda)$), which quantify the chromatic response of the average observer. The CIE 1931 color space defines the tristimulus values denoted by X, Y, and Z. In the case of the subtractive color schema (reflection and transmission) for the known light source spectral distribution $I(\lambda)$, the tristimulus values can be found as

$$X = \frac{K}{N}\int_\lambda R(\lambda) I(\lambda) \bar{x}(\lambda) \mathrm{d}\lambda \tag{17.4}$$

$$Y = \frac{K}{N}\int_\lambda R(\lambda) I(\lambda) \bar{y}(\lambda) \mathrm{d}\lambda \tag{17.5}$$

$$Z = \frac{K}{N}\int_\lambda R(\lambda) I(\lambda) \bar{z}(\lambda) \mathrm{d}\lambda \tag{17.6}$$

here $N = \int_\lambda I(\lambda)\bar{y}(\lambda)\mathrm{d}\lambda$, R is the tissue reflectance, and K is the scaling factor. The XYZ color space can be transformed into commonly used RGB color space by a simple linear transformation (multiplication on a 3 × 3 matrix).

However, the CIE XYZ color space allows decomposition into two parts: brightness and chromaticity. The CIE XYZ color space was deliberately designed so that the Y parameter is also a measure of the luminance of a color. That allows the representation of each color on 2D color space using normalization

$$x = \frac{X}{X+Y+Z} \tag{17.7}$$

$$y = \frac{Y}{X+Y+Z} \tag{17.8}$$

The chromatic coordinates (x,y) can be transformed into chromatic coordinates (u',v') in the CIELUV color space [6]:

$$u' = \frac{4x}{-2x+12y+3} \tag{17.9}$$

$$v' = \frac{9y}{-2x+12y+3} \tag{17.10}$$

17.3 Results

To assess the model performance, we have performed skin color simulations for a range of parameters. The quasi-two-layer model

(Eqs. 17.1, 17.2, and 17.3) has four variable parameters: thickness of the epithelium, L (50–120 μm), melanin concentration, c_{mel} (1–41% of the basal layer), blood concentration in the dermis, tHb (0.2–7%), and blood oxygen saturation, SO_2 (40–99%). We have selected the following values as proof of concept: $L = 100$ μm. $c_{mel} = 1\%$ (Fitzpatrick skin type I), $tHb = 1\%$, 2%, 4%, 7% and 10%, SO_2: 0–100%.

In the first step, we generated the tissue's simulated reflectance spectrum in the 380–780 nm range.

In step 2, the generated spectra were convoluted with CIE's color matching functions and light source spectrum to obtain values X, Y, and Z using Eqs. 17.4, 17.5, and 17.6. We approximated the CIE XYZ color-matching functions by a sum of Gaussian functions [10]. CIE standard illuminant E was used as the light source.

Then using Eqs.17.7 and 17.8, x and y were obtained. The result of tissue color simulations in (x,y) color space is presented in Fig. 17.1a. The solid blue and red lines depict the tissue with fully deoxygenated (blue line) and oxygenated (red line) blood for total hemoglobin content changing from 0% to 10%. The dashed traverse lines correspond to changes in the blood oxygenation given the same total hemoglobin content (1%, 2%, 4%, 7%, and 10%, respectively). The respective transformation into CIELUV color space using Eqs. 17.9 and 17.10 is depicted in Fig. 17.1b.

17.4 Discussion and Conclusions

Our initial results show that the tissue color demonstrates a complex dependence on total hemoglobin content, tHb, and blood oxygen saturation, SO_2. Also, CIELUB color space does not provide immediate benefits in visualization; however, it allows using Euclidean distance for color change characterization.

As expected, with the high blood content, in CIEXYZ color space, we see tissue color departure from the white/grey color ($x = y = 1/3$). However, the behavior of tissue oxygenation is more complex. For smaller concentrations (1% and 2% of tHb), we see the changes in the y component only (decreasing with increasing the oxygen content). However, for larger concentrations (7% and 10% of tHb), we primarily see a change in the x component.

One can see that the range of changes is significantly (5×) more prominent for the x component (0.35–0.42) compared to the y component

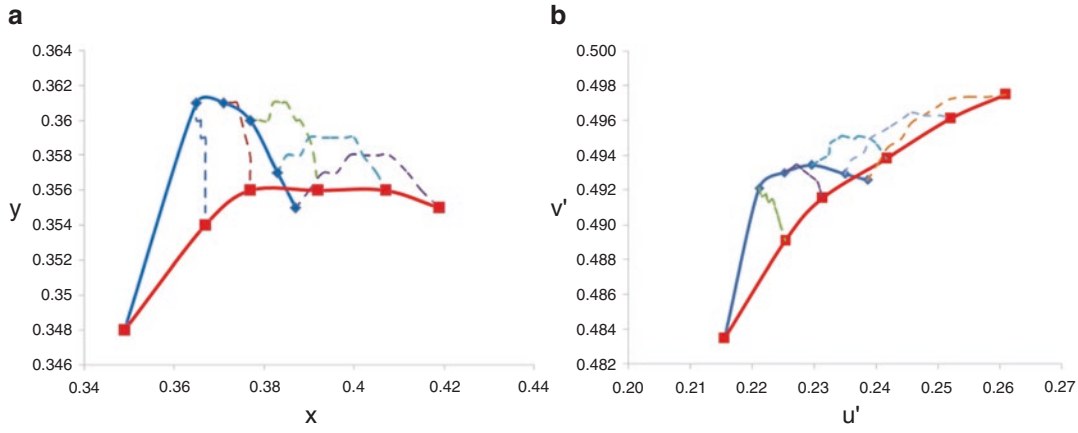

Fig. 17.1 The simulated tissue color in chromaticity diagrams. The solid blue and red lines depict the tissue with fully deoxygenated (blue line) and oxygenated (red line) blood for total hemoglobin content changing from 0% to 10%. The dashed traverse lines correspond to changes in the blood oxygenation from 0% to 100%, given the same total hemoglobin content (1%, 2%, 4%, 7%, and 10%, respectively). **Panel a**: CIE XYZ color space**. Panel b**: CIELUV color space

(0.348–0.362). Thus, it results in swings in the z component ($z = 1-x-y$), a proxy of the blue color.

The proposed model allows the interpretation of certain physiological interventions, including occlusion experiments. In such experiments, a body part (hand primarily) is occluded with the blood cuff inflated above the systolic pressure. In this case, the total hemoglobin is expected to stay approximately the same during occlusion. However, the skin's blood oxygenation drops over time. As a result, the tissue becomes whitish/grey in such conditions (blanching). These experimental observations are in sync with the proposed model for higher total hemoglobin concentrations. In particular, for tHb = 10%, the decrease of the x component (0.42- > 0.38) and increase in the z component are pretty significant (bluishness).

Similarly, the microvessels are dilated upon releasing the cuff, and the blood rushes into the tissue (reactive hyperemia). It causes an increase in tHb and SO_2, resulting in a large rise in the x and a decrease in the z component, making it reddish.

It should be noted that the current work is very preliminary. It requires validation and rigorous comparison with the gold standard (Monte Carlo simulations). In future work, we plan to investigate the effect of ambient illumination and skin tone on the obtained results. We also plan to validate the obtained results in Monte Carlo calculations.

In summary, we proposed a simple approach where the realistic tissue reflectance spectrum generated using the quasi-two-layer model is convoluted with CIE's color-matching functions and ambient light spectrum to obtain tristimulus values in XYZ color space. The proposed approach allows for analyzing the influence of tissue oxygenation and total hemoglobin on tissue color.

References

1. Burton T, Saiko G, Cao M, Douplik A (2022) Remote photoplethysmography with consumer smartphone reveals temporal differences between glabrous and nonglabrous skin: pilot in vivo study. JBP 16:e202200187
2. Moço AV, Stuijk S, de Haan G (2018) New insights into the origin of remote PPG signals in visible light and infrared. Sci Rep 8:8501
3. Fine I, Kaminsky A (2022) Scattering-driven PPG signal model. JBO 13(4):2286–2298
4. Maktabdar Oghaz M, Maarof MA, Zainal A et al (2015) A hybrid color space for skin detection using genetic algorithm heuristic search and principal component analysis technique. PLoS One 10(8):e0134828
5. MacAdam DL (1942) Visual sensitivities to color differences in daylight. J OSA 32(5):247–274
6. Colorimetry (1986) CIE publication 15.2, 2nd edn. Central Bureau CIE, Vienna
7. Jacques SL (1996) Origins of tissue optical properties in the UVA, visible, and NIR regions. In: Alfano RR, Fujimoto JG (eds) Advances in optical imaging and photon migration, vol 2. OSA, Washington, DC, USA pp 364–370
8. Saiko G (2022) Improved optical tissue model for tissue oximetry imaging applications. Adv Exp Med Biol 1395:211–215
9. Yudovsky D, Pilon L (2010) Rapid and accurate estimation of blood saturation, melanin content, and epidermis thickness from spectral diffuse reflectance. Appl Opt 49(10):1707–1719
10. Wyman C, Sloan PP, Shirley P (2013) Simple analytic approximations to the CIE XYZ color matching functions. J Comput Graph Technol 2(2):1–11

18 Tissue Concentration Analysis of Sulfur, Calcium and Oxygen in Novel Skin Primo Nodes After Acupuncture

Joonyoung Shin, Sangheon Choi, Hyungwon Kang, and Sungchul Kim

Abstract

Over the past 5000 years, acupuncture has been practiced in Korea, China, and Japan to relieve various diseases, and it is now widely used and accepted worldwide. Although the anatomical substance and function of meridians has been actively studied, it is still not clearly defined. One of the keys to acupuncture is determining the specific anatomical location exactly on or under the skin. We discovered that the skin primo node is a new anatomical structure in the skin of rats. The present study aimed to analyze the relationship between skin primo nodes and acupoints through changes in the expression of tissue concentrations of skin primo nodes. Analysis of this skin primo node confirmed that the skin primo node after acupuncture had a significantly higher concentration of sulfur and calcium than found in normal skin. And the significant pO_2 in the skin primo node was confirmed by measuring pO_2 using a needle oxygen sensor. Through sulfur, calcium, and pO_2 concentration values of skin primo nodes, we confirmed whether these nodes could be related to acupoint. To understand the clear structure and function of this node, it is necessary to further study through the known properties of acupoints and the function of Primo Vascular System (PVS).

Keywords

Primo vascular system · Skin primo nodes · Acupuncture

18.1 Introduction

The key to acupuncture treatment is determining the exact anatomical location of specific acupoints on or under the skin. The transposition method of positioning animal acupoints on the skin surface corresponding to the anatomical sites of human acupoints has been adopted by many researchers [1]. The distribution of mast cells (MCs) in the three acupoints of the rat abdomen (CV8, left and right KI16) allows estimation of the location, size, and depth of the acupoint [2]. In animal models of hypertension and colitis, acupoints associated with internal organs can be identical to the neurogenic inflammatory spots in the skin due to the activation of somatic afferents [3]. The ion distribution of the acupoints was studied using X-ray absorption microspectroscopy, which indicate significantly higher calcium, potassium, and sulfur ion concentrations at the stimulated acupoint [4].

J. Shin · S. Choi · H. Kang · S. Kim (✉)
Institute for Global Rare Disease Network, Professional Graduate School of Korean Medicine, Wonkwang University, Iksan, Republic of Korea

F. Scholkmann et al. (eds.), *Oxygen Transport to Tissue XLIV*, Advances in Experimental Medicine and Biology 1438, https://doi.org/10.1007/978-3-031-42003-0_18

Despite considerable efforts in the identification of acupoints, there are challenges in interpreting and comparing precise and distinct submillimeter boundaries for specific and reproducible acupoint locations.

We discovered a novel anatomical structure protruding from the epidermal layer of the rat skin and reproducibly confirmed the location and size anatomical characteristics of this structure, i.e., the skin primo node. This study aimed to analyze the relationship between skin primo nodes and acupoints through changes in the expression of sulfur, calcium, and oxygen concentrations of skin primo nodes.

18.2 Methods

All procedures were conducted in accordance with the Animal Experimentation Ethics Committee of Wonkwang University guidelines on the care and use of an-imals (approval number: WKU22-50). Sprague-Dawley rats (age, 7 weeks; weight, 220 ± 20 g) were purchased from the Charles River Technology Company. The animals were anesthetized by intramuscular injection of an anesthetic cocktail composed of alfaxalone (20 mg/kg; Jurox, Rutherford, Australia) and xylazine (5 mg/kg; Bayer, Leverkusen, Germany) into either side of the hind limbs. The average duration of anesthesia was 1–2 h.

When anesthesia was stably induced, the rat was laid flat and the hair on the abdomen was removed with an epilator. After the first hair removal, any remaining hair was carefully removed using a razor blade without damaging the skin. It was important to use normal saline when removing hair from the abdomen because the skin primo nodes were not clearly identified when using ethanol or shaving cream, which prevented the completeness of the experiment. After hair removal was complete and the saline was wiped off, the skin primo nodes of the abdomen were observed using experimental lighting and a microscope (SZX10; Olympus, Tokyo, Japan) equipped with a charged-coupled device camera (Digiretina 16; Olympus).

The partial pressure of oxygen in *in vivo* tissue (pO_2) was measured using an oxygen (O_2)-only needle-encased sensor (OxyLite Pro, Needle Oxygen Sensors Product code: NX-NP/O/E; Oxford Optronix Ltd., Abingdon, United Kingdom). The local pO_2 values were measured at independent locations on the rat abdomen: normal skin, skin primo nodes, and skin primo nodes after acupuncture (n = 5). The O_2 needle sensor was carefully positioned above each skin location, and the sensor current signal, which was linearly proportional to the pO_2 value, was monitored. Each procedure was repeated three times to determine the validity of the sensor measurements. When measuring the skin primo nodes after acupuncture, acupuncture treatment was performed for 15 min by inserting a stainless steel needle to a depth of approximately 4 mm based on the tip of the epidermis (0.18 × 8 mm; Dongbang Medical, Chungnam, Republic of Korea).

S and Ca concentrations were measured using inductively coupled plasma optical emission spectrometry (ICP-OES, iCAP 6000 Series; Thermo Scientific, Waltham, MA). The normal skin, skin primo nodes, and skin primo nodes after acupuncture were carefully sampled from the rat abdomen using fine scissors and forceps (n = 5). At least 0.1 g of tissue was collected in each group, and acupuncture was performed in the same way as the pO_2 analysis described above.

The carbon, hydrogen, nitrogen, sulfur, and oxygen (CHNSO) concentration was measured using an elemental analyzer (EA), an instrument that quantitatively analyzes the contents of carbon, hydrogen, nitrogen, S, and O_2, which are the main components of organic compounds. The elemental composition ratio (%) of an unknown sample can be obtained. In the case of O_2, it was analyzed as carbon monoxide after undergoing a thermal decomposition process at 1300 °C (FLASH 2000; Thermo Scientific). Tissues were collected to confirm the composition ratio (%) of CHNSO distributed in the skin primo nodes (n = 5), and the tissue sampling method was performed identical to the ICP-OES method.

Quantitative data are expressed as the mean ± standard deviation of five in-dependent experiments. All statistical analyses were performed using SPSS for Windows (version 26.0; IBM Corp., Armonk, NY). Data were compared between any two groups using a t-test, and a p-value <0.05 was considered to indicate a statistically significant difference.

18.3 Results

The mean skin primo node size was 0.94 ± 0.09 mm in diameter, 2.79 ± 0.23 mm in length, and 0.59 ± 0.03 mm in height, which made skin primo nodes observable even with the naked eye (n = 10). In the abdominal area of the rats, approximately 30 protruding structures were distributed on one side, positioned at 3.29 ± 0.66 mm (n = 10) apart from neighboring ones, but none were found along the linea alba (Fig. 18.1).

The mean pO_2 levels (mmHg) were 54.48 ± 1.98 in normal skin, 69.92 ± 3.86 in skin primo nodes, and 70.37 ± 1.41 in skin primo nodes after acupuncture. The pO_2 level was significantly higher by 1.28 times in skin primo nodes and by 1.29 times in skin primo nodes after acupuncture compared to normal skin (Fig. 18.2).

The mean O_2 ratios (%) were 22.84 ± 1.81 in normal skin, 21.07 ± 1.23 in skin primo nodes, and 22.10 ± 1.14 in skin primo nodes after acupuncture. The composition ratios of CHNS in each group, excluding O_2, were 76.54% in normal skin, 75.07% for skin primo nodes, and 74.04% in skin primo nodes after acupuncture (Table 18.1).

The mean S concentrations (mg/kg) were 1558 ± 137.10 in normal skin, 2328 ± 578.37 in skin primo nodes, and 3408 ± 975.86 in skin primo nodes after acupuncture. The S concentration was approximately 1.53 times higher in skin primo nodes than in normal skin. In the skin primo nodes after acupuncture, the S concentration was approximately 2.26 times higher than that in normal skin. The mean calcium concentrations (mg/kg) were 60.68 ± 8.43 in normal skin, 65.58 ± 9.29 in skin primo nodes, and 90.64 ± 17.76 in skin primo nodes after acupuncture. The calcium concentration was approximately 1.08 times higher in skin primo nodes than in normal skin. In the skin primo nodes after acupuncture, the calcium concentration was approximately 1.49 times higher than that in normal skin and approximately 1.38 times higher than that in the skin primo nodes (Table 18.1 and Fig. 18.3).

18.4 Discussion

We confirmed the location and size of skin primo nodes. To identify the specific characteristics of skin primo nodes, it is necessary to

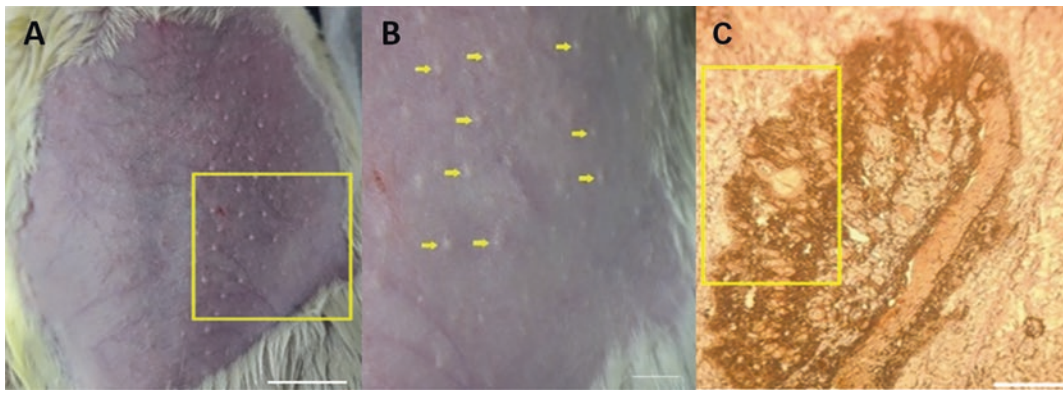

Fig. 18.1 (**a**): A skin primo node in a rat abdomen. Scale: 1.0 cm. (**b**): Magnified view of the rectangular area in (**a**); yellow arrows indicate the skin primo nodes. Scale: 5.0 mm. Fig. A(X), C(O)->(**c**): Histological observation of a skin primo node. The skin primo nodes look like straw hats on the epidermis. Scale: 0.5 mm

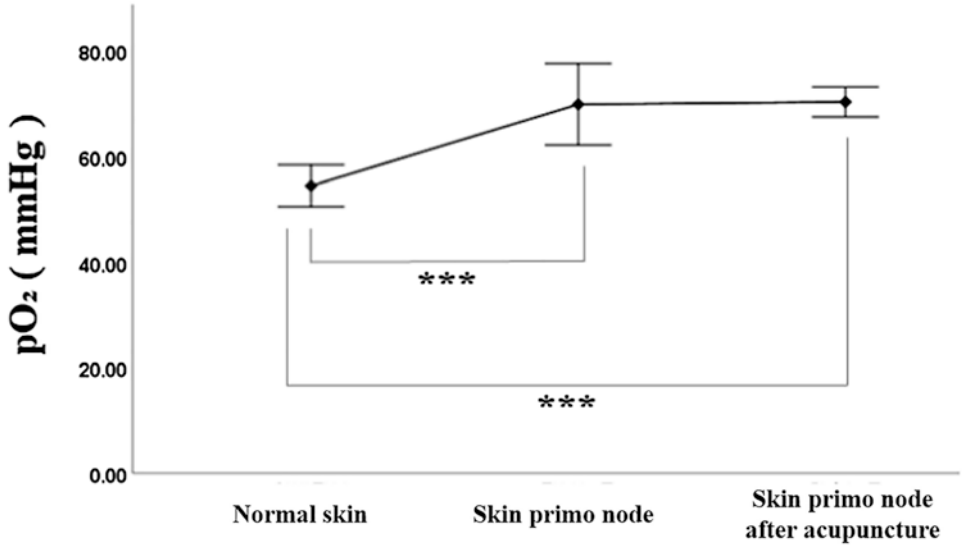

Fig. 18.2 Partial pressure of oxygen (pO_2) levels (mmHg) in normal skin, skin primo nodes, and skin primo nodes after acupuncture. Values are presented as mean ± standard deviation (n = 5). *** indicates $p < 0.001$. From left: normal skin, skin primo node, skin primo node after acupuncture

study the density of MCs in the skin primo node and to compare the anatomical positions of the acupoints and the skin primo nodes [2, 3, 5]. Analyses of the S, Ca concentration (ICP-OES) confirmed that the skin primo nodes after acupuncture had significantly higher concentrations than normal skin. As a result of applying acupuncture electrodes to rabbit acupoints, it was demonstrated that the calcium ion concentration was significantly higher than that in the location of non-meridian and non-acupoints [6]. Additionally, S has been essential for regulating various biological processes since ancient times and has been widely used for topical treatment of skin diseases and lesions [7]. It was confirmed that the pO_2 value of the skin primo nodes was significantly higher, but this EA analysis did not show significant results for oxygen. Further studies are required to find conditions that can sufficiently include the oxygen value when sampling tissue. If the S, Ca, K, and O_2 concentrations in the skin primo nodes are obviously confirmed in a future study, these values can be used as indicators to confirm the correlation between skin primo nodes and acupoints [4, 12].

Research has been actively conducted to scientifically identify the meridians system in Korea, which has been named the primo vascular system (PVS). Since the PVS was discovered by Bonghan Kim in 1961, it has been confirmed that the PVS is distributed throughout the body, and includes the lymphatic vessels [8], surface of the organs [9] and skin [10, 11] in various species of animals. Additionally, the PVS was found in the mouse embryoid body and placenta and showed a high pO_2, suggesting that the PVS plays a role in transporting O_2 throughout the body [12].

In conclusion, the significantly higher pO_2 level of the skin's primo nodes confirms the relationship with the PVS. In addition, there are significantly higher sulfur and calcium concentrations in the primo nodes and the calcium concentration were significantly increased after acupuncture. However, further studies are required to clarify the relationship between the skin's primo nodes and the acupoints.

Table 18.1 Composition ratios (%) of Carbon (C), hydrogen (H), nitrogen (N), sulfur (S) and oxygen (O_2) measured by EA. Calcium (Ca) and sulfur (S) concentration (mg/kg) measured by ICP-OES

EA	C	H	N	S	O_2	ICP-OES	Ca	S
Normal skin	54.40 ± 2.06	9.67 ± 1.74	12.36 ± 2.13	0.08 ± 0.02	22.84 ± 1.81	Normal skin	60.68 ± 8.43	1558.13 ± 137.30
Skin P-node	53.59 ± 1.26	9.18 ± 0.83	12.23 ± 2.06	0.05 ± 0.01	21.07 ± 1.23	Skin P-node	65.58 ± 9.29	2328.15 ± 578.37
Skin P-node after Acu	54.35 ± 2.27	8.81 ± 1.21	10.85 ± 1.90	0.03 ± 0.01	22.10 ± 1.14	Skin P-node after Acu	90.64 ± 17.76	3408.75 ± 975.86

Values are expressed as mean ± standard deviation (n = 5). *P-node* primo node, *Acu.* Acupuncture

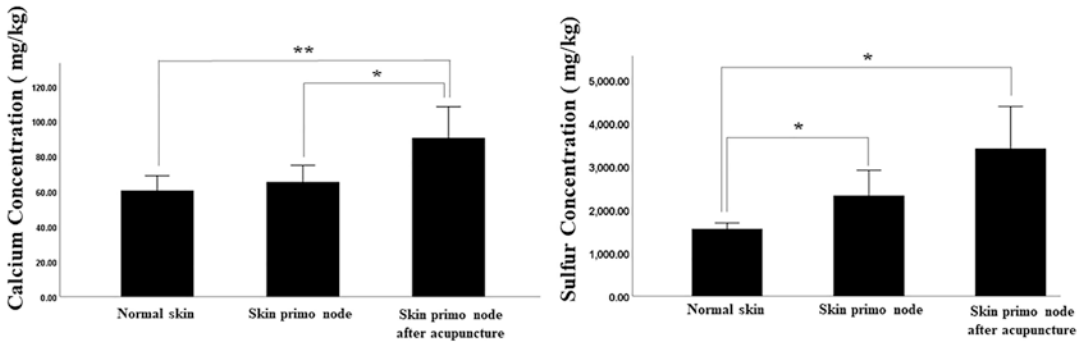

Fig. 18.3 Sulfur and calcium concentrations (mg/kg) measured by inductively coupled plasma optical emission spectrometry (ICP-OES). Values are expressed as mean ± standard deviation (n = 5). * and ** indicate $p < 0.05$ and $p < 0.01$, respectively

Acknowledgments This research was supported by a grant of the Korea Health Technology R&D Project through the Korea Health Industry Development Institute (KHIDI), funded by the Ministry of Health & Welfare, Republic of Korea (grant number: HI22C0246). I extend my heartfelt appreciation to Dr. Scholkmann Felix for his collaboration with the Korea-Switzerland international research.

References

1. Yin CS et al (2008) A proposed transpositional acupoint system in a mouse and rat model. Res Vet Sci 84(2):159–165
2. Jung SJ et al (2017) Distribution of mast cells and locations, depths, and sizes of the putative acupoints CV 8 and KI 16. Evid Based Complement Alternat Med 2017:1–10
3. Kim D-H et al (2017) Acupuncture points can be identified as cutaneous neurogenic inflammatory spots. Sci Rep 7(1):15214
4. Lee FS, Chiang TA, Lee JY (2022) Correlation between ion contents in acupuncture points and propagated sensation along channels. Acupunct Electrother Res 47(3):329–340
5. Zhang D et al (2008) Role of mast cells in acupuncture effect: a pilot study. Explore 4(3):170–177
6. Guo Y, Xu T, Chen J, Zhang C et al (1991) The study on calcium ion concentration specificity in meridian and acupoint in rabbit. Acupunct Res 16(1):66–68
7. Kopriva S et al (2015) Plant sulfur and big data. Plant Sci 241:1–10
8. Jung SJ, Bae KH, Nam M et al (2013) Primo vascular system floating in lymph ducts of rats. J Acupunct Meridian Stud 6(6):306–318
9. Lim CJ, Yoo JH, Kim Y et al (2013) Gross morphological features of the organ surface primo-vascular system revealed by hem color staining. Evid Based Complement Alternat Med 2013:350815
10. Stefanov M, Kim J (2015) Visualizing the peripheral primo vascular system in mice skin by using the polymer mercox. J Pharm 18(3):75–79
11. Bae KH, Gil HJ, Yoo YY (2015) Neurovascular primo bundles at the kidney meridian revealed using hem color staining. J Acupunct Meridian Stud 8(6):329–332
12. Hong M et al (2012) Study of the primo-vascular system and location-dependent oxygen levels for a mouse embryo. J Nanosci Nanotechnol 12(7):5168–5172

19 Primo Vessels Inside Lymphatic Vessels Are Absent in an ALS Mouse Model

Joonyoung Shin, Hyungwon Kang, and Sungchul Kim

Abstract

Amyotrophic lateral sclerosis (ALS) is a neurodegenerative disease characterized by the selective death of motor neurons in the central nervous system. It is also a representative rare disease among degenerative diseases of the nervous system. Although many drugs for the treatment of degenerative brain diseases are being developed, they are not delivered correctly to the target due to the blood-brain barrier. The present study aimed to analyze changes in the primo vascular system (PVS) in ALS mice with symptoms and the partial oxygen pressure (pO_2) in normal mice. In normal mice, we consistently observed primo vessels in lymphatic vessels (L-PVS). However, in ALS mice with symptoms, L-PVS were mostly lost, rendering them difficult to observe. The pO_2 of the L-PVS in normal mice was significantly higher than that of normal dermis and lymph nodes.

In conclusion, the relatively higher oxygen levels measured in the L-PVS than in normal dermis and lymph nodes suggest a role for the PVS in oxygen transport and enable a hypothesis that the L-PVS can function as a drug delivery pathway.

Keywords

Amyotrophic lateral sclerosis · Primo vascular system · Lymphatic vessels

19.1 Introduction

Amyotrophic lateral sclerosis (ALS) is a neurodegenerative disease that is characterized by the selective death of motor neurons in the spinal cord, brainstem, and motor cortex. Patients with ALS experience a gradual loss of motor function due to muscle atrophy and degeneration [1]. One of the causes of death is the cessation of oxygen exchange during sleep, which occurs when respiratory muscle contraction stops [2]. Degenerative brain diseases have complex causes, such as neurological damage, reduced blood flow, decreased lymphatic secretion due to aging, and the expression of disease genes [3]. One of the challenges in treating these diseases is the inability to deliver drugs properly to the CNS due to the blood-brain barrier (BBB) [4]. Therefore, studies that investigate drug delivery methods capable of bypassing the BBB are necessary.

It has been discovered that the primary pathway for draining cerebrospinal fluid, which contains brain waste, is through the meningeal lymphatic vessels (mLVs) located in the lower part of the brain. Moreover, it has been confirmed that the function of mLVs decreases with aging

J. Shin · H. Kang · S. Kim (✉)
Institute for Global Rare Disease Network, Professional Graduate School of Korean Medicine, Wonkwang University, Iksan, Republic of Korea

F. Scholkmann et al. (eds.), *Oxygen Transport to Tissue XLIV*, Advances in Experimental Medicine and Biology 1438, https://doi.org/10.1007/978-3-031-42003-0_19

[5]. These mLVs could potentially provide a solution to prevent inhibition of drug delivery by the BBB. Furthermore, there is the possibility of using the primo vessels in lymphatic vessels (L-PVS) as a pathway for delivering drugs to the brain.

Since the discovery of the primo vascular system (PVS) by Bong Han Kim in 1961, it has been confirmed that the PVS is distributed throughout the body, including the brain [6], lymphatic vessels [7], the surface of organs [8], and the dermis [9], across various animal species. Additionally, primo vessels were found in mouse embryos and placenta, and displayed a high partial pressure of oxygen (pO_2), suggesting that the PVS may serve as a means of oxygen transport throughout the body [10]. In this study, we confirmed the possibility of the L-PVS serving as an oxygen transport and drug delivery pathway by analyzing the loss of primo tissues and pO_2.

19.2 Methods

All procedures were conducted in accordance with the Animal Experimentation Ethics Committee of Wonkwang University guidelines on the care and use of animals (approval number: WKU21-83). The physiological model SPF/VAF inbred mice were purchased from Orient Bio Company. The SOD1G93A Tg mice are hemizygous transgenic B6SJL mice that carry a mutant human SOD1 gene, which has a glycine to alanine base pair mutation at the 93rd codon of the cytosolic Cu/Zn SOD1 [B6SJL − Tg (SOD1 × G93A)1Gur/J]. The transgenic mice used in this study were purchased from Jackson Laboratories. All animals were maintained under normal laboratory conditions (temperature: 21–23 °C, 12-h light-dark cycles with the light on at 6:00 AM) with unlimited access to food and water. The animals were anesthetized by intramuscular injection of an anesthetic cocktail composed of alfaxalone (20 mg/kg; Jurox, Rutherford, Australia) and xylazine (5 mg/kg; Bayer, Leverkusen, Germany) into either side of the hind limbs. To prepare for staining, a 5% Evans Blue (EB, Sigma Chemical, USA) solution in phosphate-buffered saline (PBS, Life Technologies Corporation, USA) was made. To ensure a stable EB solution, it was mixed for 3 min using a vortex and filtered using a 0.2 μm syringe filter (Sigma Chemical, USA). After incision of the subcutaneous layer of the right inguinal, the preheated EB solution was injected into the inguinal lymph node in a warm bath at 37 °C. To promote the natural circulation of lymph fluid inside the vessel, the incised inguinal was covered with warm gauze and kept for 3 h. After 3 h of EB solution injection, the surrounding adipose tissue was removed to observe the lymphatic vessels connected to the inguinal lymph nodes. The L-PVS next to the abdominal aorta were observed after an abdominal incision. All observations were made using a microscope (SZX10 Olympus, EVOS M7000 Thermo Fisher Scientific, USA) with a CCD camera (Digiretina 16, Olympus, USA).

The pO_2 was measured using an Oxygen needle sensor (OxyLite Pro, Needle Oxygen Sensors with product code "NX-NP/O/E", United Kingdom). This sensor features greater physical robustness, making it suitable for localized oxygen measurements from virtually any tissue type. The pO_2 values were measured independently at four different locations in the mouse: the normal dermis, inguinal lymph nodes, L-PVS, and arterial blood vessels. The pO_2 value of normal dermis was measured by inserting a sensor between the dermis and subcutaneous fat after incising the epidermis by about 1.5 mm. The pO_2 value of L-PVS was measured by placing one side of the sensor inserted into the needle and the lymph-primo vessel. The pO_2 value of arterial blood vessels was measured by inserting the needle sensor into the abdominal aorta. The pO_2 value of the lymph node was measured by carefully placing the sensor in the measurement position and monitoring the sensor current signal, which is linearly proportional to the pO_2 value. Indeed, the needle sensor was capable of measuring the oxygen levels in the regions of the L-PVS, inguinal lymph nodes, arterial blood vessels and normal dermis ($n = 5$). Measurements were repeated three times for each group to determine the validity of sensor measurements.

The quantitative data are expressed as the mean ± standard deviation of five independent experiments. All statistical analyses were conducted using SPSS for Windows (version 26.0; IBM Corp., Armonk, NY). Data were compared between any two groups using a t-test, and a p-value < 0.01 was considered to indicate a statistically significant difference.

19.3 Results

The lymph nodes of normal mice were milky in color, whereas lymph nodes in ALS mice with symptoms were slightly yellow (Fig. 19.1a). Lymphatic vessels connected to the inguinal lymph node did not exhibit L-PVS (Fig. 19.1b). Furthermore, the gall bladder inside the liver was very enlarged and bright yellow (Fig. 19.1c).

The pO_2 values in normal mice were measured in the normal dermis, inguinal lymph nodes, L-PVS connected to inguinal lymph nodes, and arterial blood vessels using the Needle Oxygen Sensors (Fig. 19.2). The mean pO_2 values (mmHg) were 56 ± 4 in normal dermis, 45 ± 5 in inguinal lymph nodes, 68 ± 4 in L-PVS, and 91 ± 7 in arterial blood vessels near the inguinal lymph nodes. The value of arterial blood vessels was significantly higher than that of the other groups, while the pO_2 value of L-PVS was significantly higher than that of the normal dermis and lymph nodes. After injecting the EB solution, we observed the L-PVs in the inguinal and next to the abdominal aorta. The diameter of L-PVS was 37.20 ± 12.17 μm (Fig. 19.3a) and 43.73 ± 19.35 μm (Fig. 19.3b), respectively, and the short axis size of primo nodes was 61.58 ± 19.88 μm (Fig. 19.3c).

19.4 Discussion

In ALS mice with symptoms, the absence of L-PVS was confirmed through histological analysis, making it the first case of L-PVS observation experiment in ALS mice. Considering that the function of mLVs declines with aging, which is one of the causes of degenerative brain diseases [5], the loss of L-PVS in ALS mice with symptoms suggests that L-PVS plays a major role in the waste excretion function of mLVs. While this study only confirmed the absence of L-PVS around the inguinal area in ALS mice with symptoms, further studies are needed to confirm the loss of observable L-PVS in the brain, such as mLVs [5] and superior sagittal sinus (SSS) [6]. If the loss of L-PVS in the brain is clearly confirmed, it is expected to increase the understanding of degenerative brain diseases and provide a theoretical basis for drug delivery.

The pO_2 levels of L-PVS in normal mice were found to be significant using appropriate measurement methods for each location, including normal dermis, inguinal lymph nodes, lymph-primo vessels, and arterial blood vessels. In this study, the oxygen partial pressure value of the

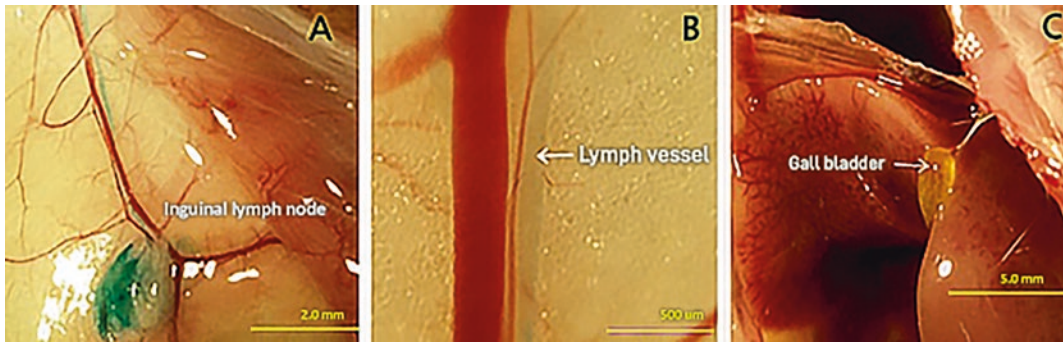

Fig. 19.1 Histological changes in the ALS mice with symptoms. (**a**): Slightly yellow discolored inguinal lymph node. Scale: 2 mm. (**b**): The L-PVS was not observed in ALS mice with symptoms. Scale: 500um. (**c**): The gall bladder discolored yellow inside the liver. Scale: 5 mm

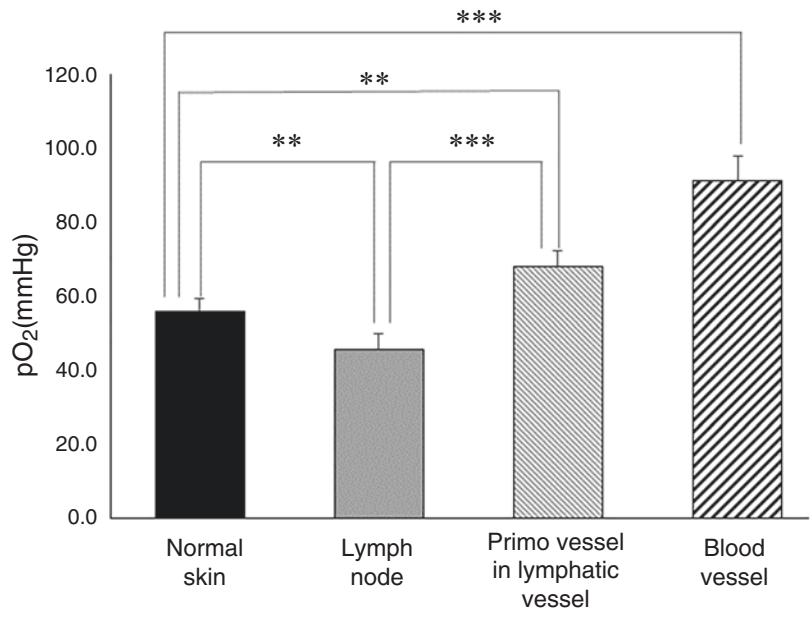

Fig. 19.2 The pO_2 values in normal mice. Values are expressed as mean ± standard deviation (n = 5). ** and *** indicate $p < 0.01$, and $p < 0.001$, respectively

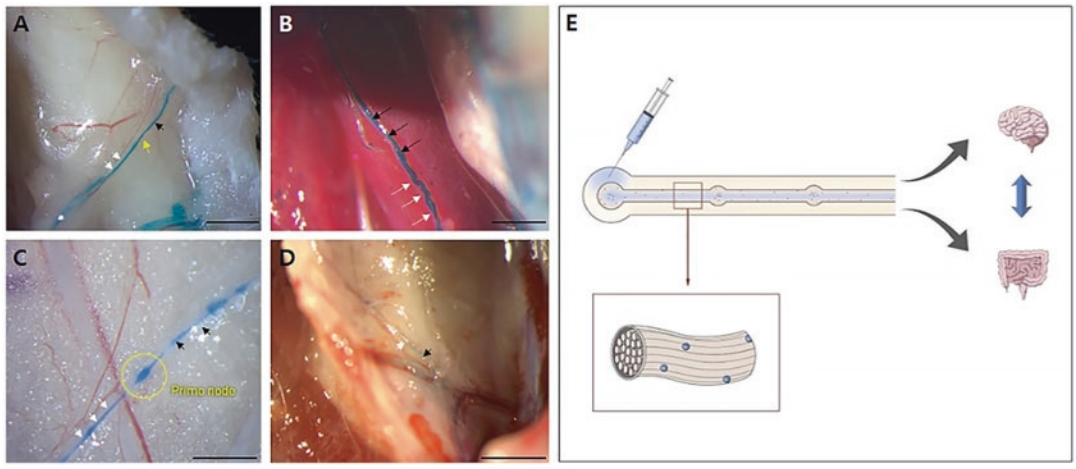

Fig. 19.3 The L-PVS in normal mice after EB injection. (**a**–**d**): black, white, and yellow arrow indicate L-PVS, lymph vessel, and primo node, respectively. Scale: **a**: 1 mm, **b**: 300 um, **c**: 300 um, **d**: 500 um. (**e**): The diagram of Kim's method for drug delivery pathway through L-PVS

entire diameter of the lymphatic vessel was obtained due to the physical size of the oxygen sensors, and a significant difference was shown compared to normal dermis and lymph nodes. However, to accurately measure the oxygen partial pressure values of the primo vessels inside the lymphatic vessels, additional research using nanopore-based amperometry with an oxygen microsensor with a pore diameter of less than 1 μm is required. Furthermore, additional research is needed to verify the oxygen transport role of L-PVS through changes in the oxygen partial pressure in the pathological model by measuring the oxygen partial pressure of the lymph vessels in mice with ALS symptoms using this microsensor. According to Kwang Sup Soh et al., the PVS is involved in transporting various materials within the body, including oxygen, car-

bon dioxide, immune-related materials, and waste [11]. PVS circulates throughout the body and controls various vital functions of living organisms. Therefore, the results of this study suggest that the PVS plays a role in oxygen transport.

In conclusion, we propose a hypothesis for the role of L-PVS as a drug delivery pathway. When the EB solution was injected into the inguinal lymph nodes, it was easily excreted due to the rapid circulation of lymphatic fluid, while L-PVS absorbed the EB solution through the wall of endothelial cells (10 ~ 20 μm) and was well preserved. By continuously tracking L-PVS, it was confirmed that even the left temporal bone area was stained (Fig. 19.3d). Drugs, oxygen, and immune substances transported through L-PVS could be delivered directly into the brain without BBB restriction. To improve this hypothesis, further studies on the spinal cord and brain are required, suggesting that it could be an innovative method for treating degenerative brain diseases such as ALS and Alzheimer's disease (Fig. 19.3e).

Acknowledgments This research was supported by a grant of the Korea Health Technology R&D Project through the Korea Health Industry Development Institute (KHIDI), funded by the Ministry of Health & Welfare, Republic of Korea (grant number : HI22C0246), and the Traditional Korean Medicine R&D Project(B110076). The authors thank the late Professor Kwang-sup Soh for gifting microscopic instruments used in this study. I extend my heartfelt appreciation to Dr. Kyounghee Bae for providing the idea for this study and Minha Kang for the illustration work, as well as to Dr. Scholkmann Felix for his collaboration with the Korea-Switzerland international research.

References

1. Kiernan MC et al (2011) Amyotrophic lateral sclerosis. Lancet 377(9769):942–955
2. Walling A (1999) Amyotrophic lateral sclerosis: Lou Gehrig's disease. Am Fam Physician 59(6):1489
3. Knight RA, Verkhratsky A (2010) Neurodegenerative diseases: failures in brain connectivity? Cell Death Differ 17(7):1069–1070
4. Jessica ML, Martin DR, Byrne ME (2014) Recent advances in delivery through the blood-brain barrier. Curr Top Med Chem 14(9):1148–1160
5. Ahn JH et al (2019) Meningeal lymphatic vessels at the skull base drain cerebrospinal fluid. Nature 572(7767):62–66
6. Nam M-H et al (2012) A primo vascular system underneath the superior sagittal sinus in the brain of a rabbit. J Acupunct Meridian Stud 5(5):210–217
7. Jung SJ et al (2013) Primo vascular system floating in lymph ducts of rats. J Acupunct Meridian Stud 6(6):306–318
8. Lim CJ, Yoo JH, Kim Y et al (2013) Gross morphological features of the organ surface primo-vascular system revealed by hemacolor staining. Evidence-Based Complementary and Alternative Medicine Article ID 350815, 12 pages
9. Stefanov M, Kim J (2015) Visualizing the peripheral primo vascular system in mice dermis by using the polymer mercox. J Pharm 18(3):75
10. Hong M et al (2012) Study of the primo-vascular system and location dependent oxygen levels for a mouse embryo. J Nanosci Nanotechnol 12(7):5168–5172
11. Soh K-S (2009) Bonghan circulatory system as an extension of acupuncture meridians. J Acupunct Meridian Stud 2(2):93–106

Part III

Tumor Oxygenation

The Impact of Heterogeneous Cell Density in Hypoxic Tumors Treated with Radiotherapy

20

Filippo Schiavo, Iuliana Toma-Dasu, and Emely Kjellsson Lindblom

Abstract

Hypoxia is frequently found in solid tumors and is known to increase the resistance to several kinds of treatment modalities including radiation therapy. Besides, the treatment response is also largely determined by the total number of clonogenic cells, i.e., cells with unlimited proliferative capacity. Depending on the duration of hypoxia, the rate of proliferation and hence also the clonogen density could be expected to differ in hypoxic compartments. The combination at the microscale between heterogeneous tumor oxygenation and clonogen density could therefore be crucial with respect to the outcome of a radiotherapy treatment. In this study it was investigated the impact of heterogeneous clonogen density on the outcome of stereotactic radiotherapy treatments of hypoxic tumors. A recently developed three-dimensional model for tissue vasculature and oxygenation was used to create realistic *in silico* tumors with heterogeneous oxygenation. Stereotactic radiotherapy treatments were simulated, and cell survival was calculated on a voxel-level accounting for the oxygenation. For a tumor with a diameter of 1 cm and a baseline clonogenic density of $10^7/cm^3$ for the normoxic subvolume, when the relative density for the hypoxic cells drops by a factor of 10 the tumor control probability (TCP) decreases by about 10% when relatively small hypoxic volumes and few fractions are considered; longer treatments tend to level out the results. With increasing size of the hypoxic subvolume, the TCP decreased overall as expected, and the difference in TCP between a homogeneous and a heterogeneous distribution of cells increased. The results demonstrate a delicate interplay between the heterogeneous distribution of tumor oxygenation and clonogenic cells that could significantly impact on the treatment outcome of radiotherapy.

Keywords

Hypoxia · Tumors · Radiotherapy

20.1 Introduction

The impact of tumor hypoxia on the outcome of radiation therapies has been extensively discussed for long time. The relationship between the poor vascular structure and a gain in resistance due to the reduced number of free radicals

F. Schiavo (✉) · I. Toma-Dasu · E. Kjellsson Lindblom
Department of Physics, Stockholm University, Stockholm, Sweden

Department of Oncology and Pathology, Karolinska Institutet, Solna, Sweden
e-mail: filippo.schiavo@fysik.su.se

F. Scholkmann et al. (eds.), *Oxygen Transport to Tissue XLIV*, Advances in Experimental Medicine and Biology 1438, https://doi.org/10.1007/978-3-031-42003-0_20

explains the higher likelihood of failure in patient presenting with tumor hypoxia [1]. Despite being overly promoted in solid tumors, neither angiogenesis nor vasculogenesis can lead to the formation of a network of fully functional capillaries orderly distributed to cover the required volume uniformly [2]. This is intimately related to the rapid tumor growth which does not allow for a proper development of new vasculature [3].

Hypoxic tumors are characterized by an accentuated expression of the hallmarks of cancer [4], enhanced signaling of factors promoting for instance their metastatic spread, escape from the immune system and cell life prolongation. However, the spectrum of radiation therapy techniques now available include treatment strategies that in some cases seem to neutralize the negative impact of the aggressive tumor phenotype. One example is the case of early stage hypoxic brain tumors when treated with high radiation doses in stereotactic radiotherapy (SRT) approaches. Other aspects may play a balancing role: while the influence of not fully understood mechanisms such as the role of the immune response or bystander effect should be accounted for, there may be other more tangible factors that could provide a justification of the observed results, such as the density of clonogens in the tumor.

While the availability of cellular oxygen and nutrients is fundamental for proliferation and growth of the tumor, hypoxic subvolumes, where there is a deficiency of organized vessels and hypoxia assumes chronic connotates, are characterized by a reduced proliferation and hence a lower count of cells per unit volume [5]. Conversely, one could expect that in the tumor periphery, being closer to the healthy tissues and generally burdened at most by cyclic and time-limited inactivation of vessels functionality (acute hypoxia), the vasculature would promote the growth and the expansion of the tumor, leading to a higher clonogenic density.

Despite the relevance of the subject and the seemingly non-difficult task, previous studies addressing the determination of volumetric cell density *in vivo* are scarce and data differ widely, while *in vitro* measures performed on 2D samples are not generalizable to more complex 3D structures. Furthermore, when organoids are produced in a laboratory, only the seeding procedure is described in terms of the initial number of cells and the final volume obtained, detaching from further cell counting at the end.

This work, through the 3D simulation of tumor vasculature and oxygenation, aims at covering the resulting gap and explores the role of the interplay between the levels of oxygenation available locally, and the proliferation status of the cells in relative terms, but based on absolute density values reported in the literature, on the probability of controlling the tumor.

20.2 Methods

20.2.1 Modelling of the Radiosensitivity and Clonogenic Density

The study was based on *in silico* modelling of the tumor vasculature and oxygenation. A recent 3D model developed by the authors was used [6], in which the vasculature is built following elements of fractal theory. In this model a spherical tumor with a diameter of 1 cm is perfused by a network of capillaries that enter the periphery in a regularized and spatially homogeneous fashion. In the core of the tumor, the regularity is lost and the density of vessels per unit volume is lower. Through a finite difference method, the oxygen transport equation is solved and the spatial pO_2 map calculated. Using a conversion function proposed previously, the oxygenation map was converted to an oxygen dose modifying factor map [7]. The radiation response of isolated hypoxic cells in the oxygenated region was assumed not to be directly related to their oxygenation but higher, in order to prevent the case when the response of the whole tumor will be dominated by their presence leading therefore to loss of tumor control.

A cross-section through the modelled tumor is depicted in Fig. 20.1b. All the simulations were performed under two scenarios: a stable condition of chronic hypoxia during the stereotactic treatment, where the tumor core was not subject

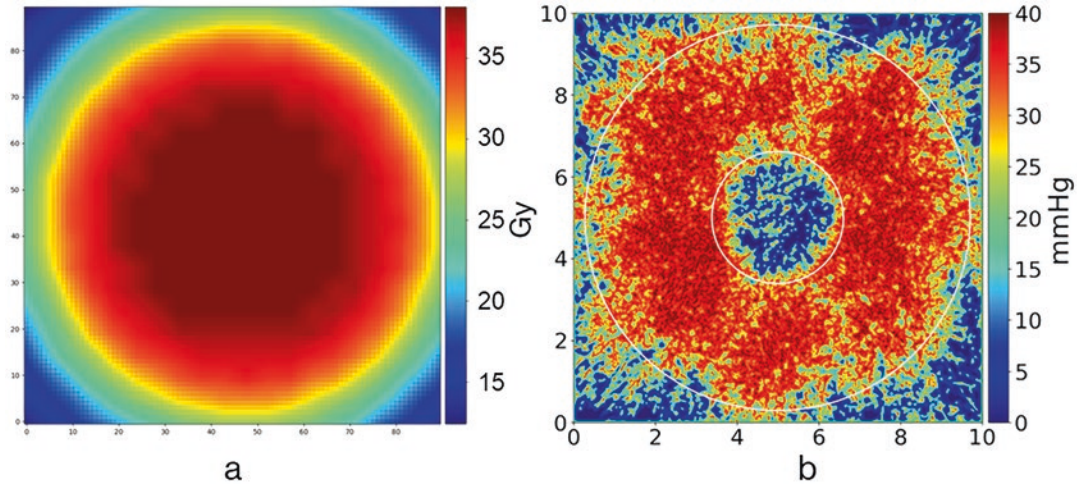

Fig. 20.1 Dose distribution of the Gamma Knife treatment plan, with color scale in Gy (**a**), and tumor oxygenation model, color scale in mmHg of pO_2 (**b**)

to changes in radiosensitivity, and a condition of cyclic hypoxia superimposed to the previous case with a fraction of vessels in the tumor core randomly inactivated at each dose fraction. Moreover, the effect of the size of the hypoxic tumor core was studied by varying it from 4% to 25% of the total tumor volume.

In order to account for the heterogeneity of the clonogenic cell density in the tumor, a 3D matrix developed in parallel with the oxygenation map was used to store the local values at voxel level. Several combinations of density were used, ranging from constant in the whole volume to a ratio of 1:20 between the hypoxic and the oxygenated subvolumes, respectively. The density and hence the total number of cells in the well-perfused region was kept constant independently of the level of heterogeneity. For the simulations with homogeneous density the total number of cells was maintained the same as for the well-oxygenated region in the corresponding heterogenous case. The baseline density used for the well-perfused region was chosen according to a study suggesting that the density of clonogens, in relation to the overall density of cells in a tumor, is commonly overestimated; therefore, the "canonical" density of 10^9 cells/cm^3 was reduced to 10^7 clonogens/cm^3 [8].

20.2.2 Clinical Radiotherapy Plans and Tumor Control Probability, TCP, Calculation

A Gamma Knife treatment plan was used in the simulations. The dose distribution characteristic of the Gamma Knife is inherently heterogeneous, with the prescribed dose typically achieved at the periphery of the tumor while the core receives up to twice the amount of radiation.

In this study a simulated tumor of 1 cm in diameter was prescribed an iso-effective dose of 60 Gy in 2 Gy per fraction on a well-oxygenated population of cells, delivered in one up to five fractions (see Fig. 20.1a for the single fraction treatment). Here, iso-effective dose refers to the biologically equivalent dose (BED) that would produce the same cell kill as the treatment schedule being studied, but with an infinite number of fractions of infinitesimally small size and well-spaced in time. This quantity is often used as touchstone when comparing different treatment schedules with respect to fractionation.

The simulations were assessed and compared in terms of TCP, which was calculated at voxel level using the typical LQ-Poisson expression:

$$TCP = \prod_i \exp\left(-N_i\, SF_i\right), \text{with } SF_i = \exp\left(-n\left(\frac{\alpha d}{OMF} + \frac{\beta d^2}{OMF^2}\right)\right) \quad (20.1)$$

where i indexes volume voxels, N_i is the number of clonogens, SF_i is the surviving fraction, n is the number of treatment fractions, α and β are radiobiological parameters of the tumor (assumed to be 0.35 Gy^{-1} and 0.035 Gy^{-2} for this study), d is the dose per fraction and OMF is the oxygen modifying factor.

20.3 Results and Discussion

Table 20.1 summarizes the results of the simulations related to a condition of stable chronic hypoxia throughout the treatment, a heterogeneous density of clonogenic cells depending on the hypoxic status and for varying fractionation scheme and varying hypoxic volume size; the condition of mutable acute hypoxia did not worsen the outcome significantly due to the already limited number of vessels in the tumor core. Figure 20.2 shows a surface plot for the 3-fractions treatment as an example of the dataset; the other fractionation schemes showed similar trends scaled according to the number of fractions.

As expected, for smaller hypoxic volumes and for lower clonogenic density associated to it one would find higher chances of tumor control, while the increase of the two parameters leads to high failure rate. Although the two parameters are correlated, it is noticeable how the volume shows a relatively higher impact on the outcome, as steps of 5–15% cover a higher extent of probabilities with respect to the counterpart in density. It is worth mentioning that such trends depend also on which sector of the TCP curve they fall, i.e., either on the steep tract of it, or in the saturating sides of the sigmoid. The combinations of values were set to avoid saturation towards low or high values of TCP, however a combination of parameters leaning towards the bending tracts of the TCP curve could slightly reduce the sensitivity to variations of the same parameters.

The general trend of higher TCP values for the treatment delivered in a larger number of fractions is explained by the fact that the BED for hypoxic cells increases with the number of fractions: for an iso-effective dose of 60 Gy for normoxic cells, the BED for the most hypoxic cells ($\alpha/\beta = 30$ Gy) increased from 33.3 to 43.5 GyBED.

The TCP values of the simulations using homogeneous densities were lower than the heterogeneous counterpart, due to the higher number of hypoxic cells considered. The difference in TCP increased for increasing clonogenic heterogeneity and for larger relative hypoxic volume, but tends to level out at increasing fractionation.

The simulation of the outcome of the treatments was therefore successfully performed although some inherent limitations of the model to account for the complexity of the factors influencing the overall response to the treatment lead initially to predictions of systematic loss of tumor control because of the presence of small volumes

Table 20.1 Tumor control probabilities (in %) in the modelled tumors for varying number of treatment fractions (fx), relative hypoxic volumes (HV) with respect to the tumor volume (TV) and relative clonogenic densities under the condition of stable chronic hypoxia

Tumor control probability (%)												
	HV = 4% TV				HV = 10% TV				HV = 25% TV			
	Relative clonogenic density hypoxic/oxygenated											
	0.5	0.33	0.1	0.05	0.5	0.33	0.1	0.05	0.5	0.33	0.1	0.05
1 fx	47	49	51	52	34	39	48	50	0	0	2	10
2 fx	65	66	67	68	58	61	66	67	0	1	21	38
3 fx	74	75	76	76	70	72	75	75	4	11	43	57
4 fx	80	80	80	80	77	78	80	80	16	27	58	68
5 fx	83	83	84	84	81	82	83	83	30	42	68	76

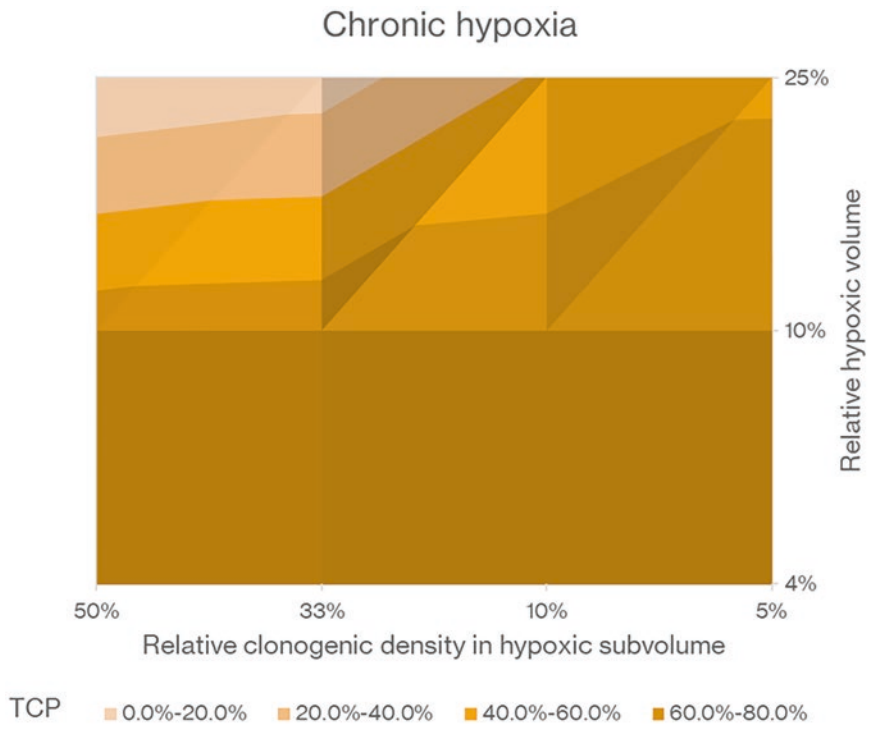

Fig. 20.2 Surface TCP plot for the 3-fractionated Gamma Knife treatment for varying relative hypoxic volume and relative clonogenic density in the hypoxic volume

of hypoxic cells in the well-oxygenated regions of the tumor. Although this can be viewed as a pitfall of the model, it is actually observed the situation of few isolated hypoxic cells even in areas of the tumor that are well-perfused [9]. The rate of success of the stereotactic radiotherapy treatments is however not as low as initially predicted, and therefore, to prevent this potential limitation of the model, these isolated hypoxic cells were assumed to have a higher radiosensitivity than predicted by their oxygenation in order to account for other possible factors that may successfully counteract their presence such as the local action of the immune response, the bystander effect, with hypoxic cells being affected by biochemicals released by surrounding dead or dying cells, or the effect of the fast re-oxygenation, where vessels previously inactivated start to transport oxygen again, due to the cyclic nature of acute hypoxia or due to a larger availability of oxygen that is no longer consumed by the eradicated radiosensitive cells.

This study offers a preliminary approach for analyzing the relations among variables associated to the hypoxic status of the patient (hypoxic volume), type of tumor (clonogenic density), and treatment schedule (number of fractions, total dose, time in-between fractions, etc.). A tool based on such premises could constitute a valuable instrument for the planner in helping to choose the treatment parameters that maximize the probability of success based on the radiobiological information available. With this tool, the realization of the concept of radiobiological optimization in radiotherapy is thus one important step closer.

20.4 Conclusions

The results demonstrate a delicate interplay between the heterogeneous distribution of tumor oxygenation, the extent of the hypoxic volumes and clonogenic cells that could significantly

impact on the treatment outcome of radiotherapy. Adding the dynamic nature of hypoxia during fractionated radiotherapy is expected to result in a more complex relationship when the vasculature is not already too deteriorated.

Acknowledgments Financial support from the Cancer Research Funds of Radiumhemmet and The Swedish Research Council (2020-04618) is gratefully acknowledged. The computations were partly enabled by resources provided by the Swedish National Infrastructure for Computing (SNIC) at "PDC Center for High Performance Computing, KTH Royal Institute of Technology" partially funded by the Swedish Research Council through grant agreement no. 2018-05973.

References

1. Overgaard J (2007) Hypoxic radiosensitization: adored and ignored. J Clin Oncol 25(26):4066–4074. https://doi.org/10.1200/JCO.2007.12.7878
2. Vaupel P, Mayer A (2007) Hypoxia in cancer: significance and impact on clinical outcome. Cancer Metastasis Rev 26(2):225–239. https://doi.org/10.1007/s10555-007-9055-1
3. Li XF, Carlin S, Urano M, Russell J et al (2007) Visualization of hypoxia in microscopic tumors by immunofluorescent microscopy. Cancer Res 67(16):7646–7653. https://doi.org/10.1158/0008-5472.CAN-06-4353
4. Hanahan D, Weinberg RA (2011) Hallmarks of cancer: the next generation. Cell 144(5):646–674. https://doi.org/10.1016/j.cell.2011.02.013
5. Li Y, Zhao L, Li XF (2021) Hypoxia and the tumor microenvironment. Technol Cancer Res Treat 20:15330338211036304. https://doi.org/10.1177/15330338211036304
6. Schiavo F, Kjellsson Lindblom E, Toma-Dasu I (2022) Towards the virtual tumor for optimizing radiotherapy treatments of hypoxic tumors: a novel model of heterogeneous tissue vasculature and oxygenation. J Theor Biol 547:111175. https://doi.org/10.1016/j.jtbi.2022.111175
7. Toma-Dasu I, Dasu A (2013) Modelling tumor oxygenation, reoxygenation and implications on treatment outcome. Comput Math Methods Med 2013:141087. https://doi.org/10.1155/2013/141087
8. Del Monte U (2009) Does the cell number 10(9) still really fit one gram of tumor tissue? Cell Cycle 8(3):505–506. https://doi.org/10.4161/cc.8.3.7608
9. Vaupel P, Mayer A (2016) Tumor hypoxia: causative mechanisms, microregional heterogeneities, and the role of tissue-based hypoxia markers. Adv Exp Med Biol 923:77–86. https://doi.org/10.1007/978-3-319-38810-6_11

21

A Critical Analysis of Possible Mechanisms for the Oxygen Effect in Radiation Therapy with FLASH

Harold M. Swartz, Peter Vaupel, and Ann Barry Flood

Abstract

The aim of this review is to stimulate readers to undertake appropriate investigations of the mechanism for a possible oxygen effect in FLASH. FLASH is a method of delivery of radiation that empirically, in animal models, appears to decrease the impact of radiation on normal tissues while retaining full effect on tumors. This has the potential for achieving a significantly increased effectiveness of radiation therapy. The mechanism is not known but, especially in view of the prominent role that oxygen has in the effects of radiation, investigations of mechanisms of FLASH have often focused on impacts of FLASH on oxygen levels. We and others have previously shown that simple differential depletion of oxygen directly changing the response to radiation is not a likely mechanism. In this review we consider how time-varying changes in oxygen levels could account for the FLASH effect by changing oxygen-dependent signaling in cells. While the methods of delivering FLASH are still evolving, current approaches for FLASH can differ from conventional irradiation in several ways that can impact the pattern of oxygen consumption: the rate of delivery of the radiation (40 Gy/s vs. 0.1 Gy/s), the time over which each fraction is delivered (e.g., <0.5 s. vs. 300 s), the delivery in pulses, the number of fractions, the size of the fractions, and the total duration of treatment. Taking these differences into account and recognizing that cell signaling is an intrinsic component of the need for cells to maintain steady-state conditions and, therefore, is activated by small changes in the environment, we delineate the potential time dependent changes in oxygen consumption and overview the cell

H. M. Swartz (✉)
Geisel School of Medicine, Dartmouth College, Hanover, NH, USA

Dartmouth Cancer Center, Dartmouth-Hitchcock Medical Center, Lebanon, NH, USA

Thayer School of Engineering, Dartmouth College, Hanover, NH, USA
e-mail: harold.swartz@dartmouth.edu

P. Vaupel
Department of Radiation Oncology, University Medical Center, University of Freiburg/Brsg., Freiburg, Germany

German Cancer Consortium (DKTK) Partner Site Freiburg, German Cancer Research Center (DKFZ), Heidelberg, Germany

A. B. Flood
Geisel School of Medicine, Dartmouth College, Hanover, NH, USA

Dartmouth Cancer Center, Dartmouth-Hitchcock Medical Center, Lebanon, NH, USA

F. Scholkmann et al. (eds.), *Oxygen Transport to Tissue XLIV*, Advances in Experimental Medicine and Biology 1438, https://doi.org/10.1007/978-3-031-42003-0_21

signaling pathways whose differential activation by FLASH could account for the observed biological effects of FLASH. We speculate that the most likely pathways are those involved in repair of damaged DNA.

Keywords

FLASH · Radiation therapy · Cancer · DNA damage repair

21.1 Introduction

Radiation oncology, in trying to achieve better patient outcomes, has generally sought to balance achieving maximum control over tumor growth/survival (by delivering a high total dose of ionizing radiation to the tumor), while minimizing damage to adjacent normal tissues (by focusing the delivery of the radiation to the tumor while minimizing the dose to the adjacent normal tissues). Recently, a new method of radiotherapy, termed "FLASH", has emerged using extremely high dose rates to deliver the total dose. The great enthusiasm among radiation oncologists for this delivery approach is fueled by evidence that using FLASH, compared to using conventional dose rates, causes less damage to normal tissues (the damage being similar to what would be expected from a conventional therapy with a 1.3–2.0 times lower total dose), while the impact on tumor tissue is equivalent to the higher total dose [1–3]. This phenomenon is referred to as the FLASH effect. While the enthusiasm for FLASH is leading to clinical studies, these are at a very preliminary stage; systematic data are available only from preclinical studies.

Despite numerous preclinical studies using FLASH (using many variants of delivery of high dose rates) and theoretical modeling, the mechanisms of action are not well understood. Because of the important role of oxygen in responses of cells to ionizing radiation, the leading theories for the mechanisms of FLASH are related to changes in the levels of oxygen in tissues during the course of treatment. But to date there is only modest evidence that oxygen plays a major role in FLASH and no definitive evidence for a particular mechanism for it [4, 5].

21.1.1 Why Is Oxygen a Prime Suspect to Explain the FLASH Effect?

Initially the principal speculations about the role of oxygen in the FLASH effect were based on the hypothesis that FLASH caused much more depletion of oxygen than conventional radiation delivery, directly decreasing the response to radiation. While it is well known that the response of cells to radiation is significantly impacted by the level of oxygen, its impact occurs principally when the oxygen tension is less than 20 mmHg [6]. While there are some plausible (but not well-proven) mechanisms for FLASH to cause more oxygen consumption per unit of energy absorbed, a key aspect is the magnitude of the consumption. This has been calculated theoretically and there also have been some direct measurements [5, 7]. The results indicate that the difference in consumption is less than a few mmHg, which would not be likely to change the response of normal tissues, whose mean oxygen levels are usually well above 20 mm Hg. In addition, tumors usually have low oxygen levels in the range of <10 mmHg, where well established evidence shows that small changes in oxygen should lead to very significant decreases in the response to radiation. Therefore, it is clear that increased consumption of oxygen by FLASH should not directly impact the classical oxygen effect on cells, i.e., this cannot explain the FLASH effect [8].

We hypothesize that if changes in oxygen have a mechanistic role for FLASH, they must occur through small, transitory changes in oxygen. Such changes could alter cell signaling, which then ultimately impacts the response of cells to radiation, but in a less direct manner.

21.1.2 How FLASH Could Impact Consumption of Oxygen and Type of Damage to DNA

Because damage to DNA is the ultimate cause of most or all of the effects of ionizing radiation on cell viability, it is especially useful to examine how irradiation using the dose rates of FLASH compared to those of conventional radiation might impact the damage to DNA and subsequent interactions with oxygen [9].

The following schema summarizes some of the pertinent reactions of a DNA radical formed by ionizing radiation. (Definitions: RH = intact DNA; R• = DNA radical; OH• = hydroxyl radical; H• = hydrogen atom; PSH = sulfhydryl; PS• = sulfhydryl radical; XY = unspecified chemical species; Y• = unspecified chemical radical; ROO• = DNA peroxy radical.)

1. **RH + radiation → primary products → R• + H•** (direct damage)
2. **RH + OH• → R• + H_2O** (indirect damage)
3. **R• + PSH → RH + PS•** (chemical repair; e.g., by SH-containing compounds or ascorbate)
4. **R• + R• → R-R** (crosslink, may be enzyme repairable)
5. **R• + XY → RX + Y•** (chemical addition, may be enzyme repairable)
6. **R• + O_2 → ROO•** (damage that is not as readily repairable; this competes with *reactions 3–5*, increasing the amount and also the type of damage)

Oxygen with its two unpaired electrons can readily react with the DNA radical, forming a peroxide (*reaction 6*) that is likely to interfere with biological repair of DNA damage.

The high dose rate of FLASH should result in higher local concentrations of primary products of radiation through both indirect (i.e., production of very reactive intermediates of water such as OH•) and direct mechanisms. This would increase the initial yields of *reactions 3–6* because of the increased amount of DNA radicals. This would result in a transient increased consumption of oxygen and other reactants. The higher density of DNA radicals also should lead to a change in the relative amounts of different types of damage to DNA. This is clearly illustrated by *reaction 4*, but probably will impact virtually all pathways of damage to DNA and the extent of the immediate chemical repair illustrated by *reaction 3*. Note that this chemical repair is different from biochemical repair mechanisms, which involve enzymatic repair to deal with damaged products. Most pertinent to this review, chemical repair mechanisms occur in very short time frames (microseconds or shorter, while biochemical repair takes place over hours and days). Importantly, because of the high rate constants for *reactions 3–6*, these reactions would not be affected by diffusion of components not already present, i.e., because the diffusion coefficient of oxygen within cells is about (0.5–1) × 10–5 $cm^2\ s^{-1}$, the pertinent oxygen for these chemical reactions would be oxygen in the vicinity of the DNA radicals [10]. Therefore, the level of oxygen for these reactions to occur during FLASH would be lower than would be the case with conventional dose rates, because the extended time over which conventional radiation is delivered would result in replenishing of oxygen through diffusion while this would not occur during FLASH, especially when considering rather shallow oxygen gradients in hypoxic cancer tissue.

21.2 FLASH Could Differentially Impact Oxygen Levels

21.2.1 Patterns of FLASH-Induced Changes of Oxygen Would Differ from Conventional Radiation

The differences potentially include:

- FLASH could transiently decrease oxygen levels more than would occur with conventional radiation dose rates.
- Reoxygenation via diffusion during the irradiation period would be less with FLASH because of the shorter duration during which radiation is delivered.
- Because FLASH is typically delivered in pulses, the pattern of transitory changes in

oxygen levels would be quite different, resulting in a series of transitory decreases in oxygen levels with an incomplete return to steady state between each pulse.
- If (as is often the case currently) FLASH is delivered in larger doses per fraction, the intervals between fractions and the total period of treatment would differ.

Because of all these potential differences between FLASH and conventional radiation delivery, their independent and interactive effects on signaling pathways need to be considered in order to conclude whether the FLASH effect is due to different amounts and patterns of transitory effects on oxygen levels. For example, cells irradiated with FLASH would likely experience a greater drop in oxygen level, but the radiation-induced consumption of oxygen would be present for a shorter time, e.g., microseconds instead of minutes. Therefore, to study whether a particular signaling pathway is being differentially impacted by FLASH, all the ways in which oxygen consumption could differ would need to be considered, e.g., its magnitude, the time sequence of consumption and reoxygenation, and the length of time during which irradiation would continue to induce changes in oxygen levels.

21.2.2 Signaling Pathways That Could Be Altered Due to FLASH

A number of cell signaling pathways that potentially respond to damage from ionizing radiation could ultimately differentially alter the impact of FLASH on normal versus malignant cells. Leading candidates for such pathways should have:

- A plausible impact on the outcome from damage from absorption of radiation;
- A plausible different pathway in normal cells *versus* tumor cells, and
- A potential for being sensitive to changes in oxygen levels.

We propose six pathways as the most likely to fit these criteria. While there is some overlap, they also differ sufficiently to make it desirable to investigate each separately. In general, data are sparse regarding the impact of local oxygen levels on the activation/inactivation of these pathways. We discuss pathways in the order of their likelihood to account for the FLASH phenomenon.

1. ***DNA repair systems*** DNA repair systems have a very significant impact on the biological consequences of the initial chemical damage to DNA and therefore are the most obvious candidates to look at for having their function modified by transient changes in oxygen levels. There are different types of radiation damage to DNA, and each is likely to be repaired by a different set of enzymes with different signaling pathways that activate them. The most obvious is the repair of single strand breaks *versus* double strand breaks [11], but other types of damage are presumably repaired through other pathways, e.g., repair of peroxides in the DNA.
2. ***Responses to hypoxia*** Several signaling pathways are triggered by the presence of hypoxia, especially those involving HIF-1α. However, even for this oxygen-responsive pathway, data on the quantitative relationship between transitory changes in oxygen levels and activation of signaling pathways is sparse and may be different in different tumor types. The numerous changes that can be induced by activating these pathways could each plausibly impact responses to damage from radiation, and these responses are likely to differ between tumor and corresponding normal tissues.
3. ***Responses to inflammation*** Several signaling pathways are activated by the presence of inflammation, and radiation damage is known to activate some of these. Among such pathways to consider are p38 MAPK, IL-6/JAK/STAT3 and PI3K, and Hippo. Recently, the Hippo pathway, which controls organ size by regulating cell proliferation, apoptosis, and stem cell self-renewal and its dysregulation has been linked to cancer development, i.e.,

has been linked to various inflammatory modulators [12] such as FoxO1/3, TNF-α, IL-6, COX2, HIF-1α, AP-1, JAK and STAT.

4. ***Responses to stress*** Radiation is a known stressor, and the effect of radiation is increased in the presence of other stressors. This has been studied most extensively for the combination of unplanned radiation exposures and concomitant trauma [13]. As an example of a pathway, the endoplasmic reticulum (ER) unfolded protein response (UPR) is activated by biosynthetic stress and leads to a compensatory increase in ER function. The JNK and p38 MAPK signaling pathways control adaptive responses to intracellular and extracellular stresses, including environmental changes such as UV irradiation, heat, and hyperosmotic conditions, and exposure to inflammatory cytokines. Metabolic stress caused by a high-fat diet represents an example of a stimulus that coordinately activates both the UPR and JNK/p38 signaling pathways [14].
5. ***Cell progression through the mitotic cycle*** The response to radiation varies significantly in the various phases of the cell cycle. Therefore, modulation of factors that regulate the cell cycle could have a significant impact on the response to radiation therapy. Cell cycle progression is mediated by a complex set of cell signaling, centering on the cyclin-dependent kinases (Cdks) and their regulatory cyclin subunits. Cdks are activated mainly by binding to their cyclin partners, whose expressions rise and fall throughout the cell cycle to mediate the temporal activation of each Cdks. Various cell cycle checkpoints exist to ensure that critical processes are engaged prior to progression to the next phase. There are three major cell cycle checkpoints: the G1/S checkpoint (also referred as restriction point), the G2/M DNA damage checkpoint, and the spindle assembly checkpoint (SAC). Growth factors also have important roles in regulating cell division [15].
6. ***Pathways associated with the immune response*** The immune response is certainly impacted by the level of oxygen [16–18]. Because the dose from FLASH is delivered over a much shorter time than by conventional radiation, it seems possible that this could have a role in the normal tissue sparing seen with FLASH. For example, the potentially greater volume of blood that would circulate through the radiation field with the longer time for conventional radiation, combined with high sensitivity of lymphocytes to ionizing radiation, could impact immune responses and some of those responses are oxygen-dependent. The signaling pathways for the impact of oxygen are not yet well-delineated but, as these become known, they would be another set of pathways to examine to account for the FLASH effect via transitory changes in oxygen.

21.3 Testing Whether the FLASH Effect Is Indirectly Due to Small Transitory Changes in Oxygen Levels Associated with Cell Signaling

21.3.1 Measurements of Oxygen

Direct testing whether oxygen plays an indirect role in the FLASH effect would require data measuring time dependent changes in local oxygen levels during and immediately after irradiation with FLASH versus conventional dose rates. While these data could potentially be calculated instead of measured, this is intrinsically difficult because there is no consensus about the radiation chemistry and physics involved in FLASH. Furthermore, such calculations would need to be specific for each type of delivery of FLASH and conventional radiation, i.e., considering source of the radiation (e.g., protons vs. photons), dose rate, and pulse structure.

Experimental measurements of the changes in oxygen would also be very challenging. Ideally, it would be desirable to have excellent resolution of the time course of the changes (at least milliseconds) within a volume no larger

than a cell nucleus. Currently no available techniques can provide such data. Development of appropriate methods using optical techniques seem most promising, e.g., developing using probes that selectively localize in the desired regions and can provide robust measurement of oxygen, and have sufficient time resolution to follow the radiation-induced changes in local oxygen. EPR oximetry could also potentially provide such data If methods are developed to place sufficient oximetry probes within the desired volume, i.e., by localizing highly sensitive EPR oximetry probes such as lithium phthalocyanine.

21.3.2 Determining Impact of Plausible Changes in Oxygen on Cell Signaling Pathways

Assuming data on the time course of changes are available through theoretical calculation and/or direct measurements, the impact of the time course of changes in oxygen should be studied for each pathway of interest. The importance of oxygen-mediated changes on signaling pathways could then be tested experimentally using small changes in oxygen with the measured or calculated patterns that occur with FLASH in combination with techniques that block or highly activate signaling pathways.

While all such plans would be very desirable, realistically, precise information on the time course of changes in oxygen from FLASH and conventional dose radiation-induced are not likely to become available, at least in the near term. In the meantime, it is possible (and indeed very desirable) to directly investigate the relevant oxygen dependence of the signaling pathways of interest by experimentally inducing small changes in patterns of oxygen levels and measuring the impact on signaling. Such investigations can and should be undertaken immediately.

21.4 Summary

While the magnitude of the changes in oxygen levels from FLASH versus radiation delivered at conventional rates is not likely to affect acute, *direct* radiation responses of normal tissues, they could be sufficient to impact signaling mechanisms in cells. Even small changes could activate cell signaling pathways, because cells and tissues are finely tuned to respond to small alterations in their microenvironment.

We delineated several patterns of transitory changes in oxygen that can differ between FLASH and conventionally administered radiation. Besides differing in magnitude, time patterns of oxygen levels can differ very significantly due to the shorter interval over which each dose of FLASH is delivered, the use of pulsed doses in FLASH, and potential differences in the number of fractions, time between fractions, and the total dose and duration of treatment.

The small, but real changes in oxygen levels during FLASH could very plausibly result in up-regulation and/or down-regulation of signaling pathways that cells utilize to maintain a more favorable environment in response to the change in critical parameters, e.g., oxygenation status. Tumors often have defects in such regulatory pathways, which could account for differences in responses between normal and tumor tissues during FLASH.

In principle, almost any signaling pathway could have altered signaling in response to transient changes in the oxygenation. We identified six different areas of signaling pathways that can differ in tumors and could be impacted by the changes in oxygen levels. Arguably, the most likely pathway that could result in the observed differences in response to injury from ionizing radiation include DNA-repair processes. But many other pathways could be affected and result in a change in the response to radiation, including systems that are specifically activated by hypoxia, inflammatory responses, stress responses, regulation of the cell cycle, and the immune system.

We wish to emphasize that the aim of this paper is to stimulate greater awareness of the opportunity and importance of studying the potential impact of small changes in oxygen levels on cellular signaling, especially as a means to rationally and effectively facilitate translating the empirical observation of the FLASH effect into improvements in radiation therapy of cancer. At a minimum, understanding the basis for the protective effect of FLASH would enable safer and more effective clinical translation of its use.

Acknowledgments This work was supported by NIH grant U01 CA260446.

References

1. Al-Hallaq H, Cao M, Kruse J et al (2019) Cured in a FLASH: reducing normal tissue toxicities using ultra-high-dose rates. Int J Radiat Onc Biol Phys 104:257–260
2. Favaudon V, Caplier L, Monceau V et al (2014) Ultrahigh dose-rate FLASH irradiation increases the differential response between normal and tumor tissue in mice. Sci Transl Med 6:245–293
3. Wilson JD, Hammond EM, Higgins GS et al (2020) Ultra-high dose rate (FLASH) radiotherapy: silver bullet or fool's gold? Front Oncol 9(1–12):1563
4. Friedl AA, Prise KM, Butterworth KT, Montay-Gruel P, Favaudon V (2022) Radiobiology of the FLASH effect. Med Phys 49:1993–2013
5. Jansen J, Beyreuther E, García-Calderón D, Karsch L, Knoll J, Pawelke J, Schürer M, Seco J (2022) Changes in radical levels as a cause for the FLASH effect: impact of beam structure parameters at ultra-high dose rates on oxygen depletion in water. Radiother Oncol 175:193–196
6. Cao X, Zhang R, Esipova TV et al (2021) Quantification of oxygen depletion during FLASH irradiation *in vitro* and *in vivo*. Int J Radiat Oncol Biol Phys 111:240–248
7. Hall EJ, Giaccia AJ (2018) Radiobiology for the radiologist, 8th edn. Lippincott Williams & Wilkins. Philadelphia, PA
8. Swartz HM, Hoopes PJ, Gladstone DJ, Demidov V, Vaupel P, Flood AB, Williams BB, Zhang R, Pogue BW (2022) A radiation biological analysis of the oxygen effect as a possible mechanism in FLASH. Adv Exp Med Biol 1395:315–321
9. Perstin A, Poirier Y, Sawant A, Tambasco M (2022) Quantifying the DNA-damaging effects of FLASH irradiation with plasmid DNA. Int J Radiat Oncol Biol Phys 113(2):437–447
10. Grote J, Suesskind R, Vaupel P (1977) Oxygen diffusivity in tumor tissue (DS-Carcinosarcoma) under temperature conditions within the range of 20-40°C. Pflug Arch 372:37–42
11. Nikitaki Z, Velalopoulou A, Zanni V, Tremi I, Havaki S, Kokkoris M, Gorgoulis VG, Koumenis C, Georgakilas AG (2022) Key biological mechanisms involved in high-LET radiation therapies with a focus on DNA damage and repair. Expert Rev Molecul Med 24(e15):1–15
12. Yeung YT, Aziz F, Guerrero-Castilla A, Arguelles S (2018) Signaling pathways in inflammation and anti-inflammatory therapies. Curr Pharm Des 24(14):1449–1484. https://doi.org/10.2174/1381612824666180327165604 PMID: 29589535
13. US Dept Human Service REMM (Radiation Emergency Medical Management). Radiation + Trauma (Combined Injury) https://remm.hhs.gov/radtrauma.htm. Accessed 6 Nov 2022
14. Hotamisligil GS, Davis RJ (2016) Cell signaling and stress responses. Cold Spring Harb Perspect Biol 8(10):a006072. https://doi.org/10.1101/cshperspect.a006072. PMID: 27698029; PMCID: PMC5046695
15. Wang Z (2021) Regulation of cell cycle progression by growth factor-induced cell signaling. Cell 10:3327. https://doi.org/10.3390/cells10123327
16. O'Hara JA, Blumenthal RD, Grinberg OY et al (2001) Response to radioimmunotherapy correlates with tumor pO_2 measured by EPR oximetry in human tumor xenografts. Radiat Res 155:466–473
17. Ohta A (2018) Oxygen-dependent regulation of immune checkpoint mechanisms. Int Immunol 30(8):335–343. https://doi.org/10.1093/intimm/dxy038
18. Multhoff G, Vaupel P (2020) Hypoxia compromises anti-cancer immune responses. Adv Exp Med Biol 1232:131–143. https://doi.org/10.1007/978-3-030-34461-0_18 PMID: 31893404

22

Hyperhydration of Cancers: A Characteristic Biophysical Trait Strongly Increasing O_2, CO_2, Glucose and Lactate Diffusivities, and Improving Thermophysical Properties of Solid Malignancies

Peter Vaupel and Helmut Piazena

Abstract

Cancers are complex, heterogeneous, dynamic and aggressive diseases exhibiting a series of characteristic biophysical traits which complement the original biological hallmarks of cancers favouring progressive growth, metastasis, and contributing to immune evasion and treatment resistance. One of the prevalent differences between most solid tumors and their corresponding, healthy tissues is a significantly higher water content (hyperhydration) in cancers. As a consequence, cancers have distinctly higher (Fick's) diffusion coefficients D [$cm^2\ s^{-1}$] for the respiratory gases O_2 and CO_2, the key substrate glucose, and for the oncometabolite lactate. In addition, cancers have (a) clearly increased specific heat capacities c_p [$J\ g^{-1}\ K^{-1}$], thus representing high-capacity-tissues upon therapeutic heating induced by electromagnetic irradiation, and (b) higher thermal conductivities k [$W\ m^{-1}\ K^{-1}$], i.e., increased abilities to conduct heat. Therefore, in diffusion analyses (e.g., when describing critical O_2 and glucose supplies or CO_2 removal, and the development of hypoxic subvolumes) and for modeling temperature distributions in hyperthermia treatment planning, these specific cancer-related data must be considered in order to reliably reflect oncologic thermo-radiotherapy settings.

Keywords

Tumor · Hyperhydration; tumor · Oxygen diffusion coefficient; tumor · Carbon dioxide diffusion coefficient; tumor · Glucose diffusion coefficient; tumor · Lactate diffusion coefficient; cancers · Thermophysical properties; tumor · Oxygen solubility; tumor · Specific heat capacity; tumor · Thermal conductivity · Cancer · Hyperhydration · Ncologic thermo-radiotherapy

P. Vaupel (✉)
Department of Radiation Oncology, University Medical Center, University of Freiburg, Freiburg/Breisgau, Germany

German Cancer Consortium (DKTK) Partner Site Freiburg, German Cancer Research Center (DKFZ), Heidelberg, Germany
e-mail: vaupel@uni-mainz.de

H. Piazena
Department of Anesthesiology and Intensive Care Medicine, Charité-University Medicine, Berlin, Germany
e-mail: helmut.piazena@charite.de

F. Scholkmann et al. (eds.), *Oxygen Transport to Tissue XLIV*, Advances in Experimental Medicine and Biology 1438, https://doi.org/10.1007/978-3-031-42003-0_22

22.1 Introduction

Cancer is a highly aggressive disease exhibiting a series of characteristic biophysical traits which complement the original biological hallmarks of cancers favouring progressive growth, metastasis and contributing to immune evasion and treatment resistance. Besides elevated solid stress, increased interstitial water spaces, elevated interstitial fluid pressure and altered material properties [1, 2], hyperhydration, i.e., increased water content C_w [wt. %] compared to their corresponding, healthy tissues is another general hallmark [3] leading to (a) higher diffusion coefficients D [$cm^2 \bullet s^{-1}$] for respiratory gases, for relevant substrates (e.g., glucose, glutamine), for lactate (substrate and/or metabolite), and for low-molecular diagnostic and therapeutic substances, (b) higher specific heat capacities c_p [$J\ g^{-1}\ K^{-1}$] (leading to preferred heat deposition in cancerous tissues, thus acting as "heat-reservoirs" upon adjuvant hyperthermia induced by electromagnetic irradiation), (c) higher thermal conductivities k [$W\ m^{-1}\ K^{-1}$], i.e., increased ability of the tumor tissues to conduct heat, and (d) higher electrical conductivities σ [$S\ m^{-1}$], i.e., easier flow of electric currents through cancers [4]. In this updated data compilation, we will focus on the distinct correlation between tissue water content of normal and cancerous tissues and biologically relevant diffusion coefficients (O_2, CO_2, glucose, lactate). In addition, selected therapeutically relevant thermophysical properties (specific heat capacity, thermal conductivity) as a function of tissue water content will be exemplarily reviewed.

22.2 Materials and Methods

Systematic literature reviews (published before September 15, 2022) of the parameters listed above were conducted to provide an updated, comprehensive data overview based on original articles, reviews and databases. Special emphasis has been placed on reliable data published in the ISOTT Proceedings series starting in 1973. Values presented in this extended review are averaged means. Reliability of summarized data has been assumed despite the use of a multitude of measuring techniques, often unknown measuring accuracies and the slightly differing tissue characteristics that are apparent in the original studies [5].

22.3 Hyperhydration of Cancer Tissues

Cancer tissues generally have a distinctly higher water content (C_w = 80–88 wt.%) compared to their adjacent or homologous healthy tissues (C_w = 53–79 wt.%) [3, 6–9]. For example, cancers of the breast, primary and metastatic lung cancers, cancers of the kidneys, skin, pancreas, liver and most prostate cancers, malignant brain tumors and intracerebral metastases have higher water contents than surrounding, healthy tissues [3, 8]. This pathophysiological characteristic, first recognized in the late 1940s [9], is mostly due to plasma leakage from the immature, hyperpermeable tumor microvessels arising during tumor angiogenesis and a compromised lymphatic drainage, both resulting in an expansion of the interstitial space [10]. Another pathogenetic factor leading to hyperhydration of malignant tumors is passive hyperaemia (vasocongestion), as seen in a series of tumor types (reviewed in [3, 11]). *Note:* Generally higher C_w-values are also found in highly proliferative embryonic and foetal tissues [3].

22.4 Diffusion Coefficients in Solid Malignancies

In the mid-1970s, the effect of percentual water content in tissues and body fluids on Fick's diffusion coefficient D [$cm^2\ s^{-1}$] of respiratory gases was investigated in order to roughly estimate/predict the diffusion coefficient (diffusion constant, "diffusivity") in various tissues with known water content (C_w) [12, 13]. Plots of available data for O_2 and CO_2 (T = 37 °C) revealed distinctly, exponentially increasing diffusion coefficients starting from C_w-values of 68 wt.% (cytosol of red blood cells), including soft tissues, body fluids and liquid water at 37 °C [12].

In this updated article, O_2, CO_2, glucose and lactate diffusion coefficients as a function of differing tissue water contents are presented in order to allow reliable analyses when modeling (critical) oxygen or glucose supply, and carbon dioxide and lactate removal in cancer tissues, respectively.

22.4.1 Diffusion Coefficients for O_2 and CO_2 of Normal Tissues *Versus* Hyperhydrated Cancers

Coefficients of free diffusion for *oxygen* in water (preferred value: 3.0–3.15 × 10^{-5} cm^2 s^{-1} at 37 °C [12, 13]), biological media and body fluids (blue circles), soft tissues (blue dots) and tumors (red dots) have been updated [14–16] and are plotted as a function of water content (65–100 wt.%) in Fig. 22.1. With lowering water content (100–65 wt. %), mean Do_2-values linearly decrease reaching approximately 50% of the value of water in tissues with a water content of ≈79 wt.% (e.g., kidneys, parenchymal lung), and ≈25% of the values of water in tissues with a water content typical for the skin, the fibro-glandular breast tissue or the aortic wall (≈65 wt.%). Due to their increased water contents, malignancies have higher O_2 diffusion coefficients than their homologous or adjacent healthy tissues. Assuming a mean increase in C_W of 15% in cancers [3], Do_2 is expected to increase by a factor of ≈1.9. In experimental mouse and rat tumor xenotransplants in the renal cortex, even moderate increases in the water content (+4 wt.%) have been shown to lead to higher O_2 diffusion coefficients (by a factor of 1.23), as described previously [15].

Note: O_2 solubilities (α_{O2}) in various tissues and tumors as a function of water content are presented in Fig. 22.2. With increasing water content, mean α_{O2} values increase linearly, the tumors having higher solubilities than the normal tissues [13, 17]. Accordingly, Krogh's diffusion coefficient (K = α D) increases with increasing C_w.

The preferred diffusion coefficient for *carbon dioxide* in water is 2.4 × 10^{-5} cm^2 s^{-1} (37 °C, [12, 14]). The quotient Do_2/Dco_2 (pure water at 37 °C) is ≈1.3. This quotient is almost constant (1.2–1.4) for soft tissues and body fluids, i.e., in the C_W-range 65–100 wt.%. Diffusion coefficients for CO_2 (37 °C) in water and body fluids (blue dots) and soft tissues (blue circles) as a function of water content (C_W) are listed in Fig. 22.3. For describing gas transfers in tumor tissues, reliable data for CO_2 diffusion coefficients are not currently available. As a rough estimate, it is proposed to use the following approximation: $Dco_2 = o_2/1.3$, taking into account the respective water content of the tissue of interest.

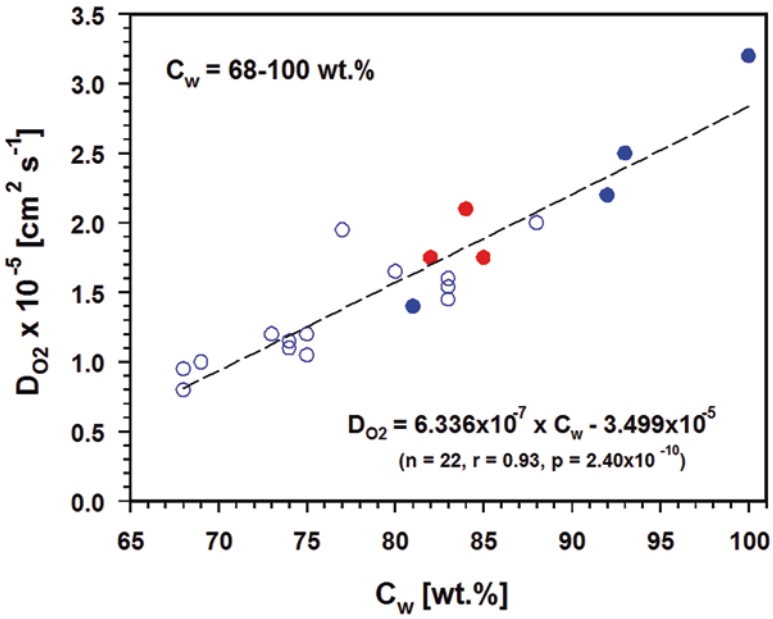

Fig. 22.1 Fick's diffusion coefficient for oxygen (Do_2) in pure water and body fluids (blue dots), healthy human tissues (blue circles) and in tumour tissues (red dots) as a function of water content within the range C_w = 68–100 wt.% (T = 37 °C). Updated values are averaged means. Within this range, Do_2 decreases linearly with decreasing water content

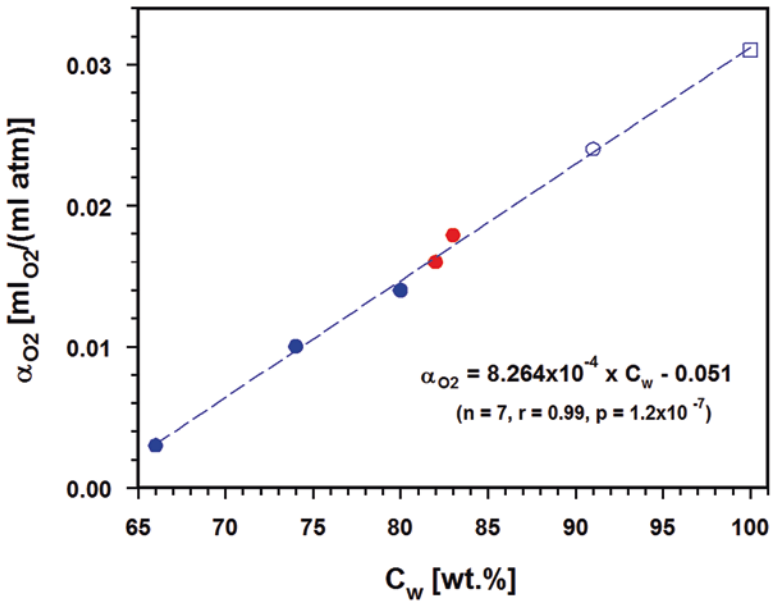

Fig. 22.2 Oxygen solubility (α_{O2}) as a function of water content in normal tissues (blue dots), in cancer tissues (red dots), and in serum (blue circle). Solubility in pure water at 37 °C: open square. (Based on data provided in [13, 17])

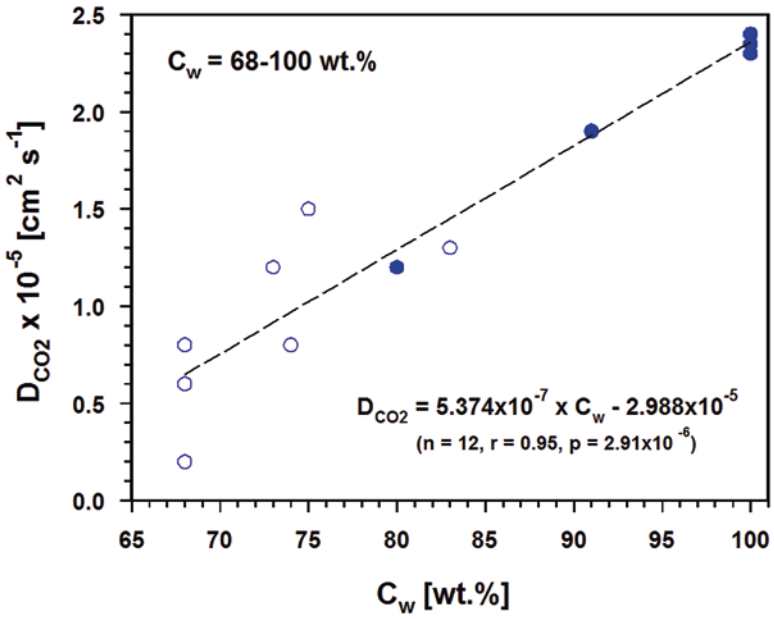

Fig. 22.3 Diffusion coefficients for carbon dioxide CO_2 (Dco_2) in pure water, body fluids (blue dots) and human tissues (blue circles) as a function of mean water content within the range C_w = 68–100 wt.% (values are averaged means). Within this range of water contents, Dco_2 decreases linearly with decreasing water content. So far, reliable Dco_2 values for tumours are not available

22.4.2 Diffusion Coefficients for Glucose and Lactate of Normal Tissues *Versus* Hyperhydrated Cancers

For malignant, *non-hypoxic tumors*, glucose is the key substrate for adequate ATP production (via complete oxidation in the mitochondria), and for the backup and diversion of glycolytic intermediates, thus facilitating the synthesis of biomass (via aerobic glycolysis, the 'Warburg Effect' resulting from metabolic reprogramming) [18]. In *hypoxic subvolumes of tumors* glucose is heavily used to maintain energy homeostasis (anaerobic glycolysis). In order to model these different metabolic situations and to estimate "critical" diffusion distances, the respective

tumor-specific diffusion coefficients for oxygen, glucose and lactate must be known.

Upon anaerobic and aerobic glycolysis, lactate is accumulated in malignant tumors (up to 40 mM). To reliably judge the diffusive supply of glucose and removal of lactate, which is a substrate of aerobic cancer cells and a metabolite which promotes metastasis, angiogenesis, antitumor immune escape, and facilitates therapeutic resistance [19], the respective diffusion coefficients must be known.

The preferred diffusion coefficient for *glucose* (D_{gluc}) in water at 37 °C is 9×10^{-6} cm^2 s^{-1} [19]. Reliable data for glucose diffusion coefficients in normal tissues and tumors have been reported less frequently [20–32]. From Fig. 22.4 there is clear evidence that the diffusion coefficient for D-glucose exponentially decreases with decreasing water fraction in different tissue types derived from a rodent sarcoma cell line, as reported in the mid-1970s [20]. The respective data for pure water [20] and cytoplasm [21] are added for comparison.

In order to demonstrate the stringent correlation between water content (C_W) and glucose diffusivity in different tissue types derived from a rodent sarcoma cell line, diffusion coefficients for glucose D_{gluc} (T = 37 °C) are plotted over a large range of water contents of biological media [20–25], of malignant tumors [20], and a series of normal tissues (skeletal muscle [26], myocardium [27], connective tissue [28], skin [29], cornea and sclera [30], dura [31], brain [32], cartilage [33] and aortic wall [34]; for a comprehensive data review see [30]). The water content of tumor specimens has been presented in [20], and the respective data for normal tissues have been comprehensively reviewed recently [3]. The decrease in D_{gluc} with diminishing water content can best be described by an exponential function (Fig. 22.5).

The preferred diffusion coefficient for *lactate* (D_{lac}) in water is 13.5×10^{-6} cm^2 s^{-1} (T = 37 °C) [23, 35]. In general, reliable data for lactate diffusion coefficients for normal and malignant tissues are scarce [23, 34–39] (Fig. 22.6). From the available data it can be concluded that lactate diffusivity exponentially declines with decreasing water contents. For an estimate of lactate diffusivity in water at 37 °C it is proposed to use the following approximation: $D_{lac} \approx 1.45\ D_{gluc}$.

Diffusion coefficients for small molecules (32 g mol^{-1} < MW < 180 g mol^{-1}) presented in this Chapter show a relationship with solute

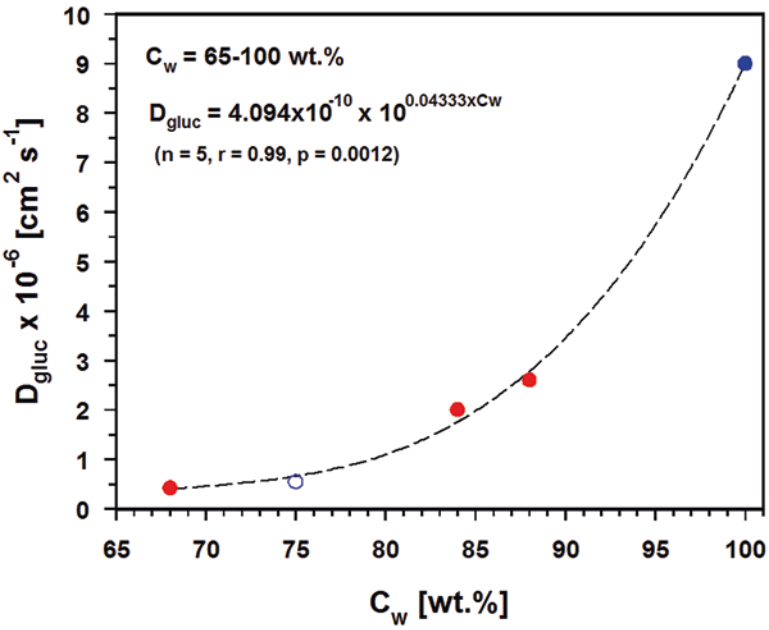

Fig. 22.4 Diffusion coefficients for glucose (D_{gluc}) in 3 different "tissue types" of a rodent sarcoma cell line strongly depend on fractional water content (C_W, red dots) [20]. Data for pure water (blue dot) [20] and cytoplasm (blue circle) [21] are also shown (broken line: best fit of data)

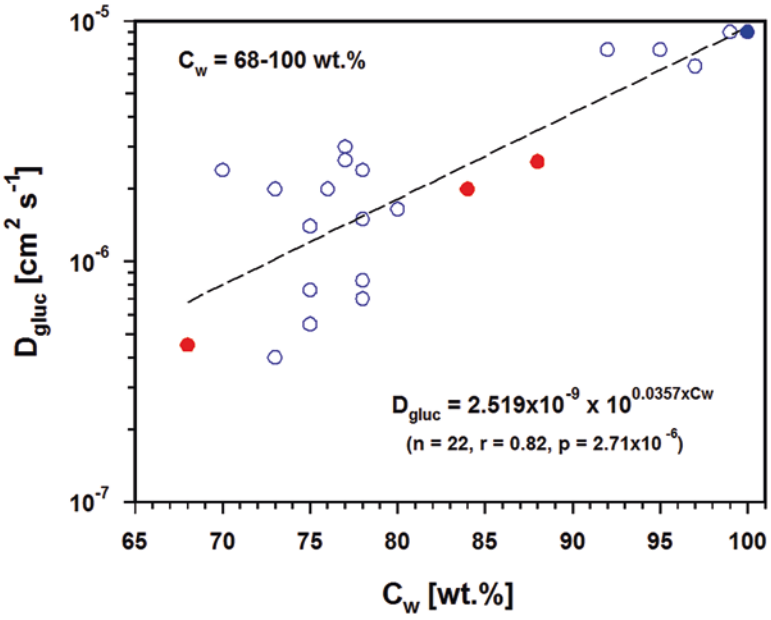

Fig. 22.5 Diffusion coefficients for glucose (D_{gluc}) in pure water (blue dot), normal tissues and body fluids (blue circles, with a noticeable scatter of the values) and in experimental tumours (red dots). Overall, D_{gluc} exponentially increases with increasing water content C_W

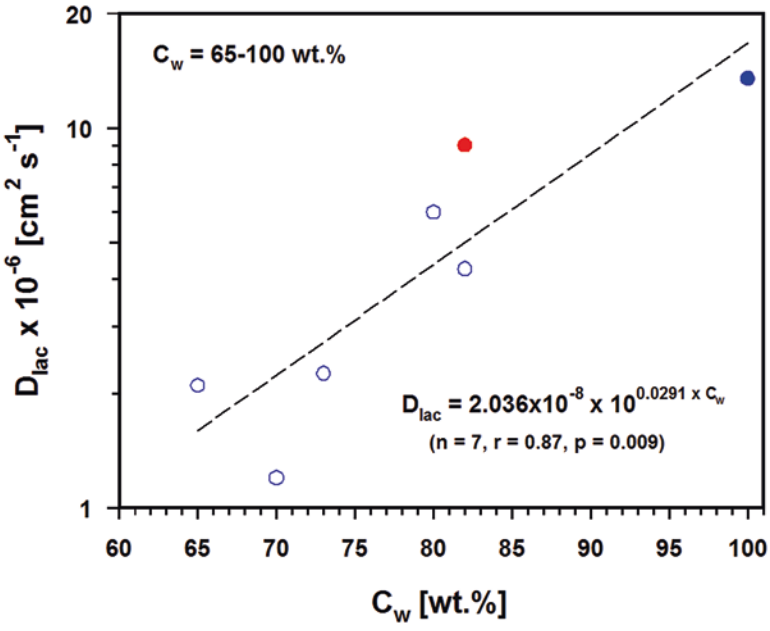

Fig. 22.6 Diffusion coefficients for lactate (D_{lac}) in pure water (blue dot), in cancer tissue (red dot) and in normal tissues (blue circles). In the "soft tissue range" lactate diffusivity rises exponentially with increasing water content (C_W = 65–100 wt.%)

molecular weight (MW) which progressively deviates from that of free diffusion in water (see Fig. 22.7). Diffusive transport in tumor tissues is "hindered" to a lesser extent than in normal tissues, which is consistent with markedly enlarged interstitial spaces in tumors [41]. Similar differences in diffusivities have also been reported with varying molecular weights: 32 g mol^{-1} < M W < 69,000 g mol^{-1} [36, 41]. The higher the MWs of the solutes the larger is the deviation from diffusion constants in water, which is in agreement with earlier observations [41, 42]. For solutes with a molecular mass < 200 g•mole^{-1} (e.g., respiratory gases, lactate, glucose) viscos-

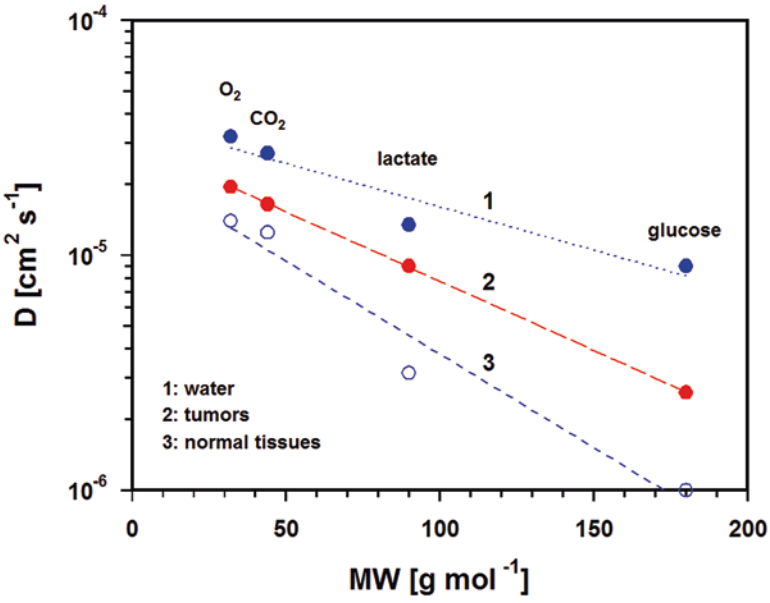

Fig. 22.7 Diffusion coefficients of small molecules distinctly increase with rising temperature (e.g., D_{O2} = 2–4%/°C [13, 40], not discussed in this Chapter), by increasing water content of tissues, and with decreasing molecular weights (MW) of solutes, as shown in this diagram. With increasing MW, diffusivity progressively deviates from that in water

ity seems to play a smaller role in free diffusion within the extracellular space of cancers than predicted by the Stokes-Einstein equation [42].

The declining diffusivities of the solutes in water as a function of increasing molecular weight is described by the following equations: $D = 3.75 \times 10^{-0.0067\ MW}$ ($p = 0.044$), $D = 3.02 \times 10^{-0.0059\ MW}$ ($p < 0.00005$) (in tumor tissues) and $D = 2.35 \times 10^{-0.0079\ MW}$ ($p < 0.02$) (in normal tissues).

22.5 Thermophysical Properties of Malignant Tumors

22.5.1 Differential Specific Heat Capacities in Normal and Cancerous Tissues

In a recent article, we described a strong correlation between specific heat capacity and water content in tissues which suggests a *preferred heat deposition* in hyperhydrated malignant tumors upon electromagnetic irradiation, i.e., causing cancers to be better heat reservoirs (i.e., tumors have a better heatability) than adjacent normal tissues [3]. Using additional, updated information, this (patho-) physiological trait is illustrated in Fig. 22.8a, b: In general, malignant tumors (solid symbols) have higher c_P-values than their homologous, normal tissues (open symbols). Over a wide range of water contents, this correlation can be described by $c_p = 0.024\ C_w + 1.781$ ($p = 8.67 \times 10^{-12}$).

22.5.2 Differential Thermal Conductivities in Normal and Cancerous Tissues

Thermal conductivity k [W m^{-1}•K^{-1}] describes the ability of a tissue (or of biological media) for internal heat dissipation caused by conductive heat flow to neighboring regions with lower temperatures (for recent reviews see [45–47]). The preferred value for k of pure water at 37 °C is ≈0.625 W m^{-1} K^{-1} [48, 49].

In normal soft tissues, k depends not only on water content but also on the tissue composition (e.g., lipid content) and stromal architectures. For many tissue types k showed an almost linear decrease with lowering water content on a double-logarithmic scale: $k = 0.0161 \times 10^{0.794\ \log C_w}$ ($p = 1.1 \times 10^{-8}$) (Fig. 22.9, blue line). This relationship is also valid for some tumor tissues, such as fibrosarcoma [50] and in human colon

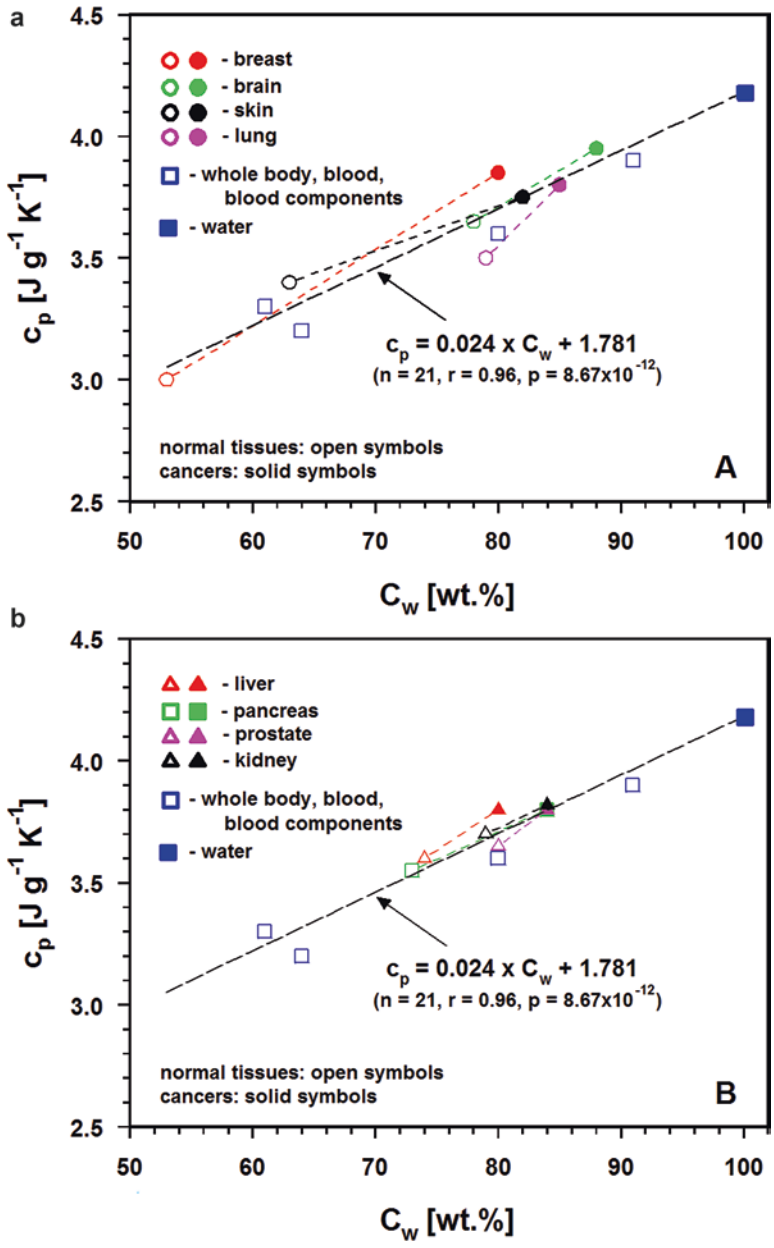

Fig. 22.8 (**a**) Correlation between tissue water content C_W and c_P-data of normal tissues (breast, brain, skin, lung; open symbols) and their malignant counterparts (closed symbols), and (**b**) normal tissues (liver, pancreas prostate, kidney; open symbols) versus their malignant pathologies (closed symbols). For additional information, c_p – values for water, human whole blood [43], blood plasma, and red blood cells [44] are also presented. Preferred value for pure water at 37 °C: 4.18 J g^{-1}•K^{-1}

cancer [51]. Due to the higher lipid content, in normal breast tissue and in breast cancer *k*-values are shifted to lower conductivities [46].

In cancer tissues, water content is the key factor obviously dominating thermal conductivity [3, 53]. Thermal conductivities higher than that of pure water (at 37 °C) seem to be related to aberrant stromal conditions, as discussed by Fujimura et al. [54] who reported values up to 0.68 W m^{-1} K^{-1} in skin lesions, i.e., about 1.6-times higher values than in normal skin. These data are in line with values of 0.64 and 0.67 W m^{-1} K^{-1} for human tumor tissues [55, 56].

22.6 Conclusions

In general, malignant tumors are hyperhydrated compared to their adjacent or corresponding, homologous tissues. Therefore, for realistic eval-

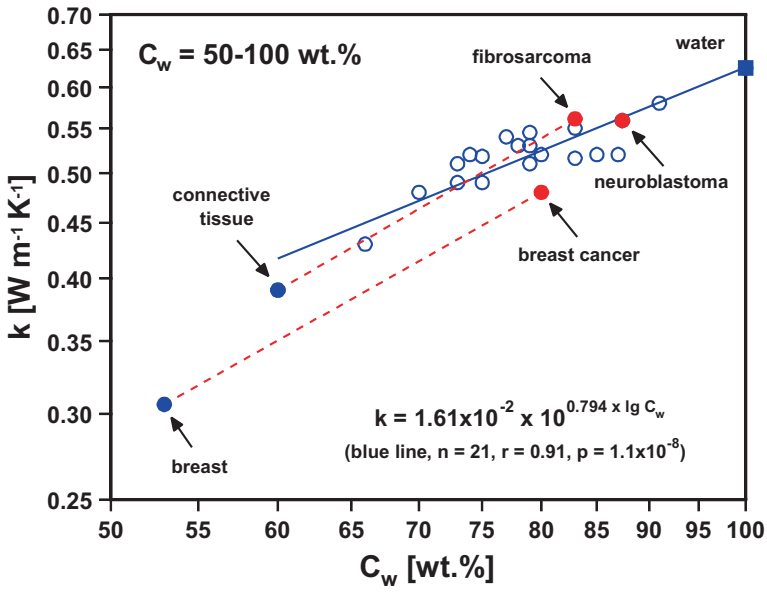

Fig. 22.9 Thermal conductivity of various normal tissues (blue circles), of different tumor tissues (red dots) and of pure water (blue square) as a function of water content within the range C_w = 50–100 wt.% (T = 37 °C). Updated values are averaged means provided in [47–52]. Within this range, k decreases linearly with decreasing water content on a double-logarithmic scale (blue line). A similar effect was found for the dependence of normal breast tissue and breast cancer on water content (lower broken red line) [46]

uations of critical diffusion distances (and supply situations in general) for oxygen and glucose, or for metabolite drainages, reliable diffusion coefficients, related to the special tissue are mandatory. For modeling temperature distributions based on Pennes' Bioheat-transfer equation [56], tumor-specific thermophysical properties (c_p, k) must be considered when adjuvant hyperthermia is part of treatment planning or schedules in oncologic thermo-radiotherapy.

Acknowledgement The authors thank Emeritus Professor A. Graham Pockley, Nottingham Trent University (UK), for linguistic support.

References

1. Nia HT, Munn LL, Jain RK (2020) Physical traits of cancer. Science 370(6516). https://doi.org/10.1126/science.aaz0868
2. Beshay PE, Cortes-Medina MG, Menyhert MM et al (2021) The biophysics of cancer: emerging insights from micro- and nanoscale tools. Adv NanoBiomed Res:2100056. https://doi.org/10.1002/anbr.202100056
3. Vaupel P, Piazena H (2022) Strong correlation between specific heat capacity and water content in human tissues suggests preferred heat deposition in malignant tumors upon electromagnetic irradiation. Int J Hyperth 39(1):987–997. https://doi.org/10.1080/02656736.2022.2067596
4. Paulides MM, Rodrigues DB, Bellizzi GG et al (2021) ESHO benchmarks for computational modeling and optimization in hyperthermia therapy. Int J Hyperth 38(1):1425–1442. https://doi.org/10.1080/02656736.2021.1979254
5. Bianchi L, Cavarzan F, Ciampitti L et al (2022) Thermophysical and mechanical properties of biological tissues as a function of temperature: a systematic review. Int J Hyperth 39(1):297–340. https://doi.org/10.1080/02656736.2020.2028908
6. Popovic ME, Minceva M (2020) Thermodynamic properties of human tissues. Thermal Sci 24(68):4115–4133
7. McIntosh RL, Andersen V (2010) A comprehensive tissue properties database provided for the thermal assessment of a human at rest. Biophys Rev Lett 5(3):129–151. https://doi.org/10.1142/SI79993048010001184
8. Camilleri JS, Farrugia L, Curto S et al (2022) Review of thermal and physiological properties of human breast tissue. Sensors 22:3894. https://doi.org/10.3390/s22103894
9. Greenstein JP (1947) Biochemistry of cancer. Academic, New York

10. Gullino PM, Grantham FH, Smith SH (1965) The interstitial water space of tumors. Cancer Res 25:727–731
11. Aronen HJ, Pardo FS, Kennedy DN et al (2000) High microvascular blood volume is associated with high glucose uptake and tumor angiogenesis in human gliomas. Clin Cancer Res 6:2189–2200
12. Vaupel P (1973) Effect of percentual water content in tissues and liquids on the diffusion coefficients of O_2, CO_2, N_2 and H_2. Pflüg Arch 361:201–204
13. Grote J, Süsskind K, Vaupel P (1977) Oxygen diffusivity in tumor tissue (DS- carcinosarcoma) under temperature conditions within the range of 20-40°C. Pflüg Arch 372:37–32
14. Langø T, Mørland T, Brubakk AO (1996) Diffusion coefficients and solubility coefficients for gases in biological fluids and tissues: a review. Undersea Hyperb Med 23(4):247–272
15. Evans NTS, Naylor PFD, Quinton TH (1981) The diffusion coefficient of oxygen in respiring kidney and tumour tissue. Respir Physiol 43:179–188. https://doi.org/10.1016/0034-5687(81)90100-6
16. Secomb TW, Bullock KV, Boas DA, Sakadzic S (2020) The mass transfer coefficient for oxygen transport from blood to tissue in cerebral cortex. J Cereb Blood Flow Metab 40(8):1634–1646. https://doi.org/10.1177/02716778X19870068
17. Zander R (1976) Cellular oxygen concentration. Adv Exp Med Biol 75:463–467
18. Vaupel P, Multhoff G (2021) Revisiting the Warburg effect: historical dogma *versus* current understanding. J Physiol 599:1745–1757. https://doi.org/10.1113/JP278810
19. Pérez-Tomás R, Pérez-Guillén I (2020) Lactate in the tumor microenvironment: an essential molecule in cancer progression and treatment. Cancers 12:3244. https://doi.org/10.3390/cancers12113244
20. Busemeyer J, Vaupel P, Thews G (1977) Diffusion coefficients of glucose in tumor tissue. Pflüg Arch 368(1977):R17
21. Thews G (1966) Diffusion und Permeation. In: Bartelheimer H, Heyde W, Thorn W (eds) D-Glucose und verwandte Verbindungen in Medizin und Biologie. Enke Publication, Stuttgart, pp 250–276
22. Lanman RC, Burton JA, Schanker LS (1971) Diffusion coefficients of some ^{13}C-labelled saccharides of biological interest. Life Sci Part 2 Biochem Gen Biol 10:803–811
23. Boubriak OA, Urban JPG, Cui Z (2006) Monitoring of metabolite gradients in tissue -engineered constructs. J R Soc Interface 3(10):637–648
24. Lindon JC, Liu M, Nicholson JK (1999) Diffusion coefficient measurement by high resolution NMR spectroscopy: biochemical and pharmaceutical applications. Rev Anal Chem 18(1–2):23–66
25. Miyamoto S, Atsuyama K, Ekino K, Shin T (2018) Estimating the diffusion coefficients of sugars using diffusion experiments in agar-gel and computer simulations. Chem Pharm Bull 66:632–636
26. Oliveira LM, Carvalho MI, Nogueira EM, Tuchin VV (2013) The characteristic time of glucose diffusion measured for muscle tissues at optical clearing. Laser Phys 23(7):075606
27. Tuchina DK, Bashkatov AN, Genina EA, Tuchin VV (2015) Quantification of glucose and glycerol diffusion in myocardium. J Innov Opt Health Sci 8(3):1541006. https://doi.org/10.1142/S1793545815410060
28. Laursen TJS, Kirk JE (1955) Diffusion coefficients of carbon dioxide and glucose for a connective tissue membrane from individuals of various ages. J Gerontol 10(3):303–305
29. Khalil E, Kretos K, Kasting GB (2006) Glucose partition coefficient and diffusivity in the lower skin layers. Pharm Res 23(6):1227–1234
30. Bashkatov AN, Genina EA, Tuchin VV (2009) Chapter 19: Measurement of glucose diffusion coefficients in human tissues. In: Tuchin VV (ed) Handbook of optical sensing of glucose in biological fluids and tissues. CRC Press, Boca Raton/London/New York, pp 587–621
31. Bashkatov AN, Genina EA, Sinichkin YP et al (2003) Glucose and mannitol diffusion in human dura mater. Biophys J 85(5):3310–3318. https://doi.org/10.1016/S0006-3495(03)74750-X
32. Reneau DD, Knisely MH, Bicher HI, Bruley DF (1971) Glucose diffusion and consumption in the human brain. In: Proceedings of the 7th National AIChE Meeting, Atlantic City
33. Maroudas A (1970) Distribution and diffusion of solutes in articular cartilage. Biophys J 10:365–379
34. Kirk JE, Laursen TJS (1955) Diffusion coefficients of various solutes for human aortic tissue: with special reference to variation in tissue permeability with age. J Gerontol 10(3):288–302. https://doi.org/10.1093/geronj/10.3.288
35. Sidell BD, Hazel JR (1987) Temperature affects the diffusion of small molecules through cytosol of fish muscle. J Exp Biol 129:191–205
36. Swabb EA, Wei J, Gullino PM (1974) Diffusion and convection in normal and neoplastic tissues. Cancer Res 34:2814–2822
37. Garcia-Perez AI, Lopez-Beltran EA, Klüner P et al (1999) Molecular crowding and viscosity as determinants of translational diffusion of metabolites in subcellular organelles. Arch Biochem Biophys 362(2):329–338
38. Eggleton GP, Eggleton P, Hill AV (1928) The coefficient of diffusion of lactic acid through muscle. Proc R Soc B Lond 103:620–628. https://doi.org/10.1098/rsb.1928.0061
39. Tannock IF (1968) The relation between cell proliferation and the vascular system in a transplantabled mouse mammary tumour. Br J Cancer 22(2):258–273
40. Bentley TB, Meng H, Pittman RN (1993) Temperature dependence of oxygen diffusion and consumption in mammalian striated muscle. Am J Phys 264:H1825–H1830. https://doi.org/10.1152/ajpheart.1993.264.6.H1825

41. Nugent LJ, Jain RK (1984) Extravascular diffusion in normal and neoplastic tissues. Cancer Res 44:238–244
42. Jain RK (1987) Transport of molecules in the tumor interstitium: a review. Cancer Res 47:303–3051
43. Mendlewitz M (1948) The specific heat of human blood. Science 107:97–98. https://doi.org/10.1126/science107.2769.97107(2769)
44. Toubal M, Asmani M, Radziszewski NB (1999) Acoustic measurement of compressibility and thermal expansion coefficient of erythrocytes. Phys Med Biol 44(5):1277–1287. https://doi.org/10.1088/0031-9155/44/5/313
45. Bianchi L, Cavarzan F, Ciampitti CM, Grilli F, Saccomandi P (2022) Thermophysical and mechanical properties of biological tissues as a function of temperature: a systematic literature review. Int J Hyperth 39(1):297–340
46. Camilleri JS, Farrgia L, Curto S et al (2022) Review of thermal and physiological properties of human breast tissue. Sensors 3894. https://doi.org/10.3390/s22103894
47. Thermal conductivity. In: Tissue properties. IT'IS Foundation. Database. https://itis.swiss/vitrual-population/tissue properties/database/thermal-conductivity/
48. Mintsa HA, Roy G, Nguyen CT, Doucet D (2007) New temperature dependent thermal conducticity data for water-based fluids. Int J Thermal Sci 48:363–371
49. Water – Thermal conductivity vs. Temperature. The Engineering Tool Box. https://www.engineeringtoolbox.com/water-liquid-gas-thermal-conductivity-temperature-pressure-d_2012.htm
50. Holmes KR, Chen MM (1979) Local thermal conductivity of Para-7 fibrosarcoma in hamster. Adv Bioeng ASME, New York, pp 147–149
51. Valvano JW, Cochran JR, Diller KR (1985) Thermal conductivity and diffusivity of biomaterials measured with self-heated thermistors. Int J Thermophys 6:301–311
52. Ahuja AS, Prasad KN, Hendee WR et al (1978) Thermal conductivity and diffusivity of neuroblastoma tumor cells. Med Phys 5:418–421
53. Müller W, Piazena H, Vaupel P (2022) From sun to wIRA. In: Vaupel P (ed) Water-filtered infrared-A (wIRA) irradiation: from research to clinical settings. Springer, Cham, pp 17–32. https://doi.org/10.1007/978-3-030-92880-3_2
54. Fujimura T, Okabe T, Tanita K et al (2019) A novel technique to diagnose non-melanoma skin cancer by thermal conductivity measurements: correlations with cancer stromal factors. Exp Dermatol 28:1029–1035
55. Selkins KM, Emery AF (1982) Thermal science for physical medicine. In: Lehmann JF (ed) Therapeutic heat and cold. Williams & Wilkins, Baltimore, pp 70–132
56. Giering K, Minet O, Lamprecht I, Müller G (1995) Review of thermal properties of biological tissues. SPIE Proc PM 25:45–65

Part IV

Muscle

No Difference in Muscle Basal Oxygenation in a Bedridden Population Pre and Post Rehabilitation

23

R. Re, A. Scano, A. Tomba, I. Pirovano, A. Caserta, L. Spinelli, D. Contini, R. Cubeddu, L. Panella, and A. Torricelli

Abstract

Long periods of bed rest for elderly population, due to a femur fracture event, can cause a deterioration in the muscular capacity. Therefore, monitoring of the muscle oxidative capacity in this fragile population is necessary to define the muscular oxidative metabolism state before and after a rehabilitation period. The time-domain near-infrared spectroscopy (TD-NIRS) technique enables the absolute values to be calculated for hemodynamic parameters such as oxy- (O_2Hb), deoxy- (HHb), total- (tHb) haemoglobin, and tissue oxygen saturation (SO_2) of the muscular tissue. In this work, we have characterized vastus lateralis muscle hemodynamics during a baseline period at two different time points: after the surgery (PRE) and after 15 days of rehabilitation (POST). The mean values for the absolute values of the hemodynamic parameters were: O_2Hb_PRE = 49.1 ± 14.1 μM; O_2Hb_POST = 47.1 ± 13.4 μM; HHb_PRE = 28.3 ± 10.3 μM; HHb_POST = 26.7 ± 9.9 μM; tHb_PRE = 77.3 ± 23.6 μM; tHb_POST = 73.8 ± 21.4 μM; SO_2_PRE = 63.9 ± 4.0% and SO_2_POST = 64.9 ± 5.6%. The hemodynamic parameters did not show significant differences at both group and single subject level. These results suggest that for this kind of population, the baseline of the hemodynamic parameters is not the best one to consider to assess the rehabilitation progresses in terms of muscular oxidative metabolism.

Keywords

Muscle oxygenation · Time-domain near-infrared spectroscopy · Rehabilitation

R. Re (✉) · A. Torricelli
Dipartimento di Fisica, Politecnico di Milano, Piazza Leonardo da Vinci, Milan, Italy

Istituto di Fotonica e Nanotecnologie, Consiglio Nazionale delle Ricerche, Piazza Leonardo da Vinci, Milan, Italy
e-mail: rebecca.re@polimi.it

A. Scano
Istituto di Sistemi e Tecnologie Industriali Intelligenti per il Manifatturiero Avanzato, Consiglio Nazionale delle Ricerche, Milan, Italy

A. Tomba · A. Caserta · L. Panella
Dipartimento di Riabilitazione, ASST Gaetano Pini CTO, Milan, Italy

I. Pirovano
Istituto di Tecnologie Biomediche, Consiglio Nazionale delle Ricerche, Segrate (MI), Italy

L. Spinelli
Istituto di Fotonica e Nanotecnologie, Consiglio Nazionale delle Ricerche, Piazza Leonardo da Vinci, Milan, Italy

D. Contini · R. Cubeddu
Dipartimento di Fisica, Politecnico di Milano, Piazza Leonardo da Vinci, Milan, Italy

F. Scholkmann et al. (eds.), *Oxygen Transport to Tissue XLIV*, Advances in Experimental Medicine and Biology 1438, https://doi.org/10.1007/978-3-031-42003-0_23

23.1 Introduction

Long periods of bed rest for the elderly population, due for example to a femur fracture event, can cause a deterioration in the muscular capacity. The physiotherapy intervention, starting from the day after the surgery, is crucial for avoiding or reducing the sarcopenic state of the patient's muscle and allowing faster recovery. In the current clinical environment, intervention in this fragile population is assessed based on a subjective evaluation of the patients and no objective marker for the muscle's oxidative state and capacity [1]. This work is a first step in the assessment of the rehabilitation progresses with personalized and objective parameters related directly to the muscular tissue.

The time-domain near-infrared spectroscopy (TD-NIRS) technique allows the absolute values to be calculated for the hemodynamics parameters, such as oxy- (O_2Hb), deoxy- (HHb), total- (tHb) hemoglobin, and tissue oxygen saturation (SO_2) of the muscular tissue in a non- invasive way directly at the patient bedside [2, 3]. These parameters will be evaluated during a baseline acquisition to estimate the oxidative muscular function at rest. The measurements were performed on the vastus lateralis muscle of the non-surgical leg of 15 patients and were considered at two different time points: before and after a 15-day rehabilitation period. The maximum voluntary contraction was also acquired to assess the improvements in terms of strength of the patients.

23.2 Methods

This study was approved by the Ethical Committee of ASST Gaetano Pini CTO and conducted on 15 female patients in accordance with the Declaration of Helsinki. Participants were seated on a chair allowing the knee angle to be fixed at 120°. Firstly, they were asked to press their leg against the chair holder as strongly as they could, to determine the maximum voluntary contraction (MVC) during an isometric contraction of the quadriceps muscle. The power exerted was recorded by a load cell fixed to the chair holder. The MVC was then calculated as the average of three consecutive trials.

TD-NIRS measurements were performed with a device previously developed by the Department of Physics at Politecnico di Milano, widely described in Re et al. [4]. The optical probe was placed on the vastus lateralis of the non-surgical leg, allowing measurements at two different interfiber distances: 1.5 and 3 cm. A 60 s baseline period was recorded at 1 Hz of acquisition rate. On the same site a ultrasonographic exam was performed to calculate the pennation angle (PA) and the adipose tissue thickness (ATT).

A two-step procedure was employed for the TD-NIRS data analysis. Applying the solution of the photon diffusion equation for a homogenous medium it is possible to calculate the nominal values for the optical properties, i.e. the absorption coefficient and the reduced scattering coefficient, at the two interfiber distances on the vastus lateralis muscle. A second fit, where these values are employed as initial values, based on a bi-layer medium, can be employed to determine the optical parameters for the two considered layers, one more superficial and the other deeper. In this way, it is possible to separate the contribution of the superficial and systemic compartments (skin, capillary bed and fat) from the muscular tissue. This method needs the knowledge of the ATT. Starting from the absorption coefficient for the deeper layer and employing the Beer law, we calculated the absolute values for the O_2Hb, HHb and tHb content, and SO_2. The baseline values for all the previous parameters were calculated as the average of the last 10 s.

The MVC and the hemodynamic parameters were acquired at two different time points: the first one (PRE) at 6–8 days after the femur fracture and around 3 days after the surgery. The second one (POST) was identified at 15 days after the PRE; during this period, the subject followed a daily physiotherapy rehabilitation program.

The distributions for the population of all the parameters were represented with boxplots, and the mean, average and standard deviation were calculated. Relations between all different parameters at the two time points were investigated with Pearson coefficient correlations and

one-way Anova analysis. Intra-subject variability was evaluated with the χ^2 test.

23.3 Results

The mean age among the 15 female subjects was 78.4 ± 6.8 years; the ATT was 9.8 ± 3.7 mm and the PA 9.2 ± 5.0°. The MVC was: 254.8 ± 44.4 N for the PRE and 312.9 ± 80.6 N for the POST. In Fig. 23.1, its distribution at the two time points is shown. We can observe that for the POST time point, the average values is higher but not significantly different with respect to the PRE but the population is more dispersed around the average. The intra-subject variability was not significant either.

The mean values for the absolute values of the hemodynamic parameters were: O_2Hb_PRE = 49.1 ± 14.1 μM; O_2Hb_POST = 47.1 ± 13.4 μM; HHb_PRE = 28.3 ± 10.3 μM; HHb_POST = 26.7 ± 9.9 μM; tHb_PRE = 77.3 ± 23.6 μM; tHb_POST = 73.8 ± 21.4 μM; SO2_PRE = 63.9 ± 4.0% and SO_2_POST = 64.9 ± 5.6%. In Fig. 23.2, their distributions are reported for the PRE and POST period. Also, for the hemodynamic parameters no significance differences were found both at group and single subject level.

23.4 Discussions and Conclusions

Nowadays, no techniques providing an objective assessment of the oxidative status of muscular tissue are routinely used in clinics. In this work, it was possible to characterize the vastus lateralis muscle of elderly and bedridden patients with TD-NIRS parameters. The absolute values for O_2Hb, HHb, tHb and SO_2 were calculated with a two-step fitting procedure based on a bilayer model, which allows to enhance the contribution coming from the muscular tissue, with respect to the superficial tissue, where skin, capillary bed and fat are mostly present. Knowledge of the ATT thanks to the ultrasound acquisition allowed to estimate those parameters with a good accuracy.

We also compare the previous parameters in two different time-points: before and after a 15-day rehabilitation period and we observed that there were no significant differences among the group values of all the considered parameters. Furthermore, also at the single subject level, no significance differences were found. These results suggest that for this kind of population, the baseline of the hemodynamic parameters is not the best one to consider to assess the rehabilitation progresses in terms of muscular oxidative metabolism. This could be due to the length of

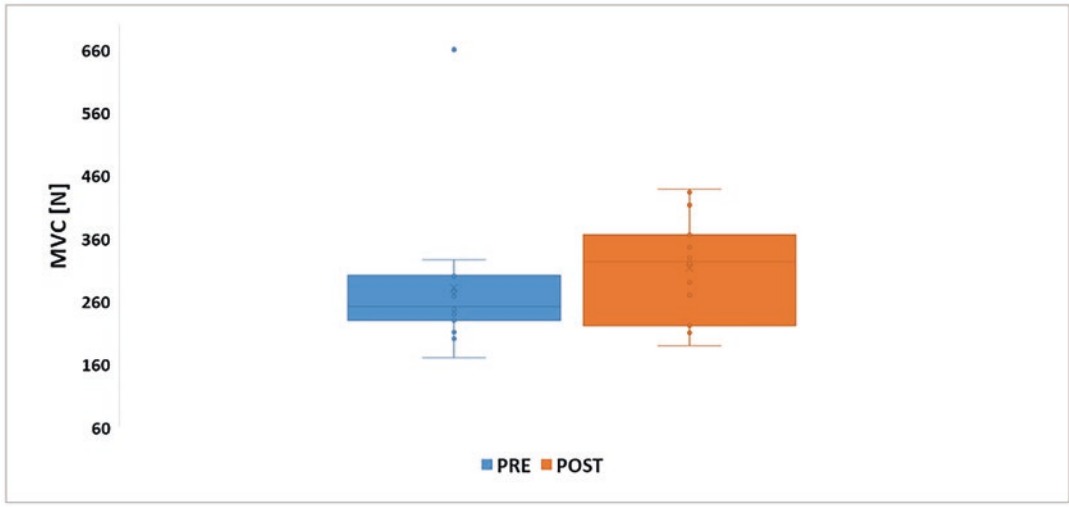

Fig. 23.1 MVC maximum voluntary contraction. Distribution at the PRE and POST time points

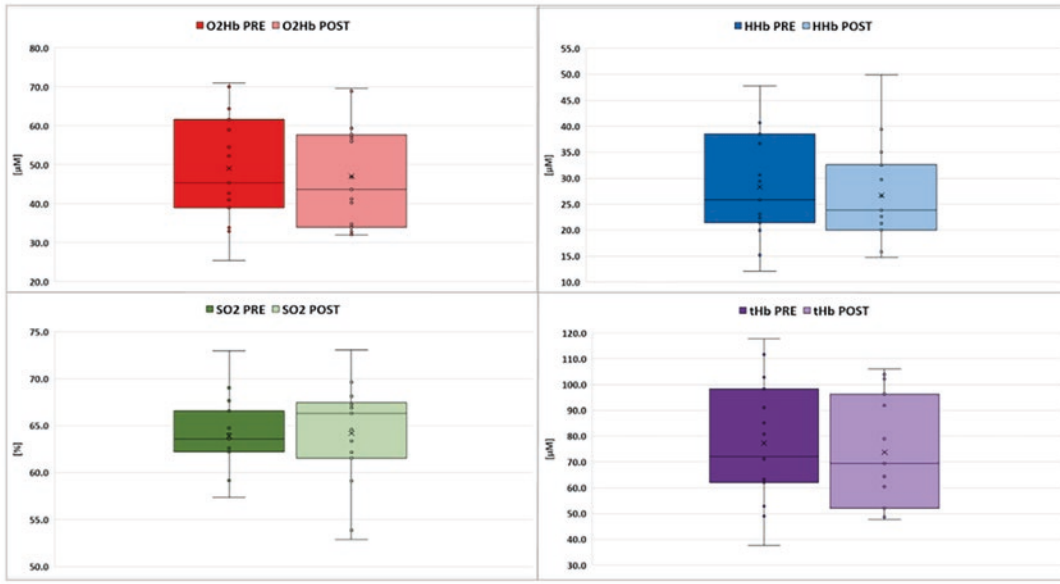

Fig. 23.2 Boxplot of the distribution of oxy- (O_2Hb), deoxy- (HHb) and total- (tHb) hemoglobin and tissue oxygen saturation (SO_2) absolute values. PRE and POST: before and after 15 days of rehabilitation

period considered, which could be not enough to stimulate changes in the basal muscular condition. To better understand these preliminary data, it will be necessary to observe the population also during longer rehabilitation periods. It will be also interesting to evaluate these patients always after 15 days of treatment, but during an exercise to observe if other outcomes related to oxidative metabolism, such as the SO_2, slope at the beginning of the onset of the exercise or at the beginning of the recovery period, are more suitable in the assessment of the rehabilitation progresses.

Acknowledgments This work has been partially supported by the project "Neuromuscular impairment in aging: a longitudinal study of structural and functional mechanistic bases of age-related alterations (Trajector-AGE)" funded by the MIUR Progetti di Ricerca di Rilevante Interesse Nazionale (PRIN) Bando 2020 -Prot. 2020477RW5.

References

1. Zembroń-Łacny A, Dziubek W, Rogowski Ł et al (2014) Sarcopenia: monitoring, molecular mechanisms, and physical intervention. Physiol Res 63:683–691
2. Torricelli A, Contini D, Pifferi A et al (2014) Time domain functional NIRS imaging for human brain mapping. NeuroImage 85:28–50
3. Grassi B, Quaresima V (2016) Near-infrared spectroscopy and skeletal muscle oxidative function in vivo in health and disease: a review from an exercise physiology perspective. J Biomed Opt 21:091313
4. Re R, Pirovano I, Contini D et al (2018) Time domain near infrared spectroscopy device for monitoring muscle oxidative metabolism: custom probe and in vivo applications. Sensors 18:1–13

24

Relationship Between Muscle Deoxygenation and Cardiac Output in Subjects Without Attenuation of Deoxygenation Hemoglobin Concentration Near the End of Ramp Cycling Exercise: A Longitudinal Study

Shun Takagi, Toshihito Katsumura, and Shizuo Sakamoto

Abstract

The aim of this study was to investigate the longitudinal relationship between the slopes of systemic and quadriceps muscle O_2 dynamics in subjects without attenuation point in deoxygenated hemoglobin concentration at vastus lateralis ($AP_{deoxy\text{-}Hb@VL}$) during high-intensity cycling. Seven young men without $AP_{deoxy\text{-}Hb@VL}$ performed ramp cycling exercise until exhaustion before and after 8 weeks, while continuing recreational physical activities throughout that period. Muscle O_2 saturation (SmO_2) and deoxy-Hb were monitored at the vastus lateralis (VL) and rectus femoris (RF) by near infrared spectroscopy oximetry during exercise. Cardiac output (CO) was also continuously assessed. During high-intensity exercise, at VL, a significantly steeper slope of deoxy-Hb was found after 8 weeks compared with before, while the slopes of deoxy-Hb at RF were not significantly changed. Though a decrease in the slope of CO after 8 weeks did not reach significance ($p = 0.12$), the change in the slope of CO was significantly related to the change in the slopes of deoxy-Hb at VL ($r_s = -0.89$, $p < 0.01$) and RF ($r_s = -0.86$, $p < 0.05$). Our data reinforces the idea that, in subjects without $AP_{deoxy\text{-}Hb@VL}$, the slope of muscle deoxygenation at VL during high-intensity cycling exercise may partly be explained by systemic O_2 supply, rather than O_2 balance in other thigh muscles.

Keywords

Muscle oxygenation · Ramp cycling exercise · Near-infrared spectroscopy

S. Takagi (✉)
Faculty of Education and Welfare, Biwako-Gakuin University, Higashiomi, Shiga, Japan

Department of Sports Medicine for Health Promotion, Tokyo Medical University, Shinjuku, Tokyo, Japan
e-mail: s-takagi@biwakogakuin.ac.jp

T. Katsumura
Department of Sports Medicine for Health Promotion, Tokyo Medical University, Shinjuku, Tokyo, Japan

S. Sakamoto
Faculty of Sport Science, Surugadai University, Hanno, Saitama, Japan

F. Scholkmann et al. (eds.), *Oxygen Transport to Tissue XLIV*, Advances in Experimental Medicine and Biology 1438, https://doi.org/10.1007/978-3-031-42003-0_24

24.1 Introduction

Muscle deoxygenated hemoglobin concentration (deoxy-Hb) evaluated by near infrared spectroscopy (NIRS) oximetry reflects the balance of O_2 unloading and blood outflow from the muscle [1]. At vastus lateralis (VL) muscle, although an attenuated point of slope of deoxy-Hb ($AP_{deoxy\text{-}Hb@VL}$) is generally observed near the end of ramp cycling exercise, no clear $AP_{deoxy\text{-}Hb@VL}$ is observed in 10–30% of subjects [2]. In a cross-sectional study, we have previously confirmed that, in subjects without $AP_{deoxy\text{-}Hb@VL}$, the slope of muscle deoxygenation during high-intensity cycling was steeper than subjects with $AP_{deoxy\text{-}Hb@VL}$, not only at VL but also at the other quadriceps muscles, and the steeper slope of deoxy-Hb at VL was related to the shallower slope of cardiac output [2]. These results lead us to speculate that the differences in subjects with and without $AP_{deoxy\text{-}Hb@VL}$ may be mainly explained by systemic O_2 supply, rather than O_2 balance in the other quadriceps muscles. However, a longitudinal study was needed to clarify the detailed mechanisms as to why the slope of deoxygenation is steeper in subjects without $AP_{deoxy\text{-}Hb@VL}$ near the end of ramp cycling exercise. The aim of this study was to investigate the longitudinal relationship between the slopes of systemic and quadriceps O_2 dynamics during ramp cycling exercise before and after 8 weeks in subjects without $AP_{deoxy\text{-}Hb@VL}$.

24.2 Methods

24.2.1 Subjects

Twenty-seven healthy young men (age 21 ± 1 years; height 176.8 ± 7.9 cm; body weight 76.7 ± 11.1 kg, mean ± SD) who engaged in around 2 days/week of recreational physical activities such as rugby-specific and/or resistance training participated in this study. The subjects maintained their physical activity habits throughout this study. This study was approved by the institutional ethics committee. All subjects were informed of the purpose of the study and written consent was obtained.

24.2.2 Experimental Design

The subjects performed 20 W/min ramp cycling exercise until exhaustion (Aerobike 75XLII, Combi, Japan). Breath-by-breath pulmonary gas exchanges were monitored continuously during cycling (AE310S, Minato Medical Science, Japan) to determine pulmonary peak O_2 uptake (VO_2). Cardiac output (CO), stroke volume (SV), and heart rate (HR) were also measured continuously using transthoracic impedance cardiography (PhysioFlow, Manatec Biomedical, France). Muscle O_2 saturation (SmO_2) and relative changes from rest in oxygenated hemoglobin concentration (oxy-Hb), deoxygenated hemoglobin concentration (deoxy-Hb), and total hemoglobin concentration (total-Hb) were evaluated at the vastus lateralis (VL) and rectus femoris (RF) muscles in the left leg by spatial resolved NIRS oximetry (Hb12–4, Astem Co., Japan). Fat layer thickness at the measurement site was checked by using an ultrasound device (EUB-7500, Hitachi Medical Corporation, Japan), and the effects of light scattering in the fat layer on NIRS data was corrected by normalizing measurement sensitivity [3]. Arterial O_2 saturation (SpO_2) was measured immediately after peak exercise by pulse oximetry (PM10N, Covidien, Japan). Fat-free mass (FFM) was evaluated by bio-impedance analysis (InBody 720, InBody Japan, Japan). VO_2, SV, and CO were normalized by FFM.

$AP_{deoxy\text{-}Hb@VL}$ was detected by piecewise double-linear analysis. The double linear fit was used at the onset of the systematic increase in the deoxy-Hb until the last data point corresponding to the end of the test [2]. In this study, $AP_{deoxy\text{-}Hb@VL}$ was defined as when the slope determined during higher intensity was shallower than the slope during lower intensity [2]. As a result, $AP_{deoxy\text{-}Hb@VL}$ was determined in 20 subjects, leaving 7 subjects without $AP_{deoxy\text{-}Hb@VL}$, who subsequently performed ramp cycling exercise again after 8 weeks. Variables between before and after 8 weeks were compared. $AP_{deoxy\text{-}Hb@VL}$ ranged from 72% to 83% of peak VO_2 in subjects with $AP_{deoxy\text{-}Hb@VL}$. As in a previous study [2], the slopes of variables in subjects without $AP_{deoxy\text{-}Hb@VL}$ were evaluated at moderate (55–70% of peak

VO_2) and high-intensity (85–100% of peak VO_2) exercise.

24.2.3 Statistical Analysis

All data are given as means ± standard deviation (SD). The amplitudes of variables during exercise were averaged over the last 10 seconds every 5% of peak VO_2. To compare changes in variables during exercise, a 2-way repeated-measures analysis of variance (ANOVA) was used, with time (before vs after 8 weeks) and exercise intensity as factors. Because of the low number of subjects, ANOVA was limited to 50, 60, 70, 80, 90, and 100% of peak VO_2. Where appropriate, the Bonferroni post hoc test was performed. To detect significance accurately despite the low number of subjects, the slopes of physiological variables and physical variables were compared between before and after 8 weeks by paired t-tests, and relationships between variables were evaluated by Spearman correlation coefficient. For all statistical analyses, significance was accepted at $p < 0.05$.

24.3 Results

In the 7 subjects without $AP_{deoxy\text{-}Hb@VL}$, $AP_{deoxy\text{-}Hb@VL}$ was detected neither before nor after 8 weeks. By ANOVA analysis, there were no significant interactions or main effects of group of any NIR_{SRS} oximetry variables at VL and RF. Similarly, no significant differences in systemic O_2 dynamics were found at group mean of any variables.

The slopes of the variables are indicated in Fig. 24.1. During high-intensity exercise, at VL, a significantly steeper slope of deoxy-Hb was found after 8 weeks compared with before ($p < 0.05$), while the slope of SmO_2 did not significantly change. At RF, before and after 8 weeks, the slopes of deoxy-Hb and SmO_2 were steeper during high-intensity exercise than moderate-intensity exercise. However, the slopes of deoxy-Hb and SmO_2 during high-intensity exercise were similar between before and after 8 weeks. During high-intensity exercise, although the slopes of CO ($p = 0.12$) and SV ($p = 0.14$) did not reach significance (probably due to the quite low number of subjects), the slopes of the variables were shallower after 8 weeks. The slopes of pulmonary VO_2 and HR during high-intensity exercise were unchanged before and after 8 weeks. During moderate intensity, the slopes of all variables were similar between groups.

The longitudinal relationships between variables are displayed in Fig. 24.2. During high-intensity exercise, the change in the slope of CO was significantly related to the change in the slopes of deoxy-Hb at VL ($r_s = -0.89$, $p < 0.01$) and at RF ($r_s = -0.86$, $p < 0.05$), even though the moderate relationship did not reach significance between the changes in the slopes of CO and SmO_2 at VL ($r_s = 0.54$, $p = 0.22$) and RF ($r_s = 0.50$, $p = 0.25$). There was a significant positive relationship between the changes in deoxy-Hb at VL and deoxy-Hb at RF during high-intensity exercise ($r_s = 0.82$, $p < 0.05$). A moderately negative but insignificant relationship was observed during moderate-intensity exercise ($r_s = -0.54$, $p = 0.21$).

No significant changes were observed in body weight, fat-free mass, fat layer thickness at measurement sites (VL: 3.7 ± 1.2 vs 3.9 ± 1.0 mm, RF: 6.3 ± 1.8 vs 6.1 ± 2.1 mm), pulmonary peak VO_2, or peak workload between before and after 8 weeks. In addition, there were no significant differences in respiratory exchange ratio (RER) or rating of perceived exertion (RPE) at peak exercise before and after 8 weeks. SpO_2 immediately after exhaustion was not significantly different between before and after 8 weeks. In all parameters shown in Fig. 24.2, no significant relationships were observed with the individual fat layer thickness.

24.4 Discussion

We observed that, although the change in the slope of CO during high-intensity exercise did not reach significance, it was shallowed after 8 weeks. The slope of HR was similar before and after 8 weeks, and therefore, the shallowed slope

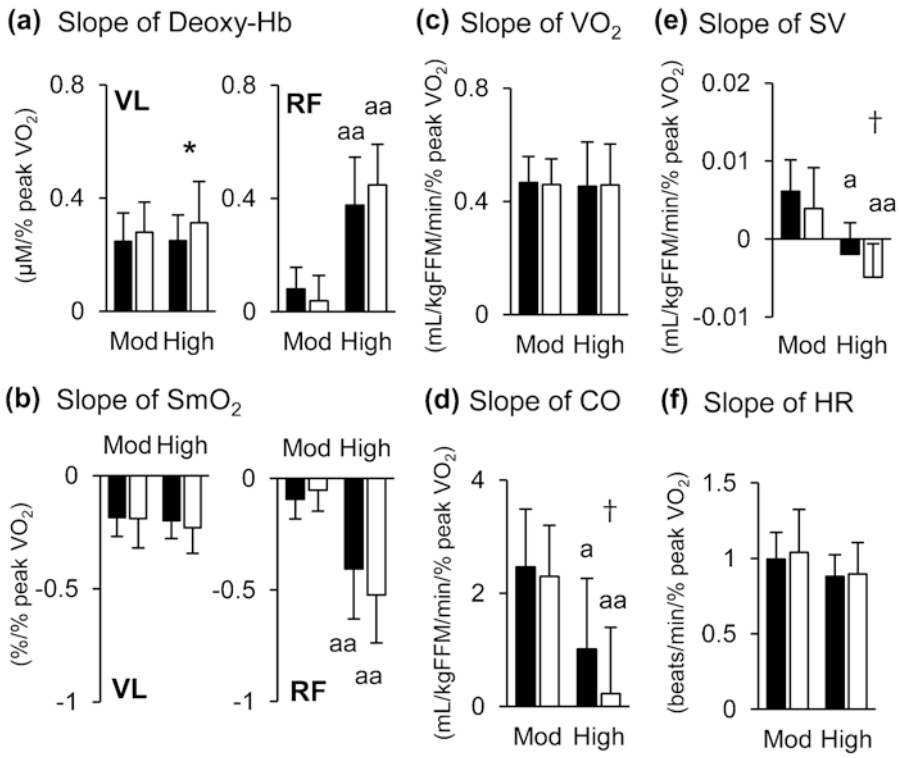

Fig. 24.1 Slopes of deoxy-Hb (**a**), SmO_2 (**b**), VO_2 (**c**), CO (**d**), SV (**e**), HR (**f**) before (black) and after (white) 8 weeks. Significant difference between groups at same exercise intensity (*: $p < 0.05$, †: $0.1 < p < 0.15$). Significant difference between exercise intensity in the same group (a: $p < 0.05$, aa: $p < 0.01$). Mod: moderate-intensity exercise (55–70% of peak VO_2), High: high-intensity exercise (85–100% of peak VO_2). Values are mean ± SD

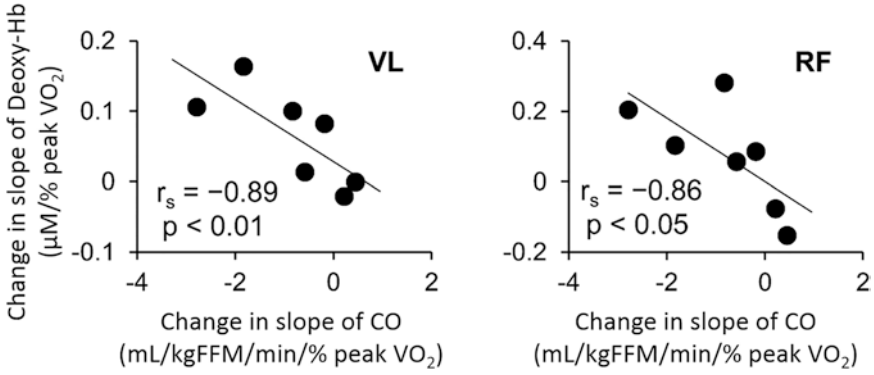

Fig. 24.2 Longitudinal relationships between change in slopes of CO and change in slope of deoxy-Hb at quadriceps during high-intensity exercise. VL vastus lateralis, RF rectus femoris

of CO can mainly be explained by the shallowed slope of SV. Previous studies reported that there was an inter-individual difference in CO during high-intensity exercise [4], and shallower slopes of CO and SV during high-intensity exercise were related to a higher fitness level in normal, non-elite-athletic subjects [5]. Therefore, in subjects who engage in recreational sport activity,

there is a possibility that maintaining physical activity for 8 weeks attenuates an increase in CO during high-intensity exercise, although, to date, details of the mechanisms are still unclear. More importantly, in this study, based on Fick's principle, the estimated slope of systemic O_2 extraction may have been increased after 8 weeks because the slope of VO_2 was unchanged for 8 weeks. We confirmed a longitudinal relationship between the shallowed slope of CO and the steepened slope of deoxygenation at VL and a positive relationship between quadriceps muscle deoxygenation. Our data therefore reinforces the idea that, in subjects without $AP_{deoxy\text{-}Hb@VL}$, the slope of muscle deoxygenation at VL during high-intensity cycling exercise may be explained by an increase in systemic O_2 extraction, secondary to a blunted increase in convective O_2 supply, rather than blood flow distribution between quadriceps muscles and/or compensatory muscle activities in other quadriceps muscles. Interestingly, during moderate-intensity exercise, a moderately negative relationship between deoxy-Hb at VL and deoxy-Hb at RF was observed, in contrast to high-intensity exercise. Hence, during moderate-intensity exercise, the slope of deoxygenation at VL may be partly affected by the other quadriceps O_2 balance, as a previous study suggested [6]. In the future, these findings should be confirmed in a larger group of subjects, due to the low number of subjects in this study.

As demonstrated in previous studies, aerobic [1] or resistance training [7] enhances muscle deoxygenation amplitude during exercise. Possibly due to low volume of training, amplitudes of muscle deoxygenation during cycling exercise were not enhanced in this study. Previous studies have demonstrated that amplitude of muscle deoxygenation is related to peak VO_2 [1], and in the present study, peak VO_2 and workloads were similar before and after 8 weeks. Therefore, the steeper slope of deoxy-Hb after 8 weeks during high-intensity exercise may not be attributed to an enhancement of amplitude of deoxy-Hb via an increase in peak VO_2. Because RER and RPE at peak exercise were also not significantly different before and after 8 weeks, degrees of exhaustion were similar. No significant difference in SpO_2 was confirmed while arterial desaturation potentially reinforced muscle deoxygenation [8]. Hence, in this study, the change in the slope of muscle deoxygenation cannot be explained by these factors.

In conclusion, our data reinforces the idea that, in subjects without $AP_{deoxy\text{-}Hb@VL}$, the slope of muscle deoxygenation at VL during high-intensity cycling exercise may partly be explained by systemic O_2 supply, rather than O_2 balance in other thigh muscles.

Acknowledgments The authors are grateful for revision of this manuscript by Andrea Hope. This work was supported in part by JSPS KAKENHI Grant Number 22 K11667 to Shun Takagi.

References

1. Takagi S (2016) Skeletal muscle oxygen dynamics and peak aerobic capacity. J Phys Fitness Sports Med 5(5):379–383
2. Takagi S, Kime R, Sakamoto S et al (2022) Systemic and quadriceps muscle O_2 dynamics in subjects without attenuation point of deoxygenated hemoglobin concentration during ramp cycling exercise. Adv Exp Med Biol 1395:429–434
3. Niwayama M, Suzuki H, Yamashita T et al (2012) Error factors in oxygenation measurement using continuous wave and spatially resolved near-infrared spectroscopy. J Jpn Coll Angiol 52:211–215
4. Trinity JD, Lee JF, Pahnke MD et al (2012) Attenuated relationship between cardiac output and oxygen uptake during high-intensity exercise. Acta Physiol (Oxf) 204(3):362–370
5. Beck KC, Randolph LN, Bailey KR (2006) Relationship between cardiac output and oxygen consumption during upright cycle exercise in healthy humans. J Appl Physiol 101(5):1474–1480
6. Takagi S, Kime R, Niwayama M et al (2013) Muscle oxygen saturation heterogeneity among leg muscles during ramp exercise. Adv Exp Med Biol 765:273–278
7. Lin TY, Lin LL, Ho TC, Chen JJ (2014) Investigating the adaptation of muscle oxygenation to resistance training for elders and young men using near-infrared spectroscopy. Eur J Appl Physiol 114(1):187–196
8. Legrand R, Ahmaidi S, Moalla W et al (2005) O_2 arterial desaturation in endurance athletes increases muscle deoxygenation. Med Sci Sports Exerc 37(5):782–788

Part V

Methods and Techniques

25 Image Reconstruction Using Deep Learning for Near-Infrared Optical Tomography: Generalization Assessment

Meret Ackermann, Jingjing Jiang, Emanuele Russomanno, Martin Wolf, and Alexander Kalyanov

Abstract

Time is one of the most critical factors in preventing brain lesions due to hypoxic ischemia in preterm infants. Since early detection of low oxygenation is vital and the time window for therapy is narrow, near-infrared optical tomography (NIROT) must be able to process the high-dimensional data provided by today's advanced systems in the shortest possible time. Deep learning approaches are attractive because they can exploit such high information density while reducing inference time. The aim of this study was to evaluate the performance of a hybrid convolutional neural network, designed for NIROT image reconstruction and trained on synthetic data. Generalization capability was assessed using measurements on phantoms of a surface topology more divergent than the range of variation in the geometries of the in-silico data, with unseen, non-spherical inclusion shapes, and with source and detector arrangements different from those used for data generation. Substantial gains in speed, localization accuracy, and high image quality were achieved even under the highly varied measurement conditions.

Keywords

Near-infrared optical tomography · Deep learning · Image reconstruction

25.1 Introduction

Near-infrared optical tomography (NIROT) is a promising modality to monitor hemodynamics and tissue oxygen kinetics. The spectrum of near infrared (NIR) light, from 650 to 1100 nm, is non-ionizing and has a high penetration depth in biological tissues. Hemoglobin is the main oxygen transporter in tissue. Oxy- and deoxyhemoglobin have distinctive absorption characteristics in the NIR range. Therefore, NIR light is well suited for diagnostic imaging in preterm infants with the aim to prevent hypoxia induced brain lesions that lead to life-long disabilities. To enable prevention, therapy must occur quickly and thus fast image reconstruction is necessary.

Sophisticated reconstruction algorithms are required for three-dimensional imaging of the optical properties. Technical advances in NIROT, e.g., single photon avalanche diode arrays, enable intensity-, space-, and time-resolved single photon detection with orders of magnitude more detectors than previously possible. This requires

M. Ackermann (✉) · J. Jiang · E. Russomanno
M. Wolf · A. Kalyanov
Biomedical Optics Research Laboratory, Department of Neonatology, University Hospital Zurich, University of Zurich, Zurich, Switzerland
e-mail: meret.ackermann@usz.ch

F. Scholkmann et al. (eds.), *Oxygen Transport to Tissue XLIV*, Advances in Experimental Medicine and Biology 1438, https://doi.org/10.1007/978-3-031-42003-0_25

algorithms that take full advantage of the high information density provided. Data-driven methods capable of learning complex, difficult-to-model underlying patterns are therefore a prime choice here, especially since traditional model-based (MB) approaches are computationally expensive along the pipeline from data acquisition to image reconstruction. Deep learning approaches shift this computational demand to offline training and consequently enable much faster online image reconstruction. Therefore, they hold the potential for real-time imaging without sacrificing image quality. Our goal was to test how deep-learned tomographic reconstruction performs for real measurements and whether it generalizes reliably to various source-detector arrangements and tissue structures. We aim to achieve significantly faster image reconstruction without compromising the prediction quality of optical properties and localization of hypoxic regions within the tissue models. We focused on the absorption coefficient (μ_a). The developed architecture can, however, be easily extended to predict reduced scattering coefficient (μ_s') values.

25.2 Methods

The image reconstruction was performed with a hybrid convolutional neural network (hCNN), a deep learning architecture previously developed. It has been trained on in-silico data to predict absolute μ_a values voxel-wise in order to localize inclusions [1]. The data was simulated based on a probe design of 8 sources symmetrically arranged and a field of view (FOV) of 437 detectors measuring in reflectance mode (Fig. 25.2Aa). Up to 5 spherical inclusions of varied size, placement, and optical properties were randomly set in the modeled tissue with different surface topologies. A data set of 23,000 input, ground truth (GT) and labeled GT volumes was split to train, validate and test the hCNN. To investigate the robustness and generalization of the approach on real data of the in-house developed time domain NIROT system, Pioneer, liquid and solid phantoms were measured as described in [2, 3], respectively. The performance of the hCNN was additionally challenged with varied probe arrangements (Fig. 25.2A): a 3- and an 11- sources setup and 264 to 276 detectors chosen based on the signal quality criteria described in [3]. To further evaluate generalization capabilities, measurements of non-spherical, letter shaped inclusions were performed on liquid phantoms (Fig. 25.3). All surfaces were flat, a surface topology not seen by the hCNN during training.

The measured time-domain data was converted to frequency domain data at 100 MHz through fast Fourier transformation. Two iterations of MB reconstructions were input to the hCNN. These were coarse reconstructions on a mesh of Ø 90 × 50 mm and 5408 nodes. We further performed traditional fully MB reconstructions for comparison using the software package NIRFASTer [4]. Specifications of the workstation used for all computations can be found in [1].

The image reconstructions were quantitatively evaluated by assessing the root mean squared error (RMSE), Dice coefficient (Dice), peak signal-to-noise ratio (PSNR) and structural similarity index (SSIM) as for the previous performance evaluation on in-silico data [1]. The generalized Dice coefficient was calculated as described in [5] and thresholding was used for the segmentation. Zero values were labeling the background. The thresholds were set by averaging the maximum and the minimum μ_a values.

25.3 Results

We demonstrated a convincing performance of the hCNN for real data and accurate reconstructions of the inclusion shapes even for the untrained shapes (Fig. 25.3), surface topology (Figs. 25.1, 25.2, and 25.3), and probe arrangement (Fig. 25.2). The deep-learning approach is powerful in reducing reconstruction time up to ten-fold, detecting inclusions with a Dice coefficient of up to 0.5, and predicting absolute values of μ_a with a RMSE in the order of 3×10^{-3} mm^{-1} (Tables 25.1, 25.2, and 25.3). The average PSNR of 49.66 and 50.19 for hCNN and MB recon-

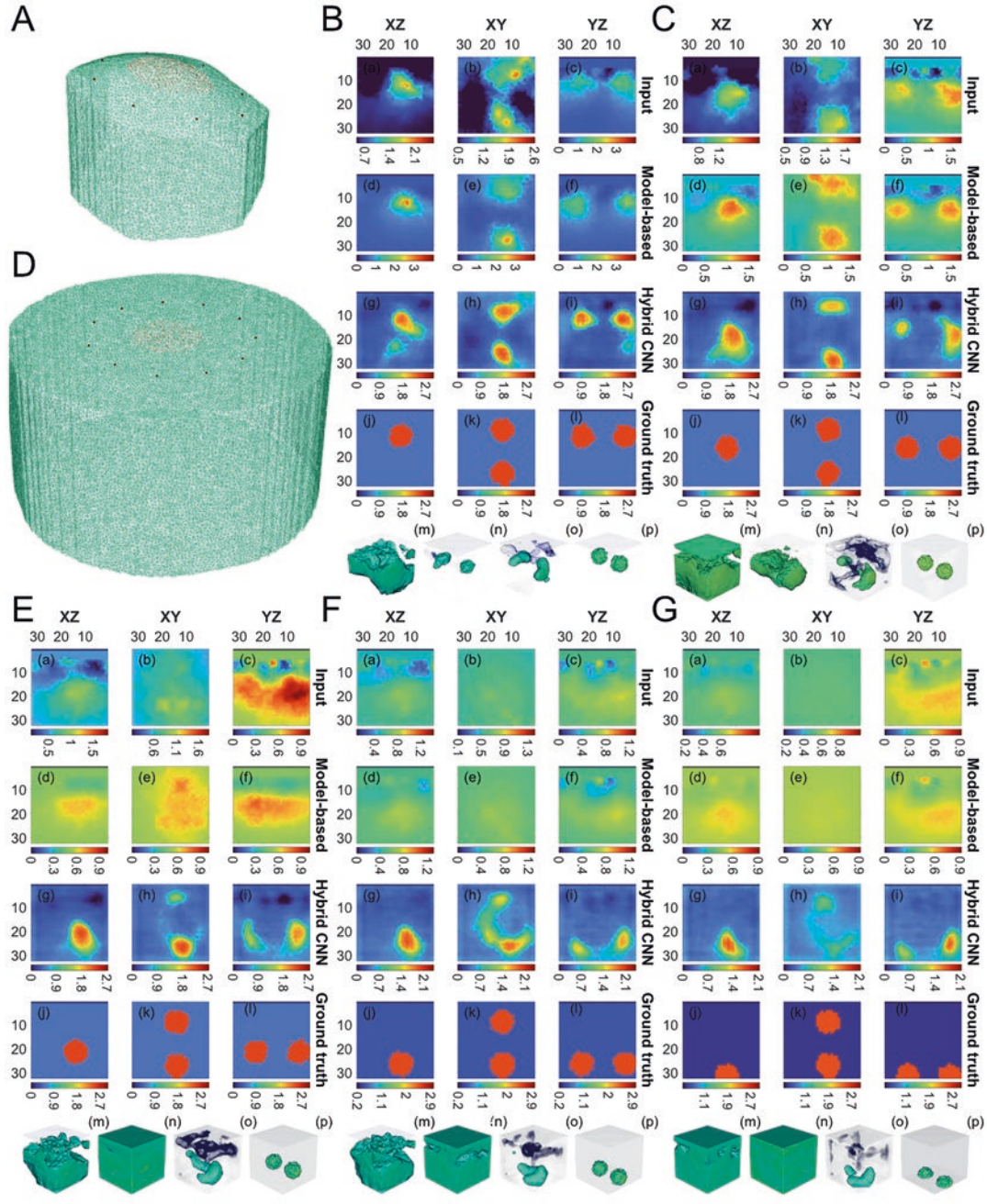

Fig. 25.1 (**A**) One of the tissue model surfaces used to train the hCNN (**D**) the mesh used for image reconstruction (**B**, **C**) and (**E–G**). Data acquisition was performed at 725 nm to reconstruct liquid phantoms (μ_a: 0.0048 mm^{-1}, μ_s': 0.35 mm^{-1}) with two inclusions (8 mm Ø, μ_a: 0.033 mm^{-1}, μ_s': 0.59 mm^{-1}) at 16 mm distance and placed at 10, 15, 20, 25 and 30 mm from the surface. The color maps represent μ_a values in 1×10^{-2} mm^{-1}. The axes are given in mm. (**a–l**) show cross sections of the (**a–c**) input (**d–f**) MB (**g–i**) hCNN and (**j–l**) GT image. (**m–p**) are volumetric visualizations of the hCNN input, full MB reconstruction, hCNN reconstruction and ground truth, respectively

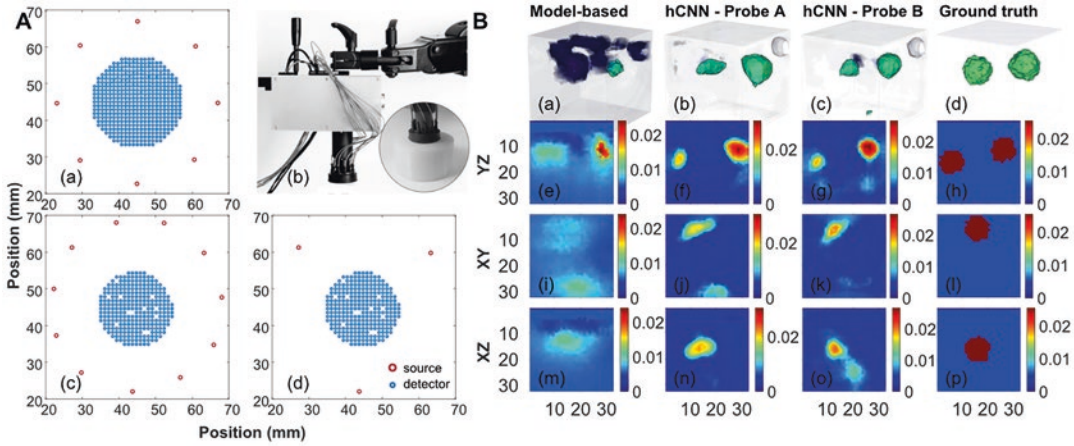

Fig. 25.2 (**A**) Probe setups: (**a**) Probe OCTA (8 sources) used for the in-silico data. (**c**) Probe UNDECA (11 sources) (**b**) placed on a solid phantom and in side view. (**d**) Probe TRI (3 sources). (**B**) Reconstruction of a solid phantom (μ_a: 0.0054 mm^{-1}, μ_s': 1.01 mm^{-1}) with two inclusions (10 mm Ø, μ_a: 0.0253 mm^{-1}, μ_s': 0.98 mm^{-1}) at different depths (10 mm, 15 mm) separated by 20 mm in the XY-plane. The measurement was done at 725 nm and with the probes UNDECA and TRI. The color maps represent μ_a values in mm^{-1}. The axes are given in mm

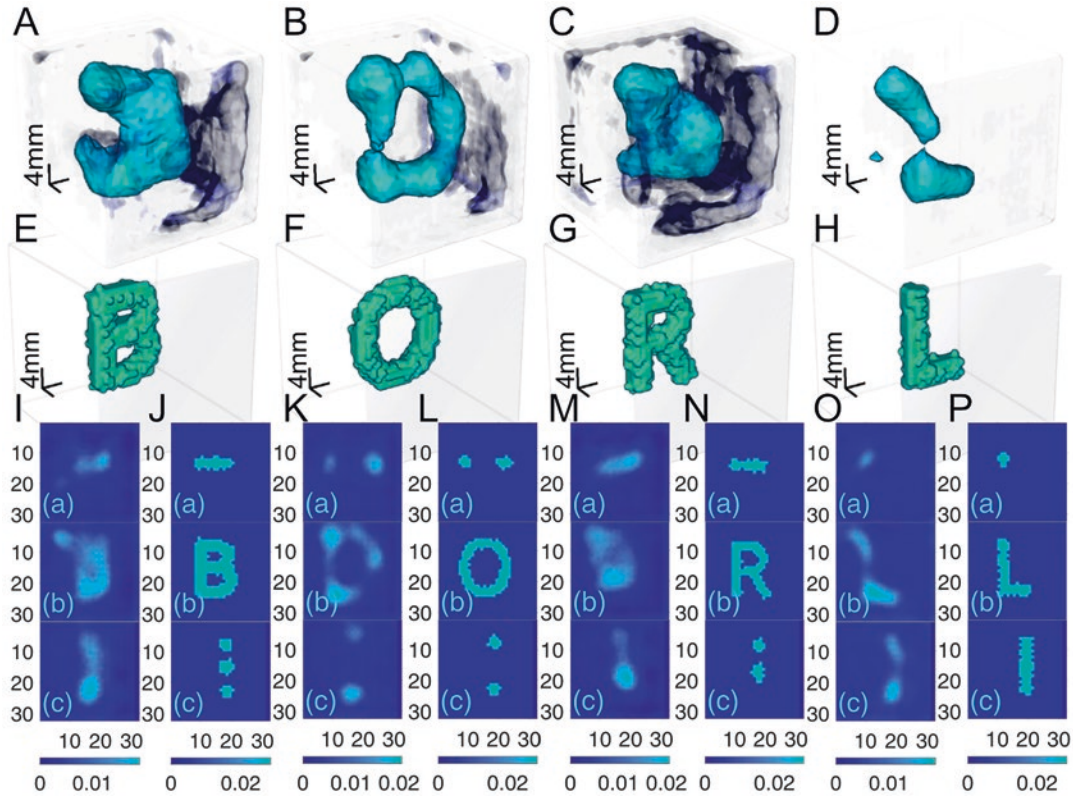

Fig. 25.3 (**A–D**) hCNN reconstructions of liquid phantoms (μ_a: 0.0048 mm^{-1}, μ_s': 0.69 mm^{-1}) with 15 mm deep letter shaped inclusions (μ_a: 0.0285 mm^{-1}, μ_s': 0.67 mm^{-1}). (**E–G**) are the corresponding GT volumes. (**I–P**) show the resp. cross sections: (**a**) XZ (**b**) XY (**c**) ZY. Measurements were performed at 689 nm. The color maps represent μ_a values in mm^{-1}. The axes are given in mm

Table 25.1 Evaluation of liquid phantom measurements with inclusions at different depths (Fig. 25.1). Comparison of evaluation metrics for hCNN and MB reconstructions

	RMSE (mm^{-1}) hCNN | MB	Dice hCNN|MB	PSNR hCNN|MB	SSIM hCNN|MB	Time (s) hCNN|MB
Depth 10 mm	3.03×10^{-3}|3.14×10^{-3}	0.53|0.40	50.38|50.05	0.996|0.996	99.01|850.38
Depth 15 mm	3.58×10^{-3}|3.18×10^{-3}	0.40|0.39	48.94|49.97	0.995|0.996	96.46|887.55
Depth 20 mm	3.49×10^{-3}|3.45×10^{-3}	0.43|0.27	49.14|49.24	0.995|0.995	96.86|646.16
Depth 25 mm	3.39×10^{-3}|3.46×10^{-3}	0.45|0.23	49.38|49.20	0.995|0.995	96.17|927.22
Depth 30 mm	2.88×10^{-3}|2.73×10^{-3}	0.39|0.08	50.82|51.29	0.996|0.996	91.75|930.38

Table 25.2 Evaluation of solid phantom measurements with varied probe arrangements (Fig. 25.2). Comparison of evaluation metrics for hCNN and MB reconstructions

	RMSE (mm^{-1}) hCNN|MB	Dice hCNN|MB	PSNR hCNN|MB	SSIM hCNN|MB	Time (s) hCNN|MB
Probe UNDECA	3.10×10^{-3}|3.14×10^{-3}	0.48|0.36	50.18|50.07	0.996|0.996	92.25|775.14
Probe TRI	3.03×10^{-3}|3.21×10^{-3}	0.53|0.36	50.37|49.89	0.997|0.996	73.57|791.00

Table 25.3 Evaluation of liquid phantom measurements with letter shaped inclusions (Fig. 25.3). Comparison of evaluation metrics for hCNN and MB reconstructions

	RMSE (mm^{-1}) hCNN|MB	Dice hCNN|MB	PSNR hCNN|MB	SSIM hCNN|MB	Time (s) hCNN|MB
Letter B	3.85×10^{-3}|3.11×10^{-3}	0.40|0.47	48.29|50.13	0.994|0.996	81.26|710.18
Letter O	3.66×10^{-3}|3.18×10^{-3}	0.40|0.28	48.72|49.96	0.995|0.996	84.47|650.71
Letter R	3.69×10^{-3}|2.96×10^{-3}	0.45|0.32	48.66|50.58	0.995|0.996	81.86|637.60
Letter L	2.70×10^{-3}|2.59×10^{-3}	0.42|0.32	51.39|51.75	0.998|0.998	80.65|670.97

structions, respectively, and the average SSIM of 0.996 for both approaches indicate that there is no loss of image quality despite increased localization accuracy and speed. The larger mesh used for the reconstruction increased the time required, but the relative gain remained at an average reduction of 89%, consistent with previously reported time benefits [1].

25.4 Discussion and Conclusion

Our time-domain NIROT system, Pioneer, provides orders of magnitude more information than previous systems. With the hCNN approach it is possible to take advantage of this information.

We achieved striking image reconstructions for real measurements. Consideration of diverse overlapping inclusions and surfaces in the training data allowed transfer to substantially different geometric conditions. Our approach features a higher localization accuracy compared to the conventional MB, particularly in very challenging conditions such as deep inclusions (Fig. 25.1E–G) and provides a clinically highly relevant increase in reconstruction speed.

It is important to ensure with further measures that the sensitivity of the hCNN approach is not sacrificed at the expense of specificity as implied in Fig. 25.2Bc, a common challenge for entropy boosted deep learning [6]. Yet, the successful generalization of hCNN shows promise for translation to clinical applications. In deep learning-based imaging, the generalization capability of an architecture is particularly important, especially for new technologies. Data-driven approaches for NIROT cannot simply rely on data abundance as real training data is scarce. Taking these considerations into account, the good performance of the developed approach on real measurements and under different acquisition conditions is an even more crucial step for-

ward. Given the extensive requirements for NIROT in the clinical setting, the proposed deep learning approach has a persuasive power that trumps traditional approaches.

Acknowledgments We gratefully acknowledge funding by the Swiss National Science Foundation (159490 and 197079), Innovationspool of the University Hospital Zurich and Innosuisse (52181.1), UZH Entrepreneur Fellowships (MEDEF21-025) and Forschungskredit K-84302-02-01. MW declares that he is president of the board and co-founder of OxyPrem AG. AK declares that he is part-time employed by OxyPrem AG.

References

1. Ackermann M, Jiang J, Russomanno E et al (2022) Hybrid convolutional neural network (hCNN) for image reconstruction in near-infrared optical tomography. Adv Exp Med Biol 1395
2. Jiang J, Ackermann M, Russomanno E et al (2022) Resolution and penetration depth of reflection-mode time-domain near infrared optical tomography using a ToF SPAD camera. Biomed Opt Express 13:6711–6723
3. Jiang J, Mata ADC, Lindner S et al (2020) Image reconstruction for novel time domain near infrared optical tomography: towards clinical applications. Biomed Opt Express 11(8):4723–4734
4. Dehghani H, Eames ME, Yalavarthy PK et al (2009) Near infrared optical tomography using NIRFAST: algorithm for numerical model and image reconstruction. Commun Numer Methods Eng 25(6):711–732
5. Crum WR, Camara O, Hill DLG (2006) Generalized overlap measures for evaluation and validation in medical image analysis. IEEE Trans Med Imaging 25(11):1451–1461. https://doi.org/10.1109/TMI.2006.880587
6. Chan R, Rottmann M, Gottschalk H (2021) Entropy maximization and meta classification for out-of-distribution detection in semantic segmentation. In: Proceedings of the ieee/cvf international conference on computer vision, pp 5128–5137

26 Neonatal Brain Temperature Monitoring Based on Broadband Near-Infrared Spectroscopy

F. Lange, V. Verma, K. Harvey-Jones, S. Mitra, and I. Tachtsidis

Abstract

We present here the initial development of a novel algorithm based on broadband near-infrared spectroscopy (bNIRS) data to estimate the changes in brain temperature (BT) in neonates. We first explored the validity of the methodology on a simple numerical phantom and reported good agreements between the theoretical and retrieved values of BT and hemodynamic parameters changes, which are the parameters usually targeted by bNIRS. However, we noted an underestimation of the absolute values of temperature and haemoglobins' concentration changes when large variations of tissue saturation were induced, probably due to a crosstalk between the species in this specific case. We then tested this methodology on data acquired on 2 piglets during a protocol that induces seizures. We showed that despite a decrease in rectal temperature (RT) over time (−0.1048 °C 1.5 h after seizure induction, 95% CI: −0.1035 to −0.1061 °C), BT was raising (0.3122 °C 1.5 h after seizure induction, 95% CI: 0.3207 to 0.3237 °C). We also noted that the piglet displaying the largest decrease in RT also displays the highest increase in BT, which could be a marker of the severity of the seizure induced brain injury. These initial results are encouraging and show that having access to the changes in BT non-invasively could help to better understand the impact of BT on injury severity and to improve the current cooling methodologies in the neonatal neurocritical care following neonatal encephalopathy.

Keywords

Brain temperature · Broadband near-infrared spectroscopy · Neonates · Neuromonitoring

26.1 Introduction

Brain tissue temperature is a dynamic balance between heat generation from metabolism, passive loss of energy to the environment, and thermoregulatory processes such as perfusion. Perinatal brain injuries, particularly neonatal encephalopathy (NE) and seizures, have a significant impact on the metabolic and haemodynamic state of the developing brain, and thereby likely induce changes in brain temperature (BT). The brain and/or body temperature elevation is indeed often associated with brain injury [1]. Moreover, therapeutic hypothermia (TH) is now a well-

F. Lange (✉) · I. Tachtsidis
Department of Medical Physics and Biomedical Engineering, University College London, London, UK
e-mail: f.lange@ucl.ac.uk

V. Verma · K. Harvey-Jones · S. Mitra
Institute for Women's Health, University College London, London, UK

F. Scholkmann et al. (eds.), *Oxygen Transport to Tissue XLIV*, Advances in Experimental Medicine and Biology 1438, https://doi.org/10.1007/978-3-031-42003-0_26

established standard to treat infants with moderate to severe hypoxic–ischemic encephalopathy (HIE) but this method is only partially effective [2]. In that context, having a tool allowing to follow the brain temperature non-invasively at the bedside can help to optimize the TH treatments and further benefit the care of infants in the neonatal intensive care unit (NICU).

Indeed, magnetic resonance spectroscopy (MRS) has been used as a viable, non-invasive tool to measure temperature in the newborn brain [3]. However, MRS thermometry requires transport to an MRI scanner and a lengthy single-point measurement. On the other hand, optical monitoring using near-infrared spectroscopy (NIRS), has the promise to overcome this limitation and be able to monitor the newborn's brain tissue temperature continuously at the bedside.

To answer this need, we propose a novel algorithm based on broadband NIRS fitting to monitor BT in real-time, together with parameters related to tissue oxygenation and metabolism. This algorithm can be deployed on our research instrument, named FLORENCE, currently in use in the NICU, that combines bNIRS and Diffuse Correlation Spectroscopy (DCS). This would allow to complement the current monitoring of the hemodynamic and metabolic brain parameters of infants.

This algorithm is based on the linear temperature-dependent changes in NIR water absorption spectra to estimate the tissue temperature. Previous algorithms have been developed in order to estimate the tissue temperatures using this feature, however, they required the use of an extra calibration step based on principal component analysis [4]. Here, we directly used the absorptivity temperature coefficients from the literature [5]. Briefly, this two-steps algorithm is based on (1) the initial fit of the optical properties based on the second derivative methods and (2) the fit of the changes in absorption considering only the oxy- and deoxyhaemoglobin ([HbO_2] and [HHb] respectively) and temperature changes.

In this work, we present the algorithm and demonstrates its capacities on a basic numerical phantom. Then, we applied it to data collected on 2 piglets in preclinical studies looking at seizures, which are known to induces BT [6].

26.2 Methods

The algorithm presented here is based on the broadband fitting method [7]. This method allows to retrieve the spectral absorption and reduced scattering coefficients of the tissue by spectrally constraining the possible solutions, both for the absorption, i.e., only considering the absorption spectra of specific chromophore, typically the haemoglobins and water, and for the scattering, by assuming it follows the Mie equation, reducing it to two parameters: a and b.

In order to estimate the temperature changes of the tissue, a two-step method is used. Firstly, the standard broadband fitting optimisation routine is applied on the baseline spectra. The fitting procedure uses the solution to the diffusion approximation for a semi-infinite medium as a reference function and is split into three steps to target individual spectral features of the chromophores: (i) the water content (WC) is found by fitting the second derivative of the reflectance spectra (R) in the range of prominent water absorption features, between 825 and 850 nm, (ii) after fixing the found WC, [HHb] is found by fitting the second derivative of R, between 700 and 800 nm, as this range has a distinct 760 nm HHb feature, (iii) for the last step, [HHb] is also set constant and [HbO_2], a and b are determined from fitting the first spectral derivative of R, between 680 to 845 nm.

This constitutes an initial fit of the optical parameters of the tissues. Then, in order to measure the temperature changes of the tissues, the information acquired by the initial fit is used to fit the differential reflectance spectra (Rdiff) from the initial point. To do so, R_{diff} is calculated as: $R_{\text{diff}_{\Delta\mu_a,\Delta\mu_s'}}(t) = R_{\mu_a,\mu_s'}(t) - R_{\mu_a,\mu_s'}(t_0)$. The parameters of $R_{\mu_a,\mu_s'}(t_0)$ are known from the initial fit, as the scattering parameters from $R_{\mu_a,\mu_s'}(t)$ that are assumed constant over time. The absorption parameters of $R_{\mu_a,\mu_s'}(t)$ are calculated as $\mu_a\,(t) = \mu_a(0) + \Delta\mu_a$, with $\mu_a(0)$ known from the initial fit and $\Delta\mu_a = \Delta T * \varepsilon_T + \Delta[HbO_2] * \varepsilon_{[HbO_2]} + \Delta[HHb] * \varepsilon_{[HHb]}$.

Here ε_x is the extinction coefficient spectra of chromophore x. Thus, in that step, ΔT, $\Delta[HbO_2]$ *and*$\Delta[HHb]$ are the fitted parameters. This fitting procedure is performed between 720 and 880 nm.

In order to investigate the accuracy of the method and potential crosstalk between the fitting parameters, simulated spectra of various tissue parameters were generated using the solution to the diffusion approximation for a semi-infinite medium [8]. Here, we will report the simulation of a concurrent change in BT and brain oxygen tissue saturation (StO_2). Here, StO_2 is defined as $StO_2 = [HbO_2] / [HbT]$, with $[HbT] = [HbO_2] + [HHb]$. We thus induce changes in temperature, $[HbO_2]$ and [HHb] but keep [HbT] constant (100 μM). This will enable us to investigate the potential crosstalk between these parameters. Maximum temperature variations of +/−2 °C were induced and the StO_2 values were varied in a range 50–85%. The theoretical values of these variables are display as solid lines in Fig. 26.1.

Finally, optical data was collected with FLORENCE on piglets monitored during a preclinical study looking at seizures. We only focused on the bNIRS data here which were recorded between 700 and 900 nm, with a 1 nm resolution, and a source/detector distance of 3 cm (reflectance mode). Briefly, the seizures were induced using bicuculine (4 mg/kg) in 2 white male piglets and were continuously monitored with a combined optical platform and continuous video EEG for 2.5 h. Systemic parameters were also recorded, and particularly the rectal temperature of the animal which was compared to the brain temperature estimated using the novel algorithm.

26.3 Results

Figure 26.1 presents the retrieved changes in BT, $[HbO_2]$ and [HHb] using the novel algorithm. The simulation emulates a large desaturation event (StO_2 drops from 75% to 50%), a plateau at low saturation (50%) and a return to normal with an overshoot to 85%. In the meantime, the temperature change was simulated in a range +2 to −2 °C, with plateau values set at different time compared to saturation plateau. This allows to investigate the crosstalk between the temperature and haemoglobins concentration changes.

We can see that the trend of both BT and haemoglobins' concentrations are retrieved with reasonable agreement. However, the maximum change in the raising temperature is underestimated by a maximum of 1 °C and, at the saturation plateau, the changes in haemoglobins' concentrations are also underestimated by a maximum of 4 μMol. We can note than the maximum of these discrepancies appears for large haemoglobins' concentration changes. Below a 10 μMol haemoglobin's concentration change, the maximum mismatch between theoretical and calculated temperature values is 0.5 °C.

Figure 26.2 focuses on the measured values of rectal and brain temperature (RT and BT respectively) changes for the 2 piglets. Both RT and BT dropped soon after seizure induction for the 2 piglets. Subsequently, a significant increase in BT was noted (0.3122 °C at 1.5 h after seizure induction, 95% CI: 0.3207 to 0.3237 °C), while RT decreased followed by a recovery and a mild increase from baseline with a trend to decrease over time. 1.5 h after the seizure induction, RT was significantly reduced by −0.1048 °C (95% CI: −0.1035 to −0.1061 °C). Finally, oscillations can be seen in the BT changes in piglet 1. These oscillations were also present in the other variables monitored (like $[HbO_2]$ and [HHb], heart rate; data not shown). We have noticed this behaviour in several piglets monitored by our system in this study and are currently exploring the possible reasons for this phenomenon to occur. However, since these oscillations are present in all the variables (both brain and systemic), we are confident that this is a real physiological signal, and not an artefact from the BT algorithm.

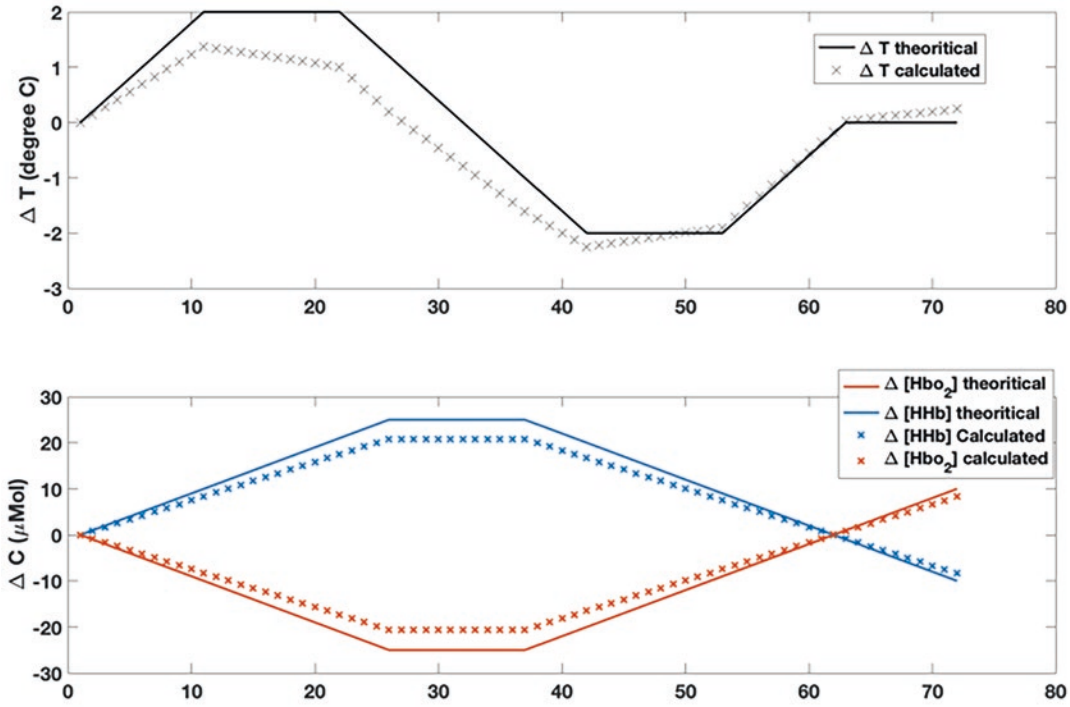

Fig. 26.1 Results of the simulation. Upper Panel – Temperature changes estimation together with theoretical values. Lower Panel – Haemoglobins' concentrations changes estimation together with theoretical values

26.4 Discussion

We report here the initial development of a novel algorithm designed to measure BT in neonates. This algorithm has been evaluated through numerical simulations emulating large changes in haemoglobins' concentrations and moderated temperature changes. This extreme scenario allows us to check for potential crosstalk between temperature and haemoglobin concentration changes. We have shown that both the temperature and haemoglobins' concentrations changes could be retrieved with reasonable agreement. However, an underestimation of the temperature and haemoglobins' concentrations changes was noted, with the maximum discrepancies between the theoretical and measured values found when haemoglobin concentrations changes were superior to 10 μMol (for [HbT] = 100 μMol), which corresponds to high values of StO_2 changes. This inaccuracy is likely due to a crosstalk between the variables when hemoglobins changes becomes significant. Thus, a more precise evaluation of this phenomena will be required if the present algorithm needed to be used in such cases. However, for moderate variation of StO_2, we can expect to retrieve accurate values of BT. This would correspond to most long-term monitoring scenarios in which we are interested, were large desaturation events are only transitory.

The current algorithm has then been tested on real datasets acquired during preclinical studies looking at the effect of seizures on the piglet brain. We could see that despite a decrease in RT induces by the seizure, the BT was increasing. This increase in BT with seizures was previously reported in the literature [6]. We can also note that the piglet displaying the largest decrease in RT temperature also displays the highest increase in BT, which could be a marker of the severity of the seizure induced brain injury. Although these are only case studies, these initial results are encouraging. However, more validation work is required at that stage. Indeed, invasive tempera-

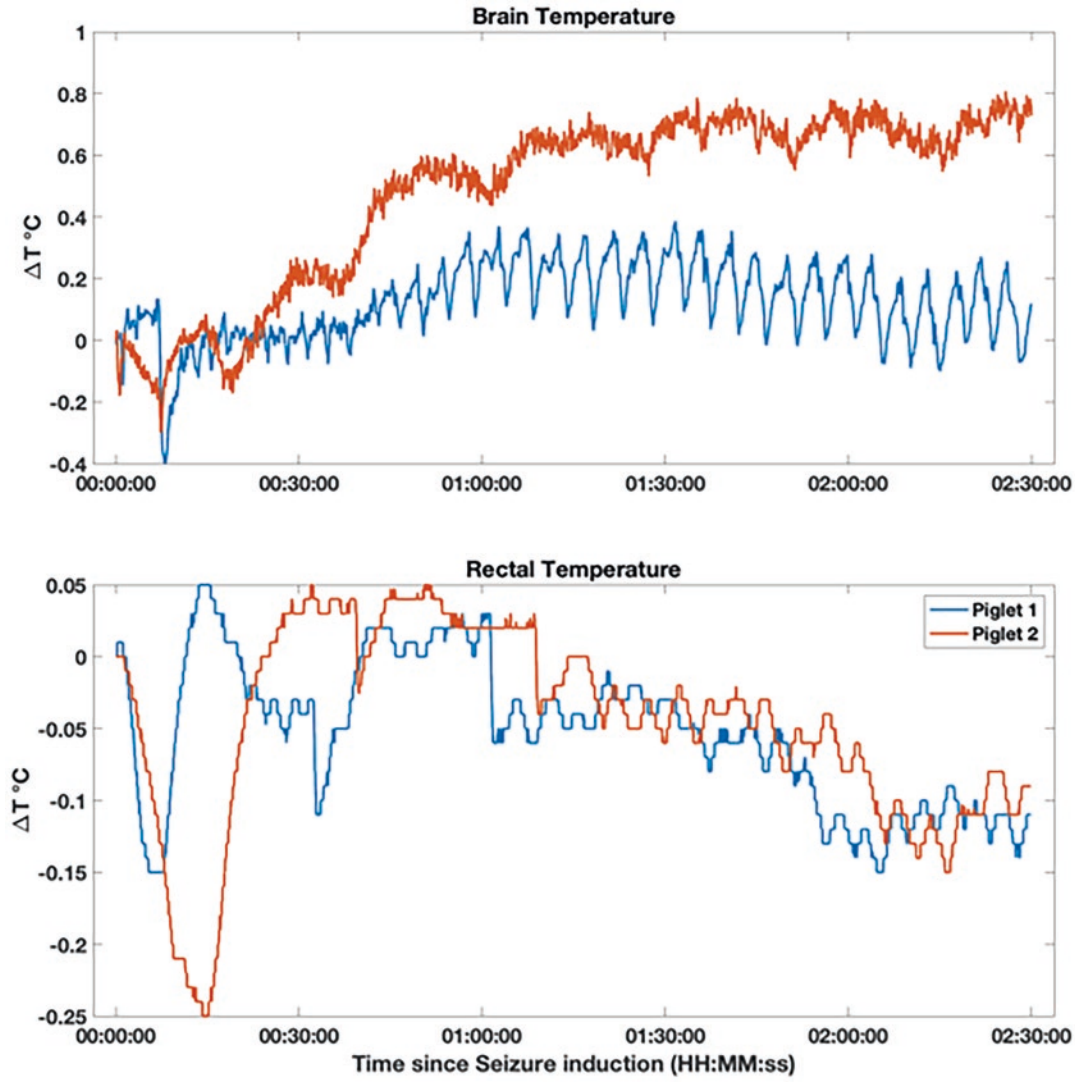

Fig. 26.2 Brain temperature (upper) and rectal temperature (lower) for the 2 piglets. Time 0 is the time of seizure induction

ture monitoring would be required in order to fully validate the accuracy of the measurement of the BT using this algorithm. Unfortunately, this data was not available for the datasets processed here. Alternatively, more complex numerical simulation, based on Monte-Carlo simulation, allowing to take into account the effect of the anatomy [9], and incorporating noise level comparable to the one of our instruments could be used to validate further our results. Nevertheless, our initial numerical simulations showed that the estimation of the BT changes could be retrieve with reasonable accuracy, and our first test on preclinical data could retrieve values of BT changes in line with values previously reported in the literature. This constitutes a good first step into the validation of the BT measurement using our methods.

In conclusion, we report the initial development of a novel algorithm based on bNIRS data to measure concurrently the BT and oxygenation changes. The initial validations steps displayed encouraging results, and we believe that providing the clinicians with such information would

help them to better understand the impact of brain temperature on injury severity and to improve the current cooling methodologies in the neonatal neurocritical care following NE.

Acknowledgments The authors are supported by the Wellcome Trust (219,610/Z/19/Z), Medical Research Council (MR/S003134/1) and National Institute for Health Research University College London Hospitals Biomedical Research Centre.

References

1. Laptook A, Tyson J, Shankaran S et al (2008) Elevated temperature after hypoxic-ischemic encephalopathy: risk factor for adverse outcomes. Pediatrics 122:491–499
2. Low E, Boylan GB, Mathieson SR et al (2012) Cooling and seizure burden in term neonates: an observational study. Arch Dis Child Fetal Neonatal Ed 97:F267–F272
3. Corbett R, Laptook A, Weatherall P (1997) Noninvasive measurements of human brain temperature using volume-localized proton magnetic resonance spectroscopy. J Cereb Blood Flow Metab 17:363–369
4. Hollis VS, Binzoni T, Delp DT (2001) Non-invasive monitoring of brain tissue temperature by near-infrared spectroscopy. Proc SPIE 4250:470–481. https://doi.org/10.1117/12.434506
5. Langford VS, McKinley AJ, Quickenden TI (2001) Temperature dependence of the visible-near-infrared absorption Spectrum of liquid water. J Phys Chem A 105:8916–8921
6. Yang X-F, Chang JH, Rothman SM (2002) Intracerebral temperature alterations associated with focal seizures. Epilepsy Res 52:97–105. https://doi.org/10.1016/s0920-1211(02)00193-6
7. Kovácsová Z (2020) A novel approach to monitor tissue oxygen saturation with broadband near-infrared spectroscopy
8. Kienle A, Patterson MS (1997) Improved solutions of the steady-state and the time-resolved diffusion equations for reflectance from a semi-infinite turbid medium. J Opt Soc Am A 14:246–254
9. Fang Q (2010) Mesh-based Monte Carlo method using fast ray-tracing in Plücker coordinates. Biomed Opt Express 1:165–175

27 Time Domain Near-Infrared Optical Tomography Utilizing Full Temporal Data: A Simulation Study

Letizia Lanini, Alexander Kalyanov, Meret Ackermann, Emanuele Russomanno, Aldo Di Costanzo Mata, Martin Wolf, and Jingjing Jiang

Abstract

The analysis of full temporal data in time-domain near-infrared optical tomography (TD NIROT) measurements enables valuable information to be obtained about tissue properties with good temporal and spatial resolution. However, the large amount of data obtained is not easy to handle in the image reconstruction. The goal of the project is to employ full-temporal data from a TD NIROT modality. We improved TD data-based 3D image reconstruction and compared the performance with other methods using frequency domain (FD) and temporal moments. The iterative reconstruction algorithm was evaluated in simulations with both noiseless and noisy in-silico data. In the noiseless cases, a superior image quality was achieved by the reconstruction using full temporal data, especially when dealing with inclusions at 20 mm and deeper in the tissue. When noise similar to measured data was present, the quality of the recovered image from full temporal data was no longer superior to the one obtained from the analysis of FD data and temporal moments. This indicates that denoising methods for TD data should be developed. In conclusion, TD data contain richer information and yield better image quality.

Keywords

Time Domain Near-Infrared Optical Tomography · Image reconstruction · Image quality

27.1 Introduction

We have developed an imaging system called Pioneer with the aim of diagnosing hypoxia in preterm infants. This is achieved by performing time-domain near-infrared optical tomography (TD NIROT) to dynamically monitor the oxygenation levels in the infant brain [1]. NIROT is set to be a significant clinical resource which

L. Lanini (✉)
Department of Physics, ETH Zürich, Zürich, Switzerland

Biomedical Optics Research Laboratory (BORL), Department of Neonatology, University Hospital Zürich, University of Zürich, Zürich, Switzerland
e-mail: laninil@student.ethz.ch

A. Kalyanov · M. Ackermann · E. Russomanno
A. D. C. Mata · M. Wolf · J. Jiang
Biomedical Optics Research Laboratory (BORL), Department of Neonatology, University Hospital Zürich, University of Zürich, Zürich, Switzerland

F. Scholkmann et al. (eds.), *Oxygen Transport to Tissue XLIV*, Advances in Experimental Medicine and Biology 1438, https://doi.org/10.1007/978-3-031-42003-0_27

allows non-invasive imaging of tissue properties. It is based on the capability of near-infrared (NIR) light to harmlessly penetrate biological tissue to a depth of several centimeters. The spatial distribution of the absorption (μ_a) and reduced scattering coefficient (μ'_s) can be reconstructed by analyzing the reflected or transmitted light after its path through the investigated material. Since the μ_a of hemoglobin strongly depends on its oxygenation level, a spectral measurement determines tissue oxygenation [2].

Pioneer applies 11 ps-laser sources to convey light into the head. A CMOS SPAD array detects the photons reemerging from the tissue and time-to-digital converters record the time-of-flight (ToF) information over 256-time bins with a temporal resolution of 48.8 ps. An FPGA board processes the ToF and stores it as histograms. The final amount of data corresponds to the multiplication of the number of sources, their wavelengths, detectors in the field-of-view (FoV) and time bins.

To extract images from these data, different image reconstruction methods are available, based on the Fourier transform (FD approach) or their integral-transform-based temporal moments (M approach) [1, 3]. Another option would be to include the full temporal data (TD approach). Among the different methods, we expect the highest image quality by TD, since it includes the whole temporal information. A critical aspect of using the Pioneer system with TD NIROT is that it requires processing an enormous quantity of data, making the analysis extremely time-consuming. Therefore, an efficient image reconstruction algorithm is necessary. The goal of this work is to optimize a 3D reconstruction algorithm in TD that uses full temporal data, and compare its performance with existing methods.

27.2 Theory and Method

A model-based image reconstruction approach consists of two parts: the forward and inverse problem. The forward problem is solved to describe light transport in the tissue of interest, and subsequently the optical coefficients of the same tissue are recovered through the inverse problem. When dealing with NIR light in biological material, the forward problem is approximated by diffusion equations (DE):

$$\left[-\nabla\cdot\kappa(\mathbf{r})\nabla+\mu_a(\mathbf{r})+\frac{1}{c_0}\frac{\partial}{\partial t}\right]\phi(\mathbf{r},t)=q(\mathbf{r},t). \tag{27.1}$$

In the DE, $\kappa = 1/[3\mu'_s]$ is the diffusion coefficient, $\boldsymbol{r}$ is the position vector, c_0 is the speed of light in the medium, $\phi(\boldsymbol{r}, t)$ is the photon density distribution, and $q(\boldsymbol{r}, t)$ represents the source term, which we consider to have Gaussian profile [4]. The forward problem is solved for the fluence rate $\Phi^S(t)$ at the detectors using a finite elements method. We implement this method using NIRFASTer, a GPU-facilitated package containing codes for modeling light propagation in tissue together with image reconstruction algorithms [5–7]. The inverse problem consists of iteratively evolving the set of optical coefficients $\boldsymbol{\mu}$ of the tissue on a coarse mesh, to minimize the difference between Φ^S and the directly measured values Φ^M. The starting optical properties $\boldsymbol{\mu_0}$ are taken from a separate measurement on a homogeneous reference phantom and the iteration continues until the improvement becomes smaller than some threshold value [5]. The final optimal coefficients $\boldsymbol{\mu}^*$ result from

$$\boldsymbol{\mu}^* = \arg\min_m \left|\left|\Phi^S(\boldsymbol{\mu})-\Phi^M\right|\right|_2^2+\lambda\left|\left|\boldsymbol{\mu}-\boldsymbol{\mu_0}\right|\right|_2^2, \tag{27.2}$$

using the Tikhonov regularization with regularization parameter λ [3].

We simulated the reconstruction process on a cylindrical mesh with two spherical inclusions at different depths. The mesh had 45 mm radius and 50 mm height, and consisted of 231,938 nodes. The coarse mesh used in the reconstruction process was made of 5532 nodes. The inclusions had 5 mm radius and were located 8 mm apart along the x-axis and at intervals of 5 mm between 10 to 30 mm depth (z-axis) inside the cylinder (Fig. 27.1a). We assigned $\mu_a = 0.0055$ mm^{-1} and $\mu'_s = 0.76$ mm^{-1} to the bulk, and $\mu_a = 0.03$ mm^{-1} and $\mu'_s = 0.9$ mm^{-1} to the spheres, so as to simulate healthy and poorly oxygenated brain tissue respectively, and study the truthful ability to

identify the latter. Eleven light sources were considered, arranged as in the Pioneer device (Fig. 27.1a), with 725 nm wavelength. For the TD approach to become affordable in terms of memory burden, the number of active detectors was reduced to 23 out of the 268 available in the FoV of Pioneer. We used the maximum number allowed by the memory of the computer, and selected the detectors so that their location still homogeneously covered the FoV area (Fig. 27.1a). The initial regularization parameter was $\lambda = 10$ and the measurement period was subdivided into 50 time bins.

Subsequently, we applied a noise model to the simulated data to test the reconstruction algorithm with noisy values. The noise model was generated from experimental data collected on silicone phantoms with optical properties comparable to those of the mesh. We considered 7 histograms, captured from randomly selected central pixels of the Pioneer camera (Fig. 27.1b). For the noise, we took the mean n and standard deviation σ'_n in the range of 180th and 256th time bin. To scale the noise values to the simulated ones we computed the mean signal value s of each histogram between the 30th and 130th time bin. We then calculated the averages $s = \overline{s'}$, $n = \overline{n'}$ and $\sigma_n = \overline{\sigma_n'}$ between the 7 histograms, whose values are reported in Fig. 27.1b. The array of noise values over time bins was obtained as $N = n + x \bullet \sigma_n$, with a different array x of normally distributed random values for each source-detector pair. Noisy data in TD were then generated as $\text{data}_{\text{noisy}} = \text{data}_{\text{simulated}} + N \bullet S$, where $S = \overline{\text{data}_{\text{simulated}}} / s$ is the scaling factor between the amplitude of the simulated data and the measured ones.

As a comparison, reconstructed images were generated for the same mesh and inclusions geometry using the already existing algorithms that exploit the data converted to FD at 100 MHz and their 0th, 1st and 2nd order temporal moments. In those cases, the simulation was performed considering the same 23 detectors as in the full temporal data case, and then repeated with all 268 available detectors active.

The workstation used to run the reconstruction processes was a GPU Nvidia Gtx Titan Xp with 12 GB of memory size and we utilized a 64 GB DDR4 memory card.

27.3 Results and Discussion

Figure 27.2a–e show the X-Z cross section of the reconstructed map of μ_a from noiseless data with inclusions at 10 mm depth. Comparable accuracy is observed between the results from TD and those

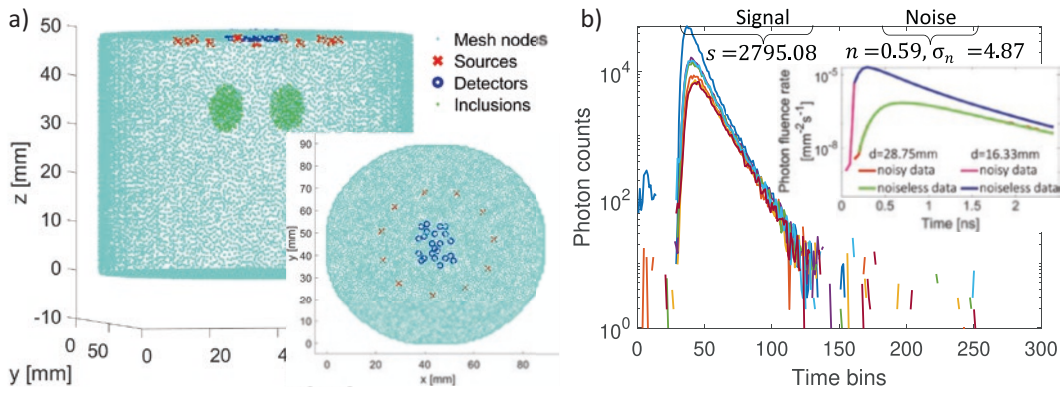

Fig. 27.1 (**a**) Cylindrical mesh and spherical inclusions, with locations of sources and detectors. (**b**) 7 histograms (represented by different colors) selected to compute the noise model, together with the mean value of the signal between the 30th and 130th time bin and the mean value and standard deviation of the noise between the 180th and 256th. The insert in (b) shows the photon fluence rate over time of 2 source-detector pairs from simulated noiseless data and from the generated noisy ones. The pair with shorter separation distance d has better SNR

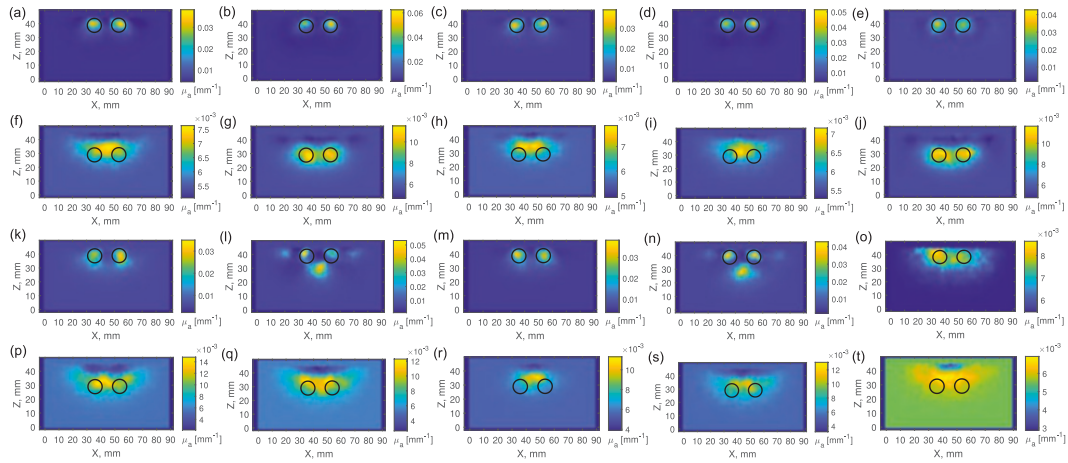

Fig. 27.2 X-Z cross section of the reconstructed distribution of μ_a [mm^{-1}] represented by a color map, with ground-truth border of the inclusions in black and axes in mm. The rows show results from: (**a-e**) noiseless data with inclusions at 10 mm depth, (**f-j**) noiseless data with inclusions at 20 mm depth, (**k-o**) noisy data with inclusions at 10 mm depth, (**p-t**) noisy data with inclusions at 20 mm depth. The columns are organized depicting the results from: (**a**, **f**, **k**, **p**) FD data from 268 active detectors, (**b**, **g**, **l**, **q**) FD data from 23 active detectors, (**c**, **h**, **m**, **r**) M data from 268 active detectors, (**d**, **I**, **n**, **s**) M data from 23 active detectors, (**e**, **j**, **o**, **t**) TD data from 23 active detectors

from FD and M analysis, as both inclusions are discernible. The Dice values in Table 27.1a confirm a good accordance with the ground-truth for all reconstruction cases. The results in Fig. 27.2f–j show that inclusions at 20 mm depth are resolved with superior accuracy and good Dice similarity from TD analysis. A comparable quality is observed only from the FD case with 23 active detectors, which has surprisingly high Dice value and low mean squared error (MSE), especially with respect to the FD case with 268 detectors. Deeper inclusions are no more separately resolved by any reconstruction method, but TD still retrieves their correct depth. Table 27.1a, b shows that the duration of the reconstruction process with full data took on average 1 hour and 8 minutes, ~4x longer than FD and M analysis with 268 detectors. The reconstruction using FD and M with just 23 active detectors took only 1/5 of the one with the respective data type but 268 detectors; the fact that high quality results were obtained in such short time is worth a further investigation.

From the results obtained by simulated noisy data (Fig. 27.2k–t), it appears already with inclusions at 10 mm depth that a better noise handling algorithm is necessary for TD analysis. In fact, while both inclusions are accurately resolved by FD and M with 268 detectors, the blurry distribution of $\boldsymbol{\mu}_a$ recovered by TD only tracks the correct general location of the inclusions, but does not distinguish the spheres. This is confirmed by the evaluation metrics in Table 27.1c, where FD and M analysis with 268 detectors have higher signal to noise ratio (SNR) and Dice values than TD. The reconstructions with FD and M with 23 detectors are less accurate than the respective case with 268 detectors and the previous noiseless analysis. When the inclusions are deeper, no data analysis type distinctly recovers the spheres and all results are comparable. The duration of the reconstruction with TD noisy data is this time shorter than with FD and M (~ 10 min), as the stopping criteria are achieved earlier. Improving the stopping criteria or the way λ is updated after each iteration could help in running the code until better image quality is reached. In this study, we used a simple noise model with a realistic level of dark photon counts added to the simulated ToF data. A better noise model from [8] will be used for the future study.

Table 27.1 Number of iterations, duration and evaluation metrics of the reconstruction processes for (**a**) noiseless data with inclusions at 10 mm depth, (**b**) noiseless data with inclusions at 20 mm depth, (**c**) noisy data with inclusions at 10 mm depth, (**d**) noisy data with inclusions at 20 mm depth

(a)	Iter.	Time [s]	SNR [dB]	MSE [mm^{-2}]	Dice	**(b)**	Iter.	Time [s]	SNR [dB]	MSE [mm^{-2}]	Dice
FD, 268 det	15	1210	16.73	6.80×10^{-7}	0.48	FD, 268 det	10	788	12.47	17.52×10^{-7}	0.16
FD, 23 det	14	187	16.44	7.43×10^{-7}	0.21	FD, 23 det	15	205	13.39	14.40×10^{-7}	0.68
M, 268 det	15	1140	16.40	7.49×10^{-7}	0.22	M, 268 det	12	904	12.28	18.11×10^{-7}	0.08
M, 23 det	14	244	16.65	7.09×10^{-7}	0.28	M, 23 det	3	52	12.34	17.98×10^{-7}	0.09
TD, 23 det	15	4045	16.37	7.51×10^{-7}	0.25	TD, 23 det	15	3933	13.35	14.50×10^{-7}	0.62
(c)	Iter.	Time [s]	SNR [dB]	MSE [mm^{-2}]	Dice	**(d)**	Iter.	Time [s]	SNR [dB]	MSE [mm^{-2}]	Dice
FD, 268 det	15	1328	13.46	16.56×10^{-7}	0.53	FD, 268 det	11	956	12.28	20.75×10^{-7}	0.29
FD, 23 det	14	208	8.52	58.86×10^{-7}	0.15	FD, 23 det	3	44	12.31	20.03×10^{-7}	0.14
M, 268 det	15	1126	15.99	8.40×10^{-7}	0.40	M, 268 det	11	875	12.28	18.30×10^{-7}	0.00
M, 23 det	14	275	9.61	48.40×10^{-7}	0.21	M, 23 det	3	56	12.48	18.90×10^{-7}	0.08
TD, 23 det	2	615	12.83	16.40×10^{-7}	0.37	TD, 23 det	2	599	12.24	18.40×10^{-7}	0.07

27.4 Conclusions

In this work, we successfully performed image reconstruction exploiting full temporal data. In noiseless simulations, we observed a superior ability of TD analysis to retrieve the correct position of deep inclusions in comparison to FD and M results, in particular when the inclusions are located at 20 mm and deeper inside the tissue and despite utilizing only a fraction of the detectors available. The results from image reconstructions with noisy values did not show an advantage of the TD compared to the FD and M methods. A better handling of the noise associated with measured data is possible and expected to improve the TD analysis to the extent that it is better than the FD and M analyses.

Acknowledgments We gratefully acknowledge Prof. Hamid Dehghani and Dr. Stanislaw Wojtkiewicz from University of Birmingham for their patient guidance to the TD modules of Nirfaster package, and funding by the Swiss National Science Foundation (159490 and 197079), Innovationspool of University Hospital Zürich, UZH Entrepreneur Fellowships (MEDEF21-025) and Forschungskredit K-84302-02-01.

Conflicts of Interest Martin Wolf declares that he is president of the board and co-founder of OxyPrem AG, and Alexander Kalyanov is working partly for this company.

References

1. Jiang J, Di Costanzo MA, Lindner S et al (2020) Dynamic time domain near-infrared optical tomography based on SPAD camera. Biomed Opt Express 11(10):5470–5477
2. Jiang J, Di Costanzo Mata A, Lindner S et al (2020) Image reconstruction for novel time domain near infrared optical tomography: towards clinical applications. Biomed Opt Express 11(8):4723–4734
3. Mozumder M, Tarvainen T (2020) Evaluation of temporal moments and fourier transformed data in time-domain diffuse optical tomography. J Opt Soc Am A 37:1845–1856
4. Jiang J, Di Costanzo Mata A, Lindner S et al (2022) 2.5 Hz sample rate time-domain near-infrared optical tomography based on SPAD-camera image tissue hemodynamics. Biomed Opt Express 13(1):133–146
5. Dehghani H, Eames ME, Yalavarthy PK et al (2009) Near infrared optical tomography using NIRFAST: algorithm for numerical model and image reconstruction. Commun Numer Methods Eng 25:711–732
6. "Nirfaster", https://github.com/nirfaster/NIRFASTer
7. Doulgerakis-Kontoudis M, Eggebrecht A, Wojtkiewicz S et al (2017) Toward real-time diffuse optical tomography: accelerating light propagation modeling employing parallel computing on gpu and cpu. J Biomed Opt 22(12):125001
8. Liebert et al (2003) Evaluation of optical properties of highly scattering media by moments of distributions of times of flight of photons. Appl Opt 42:5785–5792

28

BIAN: A Multilayer Microfluidic-Based Tissue-Mimicking Phantom for Near-Infrared Imaging

Tong Li, Alexander Kalyanov, Martin Wolf, Meret Ackermann, Emanuele Russomanno, Jingjing Jiang, and Aldo Di Costanzo Mata

Abstract

Near-infrared spectroscopy (NIRS) is a non-invasive optical method for monitoring cerebral oxygenation. Changes in regional blood flow and oxygenation due to neurovascular coupling are important biomarkers of neuronal activation. So far, there has been little research on multilayer tissue phantoms with tuneable blood flow, blood volume, and optical properties to simulate local changes in oxygenation at different depths. The aim of this study is to design, fabricate and characterize a complex dynamic phantom based on multilayer microfluidics with controllable blood flow, blood volume, and optical properties for testing NIRS instruments. We developed a phantom prototype with two microfluidic chips embedded at two depths inside a solid silicone phantom to mimic the vessels in the scalp and in the cortex. To simulate the oxygenation and perfusion of tissue, a solution with blood-like optical properties was sent into the microchannels by a pump with a programmable pressure controller. The pressure adjusted the volume of the microfluidic chips representing a distension of blood vessels. The optical changes in the superficial and deep layers were measured by a commercially available frequency domain NIRS instrument. The NIRS successfully detected the changes in light intensity elicited by the changes in the pressure input to the two layers. In conclusion, the microfluidics-based imaging phantom was

Jingjing Jiang and Aldo Di Costanzo Mata contributed equally as last authors.

T. Li (✉)
Department of Biomedical Engineering, University of Basel, Basel, Switzerland

Biomedical Optics Research Laboratory, Department of Neonatology, University of Zurich, University Hospital Zurich, Zurich, Switzerland
e-mail: tong.li@usz.ch

A. Kalyanov · M. Wolf · M. Ackermann
E. Russomanno · J. Jiang · A. D. C. Mata
Biomedical Optics Research Laboratory, Department of Neonatology, University of Zurich, University Hospital Zurich, Zurich, Switzerland

F. Scholkmann et al. (eds.), *Oxygen Transport to Tissue XLIV*, Advances in Experimental Medicine and Biology 1438, https://doi.org/10.1007/978-3-031-42003-0_28

successfully designed and fabricated and mimics brain functional activity. This technique has great potential for testing other optical devices, e.g., diffuse correlation spectroscopy, pulse oximetry, and optical coherence tomography.

Keywords

Multilayer microfluidic-based tissue-mimicking phantom · Near-infrared imaging · Microfluidic chips

28.1 Introduction

Near-infrared spectroscopy (NIRS) is a non-invasive tool to study brain activity and oxygenation. In particular it measures changes in the concentration of oxyhemoglobin and deoxyhemoglobin [1]. One important biomarker of brain activity is an increase in regional blood flow due to neurovascular coupling, i.e., there is an increased oxygen consumption in the active area, which is accompanied by an increase in cerebral blood flow (CBF) and cerebral blood volume (CBV), bringing about an increase in oxyhemoglobin and drop in deoxyhemoglobin [2]. This signal caused local neurovascular coupling related to functional brain activity and is termed "stimulus-evoked hemodynamic response" [3]. There are also NIRS signals caused by physiological factors (i.e., heart rate (HR) and blood pressure), not associated with functional brain activity: these are termed "systemic activity" [3].

In order to evaluate and validate NIRS instruments or to optimize procedures, some phantoms have been developed to simulate biological tissues [4]. As one example, we developed a solid phantom with moveable inclusion to simulate tissue oxygenation at various positions [5]. To investigate the relationship between the light intensity and the position of absorbers in the brain, Kadoya et al. [6] used a heterogeneous brain phantom. He placed absorbers at various points along the cortex layer [7]. Yet this type of phantom was not able to simulate the physiological dynamics in biological tissues. Kurth et al. [7] and Sudakou et al. [8] developed blood phantoms able to simulate changes in oxygen saturation in two layers, however, they were not capable of mimicking the complex shape of the brain. Myllyla et al. built a brain-mimicking phantom with pulsating liquid which was used to determine the minimum source-detector distance that allows sensing the deep pulsation [9]. In spite of this, it was unable to simulate the controllable pulsation that can occur both in the scalp layer and in the cortex layer of the brain.

Consequently, there is a lack of a multilayer phantom that can simulate extra-cortical contributions and systemic physiology for validating NIRS. We aimed to design, fabricate and characterize a complex dynamic phantom system based on multilayer microfluidic chips with controllable blood flow, blood volume and optical properties for testing NIRS instruments.

28.2 Materials and Methods

We designed and fabricated a two-layer phantom to mimic the vasculatures in the scalp and the cortex. We built two phantoms with different depths of the embedded chips: Phantom I (PhI) with two chips placed at depths of 3 mm and 10 mm, and phantom II (PhII) with chips at depths of 5 mm and 12 mm. As an example, the fabrication process of PhI with two microfluidic chips embedded in the silicone bulk is illustrated in Fig. 28.1a. We used SILPURAN® 2420 two-component silicone (Wacker, Germany) to produce the bulk of the phantom. To mimic the optical property of the brain tissue, silicone-compatible white ink ELASTOSIL® RAL 9010 (Wacker, Germany) was added to obtain the target reduced scattering coefficient $\mu'_s = 6.9\ cm^{-1}$ at 725 nm. The absorption coefficient $\mu_a = 0.06 cm^{-1}$ at 725 nm was adjusted by adding carbon black powder (Wacker, Germany). The ink was first mixed with component A of silicone, then component B was added to the mixture afterward. The mixture was degassed to avoid air bubbles and heated. To produce microfluidics chips, a polydimethylsiloxane (PDMS, SYLGARD® 184 silicone elastomer kit, Dow

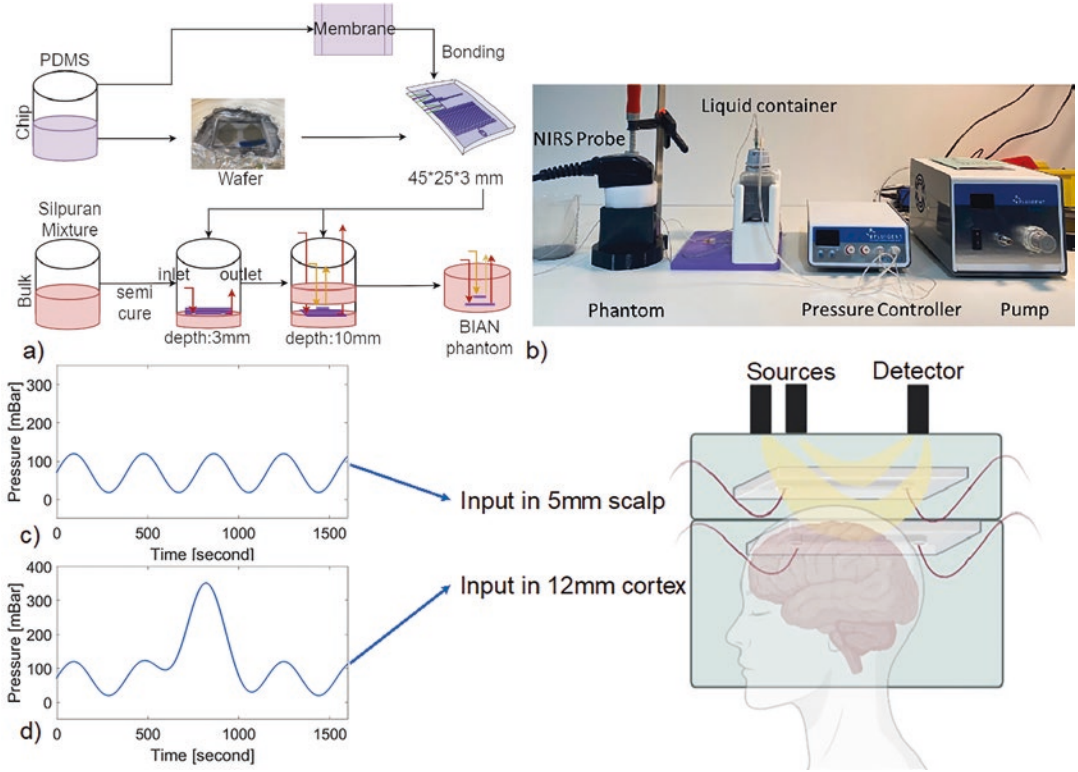

Fig. 28.1 (**a**) Fabrication process of a two-layer phantom PhI. (**b**) photo of a NIRS measurement on the phantom system. The phantom system consists of the phantom fabricated in (a), a liquid container, a pump, a pressure controller. The NIRS probe was placed on top of the phantom during the measurement. Signals generated in MATLAB as the pressure input for the chips at the depth of 5 mm (**c**) and (**d**) 12 mm of PhII

Corning, USA) mixture was poured into a wafer with negative microchannels and was placed in an oven at a constant temperature of 70 °C for curing. The microchannels had rhombus shapes with 50 microns pillars evenly spaced. Then the chip was bonded to a PDMS membrane. The optical properties of the two PDMS microfluidic chips were adjusted by the same method as for the bulk material ($\mu_a = 0.06\ cm^{-1}$, $\mu'_s = 6.9\ cm^{-1}$ at 725 nm).

The setup shown in Fig. 28.1b consisted of the phantom with the microfluidic chip [9] embedded, a container containing the blood mimicking liquid, a pump and pressure control system and a computer to program the changes of the pressure input. The blood mimicking liquid ($\mu_a = 2.5\ cm^{-1}$, $\mu'_s = 6.4\ cm^{-1}$ at 725 nm) was a mixture of 89.1 mL distilled water, 3.5 mL INTRALIPID®, and 7.5 mL diluted Indian Ink (1:20 Indian Ink to water) [10]. The liquid was perfused into microchannels of the chips by a pressure controller (Fluigent, Germany). The pressure values in the pressure were programmed in Matlab and passed to the pressure controller to pump the blood mimicking liquid from the liquid container into the microfluidic chips. This adjusted the internal volume (diameter 1–3 mm) of the chips center.

The setup was measured by a frequency domain (FD) NIRS instrument ISS Imagent® (ISS Inc., Champaign, IL, USA). The multiple distance probe of ISS Imagent® consisted of two sources that emitted light at 725 nm and one detector. We selected two channels with a source-detector separation of SD = 20 mm and SD = 30 mm. As shown in Fig. 28.1b, this probe was placed on the top surface of the phantom. The PhI was measured when the liquid was pumped into two chips at the depth of 3 mm and 10 mm. The flow pressure change

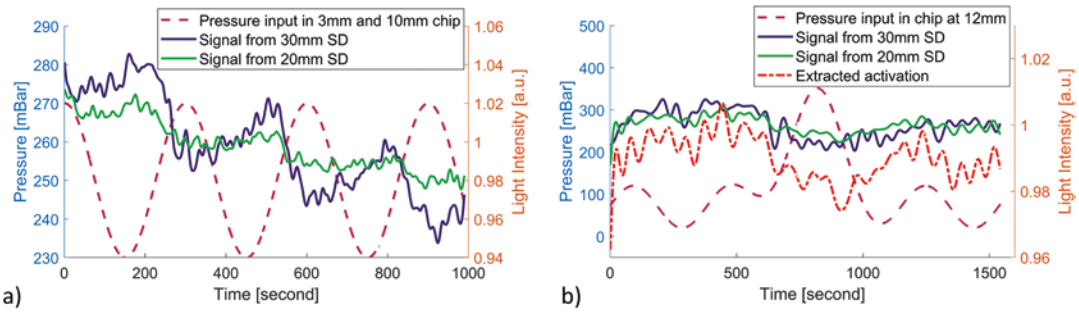

Fig. 28.2 (**a**) Results of the NIRS measurement on PhI. The green and blue solid lines show the light intensity detected by the NIRS by the channel SD = 20 mm and SD = 30 mm, for the pressure input (dashed line) in chips at 3 mm and 10 mm. The pressure input shown as the dark red line in (a) stands for the pressure input in chips at 3 mm and 10 mm. (**b**) Results of the NIRS measurement on PhII. The green line and blue line in (b) show the intensity signals. Figure 28.1c depicts the pressure input for the 5 mm chip and Fig. 28.1d shows the input to the 12 mm chip. The red rash-dot line in (b) is the extracted activation signal for the 12 mm layer. The light intensity values shown in the figures were normalized

was controlled by the pressure input shown in Fig. 28.2a, which simulates regular physiological changes. After the measurements for PhI, a 2 mm-thickness silicone sheet with the same optical properties as the bulk was placed on the top of PhI, to create PhII with chips at the depth of 5 mm and 12 mm. We used PhII to simulate a realistic scenario of brain activation. We programmed two different pressure inputs for two chips. For the superficial layer (scalp), periodic changes were designed to simulate regular physiological changes (Fig. 28.1c). For the deeper layer (brain), an activation signal was added to the periodic waves (Fig. 28.1c) for simulating brain activation (Fig. 28.1d). The periodic wave in PhII was much smaller than the one in PhI in order to measure the signal from activation in the deeper layer. The light intensity was measured for this activation measurement with PhII. The signal simulating brain activity was extracted by using a linear interpolation (Matlab function: polyfit) from removing the signal in the superficial layer.

28.3 Results and Discussion

We designed and developed a complex NIRS phantom that combines the advantages of liquid phantom and solid phantom. It enables stable structure as well as tunable optical properties. In addition, the flow perfusion is well controlled in this system.

The phantom system was tested in two experiments with two phantoms. Figure 28.2a shows the dynamic response of light intensity for the measurement on PhI. Periodic changes in light intensity for the two channels SD = 20 mm and SD = 30 mm (solid lines) were observed with a delay in time as the blood mimicking liquid was pumped into both chips with the periodic pressure input (dash line). When the input pressure increased, the flow rate and the volume of the liquid flowing into the phantom also increased. The expansion of the microfluidic channels could lead to a deformation of the phantom similar to the situation in tissue. We expect this effect to be negligible, but we will have to prove this. The expansion caused an increase in the local absorption. Consequently, the light intensity dropped. Another possible reason for the downward trend of light intensity is that the microfluidic channels are slowly expanding over time. The delay in the NIRS signal was caused by the response time in the control system. It took a certain time to change the volume of the liquid in the phantom after the pressure controller pushed the liquid from the container to the phantom. The delay in this system also came from the pressure controller responding time and the traveling time of the liquid through the tube between the container and the phantom.

The time delay needs to be characterized to make a more precise control in the perfusion.

In the activation experiment using PhII, changes in light intensity for the two channels are shown in Fig. 28.2b. The activation signal and periodic pressure changes were simultaneously applied to the chip at a depth of 12 mm, while only the periodic wave was employed for the chip at depth of 5 mm. Compared to the first measurement on PhI, here the periodic changes were not visible, because the amplitude of periodic change was intentionally set to a much smaller level (Fig. 28.2a). During the activation, the light intensity for both SD = 20 mm and SD = 30 mm decreased significantly with a time delay. The activation was more evident after the regression analysis (red solid line). The drop of the signal was expected only to be detected by SD = 30 mm, but it was also detected by SD = 20 mm. A NIRS probe that has optimal source-detector separations can potentially discriminate the signal at the two depths. The limit of the phantom is that the volume of blood-like fluid at different pressure inputs was not quantified due to the limited stability of the microfluidic chip. The dynamic optical properties of this phantom can be quantified by inputting the known volume of blood-like fluid. In addition, a mixture of Indian ink and Intralipid was used to simulate the optical properties of human blood. At near-infrared wavelengths, however, Indian ink and Intralipid have a flat absorption spectrum. In the future, the phantom can be made with different blood saturations by studying the ink or dye, which has a similar spectrum to oxy- and deoxyhemoglobin.

28.4 Conclusion

We successfully developed a novel dynamic phantom system "BIAN" for fNIRS. It can mimic the hemodynamics of the scalp and cortex. We expect the phantom system will assist in the development of NIRS devices. In addition, this phantom has a great potential to evaluate other optical devices such as e.g., near-infrared optical tomography, diffuse correlation spectroscopy, optical coherence tomography and pulse oximetry.

Acknowledgments We gratefully acknowledge funding by the Swiss National Science Foundation (159490 and 197079), the Innovationspool of the University Hospital Zurich, the UZH Entrepreneur Fellowships (MEDEF21-025), and the Forschungskredit K-84302-02-01.

Conflicts of Interest Martin Wolf declares that he is president of the board and co-founder of OxyPrem AG and Alexander Kalyanov is working partly for this company.

References

1. Pinti P, Tachtsidis I, Hamilton A et al (2020) The present and future use of functional near-infrared spectroscopy (fNIRS) for cognitive neuroscience. Ann N Y Acad Sci 1464:5–29
2. Scholkmann F, Kleiser S, Metz AJ et al (2014) A review on continuous wave functional near-infrared spectroscopy and imaging instrumentation and methodology. NeuroImage 85:6–27
3. Kozberg M, Hillman E (2016) Neurovascular coupling and energy metabolism in the developing brain. In: Progress in brain research. Elsevier, pp 213–242
4. Hacker L, Wabnitz H, Pifferi A et al (2022) Criteria for the design of tissue-mimicking phantoms for the standardization of biophotonic instrumentation. Nat Biomed Eng 6:541–558
5. Jiang J, Costanzo Mata AD, Lindner S et al (2020) Dynamic time domain near-infrared optical tomography based on a SPAD camera. Biomed Opt Express 11:5470
6. Kadoya T, Okada E (2001) In: Chance B, Alfano RR, Tromberg BJ et al (eds) Phantom experiment on relationship between activated position of cerebral cortex and NIR signal, San Jose, pp 558–565
7. Kurth CD, Liu H, Thayer WS et al (1995) A dynamic phantom brain model for near-infrared spectroscopy. Phys Med Biol 40:2079–2092
8. Sudakou A, Gerega A, Isler H et al (2021) Hemoglobin spectra and employed wavelengths affect estimation of concentration and oxygen saturation: blood-lipid phantom study. In: Contini D, Hoshi Y, O'Sullivan TD (eds) Diffuse optical spectroscopy and imaging VIII. SPIE, Online Only, Germany, p 14
9. Myllylä T, Popov A, Korhonen V et al (2013) In: Taroni P, Dehghani H (eds) Optical sensing of a pulsating liquid in a brain-mimicking phantom, Munich, p 87990X
10. Kalyanov A, Jiang J, Russomanno E, et al (2022) Development and validation of robust and cost- effective liquid heterogeneous phantom for time domain near-infrared optical tomography

29 Do Vascular and Extracellular Measurements Consistently Reflect Intracellular pO_2?

Sally C. Pias

Abstract

Oxygen measurements are routinely made either in the vasculature or in the extracellular fluid surrounding the cells of tissues. Yet, metabolic oxygen availability depends on the pO_2 *within* the cells, as does the enhancing effect of oxygen on radiotherapy outcomes. This article reports quantitative modeling work examining the effect of cellular plasma membrane composition on tissue permeability, as a window into tissue oxygen gradients. Previous application of the model indicates that lipid-mediated diffusion pathways accelerate oxygen transfer from capillaries to intracellular compartments and that the extent of acceleration is modulated by membrane lipid and protein composition. Here, the effects of broken intercellular junctions and increased gap size between cells in the model are addressed. The conclusion is reached that the pO_2 gradient will likely be consistent among similar, healthy tissues but may increase with increased interstitial fluid fraction and broken intercellular junctions. Therefore, tissue structural changes in tumors and other diseased or damaged tissues may lead to aberrations in permeability that confound interpretation of extracellular oxygen measurements.

Keywords

Tumor radiotherapy · Near-infrared spectroscopy (NIRS) · Electron paramagnetic resonance (EPR or ESR) · Molecular dynamics simulation (MD) · Traumatic brain injury (TBI) · Stroke

29.1 Introduction and Theory

Tissue oxygen measurements are typically collected in the vasculature or the interstitial fluid of the tissue of interest. Near-infrared spectroscopy (NIRS), electron paramagnetic resonance (EPR), and other important O_2 measurement techniques assess extracellular oxygen. However, the true sites of interest are *intracellular*, most commonly within cell nuclei or mitochondria. In particular, metabolic oxygen consumption depends on oxygen abundance in mitochondria, and tumor radiotherapy outcomes are enhanced by oxygen present within cells, especially within the nucleus [1].

This article addresses the fundamental question, how consistently do vascular and extracellular measurements reflect intracellular oxygenation? It does so based on a highly simpli-

S. C. Pias (✉)
Department of Chemistry, New Mexico Institute of Mining and Technology, Socorro, NM, USA
e-mail: sally.pias@nmt.edu

F. Scholkmann et al. (eds.), *Oxygen Transport to Tissue XLIV*, Advances in Experimental Medicine and Biology 1438, https://doi.org/10.1007/978-3-031-42003-0_29

fied model, in which "vascular" and "extracellular" compartments are treated as idealized and uniform in oxygen distribution. However, real measurements in these compartments carry substantial uncertainty because the vasculature and interstitium are actually complex and heterogeneous in oxygen. The simplified treatment here assumes ideal measurements and focuses, instead, on structural-physical characteristics of the tissue. Thus, to address the question of how consistently vascular and extracellular measurements reflect intracellular oxygenation, this study examines the uniformity of the oxygen gradient within the tissue.

The intracellular oxygen abundance is nearly always expected to be lower than the extracellular abundance, due to metabolic consumption inside cells. The associated gradient drives directional oxygen flux from the capillaries into the cells. As such, vascular or extracellular measurements of oxygen *via* molecular sensors are expected to reflect a greater local oxygen abundance than occurs within the cells of the tissue.

The oxygen partial pressure gradient, ΔpO_2, is the difference between the intracellular oxygen partial pressure, $pO_{2\,in}$, and the extracellular oxygen partial pressure, $pO_{2\,ex}$. Fick's first law of diffusion relates the magnitude of the gradient, together with the tissue permeability, P, to the oxygen diffusional flux, J:

$$J = -P\Delta pO_2 = -P\left(pO_{2in} - pO_{2ex}\right), \quad (29.1)$$

Solving Eq. 29.1 for the intracellular oxygen partial pressure, $pO_{2\,in}$, gives the expression

$$pO_{2in} = -\left(1/P\right)J + pO_{2ex}. \quad (29.2)$$

This equation takes the form $y = mx + b$, indicating that the intracellular oxygen partial pressure is a linear function of the diffusional flux, J, with the slope determined by the inverse tissue permeability and the y-intercept equal to the extracellular (measured) oxygen partial pressure. Therefore, we can deduce without further investigation that $pO_{2\,ex}$ is expected to reflect $pO_{2\,in}$ directly, as long as P and J are constant. Moreover, the extent to which extracellular oxygen measurements reflect the intracellular oxygen partial pressure depends on the constancy or variability of P and J.

Let us assume that the diffusional flux, J, will be coupled to the rate of oxygen consumption. Within the same tissue and across tissues sharing the same permeability, P, we can then expect that increased metabolic consumption will lead to a larger oxygen gradient (also apparent from Eq. 29.1). Variability in J may be an important factor in interpreting extracellular oxygen measurements in some instances—possibly including tumors with spatial irregularity in cellular metabolic status and/or oxygenation. However, the present study focuses on variability in P, due to tissue structural variations on the nanoscale.

The specific oxygen permeability of tissues is generally unknown and also generally ignored (i.e., taken as a universal constant). It seems safe to assume that the tissue oxygen permeability, P, should generally be consistent within healthy and age-matched tissues of the same type, which share common microstructural characteristics and gene expression. If P is indeed consistent and J is coupled to consumption, Eq. 29.1 predicts that the tissue oxygen gradient will, likewise, be consistent wherever the cellular oxygen consumption is constant.

Yet, is the permeability also uniform for diseased tissues? Previous work has indicated that the plasma membrane composition can alter cellular membrane oxygen permeability and influence cellular oxygen gradients (reviewed in refs. [1, 2]). The influence on longer-range diffusion remains relatively unexplored, especially in tissues with high interstitial fluid content. Note that cancerous tumors tend to show increased interstitial fluid fraction (reviewed in ref. [3]), along with decreased organization of the cells in the tissue. Here, a multicellular model developed in earlier work by the present author is applied, to examine oxygen gradients within tissue, especially as influenced by broken intercellular junctions and increased interstitial fluid between cells. The purpose is to approximate changes that may occur in diseased or injured tissues.

29.2 Model

The present author recently developed a quantitative model, visualized in Fig. 29.1a, which approximates tissue as a series of five cells adjacent to a capillary [2]. The model incorporates three alternative, hypothetical pathways O_2 molecules could follow as they diffuse from a red blood cell in the capillary (left) to a mitochondrion or nucleus within the cell most distant from the capillary (right). Pathways 1 and 2 are "aqueous," in that the primary medium of diffusion is water-based. Along pathway 1, oxygen diffuses across the cell bodies, while pathway 2 circumvents the cell bodies by diffusion through the interstitial fluid. Pathway 3 is "lipid-based," with oxygen diffusing primarily within the nonpolar phase of lipid bilayer membranes and making short excursions into the aqueous fluids. In contrast, along the aqueous pathways (1 and 2), oxygen travels primarily within the cytosol or the interstitial fluid and makes excursions across lipid membrane barriers.

Figure 29.2 illustrates O_2 molecule permeation across a lipid bilayer (functioning as a barrier), as well as diffusion between the lipid layers, along the bilayer midplane (functioning as a conduit). Evidence in support of such "lateral diffusion" along the midplane of lipid bilayer membranes is reviewed in ref. [2].

Prior application of the model in ref. [2] led to two main findings. First, tissue oxygen permeability is pathway-dependent. Namely, lipid-mediated pathways accelerate oxygen diffusion, relative to transfer along aqueous pathways. However, this is only true if the aqueous fluids

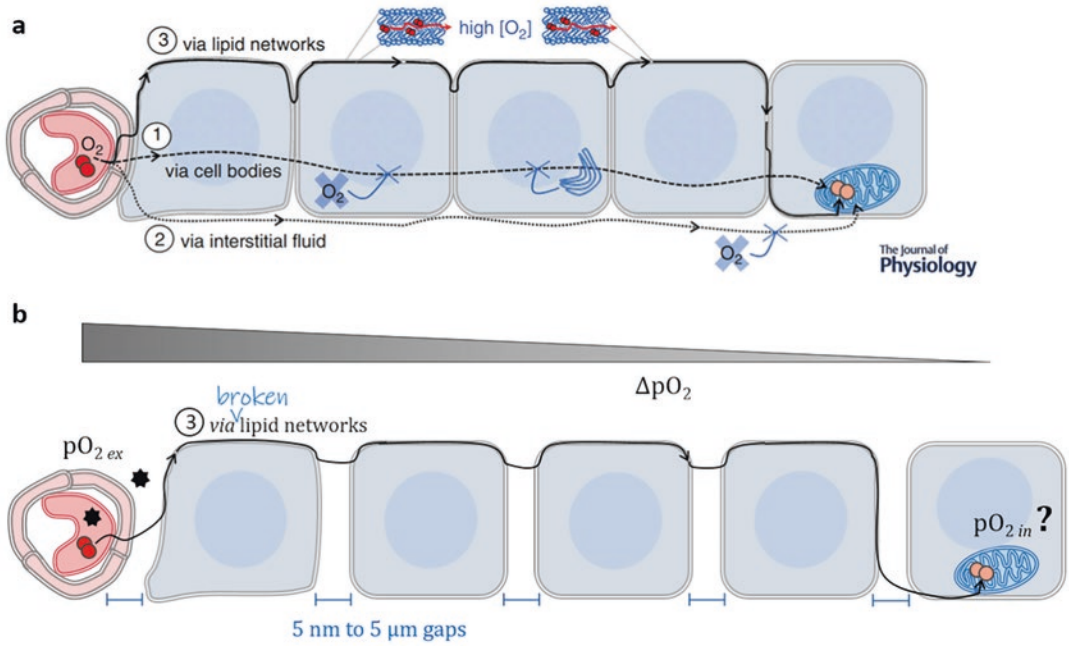

Fig. 29.1 Illustration of models used to estimate tissue oxygen permeability and associated pO_2 gradient. Tissue is approximated as a series of 5 cells adjacent to a capillary, where oxygen molecules (red/pink spheres) are released within a red blood cell (left), then diffuse to an intracellular site of consumption several cells away. Three diffusion pathways are modeled: 1. across cell bodies; 2. through interstitial fluid; and 3. by way of networked lipids, especially within the low-resistance and high solubility nonpolar phase at the midplane of lipid bilayer membranes. (**a**) Model described in ref. [2] and used here to generate baseline data for Table 29.1 (pathway 3, with 5 nm gaps between cells, overall pathway length 110 µm). Image from ref. [2], reproduced with permission. (**b**) Model of diseased/damaged tissue with broken intercellular junctions and varying interstitial fluid gap thickness. Black stars represent molecular O_2 sensors in vasculature or interstitial fluid. Oxygen gradient, ΔpO_2, arises because extracellular $pO_{2\ ex}$ is greater than intracellular $pO_{2\ in}$, which is not measured directly and is, therefore, unknown

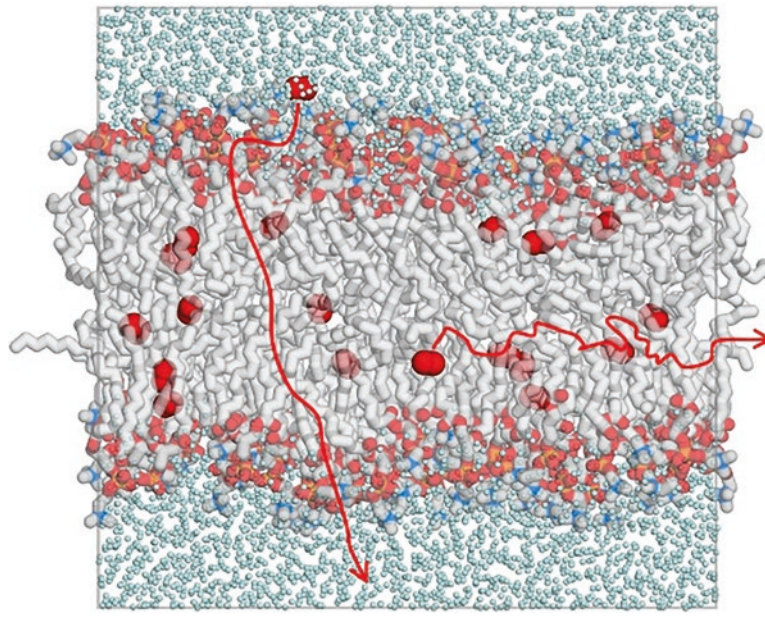

Fig. 29.2 Diffusion pathways across and within a model phospholipid bilayer membrane. Red arrows indicate hypothetical pathways of diffusion as O_2 molecules (red spheres) permeate the lipid bilayer or diffuse along its midplane, between the lipid layers. Water molecules are shown as small cyan dots. Lipids shown with carbon atoms in gray (hydrogen atoms hidden) and noncarbon atoms colored by element. (Image derived from a simulation, as described in ref. [6])

are modeled as having oxygen solubility much lower than (~1/25) that of pure water, as was observed by Longmuir [4]. Second, the cholesterol and protein content of membranes affects the rate of long-range diffusion through tissue along lipid-accelerated pathways.

The pathway model visualized in Fig. 29.1a and previously described in ref. [2] is directly applied in this work, with the exception that the thickness of the aqueous layers between cells is increased here. Relative changes in the oxygen partial pressure gradient across tissues with various intercellular gap sizes are calculated by applying Eq. 29.1, assuming constant diffusional flux, *J*.

The objective here is to test whether broken intercellular junctions, along with larger sized interstitial fluid gaps among the cells, will reduce the tissue permeability. If the tissue permeability does decrease along such a pathway, illustrated in Fig. 29.1b, then the oxygen gradient between extracellular sites of measurement and intracellular sites of interest is expected to increase.

29.3 Oxygen Gradients

In ref. [2], the oxygen permeability of both aqueous pathways 1 and 2 in Fig. 29.1a is estimated to be ~0.007 cm/s if the aqueous fluids (cytosol and interstitial fluid) are approximated to dissolve oxygen to the same extent as pure water. In contrast, where the solubility of oxygen in the aqueous layers is taken to be 1/25 that of lipid, the overall oxygen permeability of pathways 1 and 2 is reduced by two orders of magnitude, to ~0.00006 cm/s. The latter model fluid is labeled "Longmuir cytosol," as it derives from Longmuir's observations [4]. The permeability of the lipid-based pathway 3 in Fig. 29.1a is not affected by the oxygen solubility in the aqueous layers, giving an overall oxygen permeability of ~0.002 cm/s, regardless of whether the aqueous fluids are approximated as pure water or as Longmuir cytosol (with oxygen solubility 1/25 that of cellular lipid). Using the Longmuir cytosol approximation gives a lipid-based pathway 3 permeability (0.002 cm/s) that is ~30 times greater than that of aqueous pathways 1 and 2 (0.00006 cm/s). The corresponding oxygen gradient will, therefore, become 30 times smaller for the lipid-based pathways, compared with the aqueous pathways (based on Eq. 29.1, assuming constant flux, *J*).

Varying the interstitial fluid gap size for the lipid-based pathway 3 in a scheme with broken intercellular junctions, as in Fig. 29.1b, gives the data shown in Table 29.1. The model predicts that the effect of increasing the interstitial fluid gap size by 10 times, from 5 nm to 50 nm, has a minor

Table 29.1 Oxygen permeability along lipid-accelerated pathway 3 in Fig. 29.1b, with varying intercellular gap size and constant diffusional flux, *J*

Gap size	Pwy. 3 permeability	ΔpO_2 effect
5 nm	0.0017 cm/s	–
50 nm	0.0015 cm/s	↑ 13%
500 nm	0.0009 cm/s	↑ 80%
5 μm	0.0002 cm/s	↑ 8 times

5 nm is the baseline gap size used in ref. [2], with the model illustrated in Fig. 29.1a. All pathway permeabilities and oxygen concentration gradients reported or reviewed here use plasma membrane parameters based on single-component bilayers consisting of the phospholipid 1-palmitoyl,2-oleoylphosphatidylcholine (POPC) and Longmuir cytosol (aqueous fluid model v from ref. [2]) at 37 °C

effect, causing a 13% increase in the predicted oxygen gradient. Additionally increasing the gap size by another factor of 10, to 500 nm, results in a larger increase in the gradient size, of 80% relative to the baseline 5 nm gap. Finally, increasing the gap by 1000 times relative to the 5 nm baseline, to 5 μm, results in a factor of 8 increase in the oxygen gradient magnitude. It should be noted that these changes do not account for reduced effective capillary density, which is common in tumors [3].

The data in Table 29.1, based on the model depicted in Fig. 29.1b, seem to indicate that the intracellular oxygen partial pressure may not be predicted consistently from vascular or perivascular measurements where intercellular junctions are broken and intervening interstitial fluid gaps are quite a bit larger than the thickness of the plasma membranes, themselves. In addition, the data indicate that lipid-based pathway 3 consistently accelerates oxygen diffusion, compared with aqueous pathways 1 and 2, even where the interstitial fluid gaps are quite large. Namely, the largest gaps modeled here, at 5 μm, give an overall oxygen permeability of 0.0002 cm/s for pathway 3, about 3 times greater than the pathway 1 and 2 permeability of 0.00006 cm/s (with 5 nm gaps).

29.4 Discussion

Here, an analytical model has been used to examine tissue oxygen gradients as a function of estimated tissue permeability. In particular, attention has been given to permeability changes that may occur in diseased or damaged tissues, due to broken intercellular junctions and increased intercellular gap size. This diseased/damaged tissue model is intended to mimic the characteristics of a tumor but might also be relevant to other tissues, such as those affected by traumatic brain injury or stroke.

Note that the current model neglects potentially important aspects of the tissue microenvironment, including macromolecular crowding and fibrous structures such as cytoskeletal and extracellular matrix components. The carbohydrate coating of cells (glycocalyx) is also omitted and to our knowledge has not been studied to date, with respect to its potential effects on oxygen transport. Lipid-based oxygen "reservoirs" may additionally play a role in modulating the amount of oxygen available in cells; candidate structures include layered membranes such as myelin sheaths [5] and lipid droplets. If any of these structural-compositional factors influence the diffusion coefficient and/or the solubility of oxygen, they may also affect the kinetics of oxygen diffusional delivery to intracellular sites. Moreover, such factors may play a role in the pO_2 gradient, by altering the tissue permeability.

Ref. [2] points out that the oxygen solubility of cytosol and interstitial fluid is critical for discerning oxygen preferential diffusion pathways, whether lipid-based or aqueous. Additional experimental study will be needed to determine this parameter with greater accuracy, and doing so is essential to knowing how oxygen diffuses within and among cells. In addition, study of the effects of transmembrane proteins on oxygen diffusion along the bilayer midplane (as illustrated in Fig. 29.1), will be necessary to refine the parameters of the model applied here.

Further study of lipid effects on oxygen diffusion may also be useful. For example, using atomistic molecular dynamics simulations as described in refs. [6, 7], Qi Wang in our research group has predicted that phospholipid tail-length changes occurring in aggressive and poorly differentiated nonmetastatic breast tumors [8] can reduce lipid bilayer permeability by up to 40%, if the saturated tail of the phospholipid is lengthened relative to the unsaturated tail (data not shown). Whether an effect of this magnitude will influence the tissue permeability and associated pO_2 gradient—as

well as tumor cell hypoxia—will depend on diffusional pathway preference and possibly other influences, such as macromolecular crowding and other membrane components.

29.5 Concluding Remarks

The modeling applied here indicates that extracellular pO_2 measurements will generally report consistently on intracellular pO_2. However, the current study suggests that diseased or damaged tissues may differ in permeability relative to healthy and whole tissues. Broken intercellular junctions, along with increased interstitial fluid intervening between cells, are predicted by this study to reduce the tissue oxygen permeability and lead to greater pO_2 gradients, such that the intracellular pO_2 may not be inferred with certainty from extracellular oxygen measurements. Therefore, in some cases, direct measurement of intracellular oxygen may be necessary [1] to assess reliably the oxygenation state of cells.

The predicted variability of oxygen permeability and associated pO_2 gradient for the diseased/damaged tissue model might confound hypoxia mapping [9] as an aid to tumor radiotherapy. Specifically, oxygen measurements in the extracellular compartment may not fully reflect the intracellular oxygen levels in some regions of a tumor, especially if intercellular junctions are broken and the interstitial fluid fraction is increased. Depending on the specific cellular-structural features of the tumor, it is possible that heterogeneous permeability may occur at boundaries between tumors and normal surrounding tissue, rendering boundary oxygen measurements particularly difficult to interpret. Repeated measurements at the same sites may help to establish a baseline, such that changes in oxygenation could be detected. However, absolute measurements are unlikely to report consistently on the intracellular pO_2, especially across normal and tumor tissues.

Acknowledgments SP acknowledges helpful communication with Harold Swartz and Joseph LaManna as well as thoughtful peer reviews. PyMOL was used for lipid bilayer model imaging [10]. The work was financially supported by gifts from the Glendorn Foundation and Clin-EPR, LLC.

References

1. Subczynski WK, Widomska J, Stein N, Swartz HM (2021) Factors determining barrier properties to oxygen transport across model and cell plasma membranes based on EPR spin-label oximetry. Appl Magn Reson. https://doi.org/10.1007/s00723-021-01412-4
2. Pias SC (2021) How does oxygen diffuse from capillaries to tissue mitochondria? Barriers and pathways. J Physiol 599:1769–1782. https://doi.org/10.1113/JP278815
3. Multhoff G, Vaupel P (2012) Radiation-induced changes in microcirculation and interstitial fluid pressure affecting the delivery of macromolecules and nanotherapeutics to tumors. Front Oncol 2. https://doi.org/10.3389/fonc.2012.00165
4. Longmuir IS (1981) Channels of oxygen transport from blood to mitochondria. Adv Physiol Sci 25:19–22. https://doi.org/10.1016/B978-0-08-027346-4.50007-3
5. Ghysels A, Vervust W (2022) Oxygen storage in stacked phospholipid membranes under an oxygen gradient as a model for myelin sheaths. Oxyg Transp Tissue. https://doi.org/10.1007/978-3-031-14190-4_49
6. Wang Q, Dotson RJ, Angles G, Pias SC (2021) Simulation study of breast cancer lipid changes affecting membrane oxygen permeability: effects of chain length and cholesterol. Adv Exp Med Biol 1269:15–21. https://doi.org/10.1007/978-3-030-48238-1_3
7. Dotson RJ, McClenahan E, Pias SC (2021) Updated evaluation of cholesterol's influence on membrane oxygen permeability. Adv Exp Med Biol 1269:23–30. https://doi.org/10.1007/978-3-030-48238-1_4
8. Hilvo M, Denkert C, Lehtinen L et al (2011) Novel theranostic opportunities offered by characterization of altered membrane lipid metabolism in breast cancer progression. Cancer Res 71:3236–3245. https://doi.org/10.1158/0008-5472.CAN-10-3894
9. Gertsenshteyn I, Giurcanu M, Vaupel P, Halpern H (2020) Biological validation of electron paramagnetic resonance (EPR) image oxygen thresholds in tissue. J Physiol 599:1759–1767. https://doi.org/10.1113/JP278816
10. The PyMOL Molecular Graphics System, Version 1.7.6.5 Schrödinger, LLC

30 Observation of Tissue Oxygenation Changes Using Remote Photoplesysmography with a Smartphone

Gennadi Saiko, Timothy Burton, Jose L. Ramirez-GarciaLuna, and Alexandre Douplik

Abstract

Background: Tissue oxygenation is a critical marker of tissue status and can be used to evaluate and track wound progress, the viability of transplanted tissue, and burns. Thus, the determination of tissue oxygenation (preferably remotely) is of great importance. Aim: Explore the impact of oxygenation changes on tissue color. Material and methods: The rPPG of both hands was acquired using a stand-mounted smartphone (iPhone 8) placed about 10 cm above the hands. A 60 s baseline was followed by occlusion of one arm using a cuff inflated to 200 mmHg for approximately 2 min. The cuff was then rapidly deflated, followed by a 60 s recovery period. The reference muscle oxygenation signal (SmO_2) was acquired using the near-infrared contact Moxy device (Fortiori Design LLC) placed on the forearm distal to the occlusion. The data were collected on both hands of 28 healthy volunteers. Results: rPPG can observe changes in tissue oxygenation, which was confirmed across 28 participants using a robust reference standard. Conclusion: We have an initial confirmation of the notion that rPPG can monitor changes in tissue oxygenation. However, a spectrum of rPPG and SmO2 reductions is observed, which should be explored in future work.

Keywords

Remote photoplesysmography · Smartphone · Tissue oxygenation

30.1 Introduction

Tissue oxygenation is a critical marker of tissue status. It can be used to evaluate and track wound progress (including complications such as diabetes), the viability of transplanted tissue, and burns.

G. Saiko (✉)
Swift Medical Inc, Toronto, ON, Canada

Department of Physics, Toronto Metropolitan University, Toronto, ON, Canada
e-mail: gsaiko@torontomu.ca

T. Burton
Department of Biomedical Engineering, Toronto Metropolitan University, Toronto, ON, Canada

J. L. Ramirez-GarciaLuna
Swift Medical Inc, Toronto, ON, Canada

A. Douplik
Department of Physics, Toronto Metropolitan University, Toronto, ON, Canada

Department of Biomedical Engineering, Toronto Metropolitan University, Toronto, ON, Canada

iBest, Keenan Research Centre of the LKS Knowledge Institute, St. Michael's Hospital, Toronto, ON, Canada

F. Scholkmann et al. (eds.), *Oxygen Transport to Tissue XLIV*, Advances in Experimental Medicine and Biology 1438, https://doi.org/10.1007/978-3-031-42003-0_30

Tissue oxygenation can be measured using invasive measurements. For example, subcutaneously inserted fiber optic sensors can capture the status of the burned tissue more accurately and guide resuscitation therapy more precisely than heart rate, blood pressure, and urine output monitoring [1].

Tissue oxygenation can also be measured non-invasively. Transcutaneous oxygen pressure ($TcPO_2$) measurement assesses the partial pressure of oxygen diffusing through the skin [2] and is considered a "gold standard" in tissue oximetry. However, it is very time-consuming as a complete exam of both lower extremities typically requires 1 h. It also cannot be applied to wound beds. Several other techniques, such as skin perfusion pressure (SPP), have been proposed for tissue oximetry; however, they are still confined to vascular labs.

Optical modalities have the potential to move tissue oxygenation measurements into point-of-care settings. For example, multispectral or hyperspectral imaging gradually penetrates wound care [3]. However, this technology is still in its naissance and cannot be universally available. Photoplesymography (PPG) is another optical technology with several well-established clinical applications (pulse oximetry as the most prolific case). In addition to clinical settings, novel PPG modalities (e.g., AppleWatch and Oura ring) rapidly penetrate digital health.

Remote photoplethysmography (rPPG) is a contactless extension of reflection PPG. rPPG allows data acquisition over regions of tissue regions without contact, enabling clinical applications for sensitive tissue assessment such as diabetic wounds. However, the primary advantage is that, unlike traditional PPG single-point measurement technologies, rPPG-based technologies can provide 2D health indicators maps, allowing spatiotemporal analysis.

Current PPG-based oxygenation measurements rely on the assumption of the validity of the volumetric model, which provides a rationale for using PPG as a surrogate of the arterial blood oxygenation curve [4]. However, we want to explore rPPG beyond its traditional applications of heart rate determination. One way to do it is to explore tissue color. For example, it is known that tissue changes its color during occlusion. Thus, tissue color can be a potential marker of tissue oxygenation.

We have previously demonstrated that rPPG can go beyond initial applications. Specifically, we have shown that it can be used for perfusion imaging in an occlusion-based ischemia model [5] and investigation of tissue physiology [6]. In the present work, we aim to explore rPPG utility for tissue oxygenation extraction and monitoring using (a) realistic (non-lab) settings, (b) a reference standard for muscle oxygenation, and (c) a larger dataset.

30.2 Methods

The subject's hands were placed on a table, with one hand undergoing occlusion through the placement of a blood pressure cuff and the other hand acting as a control. The rPPG of both hands was acquired using a stand-mounted smartphone (iPhone 8) (Fig. 30.1a) placed about 10 cm above the hands, which recorded 1080x1920-pixel video data at 60 frames per second. A 60 s baseline was followed by occlusion of one arm using a cuff inflated to 200 mmHg for approximately 2 min. The cuff was then rapidly deflated, followed by a 60 s recovery period. The process was then repeated with the other hand undergoing occlusion almost immediately after the 60 s recovery period from the first acquisition was complete. The reference muscle oxygenation signal (SmO_2) was acquired using the near-infrared contact Moxy device (Fortiori Design LLC) placed on the forearm distal to the occlusion, collecting primarily from muscle tissue. The acquisition was in a realistic (not lab) environment with varying light conditions.

The video data was manually divided into regions corresponding to the occluded hand and the control hand. Then the rPPG signals were extracted by averaging the pixel intensity in each area. SmO_2 and rPPG were normalized with respect to the initial value, and the rPPG signal from the non-ischemic hand was subtracted from the ischemic hand (Fig. 30.1b) to isolate the

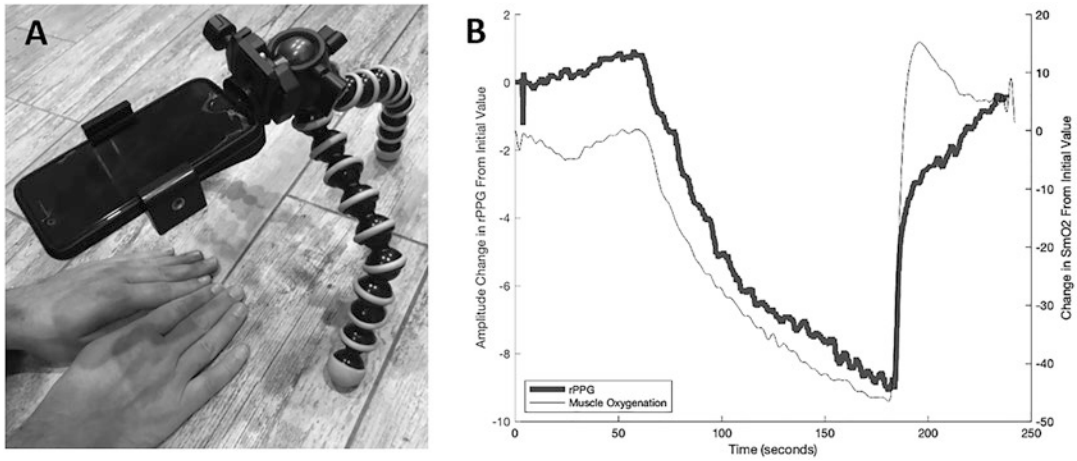

Fig. 30.1 (**a**) rPPG acquisition using the stand-mounted smartphone. (**b**) Effect of the occlusion protocol on the rPPG signal (thick line, using y-axis on the left of the plot) and muscle oxygenation (thin line, using y-axis on the right of the plot)

occlusion effect with respect to the control hand. rPPG denoising was performed by subtracting the blue channel, with the most limited sensitivity to the hemoglobin of all three channels, from the red channel. Pearson correlation between the SmO2 and rPPG signal was calculated as a measure of dataset reliability. The minimum value in the SmO_2 signal was found, and the amplitude in the rPPG was measured at the corresponding time point.

The study on volunteers was approved by REB of Toronto Metropolitan University (formerly Ryerson University) and RESEARCH REVIEW BOARD INC.

30.3 Results

Data collection was performed on 28 subjects, with each arm undergoing the described protocol for 56 total signals. The rPPG-SmO2 correlation threshold was set to 0.75, with signals below this level representing significant disagreement between the modalities and likely substantial environmental noise in either or both signals. At this threshold, 50/56 = 89% of the signals were preserved, with all 28 subjects represented. The occlusion protocol resulted in an average relative reduction rPPG of 32 ± 24% (Fig. 2a) and 77 ± 20% in SmO_2 (Fig. 30.2b). The ratio of SmO_2 reduction to rPPG reduction across the dataset was 4.0 ± 3.1 (Fig. 30.2c), indicating that, on average, the oxygenation reduction was four-fold greater than the rPPG reduction. However, as shown in Fig. 30.2, a spectrum of rPPG and SmO_2 reductions was observed.

30.4 Discussion and Conclusions

Our results indicate oxygenation-induced tissue color changes are detectable using rPPG techniques with consumer-grade cameras (smartphones).

Ambient light is one of the primary factors which affect tissue color. One of the primary aims of this work was to mitigate its impact. The relative measurements (ratio of change in a variable to baseline) were used to account for ambient light. We also investigated the use of individual color channels for oxygenation tracking purposes and found that they are prone to ambient light changes. The best denoising was achieved by subtracting the blue channel from the red channel.

With 28 subjects and 50 analyzed measurements, we expected results to start following the normal distribution. However, it was not the case

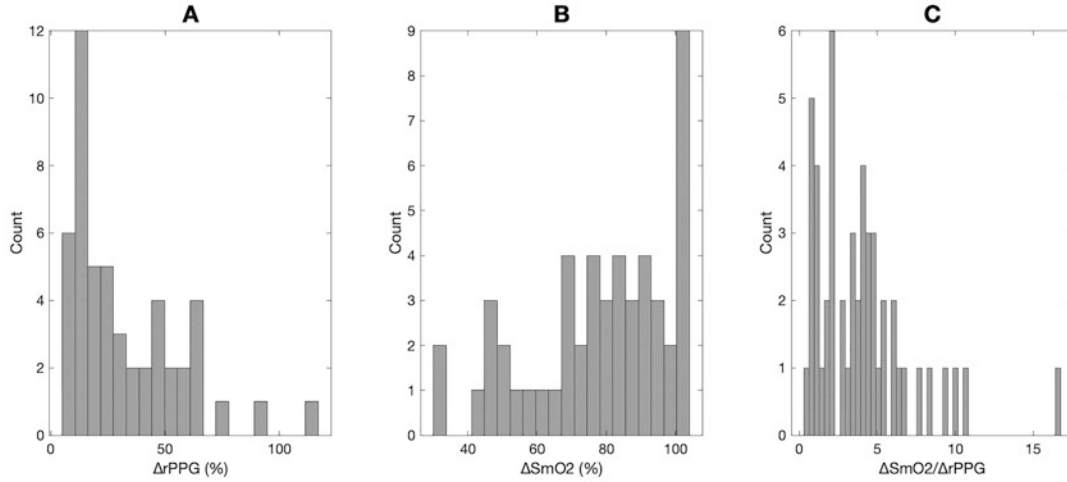

Fig. 30.2 Dataset distribution of (**a**) rPPG amplitude decline (**b**) muscle oxygenation decline, and (**c**) the ratio of muscle oxygenation decline to rPPG decline

for rPPG (Fig. 30.2a) and muscle oxygenation (Fig. 30.2b) measurements.

A spectrum of rPPG and SmO_2 reductions observed was possibly due to factors such as blood pressure (i.e., incomplete occlusion, especially given that 5–6 min may be required on average), body mass index (BMI), and skin tone, all of which should be explored in future work.

Thus, a more careful experimental design is required, which may consider confounding factors like BMI.

One of our most surprising findings was the wide range of SmO_2 reduction (see Fig. 30.2b). This observation may be related to the differences in SmO_2 magnitude and dynamics previously reported between the NIRS muscle oximeter used in the present work (Moxy), and a second device, Nimo (Nirox, Italy) [7]. Within that work, performed over 10 repeats within a single subject, the Moxy exhibited a decrease of −53% during occlusion, with dynamics of a strong rapid decline and a robust reperfusion signal. In contrast, the Nimo had a dampened response of −13% during occlusion, with dynamics of a slow decline and modest reperfusion signal. The investigators account for these differences in occlusion response by device design differences – the Moxy is multi-distance and uses an assumed value from literature to account for fat layer thickness, while the Nimo is single-distance with dynamic fat correction. Both devices also differ in models for light propagation. While the absolute value for SmO_2 is provided for each, the behavior clear differs, reflecting the precision challenges with the measurement of this parameter. While the investigators did not explore the variation across multiple subjects, it's possible that the design characteristics of the Moxy device that resulted in strong rapid declines in SmO_2 during occlusion increased sensitivity to subject characteristics, and possibly including static fat layer correction (given that the dynamic correction employed by the Nimo may be more effective), which resulted in a wide range of SmO_2 reduction. Another factor that appears to be uncorrected is skin melanin, which absorbs in the NIR region (i.e., decreasing penetration depth), and may also result in subject variability [8]. Based on these observations, we draw the following conclusions for related work:

- 200 mmHg for arterial occlusion can be insufficient. 250 mmHg is recommended.
- Further, adequate time for reperfusion must be provided. Considering the 60 s of non-occlusion at the start and end of the acquisi-

tion in the present work, there is a 2-min gap between occlusion periods – however, this would ideally be extended to substantially longer (e.g. 5 min), which is a limitation of our present work.

- SmO_2 measurement with continuous wave NIRS exhibits significant variation across subjects. If necessary, physiological calibration can be used to ensure higher quality of data [9]. However, the duration of the occlusion, in this case, should be 5–6 min [9].
- The adipose tissue thickness and skin tone affect muscle oxygenation measurements significantly despite attempted fat layer compensation (e.g. static compensation of the Moxy device). Therefore, some less affected areas (like the thenar eminence) are recommended.

In summary, we have an initial confirmation of the notion that rPPG can observe changes in tissue oxygenation. However, a spectrum of rPPG and SmO_2 reductions is observed, which should be explored in future work.

Acknowledgments We thank the volunteers who participated in our study, without whom our work would not be possible. The authors acknowledge funding from NSERC Alliance (Douplik&Saiko), NSERC Discovery (Douplik), NSERC RTI (Douplik), and Ryerson Health Fund (Douplik).

References

1. Venkatesh B, Meacher R, Muller MJ, Morgan TJ, Fraser J (2001) Monitoring tissue oxygenation during resuscitation of major burns. J Trauma Acute Care Surg 50(3):485–494
2. Severinghaus JW, Astrup PB (1986) History of blood gas analysis. IV. Leland Clark's oxygen electrode. J Clin Monit 2:125–139
3. Saiko G, Lombardi P, Au Y, Queen D, Armstrong D, Harding K (2020) Hyperspectral imaging in wound care: a systematic review. Int Wound J 17(6):1840–1856
4. Wukitsch MW, Petterson MT, Tobler DR, Pologe JA (1988) Pulse oximetry: analysis of theory, technology, and practice. J Clin Monit 4(4):290–301
5. Burton T, Saiko G, Douplik A (2022) Feasibility study of remote contactless perfusion imaging with consumer-grade mobile camera. Adv Exp Med Biol.;1395:289–293
6. Burton T, Saiko G, Cao M, Douplik A (2023) Remote photoplethysmography with consumer smartphone reveals temporal differences between glabrous and nonglabrous skin: pilot in vivo study. J Biophotonics 16(1):e202200187
7. Scholkmann F, Scherer-Vrana A (2020) Comparison of two NIRS tissue oximeters (moxy and nimo) for non-invasive assessment of muscle oxygenation and perfusion. In: Oxygen Transport to Tissue XLI, pp 253–259
8. Wassenaar EB, Van den Brand JGH (2005) Reliability of near-infrared spectroscopy in people with dark skin pigmentation. J Clin Monit Comput 19:195–199
9. Chance B, Dait MT, Zhang C, Hamaoka T, Hagerman F (1992) Recovery from exercise-induced desaturation in the quadriceps muscles of elite competitive rowers. Am J Physiol Cell Physiol 262(3):C766–C775

31 Neurovascular, Metabolic, and Glymphatic Dynamics of the Brain Measured with fNIRS

Gentaro Taga and Hama Watanabe

Abstract

We developed a multidistance and multiwavelength continuous wave NIRS instrument to detect dynamic changes in oxygenated and deoxygenated hemoglobin (oxy- and deoxy-Hb), oxidized cytochrome-c-oxidase (oxCCO) and water of the brain and muscle. We performed measurements of the forehead during resting state and paced breathing and of the forearm during ischemic challenge in human adults. Time series analysis focusing on rhythmic signals over different time scales and different depths of the tissue revealed specific patterns of phase relationships among the signals in each of the measurement. This method can be a promising tool to understand the dynamic interaction among the neurovascular, metabolic and glymphatic system in a wide variety of subject fields.

Keywords

Functional near-infrared spectroscopy · Phase relationships · Neurovascular coupling · Metabolism glymphatic system

G. Taga (✉) · H. Watanabe
Graduate School of Education, The University of Tokyo, Tokyo, Japan
e-mail: taga@p.u-tokyo.ac.jp

31.1 Introduction

Rhythm exists everywhere in life: brain activity, respiration, heartbeat, walking and sleeping [1]. The development of noninvasive technology to measure dynamics of the brain and body in ordinary life is crucial to understand the mechanism underlying living state. Functional near infrared spectroscopy (fNIRS) has been used as a safe technique to measure changes in oxygenated and deoxygenated hemoglobin (oxy- and deoxy-Hb) to reveal oxygenation of the brain and the muscles induced by the blood flow and metabolism in relation to functional activity [2, 3]. While the path length of light due to scattering in the tissue must be known to determine absolute concentrations, the phase differences between relative changes in signals contain rich information. For instance, the hemoglobin phase of oxygenation and deoxygenation (hPod) is valid as an indicator of brain development [4].

While a few wavelength NIR lights have been used for the measurement of oxy- and deoxy-Hb, broadband NIR lights are needed to accurately measure the lower concentration of oxidized state of cytochrome c oxidase (oxCCO), which directly reflects the mitochondrial oxidative metabolism [5]. For example, the relationship between changes in cerebral oxygenation and oxidation in response to peripheral oxygen saturation in neonates was associated with outcome [6]. Furthermore, NIRS can be used to measure water

F. Scholkmann et al. (eds.), *Oxygen Transport to Tissue XLIV*, Advances in Experimental Medicine and Biology 1438, https://doi.org/10.1007/978-3-031-42003-0_31

volume changes, which reflect transport of the cerebrospinal fluid (CSF) [7, 8]. Recent studies showed that the glymphatic system controlling the flow of the CSF is responsible for the clearance of metabolic waste products in the brain and dysfunctioning is associated with neurodegenerative diseases [9].

The aim of the present study is to establish a multidistance and multiwavelength NIRS system for simultaneous measurement of tissue oxygenation (oxy- and deoxy-Hb), oxidative metabolism (oxCCO) and glymphatic dynamics (water) with a high sampling rate enough to detect the cardiac pulsation. In particular, we focused on phase relationships among the signals depending on different time scales [4, 10–13] and different depths of measurement volume of the tissue [14]. To perform *in-vivo* validation, we measured spontaneous activity in the brain during resting state [10, 11] and the brain response to breathing manipulation [15, 16] and the muscle response to ischemic challenge [5, 17].

31.2 Methods

We developed a multidistance and multiwavelength NIRS system with 8-wavelength continuous-wave laser light sources and 4 avalanche photodiode (APD) detectors (OEG-17APD and 8 wavelength laser unit, manufactured by Spectratech Inc. Japan). We chose the wavelengths of laser light sources: 730, 780, 800, 811, 830, 840, 880, and 940 nm. This combination of wavelengths was considered to make balance of sensitivity among the higher absorption to deoxy-Hb (730 and 780 nm), oxCCO (800, 811, 830, and 840 nm), oxy-Hb (840, 880, and 940 nm), and water (940 nm) [5, 18]. The total laser power of 8 wavelengths was adjusted to less than 9 mW (IEC60825 class 1 M). Sampling time was set at 81.92 ms. A probe was created by placing four bio-attachable optical fibers with 1 input and 1 output on the receiving side at distances of 1, 2, 3, and 4 cm in a straight line from one optical fiber with 8 inputs and 1 output on the transmitting side.

We assumed that the modified Lambert-Beer equation holds [3, 5] between the changes in the detected light intensity of the 8 wavelengths $\Delta A(\lambda_i)$ (i = 1, 8) and the concentration changes Δ[oxy-Hb], Δ[deoxy-Hb], and Δ[oxCCO] [mM], and water content change ΔWC [%] in volume as

$$\Delta A(\lambda_i) = \begin{pmatrix} \varepsilon_{\text{oxy-Hb}}(\lambda_i)\Delta[\text{oxy-Hb}] + \\ \varepsilon_{\text{deoxy-Hb}}(\lambda_i)\Delta[\text{deoxy-Hb}] + \\ \varepsilon_{\text{oxCCO}}(\lambda_i)\Delta[\text{oxCCO}] + \mu_{\text{H2O}}(\lambda_i)\Delta WC \end{pmatrix} \times DPF(\lambda_i) \times d$$

where DPF is diffrential path length factor, and d is sorce-detector distance. The extinction coefficients $\varepsilon_{\text{oxy-Hb}}$, $\varepsilon_{\text{deoxy-Hb}}$, and $\varepsilon_{\text{oxCCO}}$ [mm^{-1} mM^{-1}] and absorption coefficient [mm^{-1}] were taken from literatures (oxy- and deoxy-Hb and oxCCO [19] and liquid water [20]). The differential path length factor was chosen to be DPF = 6.32 and 4.48 for adult forehead and arm, respetively, based on a literature [21]. The pseudo-inverse matrix to calculate the relative changes of the 4 signals from the light intensity changes at 8 wavelengths was obtained by a Fortran program with LAPACK (Linear Algebra Package) routine.

We performed 3 types of measurement with 2 adults: Adult 1 (female) and Adult 2 (male). In study 1, the left forehead was measured during rest for 10 minutes. In study 2, the same region was measured during paced breathing, which consists of two conditions: one is an initial 1-min rest, 30 times repetition of 4 s inspiration and 4 s expiration (period 8 s) following visual cue of a metronome, and a 1-min rest, and another is an initial 1-min rest, 30 times repetition of 6 s inspiration and 6 s expiration (period 12 s), and a 1-min rest. In study 3, the left forearm muscle was measured. After an initial 1-min period in the resting state, the cuff was inflated to a pressure more than 200 mmHg and maintained for 3 min. Then, the cuff was released and measurement continued another 3 min.

Obtained time-series data for each signal were decomposed by using band-pass filters with frequency ranges for hemodynamics (0.01–0.033 and 0.033–0.1 Hz), respiration (0.1–0.8 Hz), pulse wave (0.8–1.8 Hz), and measurement noise

(1.8- Hz). Hilbert transforms were applied to each of the filtered signals to extract instantaneous phase for each signal for each source-detector distance. Analysis of relative phase differences among the signals were performed [4, 10].

31.3 Results

We obtained consistent changes in oxy- and deoxy-Hb, oxCCO and water in each study in both participants. In study 1, spontaneous changes in the signals on the forehead were measured. At the shortest distance, the band-pass filtered signals with heartbeat frequency showed an in-phase pattern between oxy- and deoxy-Hb, an anti-phase pattern between oxy-Hb and oxCCO, and an anti-phase pattern between oxy-Hb and water, as shown in Fig. 31.1a. They were likely to reflect the heartbeat induced changes in blood volume, oxidation and CSF. In contrast, at the longer distance, the band-pass filtered signals with slow hemodynamics frequency showed an anti-phase pattern between oxy- and deoxy-Hb, an in-phase pattern between oxy-Hb and oxCCO, and an anti-phase pattern between oxy-Hb and water, as shown in Fig. 31.1b. They were likely to reflect the tissue oxygenation, oxidative metabolism, and fluid transportation in the gray matter.

The phase relationships among the signals were quantified by vector representation on the plane of source-detector distance (tissue depth) vs. frequency (hemodynamics, respiration, and heartbeat) as shown in Fig. 31.2. The direction and length of vector represent the value of relative phase between signals and the strength of phase locking, respectively. The oxy- and deoxy-Hb relationship (hPod) showed an in-phase pattern in the short distance and anti-phase pattern in the longer distances and slower frequency. The oxy-Hb and oxCCO relationship showed an in-phase pattern in the slower frequencies and an anti-phase pattern in the faster frequency. The deoxy-Hb and oxCCO showed an anti-phase pattern regardless of the frequency range. The oxy-Hb and water relationship mostly showed an anti-phase pattern.

In study 2, periodic inspiration and expiration of breathing strongly induced specific patterns of response of signals. To calculate averaged responses to period 8 s and 12 s of breathing, band-pass filtered signals with frequency range of 0.1–0.17 Hz and 0.071–0.1 Hz were used respectively. The reversal of averaged response patterns between the 2 conditions (Fig. 31.3a and b) indicated typical responses of the sluggish system to the faster and slower inputs. Vector representation in each condition showed a consistent pattern with the one of spontaneous changes as shown in Fig. 31.2.

In study 3, the response of the forearm muscle to the occlusion of the brachial arterial and venous blood flow. As shown in Fig. 31.4, the progression of ischemia due to the cuff exhibited a mirror image change in oxy-Hb decrease and deoxy-Hb increase, few change in blood volume calculated by sum of oxy-Hb and deoxy-Hb, few change in water, and a slight decrease in oxCCO. The release of cuff produced a rapid oxy-Hb increase and deoxy-Hb decrease, a rapid increase in blood volume, a delayed decrease in water, and a slight increase in oxCCO. After these rapid changes induced by the cuff release, all of the signals returned to the initial baseline.

31.4 Discussions and Conclusions

We demonstrated that 8 wavelength NIRS can detect consistent phase relationships among oxy-Hb, deoxy-Hb, oxCCO, and water in the adult brain during rest and paced breathing and in the muscles during ischemic challenge. The depth and frequency dependence of the phase relationships among the measured signals at the forehead during rest indicated a successful decomposition of the signals without crosstalk. The result also showed that the cardiac pulse and respiration induced phase-locked changes not only in hemodynamics but also in oxidative metabolism and CSF. The anti-phase changes between blood volume and CSF showed fluid transportation mechanisms in the glymphatic system. The results revealed separate mecha-

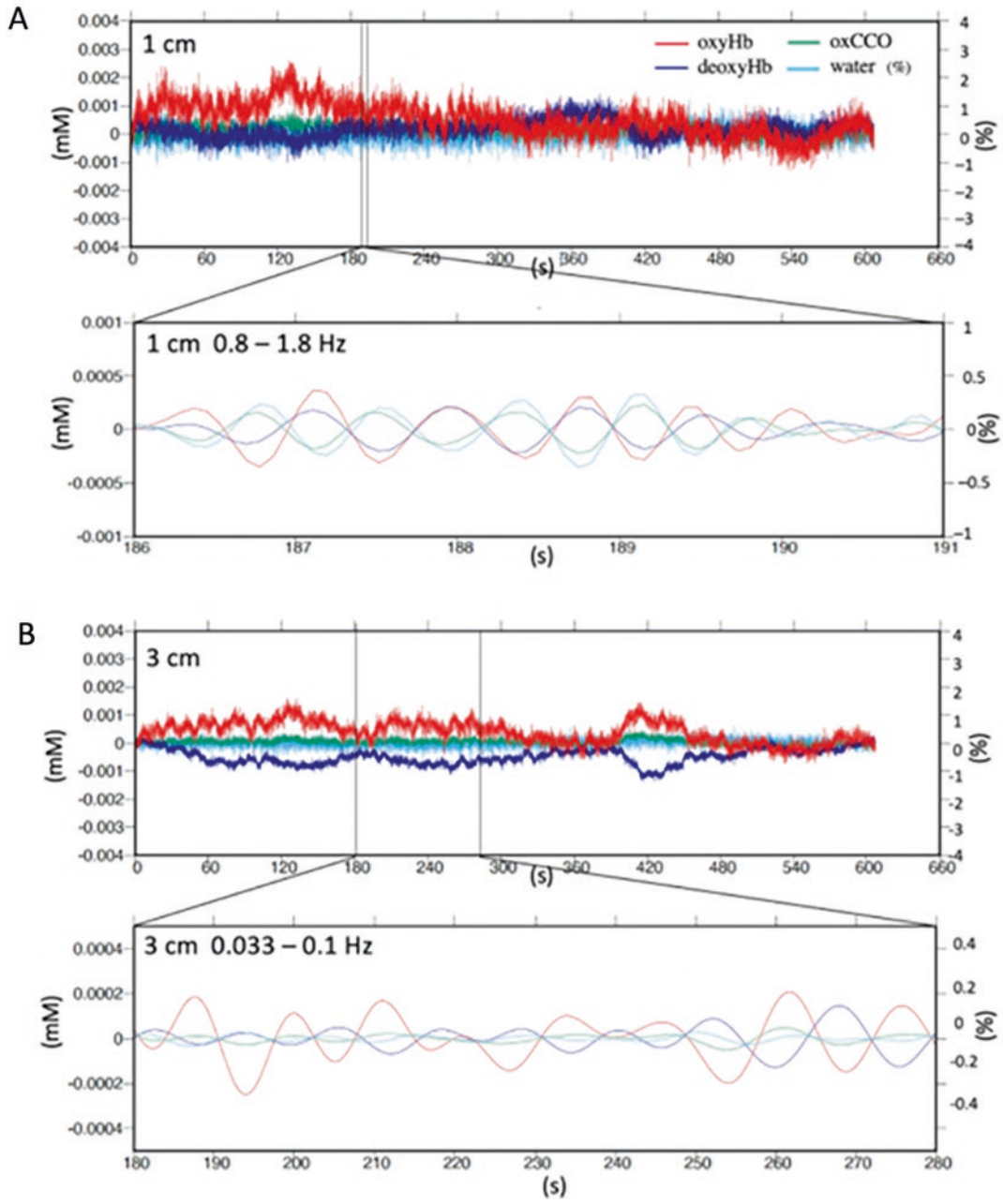

Fig. 31.1 Spontaneous changes in oxy- and deoxy-Hb, oxCCO, and water in study 1. (**a**) frequency (0.8–1.8 Hz) and distance (1 cm). (**b**) Frequency (0.033–0.1 Hz) and distance (3 cm). Data is from Adult1

nisms for the hemodynamics, oxidative metabolism, and fluid transport between the extracerebral and the cerebral tissues. The technique is promising to probe dynamic interaction among the neurovascular, metabolic, and glymphatic systems in the infant developing brain and in the elderly degenerative brain in future studies.

Acknowledgments This work was partly supported by JSPS Grant-in-Aid for Scientific Research Number 20 K20601 to G. T.

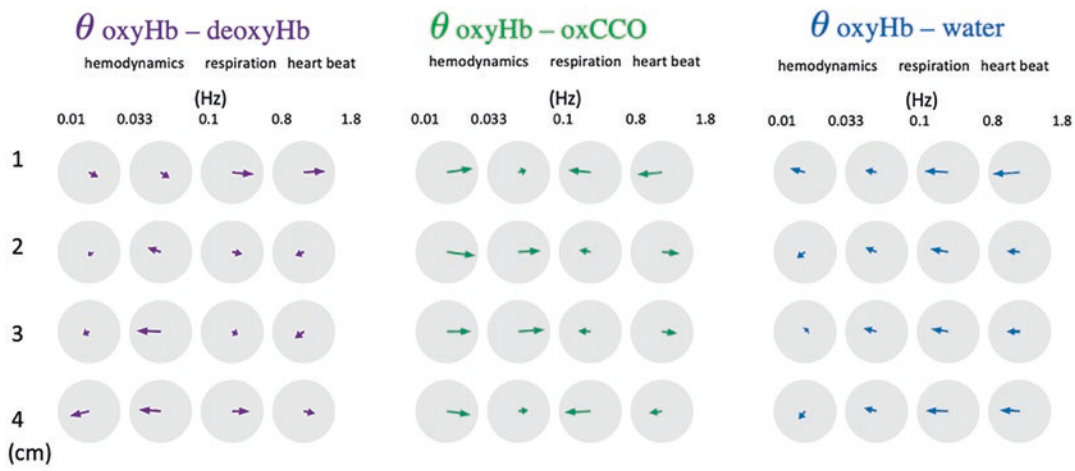

Fig. 31.2 Vector representation of phase differences of deoxy-Hb, oxCCO, and water in reference to oxy-Hb over the plane of source-detector distance vs. frequency in study 1. Direction of vector shows value of relative phase difference (right: 0, up 90, left 180, and down 270°). Data is from Adult1

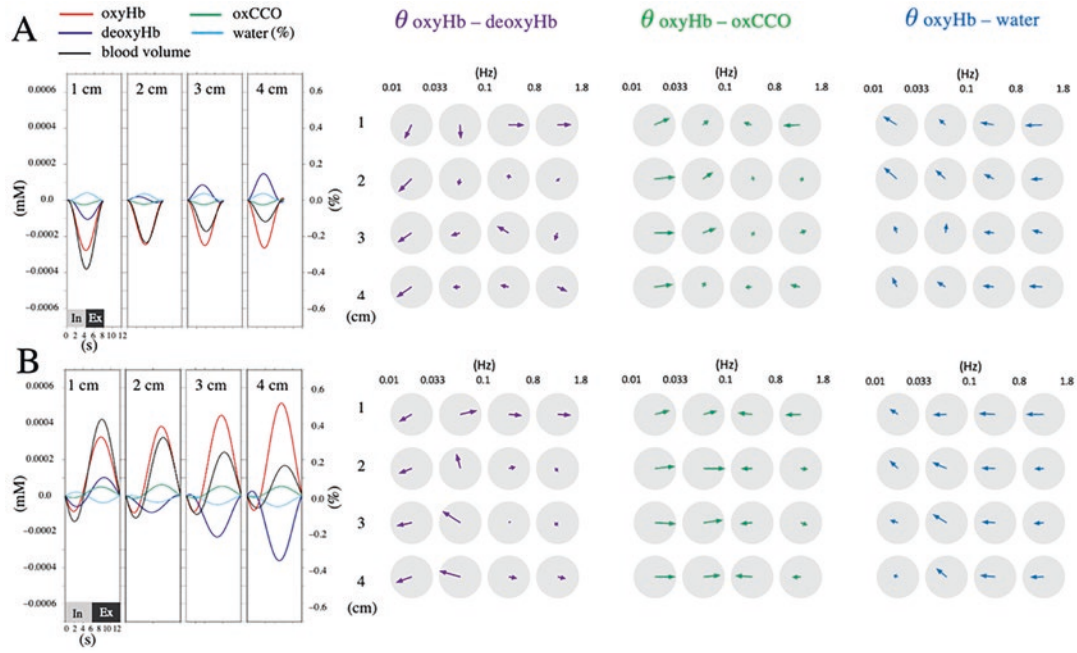

Fig. 31.3 Averaged response of oxy-, deoxy-Hb, oxCCO, and water in response to periodic inspiration and expiration and vector representation of phase differences in study 2. (**a**) period 8 s. (**b**) period 12 s. Data is from Adult1

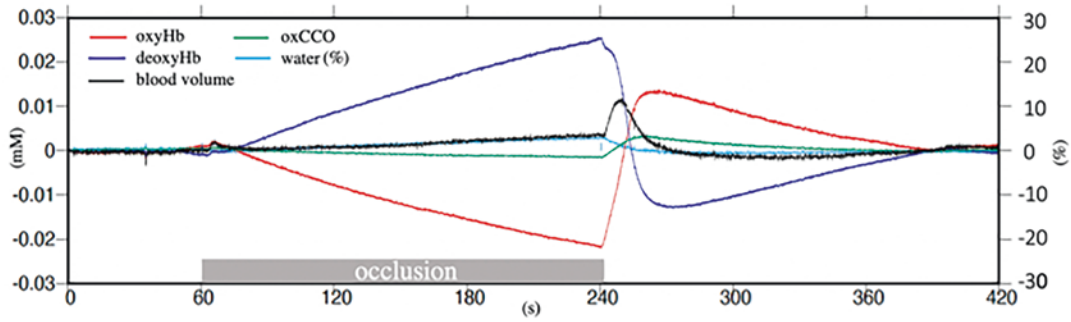

Fig. 31.4 Forearm muscle response to occlusion of arterial and venous blood flow in study 3. Data is from Adult 2

References

1. Taga G (2021) Global entrainment in the brain–body–environment: retrospective and prospective views. Biol Cybern 115:431–438
2. Taga G, Asakawa K, Maki A et al (2003) Brain imaging in awake infants by near-infrared optical topography. PNAS 100:10722–10727
3. Scholkmann F, Kleiser S, Metz AJ et al (2014) A review on continuous wave functional near-infrared spectroscopy and imaging instrumentation and methodology. NeuroImage 85:6–27
4. Watanabe H, Shitara Y, Aoki Y et al (2017) Hemoglobin phase of oxygenation and deoxygenation in early brain development measured using fNIRS. PNAS 114:E1737–E1744
5. Bale G, Elwell CE, Tachtsidis I (2016) From Jöbsis to the present day: a review of clinical near-infrared spectroscopy measurements of cerebral cytochrome-c-oxidase. J Biomed Opt 21:091307
6. Bale G, Mitra S, de Roever I et al (2019) Oxygen dependency of mitochondrial metabolism indicates outcome of newborn brain injury. J Cereb Blood Flow Metab 39:2035–2047
7. Myllylä T, Harju M, Korhonen V et al (2018) Assessment of the dynamics of human glymphatic system by near-infrared spectroscopy. J Biophotnics 11:e201700123
8. Borchardt V, Korhonen V, Helakari H et al (2021) Inverse correlation of fluctuations of cerebral blood and water concentrations in humans. Euro Phys J Plus 136:1–14
9. Rasmussen MK, Mestre H, Nedergaard M (2022) Fluid transport in the brain. Physiol Rev 102:1025–1151
10. Taga G, Konishi Y, Maki A et al (2000) Spontaneous oscillation of oxy-and deoxy-hemoglobin changes with a phase difference throughout the occipital cortex of newborn infants observed using non-invasive optical topography. Neurosci Lett 282:101–104
11. Obrig H, Neufang M, Wenzel R et al (2000) Spontaneous low frequency oscillations of cerebral hemodynamics and metabolism in human adults. NeuroImage 12:623–639
12. Sasai S, Homae F, Watanabe H et al (2011) Frequency-specific functional connectivity in the brain during resting state revealed by NIRS. NeuroImage 56:252–257
13. Matsuda T, Homae F, Watanabe H et al (2022) Oscillator decomposition of infant fNIRS data. PLoS Comp Biol 18:e1009985
14. Taga G, Homae F, Watanabe H (2007) Effects of source-detector distance of near infrared spectroscopy on the measurement of the cortical hemodynamic response in infants. NeuroImage 38:452–460
15. Pierro ML, Hallacoglu B, Sassaroli A et al (2014) Validation of a novel hemodynamic model for coherent hemodynamics spectroscopy (CHS) and functional brain studies with fNIRS and fMRI. NeuroImage 85:222–233
16. Guerouah Z, Lin S, Toronov V (2021) Measurement of adult human brain responses to breath-holding by multi-distance hyperspectral near-infrared spectroscopy. Appl Sci 12:371
17. Matcher SJ, Elwell CE, Cooper CE et al (1995) Performance comparison of several published tissue near-infrared spectroscopy algorithms. Anal Biochem 227:54–68
18. Arifler D, Zhu T, Madaan S et al (2015) Optimal wavelength combinations for near-infrared spectroscopic monitoring of changes in brain tissue hemoglobin and cytochrome c oxidase concentrations. Biomed Opt Exp 6:933–947
19. Cope M (1991) The application of near infrared spectroscopy to non invasive monitoring of cerebral oxygenation in the newborn infant. Department of Medical Physics and Bioengineering, p 342
20. Bigio IJ, Fantini S (2016) Quantitative biomedical optics: theory, methods, and applications. Cambridge University Press
21. Essenpreis M, Elwell CE, Cope M et al (1993) Spectral dependence of temporal point spread functions in human tissues. Appl Optic 32:418–425

32 Imaging Cerebral Blood Vessels Using Near-Infrared Optical Tomography: A Simulation Study

D. Yacheur, M. Ackermann, T. Li, A. Kalyanov, E. Russomanno, A. Di Costanzo Mata, M. Wolf, and J. Jiang

Abstract

Cerebral veins have received increasing attention due to their importance in preoperational planning and the brain oxygenation measurement. There are different modalities to image those vessels, such as magnetic resonance angiography (MRA) and recently, contrast-enhanced (CE) 3D gradient-echo sequences. However, the current techniques have certain disadvantages, i.e., the long examination time, the requirement of contrast agents or inability to measure oxygenation. Near-infrared optical tomography (NIROT) is emerging as a viable new biomedical imaging modality that employs near infrared light (650–950 nm) to image biological tissue. It was proven to easily penetrate the skull and therefore enables the brain vessels to be assessed. NIROT utilizes safe non-ionizing radiation and can be applied in e.g., early detection of neonatal brain injury and ischemic strokes. The aim is to develop non-invasive label-free dynamic time domain (TD) NIROT to image the brain vessels. A simulation study was performed with the software (NIRFAST) which models light propagation in tissue with the finite element method (FEM). Both a simple shape mesh and a real head mesh including all the segmented vessels from MRI images were simulated using both FEM and a hybrid FEM-U-Net network, we were able to visualize the superficial vessels with NIROT with a Root Mean Square Error (RMSE) lower than 0.079.

Keywords

Near-infrared optical tomography · Cerebral vessels · Imaging

32.1 Introduction

For many years, people have revered the brain as one of the most ingenious and complicated organs created by nature, with its amazing anatomical composition and interwoven functions. Stroke and related cerebrovascular diseases are a major cause of mortality and disability. Imaging of brain vessels and their oxygenation is important to address these diseases. Near-infrared optical tomography (NIROT) is emerging as a viable new biomedical imaging modality that employs near infrared light (650–950 nm) to image blood vessels and quantitatively their oxygenation. NIROT easily penetrates the skull with a penetration depth of up to ~6 cm in the head

D. Yacheur (✉) · M. Ackermann · T. Li
A. Kalyanov · E. Russomanno · A. D. C. Mata
M. Wolf · J. Jiang
Biomedical Optics Research Laboratory (BORL), Department of Neonatology, University Hospital Zurich, University of Zurich, Zurich, Switzerland
e-mail: djazia.yacheur@uzh.ch

F. Scholkmann et al. (eds.), *Oxygen Transport to Tissue XLIV*, Advances in Experimental Medicine and Biology 1438, https://doi.org/10.1007/978-3-031-42003-0_32

[1] and, therefore, enables the brain vessels to be assessed. NIROT will be applied in e.g., for early detection of neonatal brain injury and ischemic strokes [2] or functional brain imaging [3]. NIRFAST which is an open source software package for multi-modal optical molecular imaging, has been used for NIROT and accurate modeling and image reconstruction from clinical data [4]. The goal of this project is to demonstrate using light diffusion simulations the capacity of time-domain NIROT to image brain vessels.

32.2 Methods

We conducted simulation studies for various tissue volumes. The forward problem of light transport in tissue was modeled with NIRFASTer, which is based on finite element method (FEM). Image reconstructions were performed on a separate workstation (128 GB RAM, AMD® Ryzen 9 5950x 16-core processor × 32 CPU, NVIDIA Corporation GPU), with both a model-based and a data-driven method.

32.2.1 Mesh Generation

We started by generating simple tissue models, i.e., homogeneous (Fig. 32.1a) and multiple layer meshes (Fig. 32.1b). An x-shape inclusion reflects blood vessel with the appropriate **μ** inside a cylindrical volume. Different depths of the inclusion were tested. The simulation was also performed with a mesh of an adult head generated based on a segmented MRI image (Fig. 32.2a) (T1 and T2 weighted images). For each segment, optical properties from the literature (Table 32.1) were assigned (Fig. 32.2b). The geometrical arrangement of light sources and detectors on top of each mesh (Figs. 32.1c and 32.2c) is the same as for the time domain near infrared optical tomography (TD NIROT) system "Pioneer" developed by our lab [5–7].

32.2.2 Image Reconstruction

32.2.2.1 Finite Element Methods (FEM) -Based Method

Finite element methods (FEM) are widely used to numerically solve the diffusion equations (DEs) for complex geometries. We applied NIRFASTer, an FEM open-source software that facilitates GPUs to model the forward and inverse problem [8–10]. To achieve a fast (minutes) 3D image reconstruction and to reduce memory usage, we took the frequency-domain (FD) solution at ω = 100 MHz. The 3D image reconstruction was achieved by solving a least-squares minimization problem [11].

32.2.2.2 Hybrid FEM: U-Net Network

U-Net is a convolutional neural network that was developed for biomedicine. Within this project we employed a hybrid convolutional neural network (hCNN) [12] that learns image reconstructions (IR) from the inherent pattern of 2-iteration rough numerical IRs. This hCNN is based on an extension of the well-known V-net architecture [13]. It simultaneously learns a segmentation and regression task by minimizing a joint cost function to obtain inclusion localizations and absorption coefficients (μ_a). This network was trained on a dataset with spherical inclusions. The aim was to achieve high quality IRs in diverse geometries at a fraction of the time required for an iterative model-based method.

32.3 Results and Discussion

Both simple shape meshes (Fig. 32.1) and a real head mesh including all the segmented layers and vessels (Fig. 32.2), were simulated and compared to the ground truth.

For the simple cylinder mesh (Fig. 32.1d, g) and the FEM based results (Fig. 32.1e, h), we see that the shape of the cross was detected correctly, even though some parts were missing. The μ_a was predicted approximately correctly with a RMSE of 0.0139 and 0.0199 for the 10 mm and 15 mm depth inclusions.

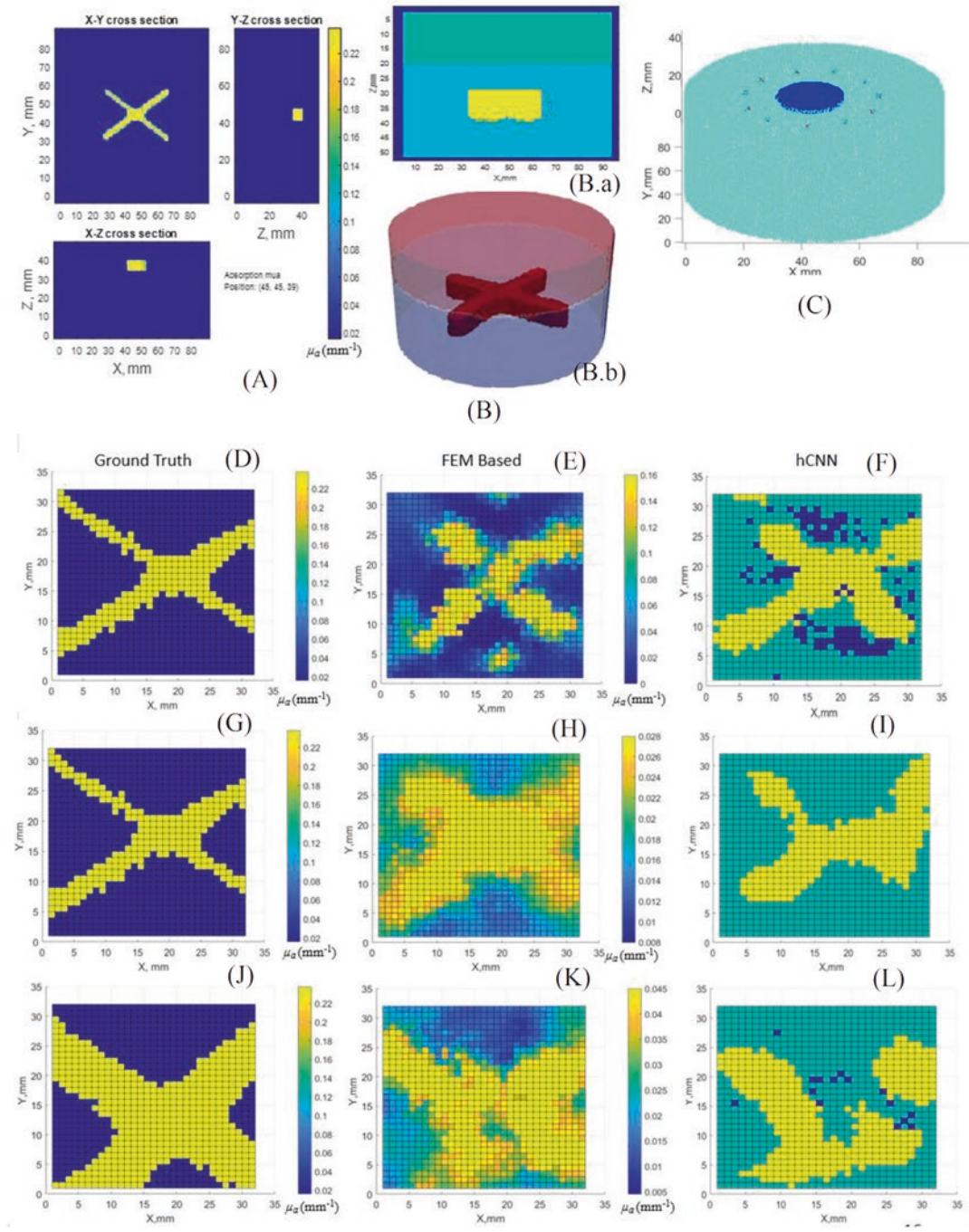

Fig. 32.1 Simple shape mesh simulation, (**a**) homogeneous cylinder mesh with an inclusion, (**b**.a) Cylinder mesh with two layers with an inclusion within the second layer, (**b**.b). 3D illustration of the cylinder mesh with two layers with an inclusion within the second layer (**c**) Placement of the sources and Detectors, (**d**) homogeneous cylinder mesh with a 10 mm depth inclusion, (**e**) FEM results for the homogeneous mesh with a 10 mm depth inclusion, (**f**) hCNN results for the homogeneous mesh with a 10 mm depth inclusion, (**g**) homogeneous cylinder mesh with a 15 mm depth inclusion, (**h**) FEM results for the homogeneous mesh with a 15 mm depth inclusion, (**i**) hCNN result for the homogeneous mesh with a 15 mm depth inclusion, (**j**) cylinder mesh with two layer, (**k**) FEM result for the two layers mesh, (**l**) hCNN simulation for the two layers mesh

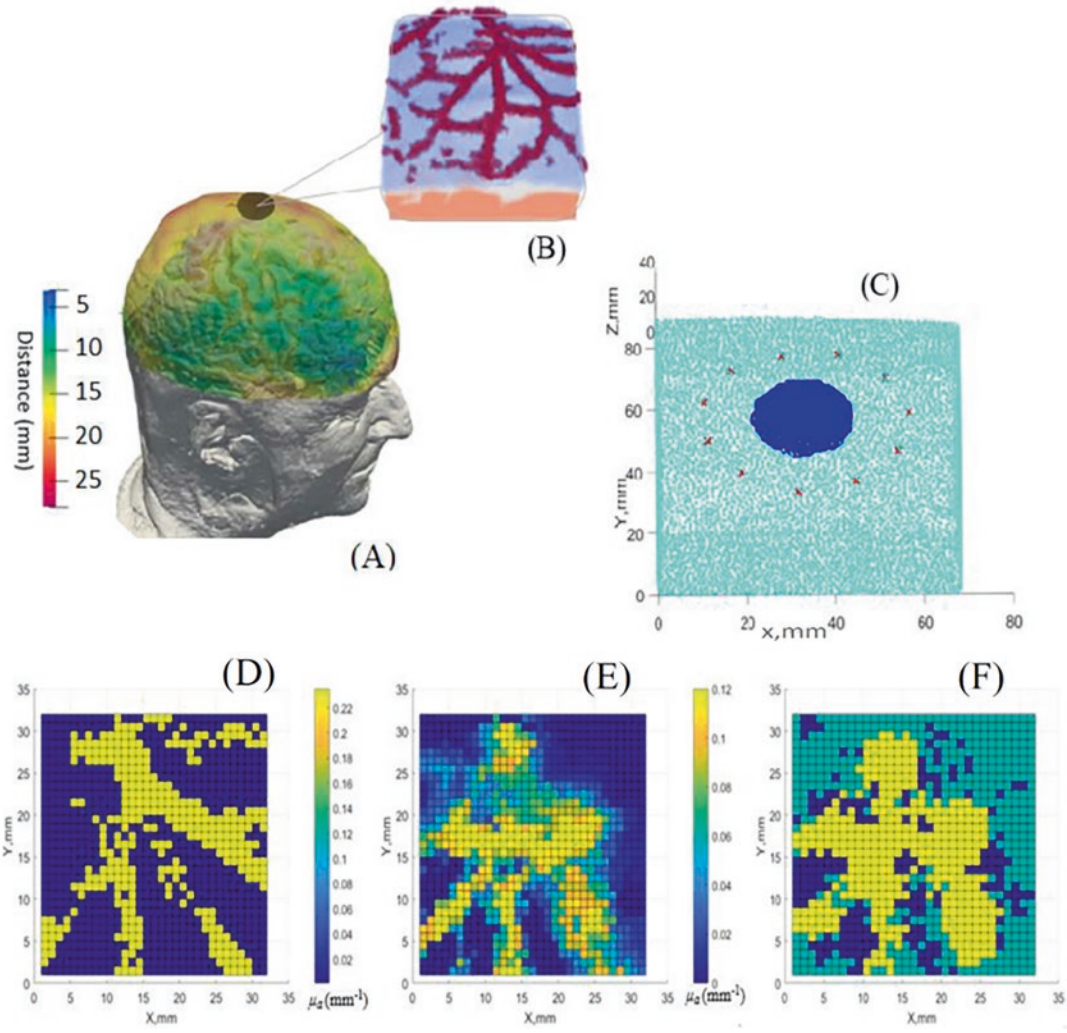

Fig. 32.2 Head mesh simulation, (**a**) segmented head mesh illustrating the depth of the brain with a color map, (**b**) the target region, (**c**) placement of the sources and detectors, (**d**) cropped mesh for the simulation, (**e**) FEM Base results, (**f**) hCNN simulation results

Table 32.1 Optical properties of head tissues for 800-nm where μ_s' is the reduced scattering coefficient and μ_a the absorption coefficient. This table is based on an unpublished review of Dr. A. Pifferi, Politecnico di Milano

Layers	μ_s' (mm^{-1})	μ_a (mm^{-1})
Scalp	1.5	0.018
Skull	1.4	0.016
CSF	0.3	0.004
Gray Matter	1	0.015
White Matter	1	0.01
Arterial blood	5	0.233
Venous blood	5.222	0.235

For the hCNN segmentation (Fig. 32.1f, i), which only uses categories such as blood vessel or other tissue, the cross is generally well detected at 10 mm (RMSE = 0.06886) depth and still recognizable at 15 mm (RMSE = 0.07410). There are some artifacts at the borders and some breaks.

For the mesh of two layers (Fig. 32.1j) with an inclusion in the second layer (the deeper one), we obtained the correct shape of the cross but not the inclusion with the FEM method (RMSE = 0.0344) (Fig. 32.1k). With the hCNN we detected approx-

imately the cross and the inclusion (RMSE = 0.03956) (Fig. 32.1l).

The head mesh was cropped (Fig. 32.2d) for the simulation to reduce the computing time to a reasonable level. The results of the FEM method were convincing (RMSE = 0.0551): even if there were some artifacts, we detected the majority of the vessels (Fig. 32.2e). For the hCNN (Fig. 32.2f), we were also able to detect the vessels, though the shape was not completely correct (RMSE = 0.07876) e.g. some vessels were merged.

The FEM method gives good results for the superficial inclusions down to 10 mm. Whereas the hCNN does not reconstruct the shape perfectly and there are artifacts even in the superficial layers. This can be improved by better training of the hCNN.

32.4 Conclusion

This article is one of the first articles exploring the possibility of imaging the cerebral blood vessels using NIROT. It is already possible to image these quite well at low depth. This is only the first step and the image quality is expected to improve substantially with future improvements in both image reconstruction algorithms and hardware arrangements.

Acknowledgments We gratefully acknowledge funding by the Swiss National Science Foundation (159490 and 197079), the Innovation spool of the University Hospital Zurich, the UZH Entrepreneur Fellowships (MEDEF21-025), and the Forschungskredit K-84302-02-01.

Conflicts of Interest Martin Wolf declares that he is president of the board and co-founder of OxyPrem AG and Alexander Kalyanov is working partly for this company.

References

1. Mora AD, Contini D, Arridge S et al (2015) Towards next-generation time-domain diffuse optics for extreme depth penetration and sensitivity. Biomed Opt Express 6(5):1749–1760. https://doi.org/10.1364/BOE.6.001749. eCollection 2015 May 1. PMID: 26137377
2. Arri T, Muehlemann S, Biallas M et al (2011) Precision of cerebral oxygenation and hemoglobin concentration measurements in neonates measured by near-infrared spectroscopy. J Biomed Opt 16(4):047005
3. Eggebrecht AT, Ferradal SL, Robichaux-Viehoever A et al (2014) Mapping distributed brain function and networks with diffuse optical tomography. Nat Photonics 8(6):448–454
4. Dehghani H, Eames ME, Yalavarthy PK, Davis SC, Srinivasan S, Carpenter CM, Pogue BW, Paulsen KD (2008) Near infrared optical tomography using NIRFAST: algorithm for numerical model and image reconstruction. Commun Numer Methods Eng 25(6):711–732. https://doi.org/10.1002/cnm.1162. PMID: 20182646; PMCID: PMC2826796
5. Jiang J, Costanzo Mata AD, Lindner S, et al. 2.5 Hz sample rate time-domain near-infrared optical tomography based on SPAD-camera image tissue hemodynamics
6. Jiang J, Costanzo Mata AD, Lindner S et al (2020) Dynamic time domain near-infrared optical tomography based on a spad camera. Biomed Opt Express 11(10):5470–5477. PMID: vol. 3314
7. Jiang J, Costanzo Mata AD, Lindner S et al (2020) Image reconstruction for novel time domain near infrared optical tomography: towards clinical applications. Biomed Opt Express 11(8):4723–4734. PMID: vol. 3292
8. [Online]. Available: https://github.com/nirfaster/NIRFASTer
9. Doulgerakis-Kontoudis M, Eggebrecht A, Wojtkiewicz S et al (2017) Toward real-time diffuse optical tomography: accelerating light propagation modeling employing parallel computing on gpu and cpu. J Biomed Opt 22(12):125001
10. Dehghani H, Eames ME, Yalavarthy PK et al (2009) Near infrared optical tomography using nirfast: algorithm for numerical model and image reconstruction. Commun Numer Meth Eng 25(6):711–732
11. Yalavarthy PK, Pogue BW, Dehghani H et al (2007) Weight-matrix structured regularization provides optimal generalized least-squares estimate in diffuse optical tomography. Med Phys 34(6):2085–2098
12. Ackermann M, Jiang J, Russomanno E, Wolf M, Kalyanov A (2022) Hybrid Convolutional Neural Network (hCNN) for image reconstruction in near-infrared optical tomography. Adv Exp Med Biol 1395:165–170. https://doi.org/10.1007/978-3-031-14190-4_28
13. Milletari F, Navab N, Ahmadi S-A (2016) V-net: Fully convolutional neural networks for volumetric medical image segmentation. In: 2016 fourth international conference on 3D vision (3DV). IEEE, pp 565–571

Part VI

Clinical Application

33 Reduced Cerebrovascular Oxygenation in Individuals with Post-Acute COVID-19 Syndrome (PACS) ("long COVID")

Damilola D. Adingupu, A. Soroush, A. Hansen, R. Twomey, and J. F. Dunn

Abstract

There is evidence that hypoxia occurs in the brain of some individuals who contracted the COVID-19 disease. Furthermore, it has been widely reported that about 13% of individuals who contracted the COVID-19 disease report persistent symptoms after the acute infection stage (>2 months post-acute infection). This is termed post-acute COVID-19 syndrome (PACS) or ("long COVID"). In this study, we aimed to determine if hypoxia measured non-invasively with frequency domain near-infrared spectroscopy (fdNIRS) occurs in asymptomatic and symptomatic individuals with post-acute COVID-19 disease. We show that 26% of our symptomatic group, measured on average 9.6 months post-acute COVID-19 disease, were hypoxic and 12% of the asymptomatic group, measured on average 2.5 months post-acute infection, were hypoxic. Our study indicates that fdNIRS measure of hypoxia in the brain may be a useful tool to identify individuals that are likely to respond to treatments targeted at reducing inflammation and improving oxygenation.

Keywords

Post-acute COVID-19 syndrome · Long COVID · Cerebrovascular oxygenation · Hypoxia

33.1 Introduction

About 1 in 10 adults who contracted the COVID-19 disease caused by severe acute respiratory syndrome coronavirus 2 (SARS-CoV-2) will have persistent symptoms long after the acute infection [1, 2]. This is termed "post-acute COVID-19 syndrome" (PACS) or "long COVID". In PACS, individuals have a range of symptoms that are not explained by an alternative diagnosis still occurring at least 3 months from onset of COVID-19,

D. D. Adingupu (✉)
Department of Radiology, University of Calgary, Calgary, AB, Canada
e-mail: Deborah.adingupu@ucalgary.ca

A. Soroush · J. F. Dunn
Department of Radiology, University of Calgary, Calgary, AB, Canada

Hotchkiss Brain Institute, University of Calgary, Calgary, AB, Canada

Department of Clinical Neurosciences, University of Calgary, Calgary, AB, Canada

A. Hansen
Department of Radiology, University of Calgary, Calgary, AB, Canada

Department of Clinical Neurosciences, University of Calgary, Calgary, AB, Canada

R. Twomey
Faculty of Kinesiology, University of Calgary, Calgary, AB, Canada

F. Scholkmann et al. (eds.), *Oxygen Transport to Tissue XLIV*, Advances in Experimental Medicine and Biology 1438, https://doi.org/10.1007/978-3-031-42003-0_33

which negatively impacts the individual's quality of life [1, 3]. Inflammation is a key immune response to SARS-CoV-2 infection and in some patients systemic hypoxia have been described [4]. It is however unclear whether there is inflammation and/or hypoxia in the brain of individuals who have post-COVID-19 condition. We previously proposed that inflammatory responses within the brain can result in hypoxia and that this hypoxia can worsen inflammation [5]. We can measure absolute cortical microvascular oxygen saturation and detect hypoxia non-invasively using frequency domain near-infrared spectroscopy (fdNIRS). Details of the fdNIRS technique is described in detail elsewhere [6–9]. The ratio of oxygenated hemoglobin (HbO) to total hemoglobin (tHb) provides a measure of the absolute cortical microvasculature hemoglobin oxygen saturation (S_tO_2), which is a value that is used as an indicator of the brain's oxygenation status [10].

Given the proposed relationship between hypoxia and inflammation, and the known fact that COVID-19 disease is an inflammatory condition, we aimed to investigate if microvascular cortical hypoxia measured with fdNIRS occurs in post-COVID-19 condition.

33.2 Methods

To quantify S_tO_2 in the prefrontal cortical tissue, we used fdNIRS (ISS OxiplexTS Frequency Domain Near-Infrared Spectrometer model 96208, ISS Inc., Champaign, IL USA). The fdNIRS system was warmed up for at least 30 minutes and the system was calibrated using a phantom calibration block with known absorption and scattering coefficients prior to data collection. During data acquisition, participants were asked to sit quietly and upright in a chair. The probe was placed symmetrically on both the right and left side of the participant's forehead, about 2 cm from the eyebrow and data was collected for about 1 minute on each side and averaged.

Eighteen healthy controls data were extracted from a database of participants recruited at a time prior to the pandemic, 17 participants with no persistent symptoms (asymptomatic) and 20 with persistent symptoms (symptomatic) after acute SARS-CoV-2 infection were actively recruited from the community. Controls self-identified as non-smoker (nicotine or Marijuana), with no history of cardiovascular or vascular disease, no history of other systemic inflammatory disease like inflammatory bowel syndrome, asthma, autoimmune diseases, coeliac disease, glomerulonephritis, and hepatitis and no neuropsychological condition. Persistent symptoms were defined as not having returned to pre-COVID-19 level of health and function ≥2 months after acute infection and having ≥3 symptoms that suggest long-COVID. Date of COVID-19 diagnosis for asymptomatic participants ranged from April 2020–April 2022, and measurements were taken on average 3 months (range 2–17) from diagnosis. For symptomatic participants, diagnosis was between February 2020 and May 2021, and measurements were taken 10 months (range 4–19) from diagnosis.

Arterial saturation of oxygen (S_aO_2), and heart rate (HR) were measured using a pulse oximeter. Age and sex were also collected. Tympanic temperature was measured (Braun IRT6520CA ThermoScan® 7 Ear Thermometer with Age Precision). Fatigue was measured using the Functional Assessment of Chronic Illness Therapy – Fatigue (FACIT-F), and depression and anxiety were measured using the Beck Depression Inventory (BDI-II) in the post-acute COVID-19 participants only. Cognitive domain for visual processing speed and episodic memorization was assessed using the symbol digit modalities test (SDMT).

All participants provided written informed consent prior to commencement of the study. This study complied with the Declaration of Helsinki. Ethics approval was obtained from the Conjoint Health and Research Board at the University of Calgary.

33.3 Results

Eighty percent of symptomatic participants have had at least one dose of COVID-19 vaccination while 20% had not prior to data collection. Sixty-five percent of asymptomatic participants have had at least one dose of COVID-19 vaccination, 24% had not and 11% declined to provide that information. Data were collected at least 1 month post vaccination. Table 33.1 summarizes the data for group comparison for all groups. Statistical analysis was done using One-way ANOVA for parametric, or Kruskal-Wallis test for non-parametric data. Turkey HSD or Dunn test was used for the post hoc analysis.

Symptomatic post-acute COVID-19 disease participants were older than the asymptomatic group, but not significantly different from controls. Symptomatic post-acute COVID-19 disease participants had spent fewer years in education compared with controls, but this was not significantly different from the asymptomatic group. There was no difference between groups for S_aO_2.

Although nearly missing the criterion for statistical significance ($p = 0.052$), HR was slightly elevated in the symptomatic group (68 ± 8, 68 ± 10, 76 ± 12 (BPM) in controls, asymptomatic and symptomatic groups, respectively (mean ± SD)). Tympanic temperature was higher in the symptomatic group compared with the control and asymptomatic group. Fatigue measured using the FACIT-F was particularly severe in the symptomatic group, with a group mean score that indicates moderate-severe depression.

S_tO_2 was 62.8 ± 3.6, 62.6 ± 8.5, and 58.7 ± 5.0 (%) in controls, asymptomatic and symptomatic groups, respectively (mean ± SD). S_tO_2 was lower in the symptomatic post-COVID-19 participants vs. controls ($p = 0.013$). S_tO_2 values that were 2 standard deviations below the control group mean were defined as hypoxic ($S_tO_2 < 55.6\%$).

Twenty-six percent of the symptomatic group were categorized as hypoxic, vs. 12% in the asymptomatic group (Fig. 33.1). Worse performance in a cognitive task (SDMT) was observed

Table 33.1 Demographic, measure of depression, fatigue, processing speed and oxygen saturation, measured in healthy controls, asymptomatic and symptomatic post-COVID19 participants. Data presented as mean ± SD or median (95% CI)

					Post-hoc p values		
	Healthy control (HC)	Asymptomatic (Asymp)	Symptomatic (Symp)	ANOVA/ Kruskal p value	HC vs. Asymp	HC vs. Symp	Asymp vs. Symp
Age	33(24–48)	26(23–49)	44.5(42–50)	0.041	>0.999	0.248	0.044
Sex	Male, n = 8 Female, n = 10	Male, n = 9 Female, n = 8	Male, n = 2 Female, n = 18				
Education (years)	17(16–18)	16(16–16)	16(14–16)	0.010	0.363	0.007	0.413
S_aO_2 (%)	97.2 ± 1.2	96.6 ± 1.2	96.8 ± 1.5	0.392	No post-hoc tests when Anova not significant		
HR (BPM)	67.9 ± 8.0	68.3 ± 10.2	75.5 ± 12.3	0.052			
Tymp temp (°C)	36.8(36.6–37.1)	36.8(36.6–36.9)	37.1(37.05–37.2)	0.004	>0.999	0.047	0.004
FACIT_F		38.8 ± 8.3	14.8 ± 7.5	<0.001			
BDI-II		9.5 ± 8.0	23.3 ± 8.0	<0.001			
SDMT - oral z score	0.89 ± 1.12	−0.27 ± 1.24	−0.88 ± 1.12	<0.001	0.046	<0.001	0.097
StO_2 (%)	62.8 ± 3.6	62.6 ± 8.5	58.7 ± 5.0	0.013	>0.999	0.065	0.020

Healthy control (HC) (n = 18), Asymp (asymptomatic post-COVID-19 participants) (n = 17), Symp (symptomatic Post-COVID-19 participants) (n = 20), Heart rate (HR), Tympanic temperature (Tymp temp), Functional Assessment of Chronic Illness Therapy (FACIT) Fatigue Scale (FACIT_F), Beck Depression Inventory-II (BDI-II), Symbol Digit Modalities Test (SDMT)

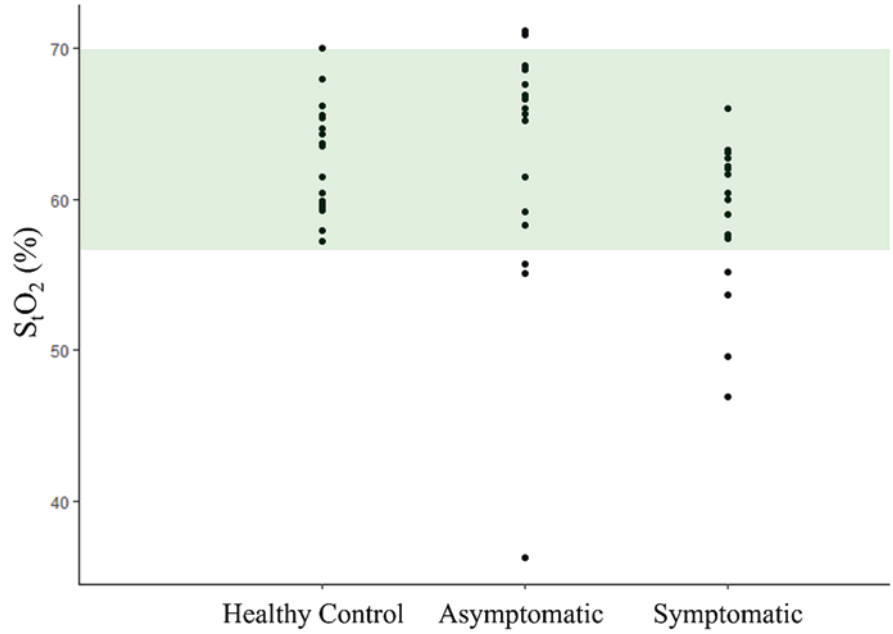

Fig. 33.1 fdNIRS measurement of microvascular cortical oxygenation (S_tO_2) in healthy controls and asymptomatic and symptomatic post COVID-19 participants, showing the data distribution. Each dot represents one participant. Green shaded area represents 2 × SD around the healthy control mean. All points below the shaded area are 2 × SD below the controls (classed as hypoxic)

in both symptomatic and asymptomatic post-COVID-19 participants compared with controls. There was a relationship between S_tO_2 and age, as well as fatigue (Fig. 33.2).

33.4 Conclusions

We show that fdNIRS technology may be useful in identifying individuals with brain hypoxia post-acute COVID-19 disease. A higher percentage of symptomatic post-acute COVID-19 disease participants were hypoxic compared with asymptomatic participants, and this was related with increasing age and fatigue. This suggests that older individuals who have had the COVID-19 disease may be more predisposed to lower cortical microvascular oxygenation, which in turn could result in fatigue. It is well documented that there is an age-related risk of developing serious complications with the COVID-19 disease [11]. Furthermore, the elevated HR in the symptomatic group with corresponding reduction in S_tO_2 could be suggestive that the S_tO_2 may be lower than reflected, given the findings by Scholkmann et al., which showed that resting-state S_tO_2 values from the frontal lobe are positively related with the resting-state HR values [12]. Increased HR reported in the symptomatic group could have acted as a confounder, serving to further increase S_tO_2 in this group, albeit not enough to match those of the controls and asymptomatic group.

COVID-19 disease is known to be an inflammatory disease; however, there is no consensus in literature yet if there is infiltration of the virus into the brain. We propose that microvascular damage in the brain reported in individuals deceased of COVID-19 disease [13, 14], may be present in some convalescent individuals post-acute COVID-19 disease. The results presented here could therefore be indicative of residual

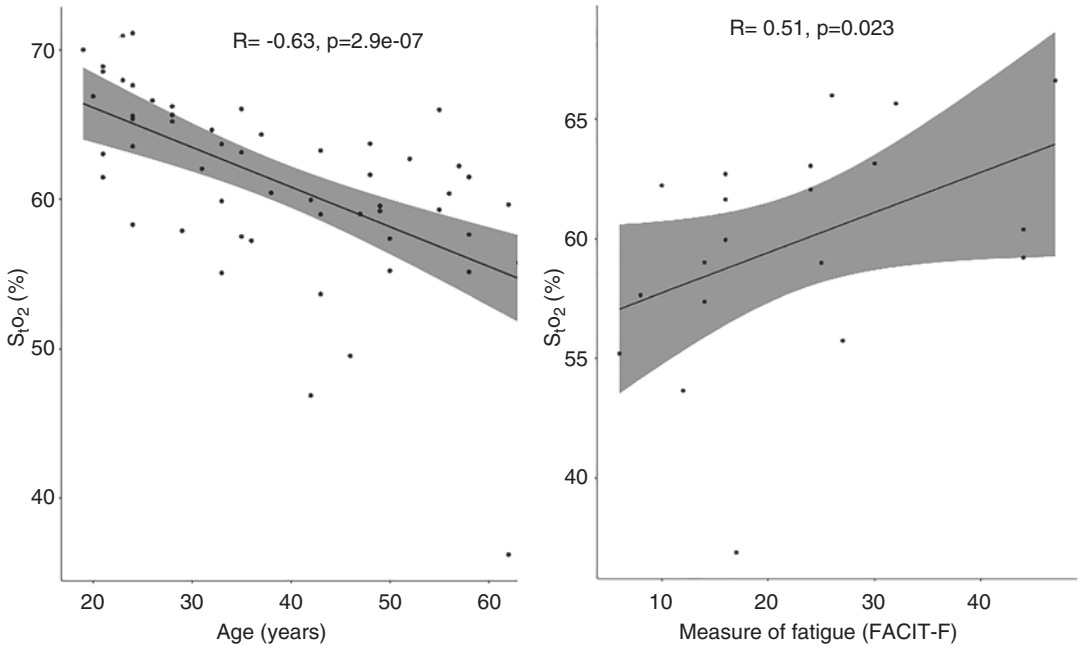

Fig. 33.2 Correlation analysis between S_tO_2 (%), age (years) for all participants and FACIT-F analyzed for all post-acute COVID-19 participants

microvascular damage in the grey matter of some individuals because of the SARS-CoV-2 infection.

Inflammation within the CNS may relate to hypoxia through the hypoxia/inflammation cycle, where inflammatory responses within the brain can cause hypoxia, and hypoxia can worsen inflammation [5]. This vicious cycle may result in alterations in brain function. Furthermore, it has been proposed that possible mechanisms involved in PACS could include neuroinflammation, damage to blood vessels by coagulopathy, endothelial dysfunction, and injury to neurons [2]. These mechanisms will also explain our findings.

This body of work shows that the fdNIRS technology may provide a non-invasive method to identify individuals with pathological presentations in the brain. fdNIRS measures of hypoxia in the brain may therefore be a useful tool to identify individuals that are likely to respond to treatments targeted at reducing inflammation and improving oxygenation.

Acknowledgments This study was funded by the National Multiple sclerosis Society, grant number: RG-1806-31457.

References

1. Ballering AV, van Zon SKR, Hartman TCO, Rosmalen JGM (2022) Persistence of somatic symptoms after COVID-19 in The Netherlands: an observational cohort study. Lancet 400:452–461
2. Davis HE, McCorkell L, Vogel JM, Topol EJ (2023) Long COVID: major findings, mechanisms and recommendations. Nat Rev Microbiol 21:133–146
3. WHO (2021) A clinical case definition of post COVID-19 condition by a Delphi consensus, 6 October 2021
4. Simonson TS, Baker TL, Banzett RB, Bishop T, Dempsey JA, Feldman JL et al (2021) Silent hypoxaemia in COVID-19 patients. J Physiol 599:1057–1065
5. Yang R, Dunn JF (2019) Multiple sclerosis disease progression: contributions from a hypoxia-inflammation cycle. Mult Scler 25:1715–1718
6. De Blasi RA, Fantini S, Franceschini MA, Ferrari M, Gratton E (1995) Cerebral and muscle oxygen saturation measurement by frequency-domain near-infra-red spectrometer. Med Biol Eng Comput 33:228–230

7. Fantini S, Hueber D, Franceschini MA, Gratton E, Rosenfeld W, Stubblefield PG et al (1999) Non-invasive optical monitoring of the newborn piglet brain using continuous-wave and frequency-domain spectroscopy. Phys Med Biol 44:1543–1563
8. Gatto R, Hoffman W, Mueller M, Flores A, Valyi-Nagy T, Charbel FT (2006) Frequency domain near-infrared spectroscopy technique in the assessment of brain oxygenation: a validation study in live subjects and cadavers. J Neurosci Methods 157:274–277
9. Hallacoglu B, Sassaroli A, Wysocki M, Guerrero-Berroa E, Schnaider Beeri M, Haroutunian V et al (2012) Absolute measurement of cerebral optical coefficients, hemoglobin concentration and oxygen saturation in old and young adults with near-infrared spectroscopy. J Biomed Opt 17:081406–081401
10. Yang R, Dunn JF (2015) Reduced cortical microvascular oxygenation in multiple sclerosis: a blinded, case-controlled study using a novel quantitative near-infrared spectroscopy method. Sci Rep 5:16477
11. Romero Starke K, Reissig D, Petereit-Haack G, Schmauder S, Nienhaus A, Seidler A (2021) The isolated effect of age on the risk of COVID-19 severe outcomes: a systematic review with meta-analysis. BMJ Glob Health 6:e006434
12. Scholkmann F, Zohdi H, Wolf M, Wolf U (2022) Frontal cerebral oxygenation in humans at rest: a mirror symmetry in the correlation with cardiorespiratory activity. In: Oxygen transport to tissue XLIII, Cham, pp 45–51
13. Lee M-H, Perl DP, Nair G, Li W, Maric D, Murray H et al (2020) Microvascular injury in the brains of patients with Covid-19. N Engl J Med 384:481–483
14. Østergaard L (2021) SARS CoV-2 related microvascular damage and symptoms during and after COVID-19: consequences of capillary transit-time changes, tissue hypoxia and inflammation. Physiol Rep 9:e14726

34

Insufficient Oxygen Supplementation During Cardiopulmonary Resuscitation Leads to Unfavorable Biological Response While Hyperoxygenation Contributes to Metabolic Compensation

Tomoaki Aoki, Vanessa Wong, Kei Hayashida, Lance B. Becker, and Koichiro Shinozaki

Abstract

Sudden cardiac arrest (CA) is the third leading cause of death. Immediate reoxygenation with high concentrations of supplemental oxygen (O_2) during cardiopulmonary resuscitation (CPR) is recommended according to the current guidelines for adult CA. However, a point in controversy exists because of the known harm of prolonged exposure to 100% O_2. Therefore, there have been much debate on an optimal use of supplemental O_2, yet little is known about the duration and dosage of O_2 administration. To test whether supplying a high concentration of O_2 during CPR and post resuscitation is beneficial or harmful, rats subjected to 10-minute asphyxia CA were administered either 100% O_2 (n = 8) or 30% O_2 (n = 8) for 2 hours after CPR. Two hours after initiating CPR, the brain, lung, and heart tissues were collected to compare mRNA gene expression levels of inflammatory cytokines, apoptotic and oxidative stress-related markers. The 100% O_2 group had significantly shorter time to return of spontaneous circulation (ROSC) than the 30% O_2 group (62.9 ± 2.2 and 77.5 ± 5.9 seconds, respectively, $P < 0.05$). Arterial blood gas analysis revealed that the 100% O_2 group had significantly higher $PaCO_2$ (49.4 ± 4.9 mmHg and 43.0 ± 3.0 mmHg, $P < 0.01$), TCO_2 (29.8 ± 2.7 and 26.6 ± 1.1 mmol/L, $P < 0.05$), HCO_3^- (28.1 ± 2.4 and 25.4 ± 1.2 mmol/L, $P < 0.05$), and BE (2.6 ± 2.3 and 0.1 ± 1.4 mmol/L, $P < 0.05$) at 2 hours after initiating CPR, but no changes in pH (7.37 ± 0.03 and 7.38 ± 0.03, ns). Inflammation- (*Il6*, *Tnf*) and apoptosis-(*Casp3*) related mRNA gene expression levels were significantly low in the 100% O_2 group in the brain, however, oxidative stress moderator *Hmox1* increased in the 100% O_2 group. Likewise, mRNA gene expression of *Icam1*, *Casp9*, *Bcl2*, and *Bax* were low in the 100% O_2 group in the lung. Contrarily, mRNA gene expression of *Il1b* and *Icam1* were low in the 30% O_2 group in the heart. Supplying 30% O_2 during and after CPR significantly delayed the time to ROSC and increased inflammation−/apoptosis- related gene expression in the brain

T. Aoki (✉) · V. Wong · K. Hayashida · L. B. Becker
K. Shinozaki
Feinstein Institutes for Medical Research, Northwell Health System, Manhasset, NY, USA
e-mail: taoki@northwell.edu

F. Scholkmann et al. (eds.), *Oxygen Transport to Tissue XLIV*, Advances in Experimental Medicine and Biology 1438, https://doi.org/10.1007/978-3-031-42003-0_34

and lung, indicating that insufficient O_2 was associated with unfavorable biological responses post CA, while prolonged exposure to high-concentration O_2 should be still cautious in general.

Keywords

Cardiopulmonary resuscitation · Hyperoxygenation · Metabolic compensation

34.1 Introduction

Sudden cardiac arrest (CA) stands as the third most prevalent cause of mortality in the United States [1]. The present guidelines for adult CA patients recommend immediate reoxygenation through the utilization of high concentrations of supplemental oxygen (O_2) during cardiopulmonary resuscitation (CPR). Nevertheless, the appropriateness of this approach remains a matter of debate due to the recognized adverse effects associated with prolonged exposure to 100% O_2 [2]. Consequently, a comprehensive understanding of the optimal management strategies for supplemental O_2 is yet to be achieved, as the duration and dosage of O_2 administration lack clarity, impeding progress in the field of resuscitation. We aimed to test whether supplying high concentration O_2 during CPR and subsequent post resuscitation care is beneficial or harmful.

34.2 Methods

34.2.1 Animal Preparation

The Institutional Animal Care and Use Committees of Feinstein Institutes for Medical Research approved the animal protocol. We performed all instrumentation according to the previously described protocol [3–5]. In brief, adult male Sprague-Dawley rats aged 12–16 weeks and weighing 400–500 g (Charles River Laboratories, Wilmington, MA, USA) were anesthetized with 4% isoflurane (Isosthesia, Butler-Schein AHS, Dublin, OH, USA) and intubated with a 14-gauge plastic catheter (Surflo, Terumo Medical Corporation, Tokyo, Japan). Mechanical ventilation was performed using a Harvard Apparatus ventilator model 683 (Holliston, MA, USA) at a minute ventilation (MV) volume of 180 ml per minute and a respiratory rate of 45 breaths per minute. Positive end-expiratory pressure (PEEP) was set at 2 cm H_2O. Carbon dioxide (CO_2) was continuously monitored in the exhaled air using a CO_2 gas monitor (OLG-2800, Nihon Kohden Corp., Tokyo, Japan) with a CO_2 sensor (TG-970P, Nihon Kohden Corp., Tokyo, Japan) and an airway adapter (YG-211T, Nihon Kohden Corp., Tokyo, Japan). Anesthesia was maintained using 2% isoflurane with a fraction of inspired O_2 (FIO_2) of 0.3. Core body temperature was maintained at 36.5 ± 1.0 °C throughout the surgical procedure. After the instrumentation, neuromuscular blockade was achieved by administering 2 mg/kg of vecuronium bromide (Hospira, Lake Forest, IL, USA) intravenously at a slow rate. Asphyxia was induced by ceasing the ventilator, leading to CA occurring within 3 to 4 minutes. The CA group received CPR after 10-minute asphyxia. We defined CA as a mean arterial pressure (MAP) dropped below 20 mmHg; CA was completely untreated during the initial 10 minutes. Following the 10-minute asphyxia period, mechanical ventilation was resumed with an FIO_2 of either 1.0 or 0.3, and manual chest compression CPR was initiated concurrently. Chest compressions were administered at a rate of 260 to 300 per minute using two fingers placed over the sternum. At 30 seconds after the start of CPR, a 20 μg/kg bolus of epinephrine was given to rats through a venous catheter. CPR was ceased upon the return of spontaneous circulation (ROSC), defined as a MAP exceeding 60 mmHg. Arterial blood gas analysis was conducted at 10, 20, 30, 45, 60, and 120 minutes after initiating CPR. At 2 hours after initiating CPR, mechanical ventilation was discontinued, and rats were euthanized to obtain tissue samples. Furthermore, volumetric metabolic measurements were performed for each group to assess O_2 consumption (VO_2) and CO_2 generation (VCO_2).

34.2.2 Real-Time PCR

The brain, lung, and heart were collected at 2 hours after CPR for mRNA extraction, followed by cDNA synthesis and real-time PCR. Additionally, tissues of control (naive) rats were collected for references of mRNA gene expression. Total RNAs were extracted from tissue homogenates and reverse transcribed using TRIzol Reagent® (Invitrogen, Carlsbad, CA, USA) and SuperScript™ IV VILO™ Master Mix with ezDNase™ Enzyme (Invitrogen, Carlsbad, CA, USA), respectively. Real-time PCR was performed using TaqMan™ Fast Advanced Master Mix (Applied Biosystems™, Waltham, MA, USA) on the LightCycler 480 system (Roche Diagnostics, Mannheim, Germany). All primers were purchased from Thermofisher: *Glyceraldehyde-3-phosphate dehydrogenase* (*Gapdh*, TaqMan Assay ID: Rn01775763_g1), *Interleukin-1 beta* (*Il1b*, Rn00580432_m1), *Interleukin-6* (*Il6*, Rn01410330_m1), *Tumor necrosis factor* (*Tnf*, Rn01525859_g1), *Intracellular adhesion molecule-1* (*Icam1*, Rn00564227_m1), *Heme oxygenase-1* (*Hmox1*, Rn00561387_m1), *Caspase-3* (*Casp3*, Rn00563902_m1), *Caspase-9* (*Casp9*, Rn00581212_m1), *B-cell leukemia/lymphoma-2* (*Bcl2,* Rn99999125_m1), and *Bcl2 associated X protein* (*Bax*, Rn02532082_g1).

34.2.3 Statistical Analysis

Data are shown as the means and standard error (SE) for continuous variables. Two-tailed *P* values were calculated, and $P < 0.05$ was considered statistically significant. Prism 9.1.0 (GraphPad, San Diego, CA, USA) were used for statistical analyses.

34.3 Results

ROSC was achieved in all animals. Figure 34.1 shows that the 100% O_2 group achieved ROSC significantly faster than the 30% O_2 group (62.9 ± 2.2 and 77.5 ± 5.9 seconds, respectively, $P < 0.05$). The vital signs were recorded up to 120 minutes after CPR initiation, revealing that there were no significant differences between the groups in MAP, esophageal temperature, or $EtCO_2$, while the 30% O_2 group showed higher heart rates at some points within the first 120 minutes. As it was expected, PaO_2 was increased in the 100% O_2 group through the observation period (Fig. 34.2). A representative data of volumetric metabolic measurement indicated that the 100% O_2 group might have higher VO_2 as compared to the 30% O_2 group, implying that 100% O_2 might lead to hypermetabolism in the early phase post CA. Consistently with metabolic measurements, arterial gas analysis revealed that $PaCO_2$, HCO_3^-, TCO_2, and BE significantly increased in the 100% O_2 group than the 30% O_2 group, as a result, no change in pH was identified between the groups. Table 34.1 summarizes arterial blood gas data at 120 minutes after CPR initiation. For the assessment of biological responses, mRNA gene expression in the brain, lung, and heart were shown in Fig. 34.3. Inflammation- (*Il6*, *Tnf*) and apoptosis- (*Casp3*, *Bax*) related mRNA gene expression levels were significantly low in the 100% O_2 group in the brain, however, oxidative stress moderator *Hmox1* increased in the 100% O_2 group. Likewise, mRNA gene expression of *Icam1*, *Casp9*, *Bcl2*, and *Bax* were low in the 100% O_2 group in the lung. Contrarily, mRNA gene expression of *Il1b* and *Icam1* were low in the 30% O_2 group in the heart.

34.4 Discussion

These results support that the amount of supplemental O_2 during the early phase post CA may affect hemodynamics, O_2 consumption, and acid-base metabolism. Animals resuscitated with 100% O_2 achieved faster ROSC than 30% O_2, implying that higher O_2 might contribute to faster recovery of hemodynamics. Moreover, volumetric metabolic measurements and blood gas analyses suggest that 100% O_2 might induce higher VO_2 and the elevation of $PaCO_2$ resulting in more respiratory acidosis, which leads to metabolic

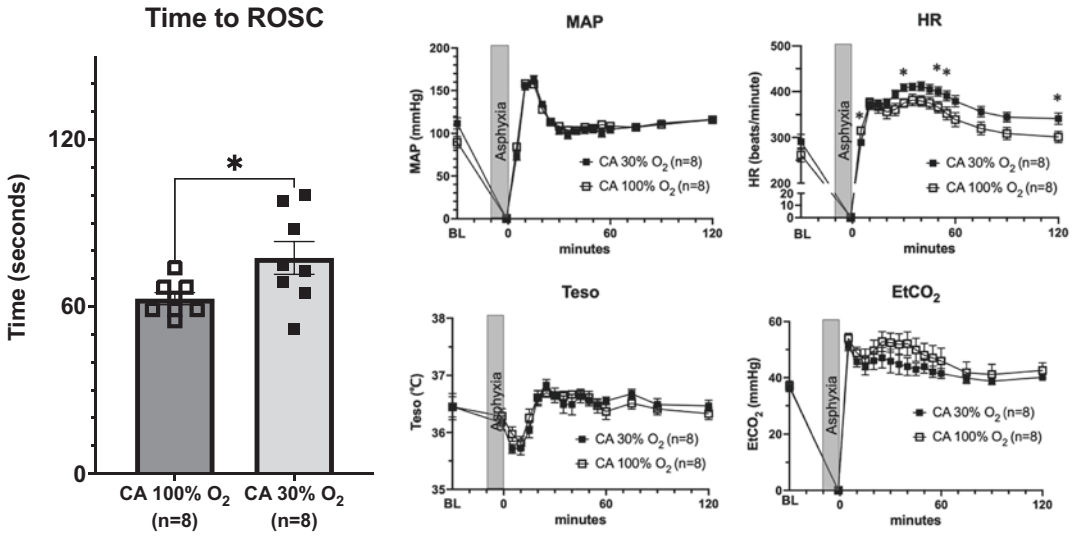

Fig. 34.1 The comparison of time from CPR to ROSC and vital signs between the groups. * $P < 0.05$, t-test

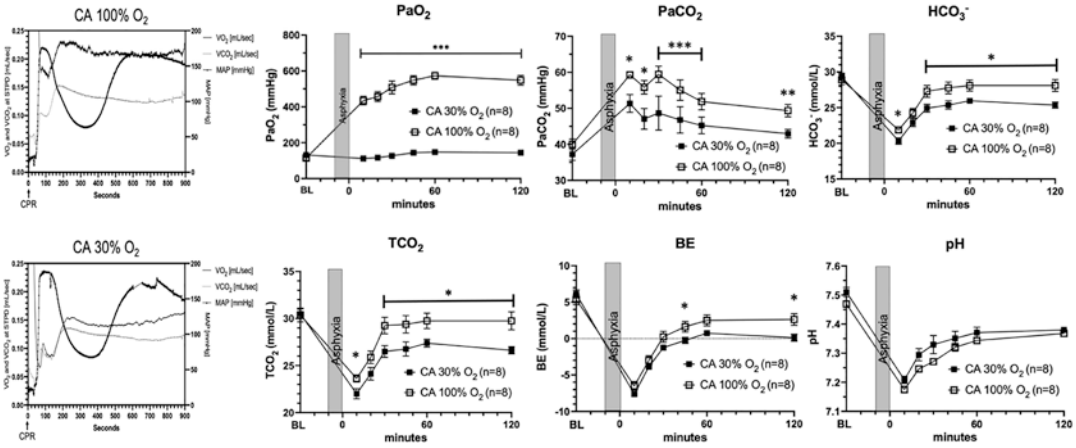

Fig. 34.2 The representative pattern of volumetric metabolic measurement for each group and the arterial blood gas analysis between the groups. * $P < 0.05$, ** $P < 0.01$, *** $P < 0.001$, t-test

compensation for respiratory acidosis. The respiratory acidosis and imposed metabolic compensation might become harmful to the animals or it might be adoptive response from the severely injured animals. In terms of biological responses, 30% O_2 group significantly upregulated inflammation, apoptosis related genes, implying that 30% O_2 might cause unfavorable biological responses 2 hours after CA compared to 100% O_2. Taking into consideration of the known harm of prolonged exposure to 100% O_2, this result can be interpreted that the benefit from faster and O_2 rich resuscitation might outweigh the biological disadvantage from oxidative stress injury induced by 100% O_2. Likewise, oxidative stress mediator *Hmox1* was upregulated in 100% O_2 group in the brain, which might suggest that hyperoxia-induced injury was more significant than that was associated with insufficient O_2 (resuscitation with 30% O_2). We also found that mRNA gene expression of *Il1b* and *Icam1* were low in the 30% O_2 group in the heart. The inconsistent results in the heart tissue may suggest a tissue specific susceptibility, which we will further investigate, in

Table 34.1 Arterial blood gas data at 120 minutes after initiating CPR, including PaO_2, $PaCO_2$, HCO_3^-, TCO_2, BE, and pH

ABG, parameter	CA 30% O_2, mean ± SD, n = 8	CA 100% O_2, mean ± SD, n = 8	*P value*
PaO_2	144.4 ± 20.1	548.3 ± 77.6	$P < 0.001$
$PaCO_2$	43.0 ± 3.0	49.4 ± 4.9	$P < 0.01$
HCO_3^-	25.4 ± 1.2	28.1 ± 2.4	$P < 0.05$
TCO_2	26.6 ± 1.1	29.8 ± 2.7	$P < 0.05$
BE	0.1 ± 1.4	2.6 ± 2.3	$P < 0.05$
pH	7.38 ± 0.03	7.37 ± 0.03	$P = 0.39$

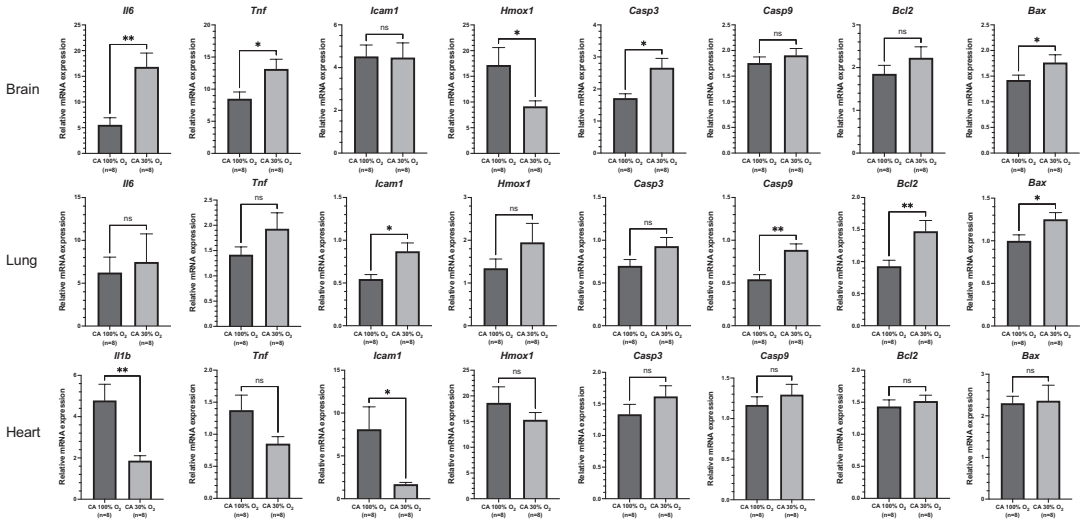

Fig. 34.3 Real time PCR was performed to compare mRNA gene expression in the brain, lung, and heart between the groups. *Il1b*, *Il6*, *Tnf*, *Icam1*, *Hmox1*, *Casp3*, *Casp9*, *Bcl2*, *Bax*. * $P < 0.05$, ** $P < 0.01$, t-test

response to hyperoxia or insufficient O_2 resuscitation. The present study has several limitations. Firstly, we studied bio-physiological insult in post-CA rats, which may be limited in generalizability when the findings are applied to patients. Secondly, we set up a group of experiments with or without high concentration O_2 from the initiation of CPR, however, optimal duration and dosage of O_2 supplementation is still unclear. Lastly, while differences were statistically significant, quite small number of animals subjected to this study require cautious attention in interpreting the significance of the results. Further exploration to determine if the observed differences lead to different biological outcomes is warranted.

34.5 Conclusions

Supplying 30% O_2 during and after CPR significantly delayed the time to ROSC and increased inflammation-/apoptosis- related gene expression in the brain and lung, while excess amount of O_2 intake accelerates O_2 consumption and subsequent CO_2 overproduction, which might have imposed metabolic compensation on the rats. Insufficient O_2 supplementation can result in unfavorable biological responses 2 hours after CA, whereas prolonged exposure to high-concentration O_2 should be still cautious in general due the possible dangers of an increase in oxidative stress.

References

1. Becker LB, Aufderheide TP, Graham R (2015) Strategies to improve survival from cardiac arrest. JAMA 314(3):223–224
2. Panchal AR, Bartos JA, Cabanas JG et al (2020) Part 3: adult basic and advanced life support: 2020 American Heart Association guidelines for cardiopulmonary resuscitation and emergency cardiovascular care. Circulation 142:S366–S468
3. Shinozaki K, Becker LB, Saeki K et al (2018) Dissociated oxygen consumption and carbon dioxide production in the post-cardiac arrest rat: a novel metabolic phenotype. J Am Heart Assoc 7(13):e007721
4. Aoki T, Okuma Y, Becker LB et al (2021) Methodological issue of mitochondrial isolation in acute-injury rat model: asphyxia cardiac arrest and resuscitation. Front Med (Lausanne) 8:666735
5. Aoki T, Wong V, Endo Y et al (2023) Bio-physiological susceptibility of the brain, heart, and lungs to systemic ischemia reperfusion and hyperoxia-induced injury in post-cardiac arrest rats. Sci Rep 13(1):3419

35

Block of the Angiotensin Pathways Affects Flow-Volume Spirometry in Patients with SARS-CoV-2 Infection

Marialuisa Sveva Marozzi, Francesca Mancini, Luciana Loponte, Antonio Giovanni Solimando, Angelo Vacca, and Sebastiano Cicco

Abstract

Background: Angiotensin Converting Enzyme 2 (ACE2) is an endothelial cell receptor used by SARS-CoV- 2 virus to enter cells. Pulmonary function tests (PFTs), mainly spirometry, are the main diagnostic tools for most respiratory diseases. PFTs are mandatory for assessing the response to therapy. Aim: We evaluated patients after the SARS-CoV-2 infection through flow-volume spirometry that evaluates the role of drugs inhibiting the ACE2 pathway. Material and methods: We evaluated 112 Caucasian patients 3–6 months after COVID-19 disease, i.e. after the date of negative molecular or antigenic nasopharyngeal swab. The series of patients showed a great variability due to a wide spectrum of age, the severity of disease manifestations, hospitalization, invasive/non-invasive ventilation, comorbidities, the presence/absence of a previous pneumological diagnosis and the variants of the virus. Patients were divided into those who were being treated with angiotensin receptor blocker (ARB) or ACE2 inhibitors (ACEi) (ARB/ACEi, group 1, 23 females and 12 males, aged 63.63 ± 10.40), and those who were not treated with these drugs (group 2, 38 females and 37 males, aged 55.12 ± 16.51). Distal airflow obstruction (DAO) was evaluate as forced expiratory flow (FEF) at 25%, 50% and 75% of total flow. Results: Group 1 presented lower peripheral oxygen saturation percentage vs group 2 (96.54 ± 3.06 vs 97.30 ± 1.19%, $p < 0.05$). Spirometry data were worst in group1: Forced expiratory volume at first minute (FEV1) (91.20 ± 17.09 vs 97.56 ± 16.40%, $p < 0.05$), Forced vital capacity (94.06 ± 17.48 vs 99.13 ± 17.71%, $p < 0.05$), and Tiffenau Index (0.78 ± 0.12 vs 0.84 ± 0.10, $p < 0.05$). There was a DAO in group1. In group 1, we found also a reduction in FEF 25 (73.97 ± 27.28 vs 86.89 ± 22.44%, $p < 0.05$), FEF 50 (74.69 ± 33.01 vs 85.67 ± 23.74%, $p < 0.05$), and FEF 25-75 (74.14 ± 35.03 vs 83.92 ± 25.38%, $p < 0.05$) but not in FEF 75 (73.06 ± 39.37 vs 82.27 ± 43.33%, $p < 0.05$). Discussion: In patients treated with ARB/ACEi the indexes of respiratory function were shifted towards the lower limits (albeit within normal limits). These parameters were significantly reduced compared to patients not treated with these drugs. This indicates that the COVID-19 disease is not only a pulmonary disease, but also a vascular one.

Keywords

SARS-CoV-2 · Angiotensin pathway · Flow-volume spirometry

M. S. Marozzi (✉) · F. Mancini · L. Loponte
A. G. Solimando · A. Vacca · S. Cicco
Unit of Internal Medicine "G. Baccelli" Department of Precision and Regenerative Medicine and Ionian Area, University of Bari, A.O.U.C. Policlinico di Bari, Bari, Italy

F. Scholkmann et al. (eds.), *Oxygen Transport to Tissue XLIV*, Advances in Experimental Medicine and Biology 1438, https://doi.org/10.1007/978-3-031-42003-0_35

35.1 Introduction

SARS-CoV-2 virus enters endothelial cells using angiotensin converting enzyme 2 (ACE2). Despite acting as a surface receptor, ACE2 degrades the master regulator of the renin-angiotensin-aldosterone system, angiotensin II, thereby converting it into vasodilatory molecules. Viral spike protein (S) on the surface of the virus binds to ACE2, during SARS-CoV-2 infection. Then, the viral particle is endocytosed and acidification of the endosome leads to viral and cellular membrane fusion and release of viral single-stranded RNA into the cytosol. This is one of cellular proinflammatory pathways that support virus-induced downregulation of ACE2 and upregulation of ADAM-17 [1].

The stimulation of the proinflammatory pathways produced a proliferation of pneumocyte type II and an immune cell infiltration, which causes micro-thrombi [2]. Therefore the SARS-CoV-2 infection induces a robust systemic inflammation that presents in a large range of symptoms from mild to severe. Dyspnea, fatigue, fever, malaise and anosmia are the more common symptoms that characterize the coronavirus disease 2019 (COVID-19). The disease may progress to more severe complications, including pneumonia and acute respiratory distress syndrome [3]. Moreover, the disease could have long-term and chronic outcomes as pulmonary fibrosis, chronic thromboembolism and pulmonary hypertension [2, 4].

Pulmonary function tests (PFTs), mainly spirometry, are the main diagnostic tools for most respiratory diseases. PFTs are mandatory for assessing the response to therapy. During the COVID-19 pandemic, the risk of virus transmission by aerosol droplets raised doubts about the safety of PFTs. However, the latest scientific knowledge about Sars-CoV-2 and the vaccination shows that the use of disposable turbines and the application of safety protocols can guarantee a safe procedure for patients and health workers [5].

Spirometry represents a significant means of contagion of COVID-19 during pandemic, due to the particles emitted with the breath and cough. Not until August 2020 was the first summary published of the main international and national guidelines and recommendations regarding the indications for the execution of respiratory function tests in COVID-19 patients and the prevention measures to be adopted by health workers in the PFT laboratories [6].

We evaluated patients after the SARS-CoV-2 infection through flow-volume spirometry that could assess the role of drugs inhibiting the ACE2 pathway. The study evaluates patients who recovered after COVID19 that were under treatment with ACE2 pathway inhibitors both as ACE2 inhibitors (ACEi) or angiotensin receptor blockers (ARB) and ponder the possible correlation between assumption of ACEi and lower indexes of respiratory function after SARS-CoV-2 infection.

35.2 Materials and Methods

35.2.1 Study Population

We retrospectively evaluated 112 Caucasian patients, who were referred to the Unit of internal Medicine "G.Baccelli" of Bari University Hospital for pulmonary evaluation. Patients were evaluated three months after the SARS-CoV-2 infection, that occurs from august 2020 to february 2022. Patients were divided into two groups: Group 1 comprised 35 patients (23 females and 12 males, aged 63.63 ± 10.40) chronically treated for cardiovascular disease/arterial hypertension (Table 35.1) with ARB (28 patients) or ACEi (7 patients). Group 2 comprised 77 patients (38 females and 37 males, aged 55.12 ± 16.51) that were not treated with these drugs. Long COVID and heart failure patients were excluded from the study. Each patient underwent medical examination, peripheral saturation measurement and PFTs, including forced expiratory volume at first minute (FEV1), forced vital capacity (FVC), Tiffenau Index and forced expiratory flow (FEF). The fewest part of both groups had been vaccinated, in particular because a great part of them was infected before the free access to the first dose. Nobody performed second dose before the infection.

Table 35.1 Differences between group 1 and group 2

	Group 1	Group 2	p value
Age	63.63 ± 10.40	55.48 ± 16.49	0.008
Sex (M/F)	23/12	38/39	0.036
Smoke	6	15	Ns
Obesity	2	2	Ns
Lung disease	6	15	Ns
Any cardiovascular disease	35	21	0.0001
Hypertension	34	11	<0.0001
Hospitalization	20	41	Ns
COVID-19 vaccination (first dose)	4	15	Ns

35.2.2 Flow-Volume Spirometry

Flow-volume spirometry was performed 3–6 months after Covid-19 disease recovery, i.e., after the date of negative molecular or antigenic nasopharyngeal swab. Distal airflow obstruction (DAO) was evaluated as FEF at 25%, 50% and 75% of total flow. The same operator performed all flow-volume spirometry, and the same second operator validate the flow-volume spirometry evaluation. Flow volume spirometry was performed with MicroLab portable (CareFusion) and all results were processed by Spirometry PC Software (vyaiere medical).

35.2.3 Statistics

Data were analyzed using SPSS version 21.0 (IBM, USA) and expressed as means ± SD for parametric data and median and interquartile range [IQR] for non-parametric ones. The distribution of dichotomous values was analyzed with Chi-square test. As concerns non-normally distributed data, we performed a non-parametric Mann-Whitney test for comparisons and Spearman distribution for correlations. Normally distributed data were studied with parametric unpaired t-test for comparisons. Statistical significance was indicated with a value of $p < 0.05$.

35.3 Results

35.3.1 Population Differences

Group 1 was older than group 2 (63.63 ± 10.40 vs 55.12 ± 16.51). Moreover, in group 1 there were more male participants than in group 2 (23 females and 12 males vs 38 females and 37 males). The two groups were comparable when it came to smoking habit, BMI, lung disease and course of the disease, however. It appears that group 1 was more affected by cardiovascular disease (35 vs 21) (Table 35.1).

35.3.2 Peripheral Oxygen Saturation Percentage Evaluation

Group 1 presented lower peripheral oxygen saturation percentage (SpO_2) vs group 2 (96.54 ± 3.06 vs 97.30 ± 1.19%, $p < 0.05$) (Fig. 35.1).

35.3.3 Flow Volume Spirometry Evaluation

Analyzing flow volume spirometry data, group 1 showed significant worsening in FEV1, FEF 25-75 and FEF 50 evaluated as absolute volume (Fig. 35.2). However, these results could be conditioned by differences between the two groups.

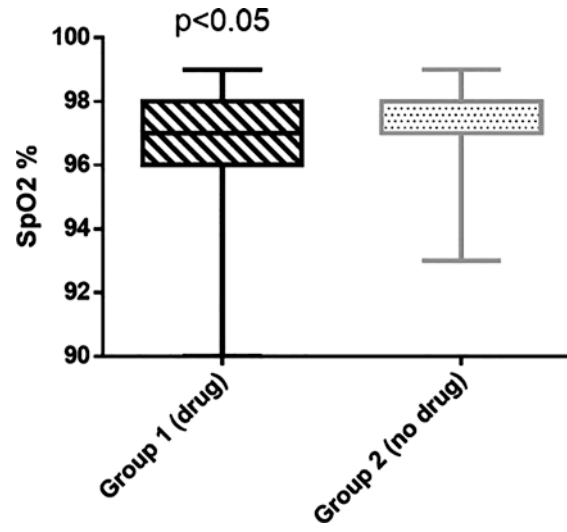

Fig. 35.1 SpO_2 in the two study groups

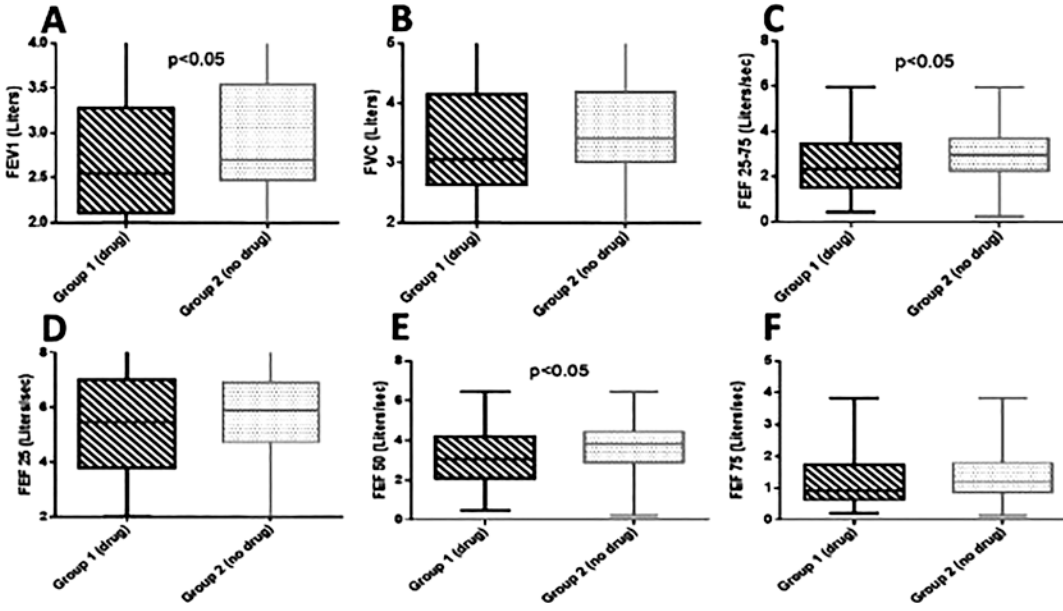

Fig. 35.2 Spirometry flow volume data of group 1 and group 2 in liters. Parameters evaluated are forced expiratory volume at first second (FEV1 – panel **A**), forced vital capacity (FVC – panel **B**), forced expiratory flow (FEF) between 25% and 75% (FEF 25-75 – panel **C**), at 25% (panel **D**), 50% (panel **E**), and at 75% (panel **F**) of vital capacity percent predicted

When adjusted and related to age, sex and body weight, spirometry data were confirmed and showed worse results in group 1 that predicted as a percentage: FEV1 (91.20 ± 17.09 vs 97.56 ± 16.40%, $p < 0.05$), FVC (94.06 ± 17.48 vs 99.13 ± 17.71%, $p < 0.05$), and Tiffenau Index (0.78 ± 0.12 vs 0.84 ± 0.10, $p < 0.05$) (Fig. 35.3).

In group 1, we also found a reduction in FEF 25 (73.97 ± 27.28 vs 86.89 ± 22.44%, $p < 0.05$), FEF 50 (74.69 ± 33.01 vs 85.67 ± 23.74%, $p < 0.05$), and FEF 25–75 (74.14 ± 35.03 vs 83.92 ± 25.38%, $p < 0.05$) but not in FEF 75 (73.06 ± 39.37 vs 82.27 ± 43.33%, $p < 0.05$) (Fig. 35.4).

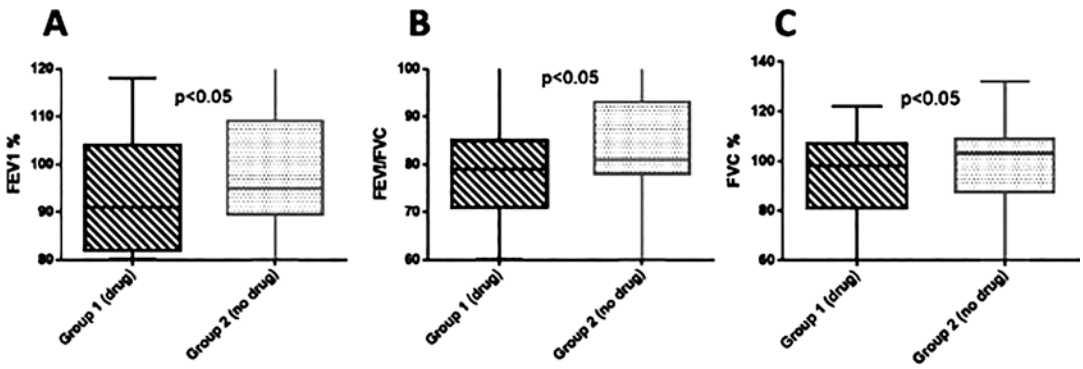

Fig. 35.3 Spirometry flow volume data of group 1 and group 2 in percentage, optimized for age, sex and body weight. Parameters evaluated are forced expiratory volume at first second (FEV1 – panel **A**), Forced vital capacity (FVC – panel **B**) and Tiffenau Index as the ratio between FEV1/FVC (panel **C**)

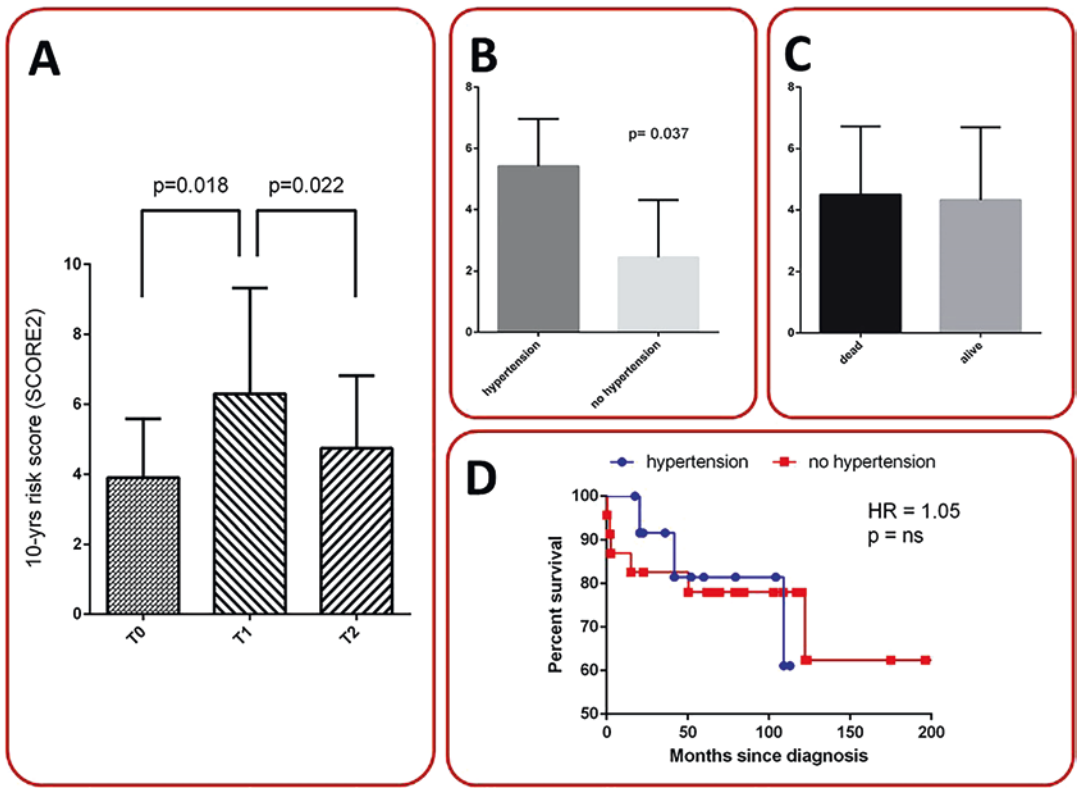

Fig. 35.4 Distal airflow obstruction in flow volume spirometry in group 1 and group 2, evaluated as forced expiratory flow (FEF) between 25% and 75% (FEF 25–75 – panel **A**), at 25% (panel **B**), 50% (panel **C**), and at 75% (panel **D**) of vital capacity percent predicted

All these results were not significant comparing patients who were under ACEi treatment and those with ARB. This may be because the small simple size.

35.4 Discussion

During the COVID-19 pandemic, flow volume spirometry was interdicted for the risk of infec-

tion, until several studies proved that, provided specific guidelines were observed, it could be performed with a very low risk of contagion [6]. Many studies demonstrated the abnormal pulmonary function parameters in patients with previous COVID-19 disease. Moreover, these patients also performed DLCO with overlapping results [7, 8]. Patients treated with ACEi/ARB presented controversial results on PFTs [9–11]. Recently, ACEi appeared to be more related to a deterioriation compared to ARB [9], but conclusive data are yet to be established. COVID-19 patients were affected by an increased risk of cardiovascular disease [12–14]. Furthermore, in literature is proved that ACEi/ARB was not associated with an increase of COVID-19 risk or a worse prognosis [15] and had positive effect on reducing D-dimer and symptoms [16]. The several controversial about this topic has been evaluated also by the Italian Ministry of Health, showing a significant protective effect of ACEi/ARB with a better prognosis [17]. In fact, it has been confirmed that elderly patients who had recovered from severe SARS-CoV-2 infection and were previously treated with ARB/ACEi, present with a decrease in lung damage evaluated with DLCO spirometry, despite the same result not being detected in younger patients [18]. The data that we collected and analyzed in this study underline others results. SpO_2 and DAO in patients who have been affected by COVID-19 disease and consumed ARB/ACEi long term are worse than those did not consume these drugs. Furthermore, the most significant results are in the latest part of FEF. Although the results are worse, the data are within the normal range with a deflection of the flows of the small airways. Therefore, from a diagnostic point of view, the data we found are comparable with those already present in the literature, highlighting however how DAO in patients who assumed ACEi/ARB undergoes a significant deterioration compared to patients who did not take this therapy. In conclusion, these numbers suggest that ARB/ACEi could have a cardiovascular protective role and could reduce SARS-CoV-2-related lung injury. However, investigation is still needed as to how the infection acts more on the small airways and if these values are confirmed 1 year after recovery, or if there is a complete recovery of lung function in these patients.

35.4.1 Limitations

This study has clear limitations. First, it is a single-center study with a small cohort of patients. This impacts also on the possibility to have a good comparison among ACEi and ARB. Moreover, flow volume spirometry before COVID-19 disease has not been performed and we do not have data to make a comparison of DAO before and after the disease. Furthermore, performing a DLCO to all patients could have helped interpret results. Finally, there was no COVID-free group as a double negative control group to test if it is possible that these results could be related to the drugs. Further studies are needed to understand the role of SARS-CoV- 2 and/or of ACEi/ARB in tissue oxygenation. Finally, type of SARS-CoV-2 variant was not available and we are not able to identify a more specific variant effect on DAO. However, considering the time of recruitment and epidemiology in Italy and Europe19, we could estimate the patients may be infected from Alpha up to Omicron BA.3 variants.

35.5 Conclusions

In patients treated with ARB/ACEi the indexes of respiratory function were shifted towards the lower limits (albeit within normal limits). These parameters were significantly reduced compared to patients not treated with these drugs. This may support that COVID-19 disease is not only a pulmonary, but also a vascular disease. Although the increase in group 1 of male and older patients is significant, the indexes of spirometry values are corrected for age, sex and body weight, so it doesn't influence the results of the DAO and the reduction of FEV1 and FVC. Further studies may be useful to understand the role of ARB/ACEi in long-COVID-19 lung disease and the role of ARB/ACEi and/or SARS-CoV-2 in tissue oxygenation.

References

1. Groß S, Jahn C, Cushman S, Bär C, Thum T (2020) SARS-CoV-2 receptor ACE2-dependent implications on the cardiovascular system: from basic science to clinical implications. J Mol Cell Cardiol [Internet] 144(April):47–53. Available from: https://doi.org/10.1016/j.yjmcc.2020.04.031
2. Cicco S, Vacca A, Cittadini A, Marra AM (2020) Long-term follow-up may be useful in coronavirus disease 2019 survivors to prevent chronic complications. Infect Chemother [Internet] 52(3):407. Available from: https://doi.org/10.3947/ic.2020.52.e44
3. Berlin DA, Gulick RM, Martinez FJ (2020) Severe Covid-19. N Engl J Med 383(25):2451–2460
4. Cicco S, Albanese F, Didonna R, et al (2023) Pulmonary embolism in Covid-19 patients is not related to a deterioration of tissue oxygenation. Adv Exp Med Biol; Oxygen Tra
5. Klain A, Indolfi C, Dinardo G, Decimo F, Miraglia Del Giudice M (2022) Covid-19 and spirometry in this age. Ital J Pediatr 48(1):4–9
6. Crimi C, Impellizzeri P, Campisi R, Nolasco S, Spanevello A, Crimi N (2021) Practical considerations for spirometry during the COVID-19 outbreak: literature review and insights. Pulmonology [Internet] 27(5):438–447. Available from: https://doi.org/10.1016/j.pulmoe.2020.07.011
7. Jennings G, Monaghan A, Xue F, Mockler D, Romero-Ortuño R (2021) A systematic review of persistent symptoms and residual abnormal functioning following acute covid-19: Ongoing symptomatic phase vs. post-covid-19 syndrome. J Clin Med 10(24):5913
8. Torres-Castro R, Vasconcello-Castillo L, Alsina-Restoy X et al (2021) Respiratory function in patients post-infection by COVID-19: a systematic review and meta-analysis. Pulmonology [Internet] 27(4):328–337. Available from: https://doi.org/10.1016/j.pulmoe.2020.10.013
9. Jabbar AS, Neamah NF, Al-Darraji AH (2022) Comparative effects of angiotensin-converting enzyme inhibitors and angiotensin II receptor blockers on pulmonary function in hypertensive patients. J Basic Clin Physiol Pharmacol 33(2):207–212
10. Faggiano P, Lombardi C, Sorgato A, Ghizzoni G, Spedini C, Rusconi C (1993) Pulmonary function tests in patients with congestive heart failure: effects of medical therapy. Cardiology 83(1–2):30–35
11. Riska H, Sovijärvi ARA, Ahonen A, Salorinne Y, Sundberg S, Stenius-Aarniala B (1990) Effects of captopril on blood pressure and respiratory function compared to verapamil in patients with hypertension and asthma. J Cardiovasc Pharmacol [Internet] 15(1):57–61. Available from: http://journals.lww.com/00005344-199001000-00009
12. Mozzini C, Cicco S, Setti A et al (2021) Spotlight on cardiovascular scoring systems in Covid-19: severity correlations in real-world setting. Curr Probl Cardiol [Internet] 46(5):100819. Available from: https://doi.org/10.1016/j.cpcardiol.2021.100819
13. Cicco S, Mozzini C, Marozzi M et al (2022) Cardiovascular risk score may be useful in stratify death risk in hospitalized Covid19 patients. J Hypertens [Internet] 40(Suppl 1):e172. Available from: https://journals.lww.com/10.1097/01.hjh.0000837136.87315.11
14. Cicco S, Mozzini C, Carella R, et al (2023) Cardiovascular risk score and pulmonary gas exchange in COVID-19 patients show no correlation. Adv Exp Med Biol; Oxygen Tra
15. Azevedo RB, Botelho BG, de Hollanda JVG et al (2021) Covid-19 and the cardiovascular system: a comprehensive review. J Hum Hypertens [Internet] 35(1):4–11. Available from: https://doi.org/10.1038/s41371-020-0387-4
16. Xue Y, Sun S, Cai J et al (2020) Effects of ACEI and ARB on COVID-19 patients: a meta-analysis. JRAAS - J Renin-Angiotensin-Aldosterone Syst 21(4):1470320320981321
17. Cippà PE, Cugnata F, Ferrari P et al (2020) A data-driven approach to identify risk profiles and protective drugs in COVID-19. Proc Natl Acad Sci U S A 118(1):1–7
18. Gori M, Ghirardi A, D'Elia E et al (2022) Association between inhibitors of the renin-angiotensin system and lung function in elderly patients recovered from severe COVID-19. Eur J Prev Cardiol 29(5):E196–E199

36

A Prospective Observational Pilot Study on the Effects of the Activity-Based Stress Release Program on the Mental State and Autonomic Nervous System in Psychiatric Patients

Evelyne Kloter, Lorena Walder-Rohner, Harald Haas, Theodor Hundhammer, and Ursula Wolf

Abstract

Background: In our pilot study, we investigated the psychological (well-being and personal coping strategies) and physiological (assessed by heart rate variability (HRV)) effects of the newly developed activity-based stress release (ABSR) program for people with depressive disorders, also in combination with burnout symptoms and/or anxiety disorders. Methods: A single-arm prospective observational study was carried out. Twenty participants diagnosed with depression and burnout or anxiety disorders were invited to participate in the 8-week ABSR program. All participants filled in two questionnaires (the multidimensional mental state questionnaire and the Ehrenfeld inventory on coping style) before, directly after and 2 months after the 8-week ABSR program. In addition, all participants were offered a 24-hour Holter ECG measurement before, directly after and 2 months after the 8-week ABSR program to measure HRV. Results: Calmness and serenity showed a statistically significant improvement after the 8-week ABSR program. However, complete questionnaire sets were not available from all of the participants. In the four individuals who had agreed to a 24-hour Holter ECG, the overall HRV and parasympathetic activity increased. Conclusions: The ABSR program is an encouraging novel therapeutic approach: A significant improvement in calmness and serenity was observed after ABSR. A larger and controlled trial of this treatment option in depression and burnout is recommended. It should be further investigated how ABSR affects task-evoked and resting brain activity, and what effects it has on the cardiovascular system in general (better blood flow and normalization of activity are to be expected).

Evelyne Kloter and Lorena Walder-Rohner shared the first authorship.

E. Kloter · L. Walder-Rohner · U. Wolf (✉)
Institute of Complementary and Integrative Medicine, University of Bern, Bern, Switzerland
e-mail: ursula.wolf@unibe.ch

H. Haas
Private Practice for Psychiatry and Psychotherapy, Bern, Switzerland

T. Hundhammer
Private Practice for Eurythmy Therapy, Bern, Switzerland

F. Scholkmann et al. (eds.), *Oxygen Transport to Tissue XLIV*, Advances in Experimental Medicine and Biology 1438, https://doi.org/10.1007/978-3-031-42003-0_36

Keywords

Activity-based stress release · Depression · Autonomic nervous system

36.1 Introduction

Depression can occur at any age and in any social class. The risk of developing depression is increased in case of poverty, unemployment, life events such as the death of a loved one or separation, physical illness, and alcohol or drug abuse. Depression can be treated with psychological approaches such as cognitive behavioral therapy or interpersonal psychotherapy and with antidepressant medication. There is also evidence that mindfulness-based interventions reduce stress, anxiety and depression and help to improve psychological functioning [1–3].

The activity-based stress release (ABSR) program was developed in the 2000s based on the ideas of anthroposophic medicine and the publication "Overcoming Nervousness" by R. Steiner [4]. The basic idea of the program is that through mindfulness of one's own thinking, feeling and acting, one's relationship to the world can be transformed toward more self-determined and interactive participation in everyday life [5]. Anthroposophic medicine is based on, and fully includes, modern conventional medicine, but extends this view with methodical, diagnostic and therapeutic approaches focused on the whole person. Anthroposophic medicine accounts equally for the physical, psychological and spiritual side of the patient as well as their unique biographies [6]. Mindfulness has an effect on cognitive-affective neural plasticity [7], and mindfulness training has been shown to be associated with changes in task-evoked hemodynamic changes in the brain and resting-state brain activity [8, 9]. The aim of our pilot study was to obtain first indications of efficacy on well-being, personal coping strategies and physiological effect (i.e., changes in heart rate variability (HRV)) induced by the ABSR program in patients with a psychiatric disorder. We hypothesized that individuals with depression and burnout or other psychiatric disorders may benefit from the ABSR program. The findings should provide the basis for further research and assist in developing an evidence-based ABSR program for this population within a framework of holistic, individualized, patient-oriented and preventive programs to counteract the trend toward these illnesses.

36.2 Methods

This study was carried out as an observational prospective pilot study addressing the ABSR program in patients with a psychiatric disorder and assessing the impact of this intervention on well-being, personal coping strategies and HRV. All 20 study participants were recruited at a psychiatric practice in Bern, Switzerland. All participants were diagnosed with depressive disorders, and some of them also exhibited burnout symptoms or anxiety disorders.

With the help of a combination of mental, behavioral and eurythmy exercises, a new inner orientation may be trained and made available for everyday life. Eurythmy therapy is a mindful movement therapy developed by Rudolf Steiner in 1921. It transforms vowels and consonants of speech into specific gestures and artistic movements. The whole ABSR program was conducted three times with three different groups. The program included a training session once a week over a period of 8 weeks. A single training session lasted 1 hour and 45 minutes and was performed in the group. Participants were also encouraged to share their experiences of the program with each other. Toward the end of the training session, the participants were familiarized with a sequence of eurythmy exercises. In between the group sessions, participants conducted regular individual training at home for the mental, behavioral and eurythmy exercises. In all three groups, a follow-up meeting took place 2 months after completion of the ABSR program.

To record psychological changes, all participants were invited to complete two questionnaires, the Multidimensional mental state questionnaire (MDSQ) and the Ehrenfeld inventory on coping style (EICS). The questionnaires

were distributed and collected at three different timepoints: (i) At the beginning of the first meeting (baseline), (ii) up to 2 weeks after completion of the ABSR program (post-measurement) and (iii) between 8 and 12 weeks after completion of the ABSR program (follow-up).

To record physiological changes, 24-hour Holter ECGs were carried out with a 3-channel ECG device (Schiller - medilog®AR12 plus) to determine HRV at these three different timepoints: (1) During the first half of the ABSR program (baseline), (2) immediately or up to 4 weeks after completion of the ABSR program (post-measurement) and (3) between nine and 12 weeks after completion of the ABSR program (follow-up). The participants were asked to follow their normal daily activities and to keep an activity protocol throughout the measurement period. The ECG recordings were evaluated during the first 3.5 hours of sleep, because all participants had valid ECG signals at that time. In the activity protocol, the participants recorded the time they went to bed. This time was verified with the motion sensor in the ECG device. The sleep phase was defined as the period starting 30 minutes after bedtime and containing minimal movements. The following HRV parameters were evaluated in this study: (i) Standard deviation of all NN intervals (SDNN), (ii) Percentage of heartbeats with a duration of NN ≥50 ms (pNN50), (iii) Root mean square of successive RR interval differences (RMSSD), (iv) High-frequency component of HRV (HF). The ECG signals were read into the Medilog Darwin 2 software before being exported as ".edf" files into the Kubios HRV software (kubios.com, Kuopio, Finland) for data analysis. In the Kubios program, artifact correction was set to "medium" and the "remove trend components" option was set to "none". The evaluation of the HRV was carried out descriptively.

Well-being was evaluated through the MDSQ. The MDSQ consists of 24 items (each with a five-step response scale) to measure three bipolar dimensions of current psychological well-being: Good-bad mood, wakefulness-fatigue and calmness-restlessness. A higher value indicates a better mood, higher wakefulness and greater calmness. All three scales can be divided into two parallel test halves, each of which can be used to measure the progression of mental well-being. Personal coping strategies were evaluated through the EICS consisting of 23 items that can be assigned to six scales: "Active problem solving", "palliative behavior", "avoidance", "social support", "depressive reaction" and "consoling thoughts". A subscale "inadequate coping" was calculated from the categories "palliative behavior", "avoidance" and "depressive reaction". The scores of both questionnaires were compared in the statistics program R version 3.2.1 (The R Foundation for Statistical Computing, Vienna, Austria) by the Friedmann test at baseline, post-measurement and follow-up. The Nemenyi test was used as a post-hoc test for a pairwise multiple comparison. All tests were performed two-sided with a significance level of 0.05. Categorical variables, are shown as numbers and percentages. Continuous variables are shown as median [25th percentile; 75th percentile].

36.3 Results

Eleven participants completed the MDSQ at all three timepoints (baseline, post-measurement and follow-up), and ten participants completed the EICS at all three timepoints, i.e., 55% and 50%, respectively, of all participants. Figure 36.1 gives an overview of the responsiveness to the questionnaires.

The median age of the participants was 50 years. Seventeen of the participants were women, which corresponds to 85%. Table 36.1 contains the scores of the questionnaires at baseline, post-measurement and follow-up.

The score of the subscale "calmness-restlessness" of the MDSQ increased from a median of 25 in the baseline-measurement to a median of 30 in the post-measurement indicating greater calmness. At 2-month follow-up, the median was also 30. This result is significant with a p-value <0.05. Two participants attended only five of the eight lessons. These two were excluded in a sensitivity analysis. The participants included in Table 36.2 attended at least six of the eight lessons.

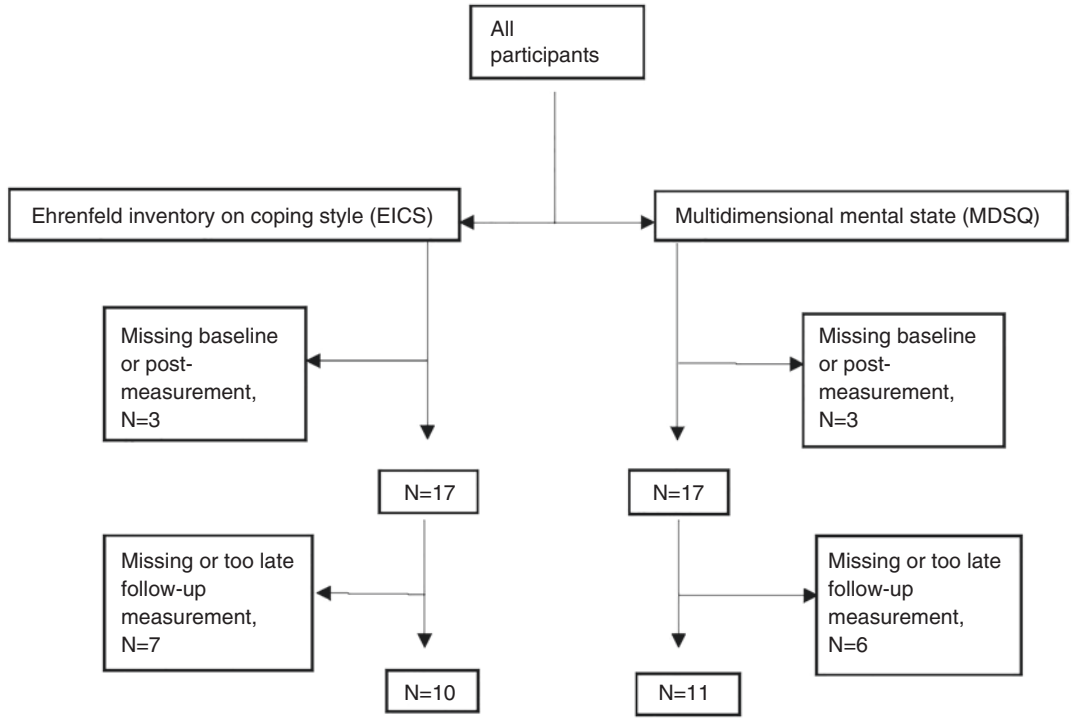

Fig. 36.1 Flow chart of responsiveness to the questionnaires

Table 36.1 Scores of the questionnaires at baseline, post-measurement and follow-up

	Baseline	Post-measurement	Follow-up	N	p-value
MDSQ					
Good-bad mood	24.0 [19.3, 31.8]	29.0 [26.3, 30.5]	29.0 [26.5, 30.0]	10	0.13
Wakefulness-fatigue	25.0 [21.8, 31.0]	24.5 [20.3, 28.8]	23.5 [12.5, 32.5]	10	0.37
Calmness-restlessness	25.0 [20.5, 28.0]	30.0 [25.5, 32.5]	30.0 [25.0, 35.0]	11	0.006*
EICS					
Active problem solving	8.0 [7.3, 9.0]	8.0 [7.0, 9.0]	8.5 [7.3, 9.8]	10	0.59
Palliative behavior	11.5 [9.5, 12.0]	10.5 [10.0, 11.8]	11.0 [11.0, 12.8]	10	0.18
Avoidance	7.0 [5.0, 10.0]	8.0 [6.0, 8.0]	6.0 [6.0, 8.0]	9	0.91
Depressive reaction	12.0 [10.3, 12.4]	9.5 [9.0, 11.4]	10.5 [9.3, 11.9]	10	0.26
Social support	7.0 [6.0, 7.8]	8.0 [5.3, 8.8]	6.5 [5.3, 8.0]	10	0.79
Consoling thoughts	7.0 [6.0, 7.0]	6.8 [6.0, 7.8]	6.5 [6.0, 8.5]	10	0.80
Inadequate coping	31.0 [28.5, 31.0]	30.0 [25.0, 31.0]	29.0 [26.0, 31.0]	9	0.40

N: Number of participants without missing data at baseline, post-measurement and follow-up Values are shown as median [25th percentile, 75th percentile] and numbers (percent)

*p-value baseline/post-measurement = 0.05; p-value baseline/follow-up = 0.02; p-value post-measurement/follow-up = 0.91 (Nemenyi post-hoc test), Baseline: during the first session of the ABSR program, Post-measurement: up to 2 weeks after completion of the ABSR program, Follow-up: between eight and 12 weeks after completion of the ABSR program

In four participants, 24-hour Holter ECG measurements were carried out to assess HRV. The average age of these four participants was 52 years (age range 50–55 y, 2 female, 2 male). One participant, who was not included in the MDSQ or EICS analysis, attended only four ABSR sessions and participated in only two 24-hour Holter ECG measurements: the post-

Table 36.2 Scores of the questionnaires at baseline, post-measurement and follow-up

	Baseline	Post-measurement	Follow-up	N	p-value
MDSQ					
Good-bad mood	24.0 [20.0, 32.0]	29.0 [27.0, 31.0]	30.0 [28.0, 30.0]	9	0.25
Wakefulness-fatigue	25.0 [21.8, 31.0]	24.5 [20.3, 28.8]	23.5 [15.3, 23.5]	10	0.37
Calmness-restlessness	24.0 [19.8, 28.0]	30.0 [24.8, 32.8]	31.0 [25.3, 35.5]	10	0.01*
EICS					
Active problem solving	8.0 [7.8, 9.3]	8.0 [7.0, 9.3]	8.5 [7.8, 10.0]	8	0.50
Palliative behavior	11.0 [8.8, 12.0]	10.0 [9.5, 11.3]	11.0 [10.5, 12.3]	8	0.19
Avoidance	7.0 [5.5, 8.5]	8.0 [5.5, 8.0]	6.0 [5.5, 7.5]	7	0.85
Depressive reaction	11.5 [10.0, 12.1]	9.0 [8.8, 10.3]	10.0 [9.0, 11.3]	8	0.34
Social support	7.0 [5.5, 7.3]	8.0 [5.5, 8.3]	6.5 [5.8, 8.3]	8	0.87
Consoling thoughts	7.0 [5.8, 7.0]	6.5 [6.0, 8.0]	7.0 [6.0, 9.0]	8	0.53
Inadequate coping	31.0 [27.3, 31.0]	28.0 [23.0, 30.5]	29.9 [24.5, 30.0]	7	0.11

N: Number of participants without missing data at the baseline, post-measurement and follow-up Values are shown as median [25th percentile, 75th percentile] and numbers (percent)
*p-value baseline/post-measurement = 0.11; p-value baseline/follow-up = 0.02; p-value post-measurement/follow-up = 0.78 (Nemenyi post-hoc test), Baseline: during the first session of the ABSR program; Post-measurement: up to 2 weeks after completion of the ABSR program; Follow-up: between eight and 12 weeks after completion of the ABSR program

measurement was missing. In the post-measurement, two out of three participants showed an increase in SDNN, pNN50% and RMSSD compared to baseline. One participant showed a decrease in SDNN, pNN50% and RMSSD. At follow-up, all four participants showed an increase in SDNN, pNN50% and RMSSD compared to baseline (shown in Fig. 36.2). The HF was greater in the follow-up measurement for all four participants compared to the baseline. Post-measurement data was obtained for three participants. In comparison to the baseline, two participants showed an increase in HF, while one participant showed a decrease in the HF (shown in Fig. 36.2).

36.4 Discussion and Conclusions

The purpose of this pilot study was to obtain a first indication of the effects of an 8-week ABSR program in patients with depression and/or burnout or other psychiatric disorders. This was the first study to test the ABSR program. In the evaluation of the questionnaires, the analysis of the MDSQ showed a significant improvement in the subscale "calmness-restlessness" with an increase from 25 to 30 points. This indicates higher calmness and serenity. Since our sample size was small, a significant result here indicates a strong effect. This is comparable to the effects of other mindfulness-based interventions against stress, such as mindfulness-based cognitive therapy. Khoury et al. reported in a meta-analysis that mindfulness-based therapies are effective for various psychological disorders and are particularly effective in reducing anxiety, stress and depression [1]. Hofmann et al. reported that mindfulness-based interventions may lead to a general reduction of stress [2]. It was further reported that mindfulness-based therapies could probably not only be used for specific diagnoses but can instead address salutogenetic processes that are important to counteract various diseases [2]. The group examined here comprised mixed diagnoses; depressive disorder was present in all participants but some had additional burnout symptoms or anxiety disorders. This shows that the salutogenetic ABSR may be beneficial for various/different diagnoses.

No significant effect on coping strategies was observed. In another study examining the effect of mindfulness meditation in women with breast cancer, a significant improvement in coping strategies was observed [10]. Weinstein et al. showed that mindful individuals reported less frequent use of avoidant coping strategies [11]. In another study, healthy subjects were shown to exhibit

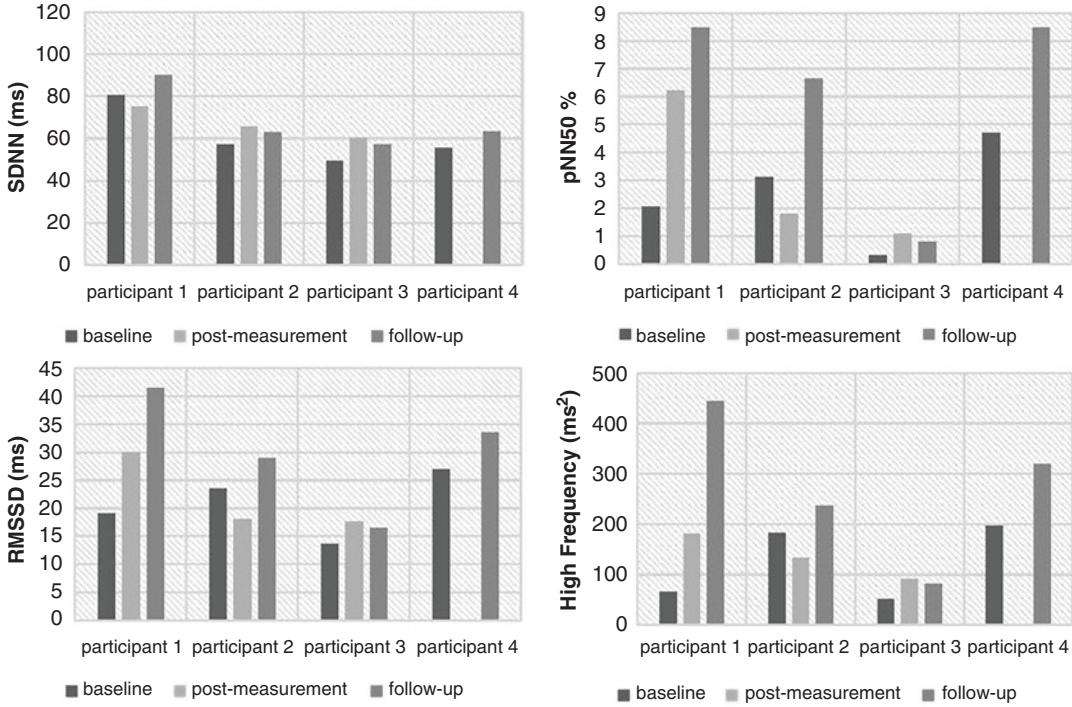

Fig. 36.2 HRV Time domain parameters: SDNN, pNN50% and RMSSD and HRV Frequency domain parameter: High-Frequency domain: parasympathetically determined oscillatory component of respiratory sinus arrhythmia (RSA) and thus the atemsynchronous heart rate fluctuation (ms^2: miliseconds squared)

healthier stress management strategies after only 6 weeks of eurythmy therapy [12]. In our study the coping improved, but not significantly ($p = 0.11$). This may mean that ABSR also improves coping strategies, but that our pilot study was not sufficiently powered to show this effect.

Regarding HRV, the study population was too small for statistical analysis. In all four participants examined here, there was an overall increase in HRV at the follow-up measurement compared to baseline, which represents a more efficient autonomic regulatory control and an increase in overall health [13]. It has to be noted that there is considerable methodological variability in the reported HRV metrics in the existing literature. This makes it difficult to compare the results of different studies. In principle, an evaluation of 24-hour ECGs would be possible. However, the conditions during these 24 hours would have to be specified more precisely than in our study to ensure comparable daily activity of participants. In healthy individuals, the 24-hour HRV is strongly dependent on activity. A comparison of 24-hour analyses with different activity levels is therefore not useful. For this reason, we only evaluate the data of the sleep phase to ensure equal activity and position between patients [14].

The results show that the proposed measures, the MDSQ, EICS and measurement of HRV are in principle feasible and likely to yield meaningful results. The strength of this study was that both psychological and physiological parameters were examined. The two questionnaires capture both the current state of mind and coping strategies. HRV is a recognized instrument for functional diagnostics of the autonomic nervous system. In this pilot study, we show that MDSQ, EICS and HRV are appropriate measures to assess the newly developed ABSR program. In a future study, the number of completed questionnaires and 24-hour Holter ECG measurements needs to be increased. A significant improvement

in calmness and serenity was observed after ABSR. Overall, this study encourages further investigations of the ABSR program in larger, controlled studies to determine the effectiveness of ABSR for patients with depression and/or burnout. It should be further investigated how ABSR affects task-evoked and resting brain activity, and what effects it has on the cardiovascular system in general (better blood flow and normalization of activity are to be expected). Furthermore, future investigations should investigate the effect of ABSR on the pulse-respiration quotient, a parameter that determines the complex regulatory states of the cardiorespiratory system [15, 16].

Acknowledgement We thank all participants of the study as well as Delphine Meier, Felix Scholkmann and Hamoon Zohdi for valuable discussion.

References

1. Khoury B, Lecomte T, Fortin G, Masse M, Therien P, Bouchard V et al (2013) Mindfulness-based therapy: a comprehensive meta-analysis. Clin Psychol Rev 33:763–771. https://doi.org/10.1016/j.cpr.2013.05.005
2. Hofmann SG, Sawyer AT, Witt AA, Oh D (2010) The effect of mindfulness-based therapy on anxiety and depression: a meta-analytic review. J Consult Clin Psychol 78:169–183. https://doi.org/10.1037/a0018555
3. Janssen M, Heerkens Y, Kuijer W, van der Heijden B, Engels J (2018) Effects of mindfulness-based stress reduction on employees' mental health: a systematic review. PLoS One 13:e0191332. https://doi.org/10.1371/journal.pone.0191332
4. Steiner R (2008) How to cure nervousness. Rudolf Steiner Press, p GA 143
5. Haas H, Hundhammer T (2015) Ich möchte mein Leben wandeln! - Gruppentherapie auf der Grundlage eines anthroposophischen Achtsamkeitsprogrammes. https://docplayer.org/42372196-Ich-moechte-mein-leben-wandeln.html (Accessed May 1, 2023)
6. What is anthroposophic medicine? – Anthroposophic Medicine – Medical Section Dornach, https://medsektion-goetheanum.org/en/anthroposophic-medicine/what-is-anthroposophic-medicine (Accessed May 1, 2023)
7. Allen M et al (2012) Cognitive-affective neural plasticity following active-controlled mindfulness intervention. J Neurosci 32 (44:15601–15610
8. Gundel et al (2018) Meditation and the brain – neuronal correlates of mindfulness as assessed with near-infrared spectroscopy. Psychiatry Res Neuroimaging 271:24–33
9. Sezer et al (2022) Resting-state fMRI functional connectivity and mindfulness in clinical and non-clinical contexts: a review and synthesis. Neurosci Biobehav Rev 135:104583
10. Gok Metin Z, Karadas C, Izgu N, Ozdemir L, Demirci U (2019) Effects of progressive muscle relaxation and mindfulness meditation on fatigue, coping styles, and quality of life in early breast cancer patients: an assessor blinded, three-arm, randomized controlled trial. Eur J Oncol Nurs 42:116–125. https://doi.org/10.1016/j.ejon.2019.09.003
11. Weinstein N, Brown KW, Ryan RM (2009) A multi-method examination of the effects of mindfulness on stress attribution, coping, and emotional well-being. J Res Personal 43:374–385. https://doi.org/10.1016/j.jrp.2008.12.008
12. Kanitz JL (2016) Untersuchung psychometrischer und physiologischer Wirkungen anthroposophischer Therapien aus dem Bereich der Mind-Body Therapien. Doctoral thesis, Charité Universitätsmedizin Berlin (Germany)
13. Christodoulou G, Salami N, Black DS (2020) The utility of heart rate variability in mindfulness research. Mindfulness 11:554–570. https://doi.org/10.1007/s12671-019-01296-3
14. Bauer A, Camm AJ, Cerutti S, Guzik P, Huikuri H, Lombardi F et al (2017) Reference values of heart rate variability. Heart Rhythm 14:302–303. https://doi.org/10.1016/j.hrthm.2016.12.015
15. Scholkmann F, Wolf U (2019) The pulse-respiration quotient: a powerful but untapped parameter for modern studies about human physiology and pathophysiology. Front Physiol 10:371
16. Scholkmann F, Zohdi H, Wolf U (2019) The resting-state pulse-respiration quotient of humans: lognormally distributed and centred around a value of four. Physiol Res 68(6):1027–1032

Index

F. Scholkmann et al. (eds.), *Oxygen Transport to Tissue XLIV*, Advances in Experimental Medicine and Biology 1438, https://doi.org/10.1007/978-3-031-42003-0